ADA 252 973

DISCLAIMER NOTICE

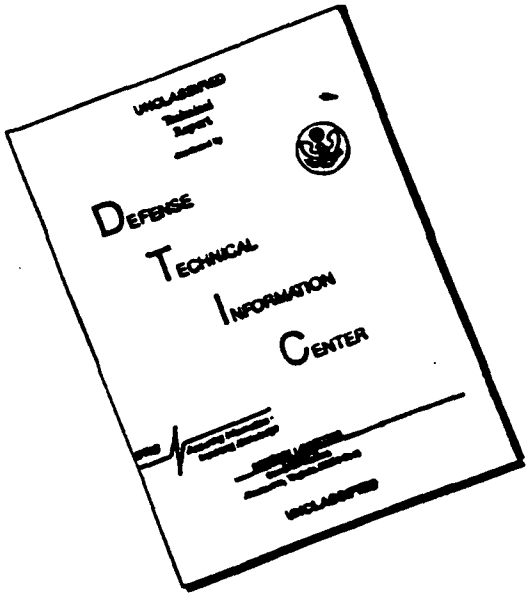

THIS DOCUMENT IS BEST QUALITY AVAILABLE. THE COPY FURNISHED TO DTIC CONTAINED A SIGNIFICANT NUMBER OF PAGES WHICH DO NOT REPRODUCE LEGIBLY.

REPORT DOCUMENTATION PAGE

Form Approved
OMB No 0704-0188

Public reporting burden for this collection of information is estimated to average 1 hour per response, including the time for reviewing instructions, searching existing data sources, gathering and maintaining the data needed, and completing and reviewing the collection of information. Send comments regarding this burden estimate or any other aspect of this collection of information, including suggestions for reducing this burden, to Washington Headquarters Services, Directorate for Information Operations and Reports, 1215 Jefferson Davis Highway, Suite 1204, Arlington, VA 22202-4302, and to the Office of Management and Budget, Paperwork Reduction Project (0704-0188), Washington, DC 20503.

1. AGENCY USE ONLY (Leave blank)	2. REPORT DATE	3. REPORT TYPE AND DATES COVERED
	May 22, 1992	Final 1/1/91-12/31/91

4. TITLE AND SUBTITLE

Organization of the 1991 Optical Society of America Photonic Science Topical Meeting Series

5. FUNDING NUMBERS

G - AFOSR-91-0176

6. AUTHOR(S)

Jarus W. Quinn

7. PERFORMING ORGANIZATION NAME(S) AND ADDRESS(ES)

Optical Society of America
2010 Massachusetts Ave. NW
Washington, DC 20036

8. PERFORMING ORGANIZATION REPORT NUMBER

AFOSR-TR- 2 0512

9. SPONSORING/MONITORING AGENCY NAME(S) AND ADDRESS(ES)

US Air Force Office of Scientific Research
Department of the Air Force
Bolling Air Force Base
Washington, DC 20332-6448

NE

Schlossberg

10. SPONSORING/MONITORING AGENCY REPORT NUMBER

2305/A1

11. SUPPLEMENTARY NOTES

12a. DISTRIBUTION/AVAILABILITY STATEMENT

Approved for public release
Distribution unlimited

12b. DISTRIBUTION CODE

13. ABSTRACT (Maximum 200 words)

Attach list of reports supported by Optical Society of America
Photorefractive Materials, Effects, and Devices
Integrated Photonics Research
Nonlinear Guided Wave Phenomena
Optical Amplifiers and Their Applications
Optical computing
Picosecond Electronics and Optoelectronics
Quantum Optoelectronics
Photonic Switching
Microphysics of Surfaces: Beam Induced Processes
Soft X-ray Projection Lithography
Short Wavelength Coherent Radiation, Generation & Applications
Presistent Spectral Hole-Buring: Science & Applications

14. SUBJECT TERMS

15. NUMBER OF PAGES

16. PRICE CODE

17. SECURITY CLASSIFICATION OF REPORT	18. SECURITY CLASSIFICATION OF THIS PAGE	19. SECURITY CLASSIFICATION OF ABSTRACT	20. LIMITATION OF ABSTRACT
[redacted]	[redacted]	[redacted]	[redacted]

OSA Proceedings on

SHORT-WAVELENGTH COHERENT RADIATION: GENERATION AND APPLICATIONS

Volume 11

92-15632

Accession For	
NTIS GRA&I	☑
DTIC TAB	☐
Unannounced	☐
Justification	
By	
Distribution/	
Availability Codes	
Dist	Avail and/or Special
A-1	

92 6 16 001

Technical Program Committee

Philip H. Bucksbaum, Cochair
University of Michigan

Natale M. Ceglio, Cochair
Lawrence Livermore National Laboratory

Jeffrey Bokor
AT&T Bell Laboratories

George S. Brown
Stanford University

Paul B. Corkum
National Research Council of Canada, Canada

Raymond C. Elton
U.S. Naval Research Laboratory

Roger Falcone
University of California, Berkeley

Richard R. Freeman
AT&T Bell Laboratories

Stephen E. Harris
Stanford University

Janos Kirz
SUNY-Stony Brook

Howard Milchberg
University of Maryland

Harm G. Muller
FOM Institute for Atomic and Molecular Physics, The Netherlands

Michael D. Perry
Lawrence Livermore National Laboratory

George R. Ricker
Massachusetts Institute of Technology

Eberhard Spiller
IBM Thomas J. Watson Research Center

Martin V. Zombeck
Smithsonian Astrophysical Observatory

OSA Proceedings on

SHORT-WAVELENGTH COHERENT RADIATION: GENERATION AND APPLICATIONS

Volume 11

Edited by
Philip H. Bucksbaum and Natale M. Ceglio

Proceedings of the Fifth Topical Meeting
April 8–10, 1991
Monterey, California

Sponsored by

Optical Society of America

Supported by

Air Force Office of Scientific Research
U.S. Department of Energy
National Science Foundation
Office of Naval Research

Optical Society of America
2010 Massachusetts Avenue, NW
Washington, DC 20036
(202) 223-8130

Articles in this publication may be cited in other publications. In order to facilitate access to the original publication source, the following form for the citation is suggested:

> Name of Author(s), Title of Paper, OSA Proceedings on Short-Wavelength Coherent Radiation, Philip H. Bucksbaum, Natale M. Ceglio, eds. (Optical Society of America, Washington, DC 1991), Vol. 11, pp. xx-xx.

ISBN Number 1-55752-185-9

LC Number 90-63178

Copyright © 1991, Optical Society of America

Individual readers of this proceedings and libraries acting for them are permitted to make fair use of the material in it, such as to copy an article for use in teaching or research, without payment of fee, provided that such copies are not sold. Copying for sale is subject to payment of copying fees. The code 1-55752-185-9/91/$2.00 gives the per-article copying fee for each copy of the article made beyond the free copying permitted under Sections 107 and 108 of the U.S. Copyright Law. The fee should be paid through the Copyright Clearance Center, Inc., 21 Congress Street, Salem, MA 01970.

Permission is granted to quote excerpts from articles in this proceedings in scientific works with the customary acknowledgment of the source, including the author's name, name of the proceedings, page, year, and name of the Society. Reproduction of figures and tables is likewise permitted in other articles and books provided that the same information is printed with them and notification is given to the Optical Society of America. Republication or systematic or multiple reproduction of any material in this proceedings is permitted only under license from the Optical Society of America; in addition, the Optical Society may require that permission also be obtained from one of the authors. Address inquiries and notices to the Director of Publications, Optical Society of America, 2010 Massachusetts Avenue, NW, Washington, DC 20036. In the case of articles whose authors are employees of the United States Government or its contractors or grantees, the Optical Society of America recognizes the right of the United States Government to retain a nonexclusive, royalty-free license to use the author's copyrighted article for United States Government purposes.

The views and conclusions contained in this proceedings are those of the author(s) and should not be interpreted as necessarily representing endorsements, either expressed or implied, of the editors or the Optical Society of America.

Printed in the U.S.A.

Contents

Preface xiii

Section I: Sources of Short-Wavelength Radiation

Parametric Generation and Coherent Scattering

Towards Extreme VUV by Harmonic Generation in Strong Fields 2
L. A. Lompré, A. L'Huillier, and G. Mainfray

Harmonic Generation by an Intense Picosecond Laser in an Underdense Plasma 7
X. Liu, J. S. Coe, C. Y. Chien, D. Umstadter, E. Esarey, and P. Sprangle

Four-Wave Difference-Frequency Generation at 124 nm for High-Resolution Photoabsorption Studies of O_2 12
K. G. H. Baldwin, S. T. Gibson, B. R. Lewis, J. H. Carver, and T. J. McIlrath

Instrumentation for Generating Tunable VUV Radiation Near 1215.6 Å (H 1*s* + *h*ν -> 2*s*) and 1202.8 Å (He $1s^2$ + 2 *h*ν -> $1s2s\,^1S$) 18
Xiaoxiong Xiong, Thomas J. McIlrath, and Chris I. Westbrook

Spatial Distribution of High-Order Harmonics Generated in the Tunneling Regime 23
S. Augst, C. I. Moore, J. Peatross, and D. D. Meyerhofer

Resonantly Enhanced Harmonic Generation and Above-Threshold Ionization in Krypton 28
J. K. Crane, S. W. Allendorf, K. S. Budil, and M. D. Perry

Photon accelerator: A novel method of frequency upshifting sub-picosecond laser pulses 33
Scott C. Wilks

Generation of Ultrafast VUV Radiation by Reflection from a Relativistic Ionization Front 36
Henry C. Kapteyn and Margaret M. Murnane

Incoherent Generation

X-Ray Spectral Determination of Electron Density in Dense Laser-Excited Targets 42
T. S. Luk, A. McPherson, D. A. Tate, K. Boyer, C. K. Rhodes, V. L. Jacobs, P. G. Burkhalter, A. Zigler, D. A. Newman, and D. J. Nagel

X-Ray Generation by High Irradiance Exawatt-Per-Square Centimeter Subpicosecond Lasers 47
G. A. Kyrala, R. D. Fulton, D. E. Casperson, E. K. Wahlin, L. A. Jones, G. T. Schappert, J. A. Cobble, and A. J. Taylor

Soft-X-Ray Emission Characteristics of Line-Shaped, Laser-Produced Plasmas 52
Shisheng Chen, Xiaofang Wang, Aidi Qian, and Zhizhan Xu

Characteristics of Sub-100-ps Laser Irradiation of Cylindrical Cavities 53
J. E. Balmer, B. Soom, U. Ellenberger, and R. Weber

Short-Wavelength Lasers

Multiphoton Spectroscopy Using Tunable VUV Radiation from a Raman-Shifted Excimer Laser 58
Gregory W. Faris and Mark J. Dyer

Recombination Lasers Pumped by Multiphoton Ionization 62
N. H. Burnett, F. Brunel, P. B. Corkum, G. D. Enright, C. E. Capjack, and R. Rankin

Recent advances in soft-x-ray laser research 67
Brian J. MacGowan

Temperature Determination in X-Ray Laser Plasmas by Thomson Scattering 69
D. M. Villeneuve, B. La Fontaine, H. A. Baldis, J. Dunn, G. D. Enright, M. D. Rosen, P. E. Young, and D. L. Matthews

Future Directions of Laboratory X-Ray Laser Research 73
Mordecai D. Rosen

Recent Progress in Soft-X-Ray Laser Research at the Institute of Laser Engineering 77
H. Daido, Y. Kato, H. Azuma, K. Murai, H. Shiraga, K. Yamakawa, T. Togawa, E. Miura, Y. Gang, T. Kanabe, M. Takagi, H. Takabe, K. Tanaka, M. Yamanaka, S. Nakai, C. Lewis, D. O'Neill, D. Neely, G. Pert, S. Ramsden, and M. Key

Coherent X-Ray Generation Through Laser Pumping of a Relativistic Ion Beam: Feasibility Assessment 82
S. A. Bogacz

Search for Gain on 2p–2s Transitions in a Collisionally Excited Ge Plasma 87
G. D. Enright, H. A. Baldis, J. Dunn, B. La Fontaine, D. M. Villeneuve, J. C. Kieffer, H. Pépin, and M. Chaker

Modal Study of Refractive Effects on X-Ray Laser Coherence 91
Peter Amendt, Richard A. London, and Moshe Strauss

Saturation and Kinetic Issues for Optical-Field-Ionized Plasma X-Ray Lasers 96
D. C. Eder, P. Amendt, M. D. Rosen, J. K. Nash, and S. C. Wilks

Radiation Cooling in Photopumped C VI Inversion 101
Ricardo A. Pakula

Progress Toward the Development of a Compact Capillary Discharge Soft-X-Ray Laser 106
J. J. Rocca, M. C. Marconi, B. T. Szapiro, and J. Meyer

Longitudinal Pumping by an Ellipsoidal Reflector for Short-Wavelength Lasers 111
Katsumi Midorikawa, Hideo Tashiro, Toshihisa Watabe, and Minoru Obara

Designs for Coherent X-Ray Lasers 116
R. A. London, P. Amendt, M. R. Carter, M. D. Feit, J. A. Fleck, D. L. Matthews, S. Maxon, R. E. Stewart, J. E. Trebes, and M. Strauss

Effects of Illumination Uniformity Improvement on X-Ray Lasing Plasmas 119
J. C. Kieffer, M. Nantel, M. Chaker, H. Pépin, H. Baldis, J. Dunn, G. D. Enright, and D. M. Villeneuve

Evidence of X-Ray Laser Gain Cancellation Due to Plasma Inhomogeneity 123
P. Jaegle, P. Dhez, A. Klisnick, A. Carillon, G. Jamelot, B. Gauthé, J. P. Raucourt, P. Goedtkindt, J. C. Kieffer

Optical Wiggler Free-Electron X-Ray Laser as a Two-Level Quantum Generator with Fully Inverted Medium 127
E. M. Belenov, S. V. Grigoriev, A. V. Nazarkin, and I. V. Smetanin

Section II: Applications of Short-Wavelength Radiation

X-Ray Holographic Microscopy Using Photoresists: Recent Developments 130
C. Jacobsen, S. Lindaas, and M. Howells

Broadband Diffractive Lens 135
N. M. Ceglio, A. M. Hawryluk, D. P. Gaines, R. A. London, and L. G. Seppala

Differential Phase Contrast Imaging in the Scanning Transmission X-Ray Microscope 141
J. R. Palmer and G. R. Morrison

Real World Issues for the New Soft-X-Ray Synchrotron Sources 146
Brian M. Kincaid

High-Performance Multilayer X-Ray Optics 152
D. G. Stearns, R. S. Rosen, and S. P. Vernon

Soft X-ray Optic for an Efficient Laser Plasma Spectrometer 160
S. C. Davey, R. R. Freeman, T. J. McIlrath, L. D. vanWoerkom, W. K. Waskiewicz, and T. Lucatorto

Feasibility of X-Ray Nonlinear Resonant Effects in Plasma 163
P. L. Shkolnikov and A. E. Kaplan

Normal Incidence Multilayer Reflectors for Sub-10 nm Region 167
Tai D. Nguyen, Eric Gullikson, and Jeffrey B. Kortright

Section III: High-Intensity Laser Sources

High-Damage-Threshold Gratings Using Coated Silicon Substrates 170
H. W. K. Tom, M. H. Sher, O. R. Wood II, W. M. Mansfield, U. Mohideen, R. R. Freeman, and J. Bokor

0.5-TW, 125-fs Ti:Sapphire Laser 176
J. D. Kmetec, J. J. Macklin, and J. F. Young

Multiterawatt Laser System Based on Ti:Al_2O_3 181
A. Sullivan, H. Hamster, H. C. Kapteyn, S. Gordon, W. White, H. Nathel, R. J. Blair, and R. W. Falcone

Section IV: High-Intensity Laser–Matter Interactions

Atoms

Calculations of High-Intensity Multiphoton Ionization and Photoemission from Atoms 186
K. C. Kulander, K. J. Schafer, and J. L. Krause

Integration of the Schrödinger Equation on a Massively Parallel Processor 190
Jonathan Parker, Sayoko Blodgett-Ford, and Charles W. Clark

Molecules

Subpicosecond Studies of Molecules and Solids 196
T. S. Luk, A. McPherson, D. A. Tate, K. Boyer, and C. K. Rhodes

Intense Field Nonresonant Multiphoton Absorption of Diatomic Molecules 201
B. Yang, M. Saeed, and L. F. DiMauro

Molecular Multiphoton Ionization 209
G. N. Gibson, R. R. Freeman, and T. J. McIlrath

Coulomb Explosion of Molecular Iodine with Ultrashort Pulses 216
Y. Beaudoin, D. Strickland, and P. B. Corkum

Ionization and Dissociation of Molecular Hydrogen by Ultrashort Light Pulses 222
A. Zavriyev, D. W. Schumacher, F. Weihe, P. H. Bucksbaum, J. Squier, F. Salin, and G. Mourou

High-Intensity Photoionization of H_2 227
Sarah W. Allendorf and Abraham Szöke

Multiphoton Ionization of I_2, HI, and CF_3I, and Above-Threshold Ionization in I_2 232
C. J. Zietkiewicz, Y. Y. Gu, A. M. Farkas, and J. G. Eden

Low-Density Targets

Resistance of Short Pulses to Self-Focusing 238
D. Strickland and P. B. Corkum

Reversible Multiphoton Ionization of Gases Observed by a Femtosecond Pump/Probe Schlieren Imaging Technique 240
J. P. Geindre, P. Audebert, J. C. Gauthier, R. Benattar, A. Mysyrowicz, J. P. Chambaret, and A. Antonetti

Spectral Blueshifts of Femtosecond Pulses in Atmospheric Density Kr and Xe Plasmas 244
Wm. M. Wood and M. C. Downer

Creation of Relativistic Plasmas Using Ultrahigh-Intensity Laser Radiation 247
J. N. Bardsley and B. M. Penetrante

Nonlinear Compton Scattering in a Pulsed Focused Laser Beam 252
U. Mohideen, H. W. K. Tom, R. R. Freeman, J. Bokor, and P. H. Bucksbaum

Electromagnetically Induced Transparency 257
A. Imamoglu, K. -J. Boller, and S. E. Harris

Pump-Probe Investigation of Picosecond Laser-Gas Target Interactions 262
C. G. Durfee III and H. M. Milchberg

High-Density Targets

Transport in Ultra-Dense Plasmas Produced by a 1-ps Laser Pulse 266
M. Chaker, Y. Beaudoin, J. C. Kieffer, H. Pépin, C. Y. Chien, S. Coe, and G. Mourou

Propagation Effects for a Femtosecond Laser Pulse 271
S. C. Rae and K. Burnett

Density Profile Steepening by the Ponderomotive Force of an Intense Picosecond Laser 276
D. Umstadter, X. Liu, J. S. Coe, and C. Y. Chien

Efficient Coupling of High-Intensity Subpicosecond Laser Pulses into Dilute Solid Targets 281
M. Murnane, H. Kapteyn, S. Gordon, S. Verghese, J. Bokor, W. Mansfield, R. Gnall, E. Glytsis, T. Gaylord, and R. Falcone

Direct Measurement of Nonequilibrium Electron Energy Distribution in Sub-Picosecond Laser-Heated Gold Films 285
W. S. Fann, R. H. Storz, and J. Bokor

Soft-X-Ray Spectra from Laser Plasma Effectively Heated by a Pulse Train Laser 289
Hideo Hirose, Tamio Hara, Kozo Ando, Fumiko Negishi-Tsuboi, Hidehiko Yashiro, and Yoshinobu Aoyagi

Hydrodynamic Evolution and Radiation Emission from an Impulse-Heated Solid Density Plasma 294
I. Lyubomirsky, C. G. Durfee III, and H. M. Milchberg

Index 299

Preface

The Fifth Topical Meeting on Short-Wavelength Coherent Radiation: Generation and Applications was held in Monterey, California, April 8-10, 1991. This volume contains the papers delivered at the conference, which chronicle the major advances in short-wavelength laser physics and technology since the last meeting in this series in North Falmouth, Massachusetts in September 1988. These proceedings are an important record of the rapid advances in this exciting field.

Ninety-eight scientists and students participated in the conference, which had representation from North America, Europe, the Far East, and Australia. The number and diversity of contributions to this conference series continues to grow. In keeping with past tradition, no sessions were held in parallel. The number of oral presentations was kept to 39 in order to ensure adequate time for discussion.

To accommodate the additional contributions there were 37 posters. These were presented in two sessions and provided focal points for lively discussions at breakfast and between the oral sessions. Included among the posters were nine postdeadline papers, representing last minute advances in short-wavelength laser physics.

Short-wavelength coherent radiation generation is inextricably linked to high-intensity laser-matter physics, and this meeting had more emphasis on the basic high-field light-matter interaction than ever before. There were three sessions devoted entirely to this subject, with additional papers on high-field technology and physics scattered throughout the meeting.

Since the last meeting in this series in 1988, short-wavelength projection lithography has emerged as an application of great potential commercial importance. In recognition of the broad connections between short-wavelength laser sources and this new application, the fifth Short-Wavelength meeting was held in conjunction with a special topical meeting on Soft-X-Ray Projection Lithography. The lithography conference ran from April 10-12, and the overlap on Wednesday, April 10, was a day of joint sessions between the two meetings. Some of that day's presentations are contained in this volume; the rest are to be found in the OSA Proceedings on Soft-X-Ray Projection Lithography, vol. 12.

This meeting required the efforts of many people. We particularly wish to express our appreciation to the Technical Program Committee for their help and advice. The Optical Society provided logistical support through their meetings department. We especially thank Barbara Hicks and Kevin Fitzpatrick for their efforts. Alan Tourtlotte of the Optical Society directed the publication of this Proceedings with great efficiency. Finally, we gratefully acknowledge the generous support of the U.S. Air Force Office of Scientific Research, the Office of Naval Research, the U.S. Department of Energy, the National Science Foundation, and the Optical Society of America.

Philip H. Bucksbaum
University of Michigan

Natale M. Ceglio
Lawrence Livermore National Laboratory

Section I: Sources of Short-Wavelength Radiation

Parametric Generation and Coherent Scattering

Towards Extreme VUV by Harmonic Generation in Strong Fields

L. A. Lompré, A. L'Huillier, and G. Mainfray

Centre d'Etudes de Saclay, 91191 Gif-sur-Yvette cédex, France

Abstract

Extreme VUV radiations may be produced by harmonic generation in rare gases exposed to intense laser fields. Posibilities and limitations will be discussed.

1- Introduction

The absorption of a large number of photons by an atomic system may lead to very interesting features, and significant advances have been made in this domain : above threshold ionization, multiply charged ion production and more recently high order harmonic generation. As far as harmonic generation is concerned, most of the experiments in a gaseous medium use short incident wavelength in order to obtain the shortest generated wavelength[1-5]. McPherson *et al*[4] have reported up to the 17th harmonic in Ne (λ = 15 nm; 85 eV) using a KrF laser (λ = 248 nm; 5 eV) for a laser intensity of the order of 10^{16} W/cm^2. More recently, Sarukura *et al*[5] using the same type of laser but with a laser intensity of the order of 10^{17} W/cm^2 have observed the 23rd harmonic in Ne and the 17th harmonic in He. But recent experiments have shown that with a photon energy of 1.165 eV (YAG laser), it is also possible to generate short wavelength through harmonic generation[6,7].

The purpose of the present paper is to discuss some VUV or XUV light emission by harmonic generation in a rare gas medium irradiated by an intense 1064 nm laser field. The main results obtained in the 10^{13}-10^{14} W/cm^2 intensity range will be presented in order to explain the main features which govern short wavelength production. The different processes which may affect the harmonic production will be discussed, mainly the Stark shift effect induced by the laser intensity and the limitation due to ionization of the medium which occurs at such laser intensity and their consequences on the propagation of the harmonics.

2- Experiment and main features.

The experimental setup has been described in details elsewhere[6,7]. A brief description will be given here. The laser used is a 30 ps mode-locked Nd-YAG laser

Proceedings on Short-Wavelength Coherent Radiation, Vol. 11, Philip H. Bucksbaum and Natale M. Ceglio (eds.)
© 1991 Optical Society of America

operating at 10 Hz. It is focused into a vacuum chamber by a lens with a focal length of 200 mm. The gaseous target is provided by a pulsed gas jet. At 0.5 mm from the nozzle, the gas density has been measured to be 15 Torr, for a baking pressure of 150 Torr[8]. The use of a gas jet limits the reabsorption of the VUV radiation and enables the detection of very short wavelengths. The VUV or XUV radiation (350 - 10 nm) emitted along the laser axis is analyzed by a monochromator. It is composed of a toroidal grating which forms an aberration free image of the interaction region. The collection solid angle is imposed by the grating size, not by the entrance slit. The VUV radiation is detected by a photomultiplier or a windowless electron multiplier depending on the spectral range.

When a spectrum is recorded, several major points come out : (1) only odd harmonics are observed. That is due to the fact that harmonics are created in an isotropic medium with inversion symmetry which excludes even harmonics. (2) the maximum number of harmonics created at the maximum laser intensity is strongly dependent on the rare gas investigated: up to the 21st in Xe, 29th in Kr and 33rd in Ar. (3) other lines than the harmonics seen in the first and second orders of the grating can be observed. They correspond to fluorescence from discrete levels of excited atom or ion[7]. These fluorescence lines can be easily resolved temporally and exhibits a significant delay with the infrared laser pulse excitation, typically few tenths of μs.

Taking into account the efficiencies of the gratings and the detectors, harmonic intensity distribution shows three different regions (Fig.1): a rapid decrease from the third to the fifth or seventh harmonic followed by a "plateau" which extends differently from one atom to the other, and then a cutoff. This is the first important observation on harmonic distribution. The second one concerns the intensity dependences of the number of harmonic photon. They behave as the number of ions versus the laser intensity. Fig.2a and 2b show the intensity dependence of the seventh and 13th harmonics. The signal first rapidly increases with the laser intensity then a saturation is observed when the medium beomes ionized[9]. It shows that the harmonic production is strongly influence by the

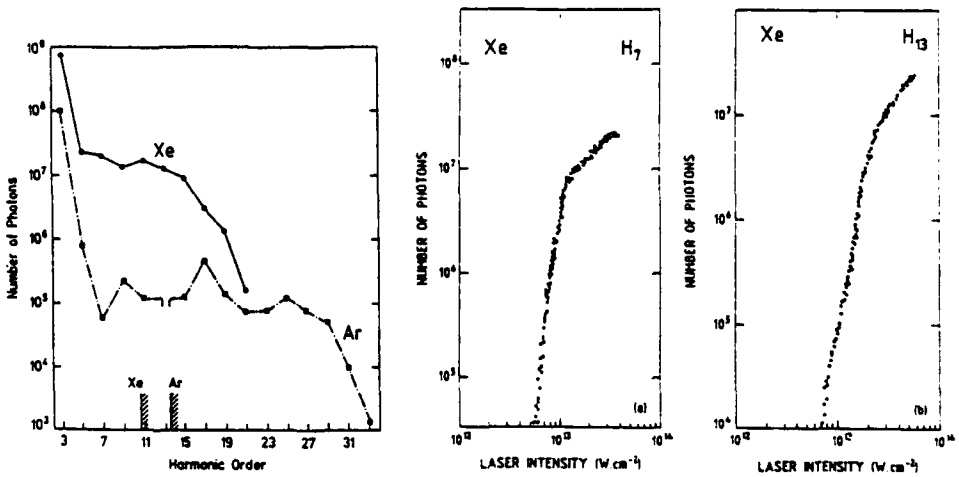

Fig.1 Fig.2a Fig2.b

Fig.1 : Harmonic distribution in Xe and Ar at 3 10^{13}W/cm^2.

Fig.2 : Intensity dependences of the 7th (a) and the 13th (b) harmonics in Xe.

presence of ions in the interaction volume. This observation has been made for all the harmonics in all the rare gases studied. Below saturation, the harmonics vary as some power law of the laser intensity. The lower harmonics ($q<9$) vary as predicted by the lowest perturbation theory. The 11th and the 13th harmonics exhibit a more complex intensity dependence. The highest harmonics vary all in the same way approximatly as the 12th power of the laser intensity. Table 1 summarizes the effective order of nonlinearity determined by a least-square fitting procedure for the different harmonics in Xe.

3- Discussion.

The theoretical interpretation of these experimental results has to take into account two steps : (1) the determination of the photon spectrum emitted by an atom exposed to a strong laser field, (2) the resolution of Maxwell equations using as a source term the sum of the atomic dipole moments created in the medium[10]. If the first step can be done by solving numerically the time-dependent Schrödinger equation, the second step points out the importance of the phase relation between the different dipoles. In strong fields, phase matching affects the conversion efficiency very strongly. But these phase matching conditions are directly related to the behavior of the atomic medium towards the laser intensity. Two important consequences of the medium properties will be discussed now : AC Stark shift effects on harmonic production, and the limitations due to ionization of the medium.

3.1- AC Stark shift effects.

One question we may ask is the following : "What could explain the behavior observed on harmonic intensity dependences ?". In fact, the laser intensity used for these experiments is of the order of 10^{13} W/cm^2. At such a laser intensity, we have to take into account the AC Stark shift of the atomic levels. If we assume that the AC Stark shift is directly correlated to the ponderomotive shift given by $U_p = 9.33\ 10^{-14}\ I(W/cm^2)\ \lambda^2(\mu m)$, then at 10^{13} W/cm^2 and $\lambda = 1.064\ \mu m$, $U_p = 1$ eV, close to the photon energy (1.165 eV) for the YAG radiation. The shift of the Rydberg levels has been directly measured for a laser intensity of 10^{10} W/cm^2 and shows lower shift values[11]. Indirect measurement through electron energy reveals that all the levels are shifted as the ionization potential[12]. But, whatever the exact value of the Rydberg level shift is, it leads to resonance effects which have to be considered. It is well known that resonances will affect the ion production, and consequently the harmonic production. In the Xe atom case, the first possible resonant state will require a minimum of 9 photons. Resonances are then expected to take place at 9, 10, 11 and possibly 12 photons. Consequently we may expect that for the lower harmonics ($q<9$) resonances would not play any role, which means that the behavior will be as expected (I^q). For the 11th or 13th harmonics, due to resonances we may expect some influences from the resonances : slopes are not any more reflecting the I^q power law (as shown in Fig2b and Table 1). For higher harmonics, it will be very difficult to predict what could be the intensity dependence : the value of the slopes is meaningless[13]. Futhermore, as for resonant electron production, in the interaction region,

Table 1. Harmonic Power Laws*

3	5	7	9	11	13	15	17	19	21
3.3 ± 0.2	6 ± 0.5	7.5 ± 0.7	8.3 ± 0.7	7.7 ± 0.7	5.3 ± 0.5	11.7 ± 0.7	12.5 ± 1	13 ± 1	12.5 ± 1

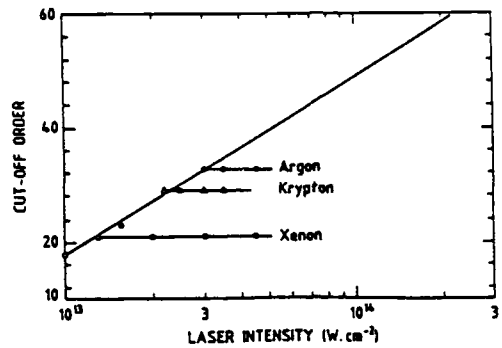

Fig.3

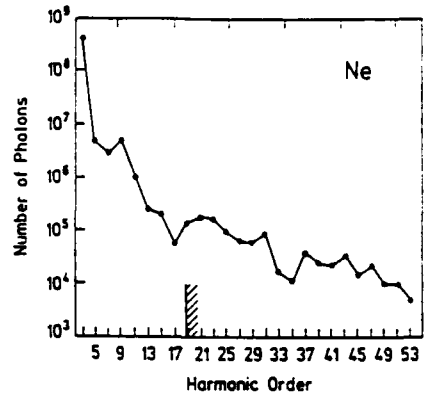

Fig.4

Fig.3 : Maximum number of harmonics versus laser intensity for Xe, Kr and Ar

Fig.4 : Harmonic distribution in Ne at around 5 10^{14} W/cm^2, laser pulse width 1.2 ps.

when the laser intensity is increased, the different region of the interaction region would not experience the same laser intensity, and therefore will contribute differently to harmonic production and phase matching because the suceptiblity in the vicinity of a resonance will change dramatically[14]. A carefull treatment of such a behavior will be very difficult but must be taken into account in any theoretical treatment.

3.2- Limitations due to ionization.

As mentioned previously the intensity dependences of the harmonics show a clear saturation when the laser intensity is increased above a given value which corresponds to the saturation of the ionization. This information is important because it clearly shows that the ionization strongly influences the harmonic production, but it may have two possible explanations. Either the harmonic production efficiency is much smaller in an ionized medium than in an atomic medium via the relative susceptibilities which could be different, or the presence of the free electrons in the interaction volume seriously affects the phase matching conditions. The contribution of the free electrons will introduce a positive phase mismatch changing the propagation conditions. Unfortunatly, the experiment does not allow to conclude which effect is the major one. But this limitation due to ionization have an important consequence. The harmonic distributions, as in Fig.1 show a clear cutoff. Similar distributions were obtained in Xe and Kr for different laser intensities. Fig.3 shows the maximum number of harmonics detected, plotted versus laser intensity for Xe, Kr and Ar. It appears clearly that, for each rare gas, when the laser intensity is below the saturation intensity, experimental cutoff points lie on the same line, independently of the gas considered. The maximum number of harmonics which can be generated is only intensity dependent, while the conversion efficiency depends on the atom. When the laser intensity is higher than the saturation intensity, the maximum harmonic order stops increasing, indicating that ionization of the medium perturbs the harmonic production or its detection. This observation confirms that the harmonics are mainly created in an atomic medium and not in an ionic medium. Let us point out that in the case of Ne or He, which have much higher saturation intensities, of the order of 5 10^{14} W/cm^2, an extrapolation of the curve shown in Fig.3 "predicts" the creation of greater number of harmonics.

4- Experimental results in Ne at 5 10^{14} W/cm^2. Conclusion.

Fig.4 shows a very recent experimental result obtained in a 15 Torr of Ne, at 5 10^{14} W/cm^2, using a picosecond Nd-Glass laser system developed in our laboratory. The laser wavelength is 1053 nm and the system may deliver up to 1 J in 1.2 ps[15]. Only a fraction of this energy has been used (25 mJ) for avoiding damaging of the VUV grating of the monochromator. After a rapid decrease for the first harmonics (up to the 13th harmonics where resonances may begin to play a role), there is a slow decay of the relative harmonic amplitude extending up to the 53rd harmonic (62 eV, 20 nm). These preliminary results are encouraging because one may expect to reach shorter wavelengths and higher efficiencies by increasing laser intensity. But it appears that effects such as AC Stark shifts (dynamic resonances), ionization or Kerr effects (which has not been discussed in the present paper) may influence considerably the production or the propagation in the medium of very short radiations in the XUV domain produced by harmonic generation in rare gas in intense laser fields with a photon energy of around 1eV.

5- References.

1- J. Reintjes, C.Y. She, and R. Rekardt, IEEE, J. Quantum Electron. QE **14**, 581 (1978).
2- J. Reintjes, L.L. Tankersley, and R. Christensen, Opt. Commun. **39**, 334 (1981).
3- J. Bokor, P.H. Bucksbaum, and R.R. Freeman, Opt. Lett. **8**, 217 (1983).
4- A. McPherson, G. Gibson, H. Jara, U. Johann, T.S. Luk, I. McIntyre, K. Boyer, and C.K. Rhodes, J. Opt. Soc. Am. B **4**, 595 (1987).
5- N. Sarukura, K. Hata, T. Adachi, R. Nodomi, M. Watanabe, and S. Watanabe, Phys. Rev. A **43**, 1669 (1991).
6- M. Ferray, A. L'Huillier, X.F. Li, L.A. Lompré, G. Mainfray, and C. Manus, J. Phys. B **21**, L31 (1988).
7- X.L. Li, A. L'Huillier, M. Ferray, L.A. Lompré, and G. Mainfray, Phys. Rev. A **39**, 5751 (1989).
8- L.A. Lompré, M. Ferray, A. L'Huillier, X.L. Li, and G. Mainfray, J. Appl. Phys. **63**, 1791 (1988).
9- A. L'Huillier, L.A. Lompré, G. Mainfray, and C. Manus, J. Phys. B **16**, 1363 (1983).
10- "Theory of High-order Processes in Atoms in Intense Laser Fields", J. Opt. Soc. Am. B **7**, N°4, (1990).
11- D. Normand, L.A. Lompré, A. L'Huillier, J. Morellec, M. Ferray, J. Lavancier, G. Mainfray and C. Manus, J. Opt. Soc. Am. B **6**, 1513 (1989).
12- R.R. Freeman, and P.H. Bucksbaum, J. Phys. B **24**, 325 (1991).
13- L.A. Lompré, G. Mainfray, and C. Manus, J. Phys. B **13**, 85 (1980).
14- A. L'Huillier, X.F. Li, and L.A. Lompré, J. Opt. Soc. Am. B **7**, 527 (1990).
15- M. Ferray, L.A. Lompré, O. Gobert, A. L'Huillier, G. Mainfray, C. Manus, A. Sanchez, and A. Gomes, Opt. Commun. **75**, 278 (1990).

Harmonic Generation by an Intense Picosecond Laser in an Underdense Plasma

X. Liu, J. S. Coe, C. Y. Chien, and D. Umstadter

Ultrafast Science Laboratories, University of Michigan, Ann Arbor, Michigan 48109-2099

E. Esarey and P. Sprangle

Beam Physics Branch, U.S. Naval Research Laboratory, Washington, D.C. 20375-5000

1 Abstract

We report both theoretical calculations and experimental observations of second harmonic (SHG) and third harmonic generation (THG) in long scale-length underdense plasmas. Second harmonic generation, normally forbidden in a uniform plasma, is allowed by a radial electron density profile that results from the laser-intensity dependent ionization. Experimental measurements of the scaling of the harmonics with density and laser intensity are presented.

2 Introduction

Modest power lasers interacting with a neutral gas have been observed to produce coherent harmonic radiation (up to the 61st harmonic) at odd multiples of the fundamental laser frequency[1]. This is a result of the laser field causing the bound electrons to oscillate in the anharmonic atomic potential. Increasing the fundamental laser intensity, however, leads to ionization of the gas and to the production of unbound electrons. Multiphoton ionization in the long wavelength, high intensity tunneling limit may also lead to harmonic generation [2]. A very high-power laser interacting with a fully ionized plasma, however, may lead to the generation of large levels of coherent radiation at high harmonics (including even harmonics) of the incident laser frequency based on an entirely new mechanism. If the laser pulse is sufficiently intense, the plasma electron mass becomes modulated because of nonlinear relativistic effects [3]. We describe in this paper the theory and some experiments in which we may have observed signatures of these mechanisms.

3 Theory

The theories of harmonics produced by lasers interacting with neutral gases and by tunneling ionization of gases are both given elsewhere [1] [2]. We will therefore only outline in this section the theory of harmonic generation by high intensity lasers interacting with a plasma.

3.1 Relativistic Harmonics

When a laser beam interacts with a fully ionized plasma, the intense electric field of the laser beam causes the plasma electrons to oscillate at the fundamental frequency of the

Proceedings on Short-Wavelength Coherent Radiation, Vol. 11, Philip H. Bucksbaum and Natale M. Ceglio (eds.)
© 1991 Optical Society of America

laser. As the laser intensity increases, the electron quiver motion develops higher harmonic components due to nonlinear relativistic effects. The process by which relativistic effects produce coherent harmonic radiation may be understood by a simplified single-particle model. This model includes only the effects of the relativistic electron quiver motion. Other effects, such as the plasma density response, will be neglected. A linearly polarized laser field will be assumed, $\mathbf{a}_1(z,t) = \hat{a}_1 \sin\psi \mathbf{e}_y$, where $a = eA/mc^2$ is the normalized vector potential and $\psi = kz - \omega t$, where k and ω are the wavenumber and frequency of the laser field.

In the single-particle model, the transverse plasma current is $J_y = -en_0 v_q$, where v_q is the relativistic electron quiver motion and n_0 is the ambient plasma density. In the 1D limit, $v_q = ca_1/\gamma_\perp$, where $\gamma_\perp = (1+a_1^2)^{1/2}$ is the relativistic factor associated with the transverse electron motion. This expression for J_y acts as the source term in the wave equation which drives the harmonic radiation, $(\nabla^2 - \partial^2/c^2\partial t^2)a = S$, where

$$S = k_{p0}^2 \hat{a}_1 \sin\psi \left(1 + \hat{a}_1^2 \sin^2\psi\right)^{-1/2},$$

and $\omega_{p0} = ck_{p0} = (4\pi e^2 n_0/m)^{1/2}$ is the plasma frequency. In the limit $\hat{a}_1^2 << 1$, the denominator in the source term S may be expanded and the component driving the ℓth *odd* harmonic ($\omega_\ell = \ell\omega$) may be determined. For example, the ratio of the third harmonic power to the fundamental is $P_3/P_1 = (\hat{a}_1^2 k_{p0}^2 L_p/16k)^2 \equiv R_{sp}$, where L_p is the laser-plasma interaction length. In the single particle limit, $P_3 \sim n_0^2 I^3$, where I ($\sim \hat{a}_1^2$) is the incident laser intensity.

3.2 Collective Effects

The single-particle model assumed that the plasma response is dominated by the electron quiver motion. This is an oversimplification and collective plasma effects, *i.e.*, the plasma density response, cannot be neglected. Including the density response, $\delta n(z,t)$, in the transverse current, gives $J_\perp = -e(n_0 + \delta n)v_\perp$. Letting $v_\perp = v_q$ gives $S = k_{p0}^2 a(1 + \delta n/n_0 - a^2/2)$, where the term $a^2/2$ arises from expanding the relativistic factor. Using 1D cold fluid theory, the density response $\delta n(z,t)$ may be calculated, giving

$$S = k_{p0}^2 \hat{a}_1 \sin\psi \left(1 - \frac{\hat{a}_1^2}{4} + \frac{3}{16}\frac{\omega_{p0}^2}{\omega^2}\hat{a}_1^2 \cos 2\psi\right).$$

Hence, the effect of including the density response is to reduce [3] the source term for the third harmonic, $\sim \exp(\pm 3i\psi)$, by the factor $3\omega_{p0}^2/4\omega^2 << 1$ as compared to the single particle model. The power in the third harmonic will be reduced by the square of this factor, $P_3/P_1 = R_{sp}(3k_{p0}^2/4k^2)^2$. Hence, in the 1D limit, $P_3 \sim n_0^4 I^3$. Physically, this reduction arises from the longitudinal ponderomotive force, $F_z \sim -\nabla_z a^2$. This modulates the density, $\delta n/n_0 \sim \exp(\pm 2i\psi)$, in such a way that it nearly cancels (to order ω_{p0}^2/ω^2) the contribution from the relativistic factor, $a^2/2$. In the absence of the space charge potential, $\omega_{p0}^2 \to 0$, this cancellation is exact and no third harmonics are generated in the 1D limit.

3.3 3D Effects

When a laser pulse interacts with a plasma with finite radial density gradients, harmonics are also generated at *even* multiples of the incident laser frequency. Radial density gradients arise when a Gaussian laser pulse produces intensity-dependent ionization of a neutral gas. Electrons undergoing quiver motion in the presence of a density gradient produce density oscillations of the form $\delta n_1 \sim \hat{a}_1 \sin\psi \cdot \nabla_\perp n/k$. This produces a source current $S_2 \simeq k_{p0}^2(\delta n_1/n_0)\hat{a}_1 \sin\psi$ which drives the second harmonic radiation. For a broad laser profile,

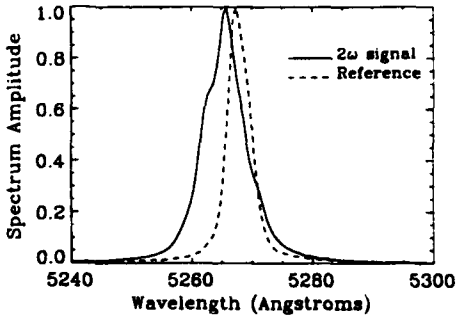

Figure 1: Spectrum of SHG signal in the forward direction from hydrogen, $p = 1$ Torr, with ω pulse energy $\sim$ 200 mJ; the frequency-shift is due to rapid ionization of the gas. The reference spectrum was obtained from a doubling crystal.

$1/kr_o << 1$, where r_o is the radial dimension of the laser field, the power in the second harmonic scales as $P_2/P_1 \sim (\hat{a}_1 k_{p0}^2 L_p/k^2 r_o)^2$. Hence, $P_2/P_1 \sim n_0^2 I^2$. Furthermore, radial density gradients also produce additional source currents which drive the third harmonic radiation. In the limit $r_o^2 k_{p0}^2 << 1$, the 3D terms dominate the 1D term and the power in the third harmonic scales as $P_3/P_1 \sim R_{sp}(1/k^2 r_o^2)^2$ and, hence, $P_3 \sim n_0^2 I^3$.

4 Experiment

In order to study harmonic generation, laser pulses from a glass laser of wavelength 1.053 μm, up to 200 mJ in energy, and 1 ps FWHM in duration were focused into a backfilled vacuum chamber using an f/16 lens. The ω light—after passing through the chamber—was blocked, first by an HR mirror, followed by two IR filters. The spectrum of the SHG in the forward direction was recorded by a 1/3 m spectrometer coupled to an optical multichannel analyzer with an intensified linear photodiode array. The resolution of the system was estimated to be $\sim$ 1.6 Å.

Harmonic generation was observed from various plasmas: hydrogen, helium, and nitrogen. The SHG spectrum for a hydrogen plasma is shown in Fig. 1, with a reference 2ω spectrum obtained using a frequency doubling crystal. The scalings of SHG and THG with gas pressure and intensity, shown in Fig. 2, were measured with a photomultiplier tube and appropriate band-pass filters.

4.1 Preliminary Analysis

The frequency shift and broadening of Fig. 1 may be explained by the rapid change of the index of refraction during the ionization of the gas [4]. The neutral gas density n_0 is assumed to be linearly proportional to the pressure through the ideal gas law, $p = n_0 kT$. The electron density n_e is assumed to be a large fraction ($n_e/n_0 > 0.1$) of n_0. Calculations indicate that tunneling ionization is the dominant ionization mechanism. Ignoring collisional damping for the low pressures considered here, the index of refraction of the plasma is $n^2 = 1 - \omega_p(t)^2/\omega^2 = 1 - (4\pi n_e(t)e^2/m)/\omega^2$, where the electron density $n_e(t)$ increases with time during the risetime of the laser pulse. The frequency shift due to this index change can be written as $\Delta\lambda/\lambda = -\Delta\omega/\omega = (z/c)dn/dt$, where z is taken to be the Rayleigh range of the laser focus. For $\lambda = 1$ μm, $z \simeq 1$ cm, and supposing that $n_e(t)$ increases from 0 to 10^{16}cm^{-3} within 100 fs, then we would expect $\Delta\lambda \sim 1$ Å. The shift in SHG spectrum is assumed to be induced by the shift in the laser and the cross-phase modulation by the laser, which is in approximate agreement with the observed frequency shift.

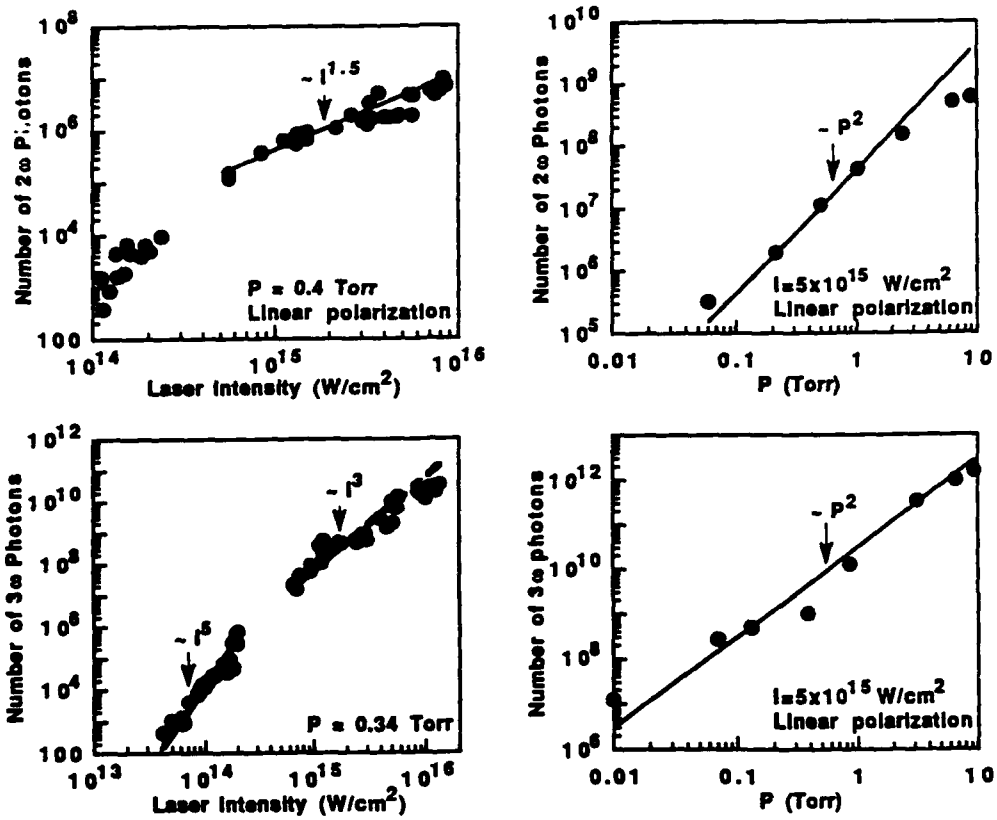

Figure 2: Scaling of SHG and THG in a hydrogen plasma. (a) Scaling of SHG with intensity for fixed pressure. At low laser intensity, the SHG scales as $P_2 \propto I^{10}$. At higher laser intensity, far above the ionization threshold, the SHG scales as $P_2 \propto I^{1.5}$. (b) Scaling of SHG with pressure for fixed intensity. (c) Scaling of THG with intensity for fixed pressure agrees with the prediction, $P_3 \propto I^3$, at intensities above the saturation threshold. (d) Scaling of THG with pressure for fixed intensity. The measured scalings of the SHG and THG with pressure shown in (b) and (d), $P_{2,3} \sim p^2$, are identical to the predicted scalings.

We also measured the polarization of SHG and THG. For linearly polarized laser input, the ratio of SHG parallel with the laser to perpendicular SHG was about 10:1. The THG was parallel with the laser. However, whereas circularly polarized laser light was found to be more efficient (a few times higher) in producing SHG than linear polarization, it produced no THG (the signal was about 2 orders of magnitude smaller than the linear polarization case, which we attribute to imperfect circular polarization produced by the waveplate). As shown in Fig. 2(a), the scaling of the SHG at low intensities agrees with the prediction of Bethune [5], in which P_2 would scale with intensity approximately as the number of photons required to ionize Hydrogen ($\sim$ 10). In this case, the origin of the SHG is attributed to electric-field–induced third-order mixing, driven by charge separation, arising from either the initial kinetic energy of the ejected electrons, observed by Malcuit, *et al.* [5], or by the ponderomotive force of the laser, observed by Augst, *et al.* [5]. At higher laser intensity, far

above the ionization threshold, the SHG scales as $P_2 \propto I^{1.5}$. The THG also scales differently above the saturation intensity threshold than below it; above it scales as predicted by the theory of Sec. 3, $P_3 \propto I^3$. Finally, it is predicted that odd harmonics may be driven by nonlinear currents due to multiphoton ionization [2], and—although nc theory has yet been done to treat this case—it is possible that a density non-uniformity may allow for SHG as it did in the theory of Sec. 3.3. In order to unambiguously determine the importance of this competing mechanism, experiments are under w~y in which the the plasma will be produced with a pre-ionizing laser pulse.

5 Acknowledgments

This work was partially funded by the National Science Foundation Center for Ultrafast Optical Science, #PHY8920108.

References

[1] J.C. Miller *et al.*, Phys. Rev. Lett. **45**, 114 (1980); M. Ferray *et al.*, J. Phys. B **21**, L31 (1988).

[2] F. Brunel, J. Opt. Soc. Amer. B, **7**, 521 (1990).

[3] P. Sprangle, E. Esarey and A. Ting, Phys. Rev. Lett. **64**, 2011 (1990); Phys. Rev. A **41**, 4463 (1990).

[4] W.M. Wood, G. Focht, and M.C. Downer, Opt. Lett. **13**, 984 (1988)

[5] D.S. Bethune, Phys. Rev. A, **23**, 3139 (1981); K. Miyazaki, *et al.*, Phys. Rev. Lett. **43**, 1154 (1979); M. Malcuit *et al.*, Phys Rev. A **41**, 3822 (1990); S. Augst, *et al.*, in *Proceedings of SPIE OE/LASE '90*, **1229**, 152, Los Angeles, CA January (1990).

Four-Wave Difference-Frequency Generation at 124 nm for High-Resolution Photoabsorption Studies of O_2

K. G. H. Baldwin, S. T. Gibson, B. R. Lewis, and J. H. Carver

Research School of Physical Sciences, Australian National University, G.P.O. Box 4, Canberra, A.C.T. 2601, Australia

T. J. McIlrath

Institute of Physical Science and Technology, University of Maryland, College Park, Maryland 20742-2431

ABSTRACT

Two-photon resonant, difference frequency four wave mixing using the $5p_{1/2}$ (J=0) level in krypton has been performed to generate tunable VUV radiation for photoabsorption measurements of oxygen resonances in the 1200 - 1300A region. This has yielded the highest resolution spectra to date of the $E^3\Sigma_u^-$ - $X^3\Sigma_g^-$ (0-0) bands in $^{16}O_2$, $^{18}O_2$ and $^{16}O^{18}O$. Striking differences in the appearance of rotational structure between the isotopic species are observed, in some cases for the first time.

INTRODUCTION

Previous VUV high resolution absorption and photo-dissociation studies of molecular oxygen in our laboratory have used stimulated anti-Stokes Raman scattering to produce tunable VUV radiation(1,2). However, such studies are limited in practice by low conversion efficiencies to wavelengths >1500A i.e. the Schumann-Runge band and continuum region.

In the present work, use is made of the versatility of four-wave difference-frequency mixing in krypton to generate radiation over a more extensive range of VUV wavelengths down to the LiF window cutoff (1050A). This technique enables high resolution (~0.15 cm^{-1}) spectroscopy of oxygen below 1300A i.e. the band systems in the window region of the O_2 spectrum. The present work is concerned with obtaining absolute cross sections of photodissociating resonances in the 1200 - 1300A region (3) which have been measured previously using conventional monochromator techniques to a resolution of ~ $3cm^{-1}$ (4,5).

EXPERIMENT

The present experiment used the excimer pumped, dual dye laser system described at the 1988 Short Wavelength meeting(6) (fig. 1). The first dye laser was operated at 425.1nm and was frequency doubled using BBO to produce 2ω radiation two-photon resonant with the 5p(1/2) (J=0) level in krypton. The second laser (Rhodamine 700) was difference frequency mixed with the 212.55nm radiation to generate VUV radiation in the 125.3 -

Proceedings on Short-Wavelength Coherent Radiation, Vol. 11, Philip H. Bucksbaum and Natale M. Ceglio (eds.)
© 1991 Optical Society of America

123.8nm region. This technique has been proposed(7) and demonstrated(8) elsewhere to generate other VUV wavelengths , but is used here to generate radiation in this region for the first time.

The generated VUV radiation was filtered by a monochromator and passed through an oxygen absorption system used previously(1). Scans were taken using a monitor photomultiplier prior to the oxygen cell to remove shot-to-shot VUV intensity fluctuations.

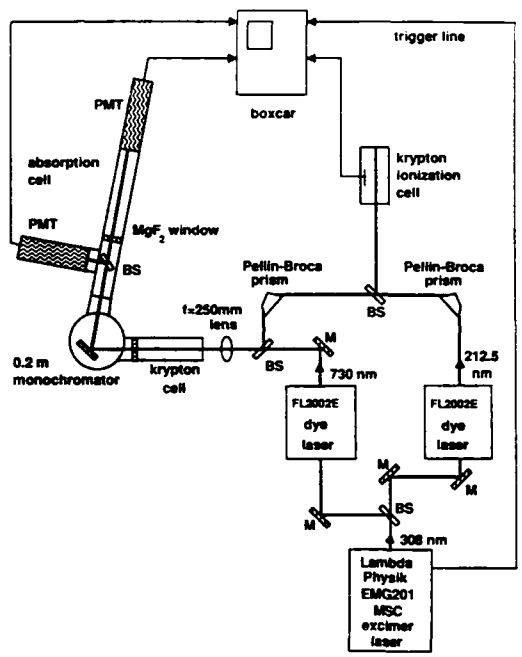

Figure 1. Schematic of the four wave difference frequency mixing experiment.

RESULTS

High resolution scans were obtained of the longest (1244A) oxygen band in the Tanaka progression at low (<0.1 torr) pressures for which pressure-broadening is negligible. For $^{16}O_2$ the spectra in fig. 2 showed smooth P and R branches with no rotational structure, which were identical with spectra obtained previously by conventional techniques(4) and were in good agreement with theory(4).

However, the measured cross sections using isotopic $^{18}O_2$ revealed detailed rotational and fine-structure (fig.3) which had been observed previously only by photographic techniques(9). The triplet fine-structure in the R branch shown in more detail in fig. 4.

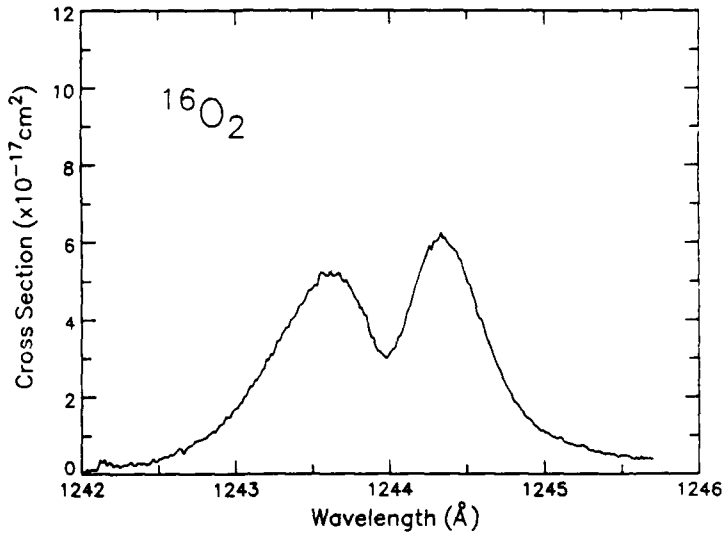

Figure 2. Measured cross section for the $E^3\Sigma_u^-$ - $X^3\Sigma_g^-$ (0-0) band in $^{16}O_2$.

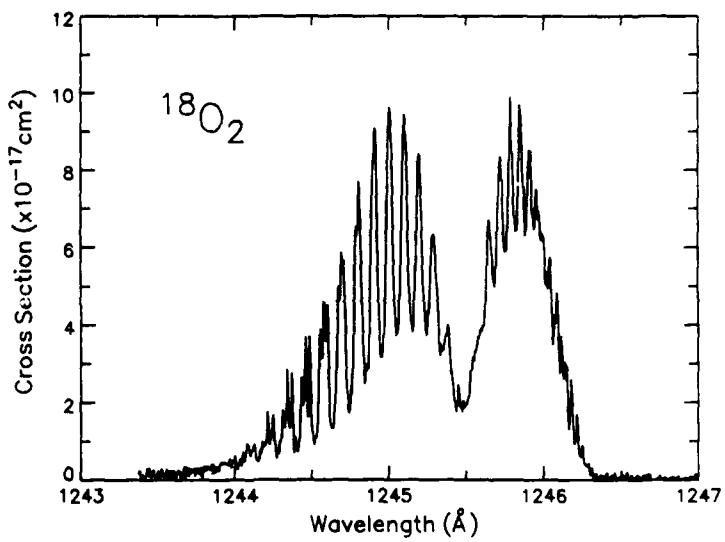

Figure 3. Measured cross section for the $E^3\Sigma_u^-$ - $X^3\Sigma_g^-$ (0-0) band in $^{18}O_2$.

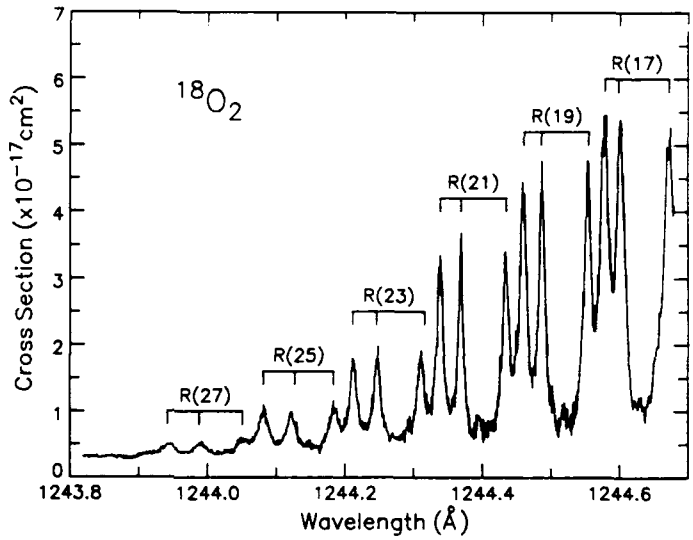

Figure 4. Detailed triplet structure in the R-branch of fig.3.

The spectra obtained using $^{16}O^{18}O$ revealed even more striking structure (fig. 5) on a wavelength scale much smaller than for $^{18}O_2$. The structure at low rotation near the band head shown is the narrowest of the three isotopes studied. The poor signal to noise ratio is mainly caused by the reduction of the data from spectra which include overlying contributions due to the other isotopic constituents.

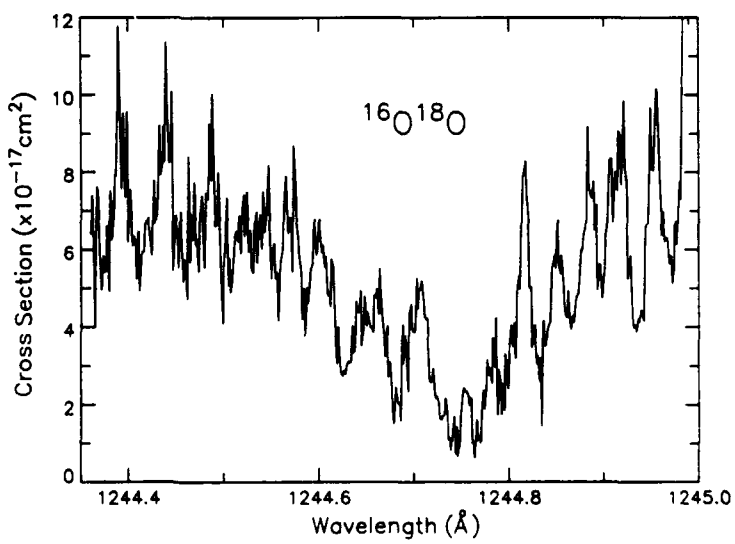

Figure 5. The same band showing finer structure for $^{16}O^{18}O$.

THEORETICAL PREDICTIONS

Our measured absolute cross-sections for the isotopic species were again in good agreement with theoretical predictions obtained using coupled Schrodinger equation theory. This theory used diabatic potentials to model the $E^3\Sigma_u^-$ - $X^3\Sigma_g^-$ absorption bands of O_2 which are predissociated and asymmetric due to strong electronic interactions between the valence and Rydberg $^3\Sigma_u^-$ states. The resultant effects are highly dependent on the isotopic species, with small changes in the rovibrational energy levels producing large changes in the rotational linewidths. These linewidths were measured experimentally for the first time here due to the use of these high resolution, nonlinear laser techniques.

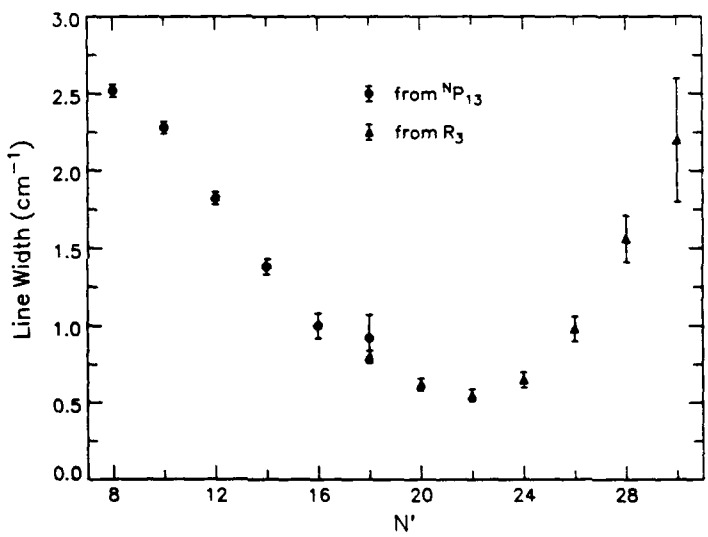

Figure 6. Rotational linewidths for $^{18}O_2$ showing experimental values.

The triplet fine structure observed in the $^{18}O_2$ spectrum exhibited a marked variation in linewidth with rotational quantum number. The R branch linewidths shown in the fig. 6 (as well as those of the weaker $^NP_{13}$ transition) reveal a pronounced non-zero minimum at N' = 22. The non-zero linewidth minimum is due to an orbit-rotation interaction between the $E^3\Sigma_u^-$ and $^3\Pi_u^-$ states. Both contributions to the linewidth are well predicted by the theoretical model.

CONCLUSIONS

The four-wave, difference-frequency mixing technique has proved versatile in the generation of high resolution, high signal-to-noise VUV spectra which will have wide applicability in future gas phase molecular spectroscopy. The novel features associated with rotational fine-structure observed in the isotopic spectra of the oxygen bands in the 1200 - 1300A window region demonstrate the usefulness of this technique.

REFERENCES

1. B.R.Lewis,S.T. Gibson, K.G.H. Baldwin and J.H.Carver, J.O.S.A. B 6, 1200 (1989).
2. S.T. Gibson, B.R.Lewis, K.G.H. Baldwin and J.H.Carver, J.Chem. Phys., 94, 1060, (1991).
3. Y.Tanaka, J.Chem.Phys. 20 , 1728 (1952).
4. B.R.Lewis, S.T. Gibson, M. Emami, and J.H.Carver, J.Q.S.R.T. 40, 1 (1988).
5. B.R.Lewis, S.T. Gibson, M. Emami, and J.H.Carver, J.Q.S.R.T. 40, 469 (1988).
6. P.B.Chapple, K.G.H.Baldwin, and H.-A. Bachor, Short Wavelength Coherent Radiation: Generation and Applications, OSA Topical Meetings (1988).
7. G. Hilber, A. Lago, and R.Wallenstein, J.O.S.A. B 4, 1753 (1987).
8. J.P. Marangos, N. Shen, H. Ma, M.H.R. Hutchinson, and J.P. Connerade, J.O.S.A. B 7, 1254 (1990).
9. M. Ogawa, Can. J. Phys. 53, 2703 (1975).

Instrumentation for Generating Tunable VUV Radiation Near 1215.6 Å (H 1*s* + *h*ν -> 2*s*) and 1202.8 Å (He $1s^2$ + 2 *h*ν -> $1s2s^1S$)

Xiaoxiong Xiong and Thomas J. McIlrath

Institute for Physical Science and Technology, University of Maryland, College Park, Maryland 20742

Chris I. Westbrook

Center for Atomic Molecular and Optical Physics, National Institute for Standards and Technology, Gaithersburg, Maryland 20899

Abstract

A system using only one tunable dye laser has been constructed for generating efficient vacuum ultraviolet (VUV) radiation by near resonant third-order frequency mixing, $\omega_{VUV} = 2\omega_{UV} - \omega_{IR}$, in krypton ($\omega_{VUV}$, ω_{UV} and ω_{IR} are the frequencies of vacuum ultraviolet, ultraviolet, and infrared radiation respectively). Enhancement effects on the generation efficiencies using various intermediate resonances and phase matched mixtures of rare gases have been investigated. This instrumentation and the schemes can be used to generate hydrogen lyman-α at 1215.6 Å and helium $1s^2$ - $1s2s\ ^1S$ two-photon resonance radiation at 1202.8 Å.

Introduction

Since the earliest nonlinear frequency mixing experiments by New and Ward [1,2], many efforts have been made to develop mixing schemes for generating vacuum ultraviolet (VUV) radiation in gases and vapors [3-6]. Among the well-established techniques are the use of intermediate resonances and the use of phase matching of the nonlinear media [3,4].

In this paper, we discuss a simple system (one dye laser and one pumping laser) constructed for generating tunable VUV radiation suitable for high resolution spectroscopy. Our special considerations are focused on the capability of generating hydrogen lyman-α at 1215.6 Å and helium two-photon excitation radiation at 1202.8 Å, and on the

Proceedings on Short-Wavelength Coherent Radiation, 18
Vol. 11, Philip H. Bucksbaum and Natale M. Ceglio (eds.)
© 1991 Optical Society of America

capability of monitoring both the intensity and the wavelength of the generated VUV radiation for precision spectroscopy. Third-order sum-difference frequency mixing, $\omega_{VUV} = 2\omega_{UV} - \omega_{IR}$, is used to generate the VUV radiation in rare gases of Kr, Xe, and Ar. The input UV frequency is tuned near, but not on, two-photon intermediate resonances (Kr: 4p - 5p) to enhance the nonlinear susceptibility $\chi^{(3)}$, and to provide the tunability of the VUV radiation. The optimal phase matching condition is achieved by mixing two oppositely dispersive gases.

Apparatus

Fig. 1a shows a parametric sum-difference frequency mixing process, $\omega_{VUV} = 2\omega_{UV} - \omega_{IR}$, using the near resonant enhancement (4p - 5p) in Kr. In the scheme shown in Fig. 1b, the input UV radiation in the region from 2125 Å to 2167 Å is produced from the dye laser (LDS 867 dye) radiation by two successive doubling processes in nonlinear crystals (KDP and BBO). In another scheme, the input UV radiation in this region is produced by summing the Nd: YAG fundamental at 1.06 μ with doubled dye laser (Fluoresein 548 dye) radiation. The input IR radiation for the two schemes is a part of the radiation from either the YAG fundamental or the fundamental of the dye laser.

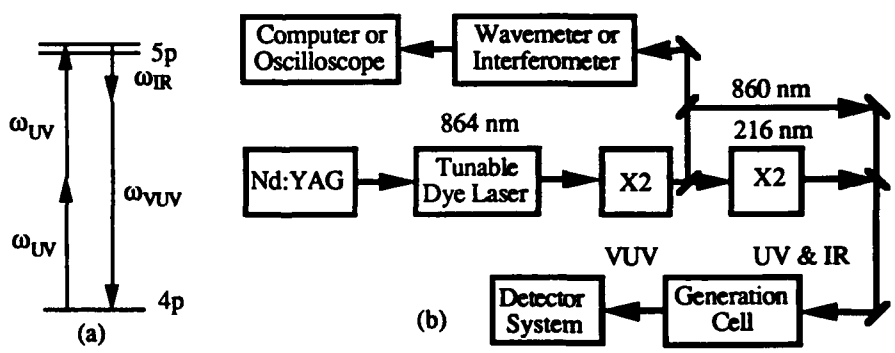

Figure 1. (a) Near resonant sum-difference frequency mixing, $\omega_{VUV} = 2\omega_{UV} - \omega_{IR}$, in Kr (4p - 5p). (b) Schematic block diagram of apparatus for generating VUV radiation by sum-difference frequency mixing.

Since near resonant schemes are used for the generation of tunable VUV radiation, only one tunable dye laser is needed in the above parametric processes, $\omega_{VUV} = 2\omega_{UV} - \omega_{IR}$. This allows the output VUV wavelength and the linewidth to be conveniently monitored during the experiment by measuring those parameters of the input tunable radiation. The generated VUV radiation is separated from the input UV and IR radiation by a dispersive lens mounted off the center axis. A

knife edge in the focal plane of the VUV allows all the generated VUV to pass through into the detector system, and blocks the remaining input UV and IR radiation. The detector system consists of a NO ionization tube and a PMT mounted to a 0.2 m monochromator. The absolute intensity is determined by measuring the NO ion current. A wavemeter and an Fabry-Perot interferometer are used to monitor the wavelength and linewidth of the driving fundamental radiation.

Results and Discussions

In addition to the dependence on the input UV and IR powers, the generated VUV power for sum-difference frequency mixing ($\omega_{VUV} = 2\omega_{UV} - \omega_{IR}$) is given by [7]:

$$P_{VUV} \propto [\chi^{(3)}]^2 N^2 e^{-|NCb|}, \tag{1}$$

where $\chi^{(3)}$ is the third-other susceptibility, N is the number density of the medium, b is the confocal beam parameter, and C (= $\Delta k/N$) is the wavevector mismatch (Δk) per atom defined as:

$$C = [k_{VUV} - (2k_{UV} - k_{IR})] / N. \tag{2}$$

VUV radiation from 1180 Å to 1240 Å has been generated using different intermediate resonances in Kr (4p - 5p). The experimental results (UV to VUV conversion efficiencies) are presented in Table 1 for on resonance sum-difference generation using pure Kr and the mixture of Kr and Xe. At each resonance, the input IR radiation is taken from either the YAG fundamental or the dye laser radiation. An enhancement factor of 2 - 10 has been obtained at different VUV wavelength by phase matching two oppositely dispersive gases.

Table 1 Absolute conversion efficiencies from UV to VUV at different Kr intermediate resonances. (a) in pure Kr; (b) in mixture of Kr and Xe. P_{UV} = 10 kW, P_{IR} = 1 MW.

Resonance	[5/2, 2]		[3/2, 2]		[1/2, 0]	
VUV Wavelength (Å)	1206	1238	1194	1227	1181	1215
Peak pressure (torr)	28	4	32	2.5	10	14
Efficiency (a) (10^{-5})	100	12	55	2	12	6
Efficiency (b) (10^{-5})	200	N.A.*	N.A.*	20	30	30

* Not Applicable (both Kr and Xe are positively dispersive)

We have measured the dispersive properties of Kr gas and found they agree with the theory very well except when the output radiation is within ~ 2 Å of a resonance in the nonlinear medium. The VUV power

dependence on the gas pressure is shown in Fig. 2. At 1215 Å, the wavevector mismatch per atom is experimentally determined to be $C_{Exp} = -1.1 \times 10^{-17}\ cm^2$, which compares favorably with the calculated value of $C_{Cal} = -1.0 \times 10^{-17}\ cm^2$ [8,9]. However at 1238 Å, which is close to the first excitation line (Kr 4p - 5s) at 1236 Å, $C_{Exp} = 4 \times 10^{-17}\ cm^2$, while $C_{Cal} = 19 \times 10^{-17}\ cm^2$ [8,9]. The rapid change of the dispersion characteristics around this excitation line, and the possible line shift due to the AC stark effect are partially responsible for the above large discrepancy.

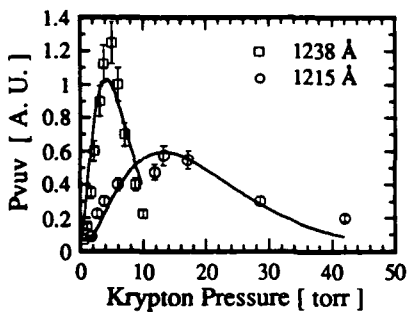

Figure 2 The VUV power dependence on the krypton gas pressure at 1238 Å and 1215 Å.

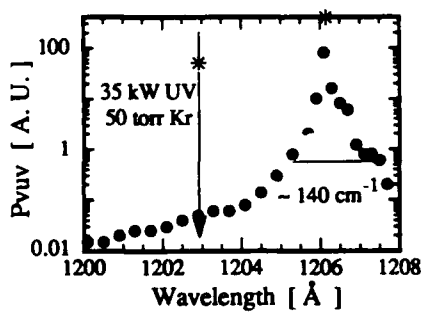

Figure 3 The VUV power versus the wavelength near Kr 4p - 5p [5/2, 2] resonance.

Several schemes in Table 1 can be used to generate the radiation at 1202.8 Å and 1215.6 Å by tuning the input UV off the exact resonance. The conversion efficiencies in pure krypton are much less for the off (but near) intermediate resonance situation than for the on resonance configuration. However, the enhancement due to phase matching is much higher for the off resonance situation. Fig. 3 displays the relative efficiencies from 1200 Å to 1208 Å when the UV frequency is tuned on and near resonance 4p - 5p [5/2, 2] in Kr. The input IR radiation is kept fixed (from YAG 1.06 μ). We can see that when the input UV is tuned away from the exact resonance by 70 cm^{-1}, the efficiency could drop as much as two orders of magnitude. At resonance, 320 W VUV radiation (1206 Å) was obtained in the phase matched mixture of Kr and Xe using 120 kW input UV. This conversion efficiency is less than we would expect, indicating possible saturation effects. For the off resonant situation, e.g. at 1203 Å (225 cm^{-1} off resonance), 80 W VUV has been generated in the mixture of Kr and Xe with 200 kW input UV (the above phase matched results are represented by "*" in Fig. 3). Similarly 40 W (~10^{11} photons/pulse) at hydrogen lyman-α radiation of 1216 Å (650 cm^{-1} off resonance) has been generated with 100 kW input UV radiation in a phase matched medium. Proper phase matching of the Kr and Xe gases with opposite dispersion provides an enhancement of more than two orders of magnitude for the non-resonant generation scheme. The

enhancement for resonant up conversion was never more than a factor of 10. Ar and Kr, having opposite dispersion in this region, have also been used in the experiment to enhance the conversion efficiency.

Conclusion

Operating near, but not on, intermediate resonances allows an efficient, tunable system with only one tunable laser. The use of phase matching with a mixture of rare gases raises the off resonance conversion efficiency to within an order of magnitude of the saturated on resonance value. Both the intensity and the wavelength of the generated VUV can be controlled with this system. The schemes of using the dye laser radiation to provide the input IR radiation and also to produce the input UV radiation (in nonlinear crystals) can be applied to the Ti: sapphire laser system, which has a maximum efficiency at 840 nm [10]. Experimental results provide useful information for generating 1202.8 Å and 1215.6 Å radiation for spectroscopy applications. This work was supported by the National Science Foundation.

References

1. G.H.C. New and J.F. Ward, "Optical Third-Harmonic Generation in Gases," Phys. Rev. Lett. **19**, 556-559 (1967).
2. J.F. Ward and G.H.C. New, "Optical Third Harmonic Generation in Gases by a Focused Laser Beam," Phys. Rev. **185**, 57-72 (1969).
3. S.E. Harris and R.B. Miles, "Proposed Third Harmonic Generation in Phase-Matched Metal Vapors," Appl. Phys. Lett. **19**, 385-387 (1971).
4. R.T. Hodgson, P.P. Sorokin, and J.J. Wynne, "Tunable Coherent Vacuum-Ultraviolet Generation in Atomic Vapors," Phys. Rev. Lett. **32**, 343-346 (1974).
5. C.R. Vidal, "Four Wave Frequency Mixing in Gases," in *Tunable Lasers*, I. F. Mollenauer, J. C. White eds. (Springer-Verlag, Heidelberg, 1987), Vol. 59.
6. J.F. Reintjes, *Nonlinear Optical Parametric Processes in Liquids and Gases* (Academic Press, 1984).
7. G.C. Bjorklund, "Effects of Focusing on Third-Order Nonlinear Processes in Isotropic Media," IEEE J. Quantum. Electron. **QE-11**, 287-296 (1975).
8. X. Xiong, Ph.D thesis to be submitted to the Graduate School at University of Maryland.
9. R. Mahon, T.J. McIlrath, V.P. Myerscough, and D.W. Koopman, "Third Harmonic Generation in Argon, Krypton, and Xenon: Bandwidth Limitations in the Vicinity of Lyman-α," IEEE J. Quantum. Electron. **QE-15**, 444-451 (1979).
10. B.W. Pease, T.J. Johnson, and W.K. Bischel, Paper CTUN 2, CLEO'90, Anaheim, CA.

Spatial Distribution of High-Order Harmonics Generated in the Tunneling Regime

S. Augst,[a] C. I. Moore,[a] J. Peatross,[a] and D. D. Meyerhofer[b]

Laboratory for Laser Energetics, University of Rochester, 250 East River Road, Rochester, New York 14623-1299

ABSTRACT

High-order harmonic production in a jet of krypton or xenon gas is studied using a 1.053-μm wavelength laser. All the harmonics in the 9th to 31st range display approximately equal angular widths with cone angles that are approximately half that of the laser. Lowest order perturbation theory predicts the angular widths to decrease with harmonic order N as $N^{-1/2}$.

The study of highly nonlinear processes in an intense laser field has become a topic of great interest. Among the possible effects is harmonic production of the laser field. In atomic gases the dipole approximation predicts the presence of only odd harmonics. We have studied the angular distribution of high-order odd harmonics (9th through 31st) and we find the results to be inconsistent with predictions of lowest order perturbation theory (LOPT). As expected, the harmonics are present when linearly polarized light is used and absent with circularly polarized light.

General features of the harmonic spectra are in agreement with previous experiments. A plateau in the intensities of the 9th through 31st harmonics is observed with a cutoff at the 23rd harmonic in xenon and the 31st harmonic in krypton. This is similar to the plateau and cutoff, which have been observed previously by several groups [1–4]. The laser intensity required to produce high-order harmonics is consistent with the findings of these other groups.

The laser used for these experiments is a Nd:glass laser, which uses the chirped pulse amplification and compression technique to produce high-intensity 1-ps laser pulses. It has been described in detail elsewhere [5,6]. Using f/20 optics (60-cm focal length lens) intensities ranging from 10^{13} to 10^{15} W/cm^2 were obtained. We have previously performed low gas density experiments to measure the degree of ionization versus laser intensity [7,8]. These experiments show that intensities of 10^{15} W/cm^2 are sufficient to produce Xe^{5+} and Kr^{4+} in the absence of collisions. The laser has also been operated in a more conventional manner with a bandwidth limited 55-ps pulse and focused intensities in

Proceedings on Short-Wavelength Coherent Radiation, Vol. 11, Philip H. Bucksbaum and Natale M. Ceglio (eds.)
© 1991 Optical Society of America

the 10^{14} W/cm^2 range. The maximum charge states obtained with this pulse were Xe^{5+} and Kr^{4+}.

The harmonics are produced in a jet of krypton or xenon gas. The gas is introduced into a vacuum chamber using a Lasertechnics model LPV pulsed nozzle. The nozzle is directed into the mouth of a 2-in. diffusion pump, which keeps the chamber pressure from rising above 10^{-5} Torr when the jet is fired. The laser is focused approximately 0.5 mm from the nozzle opening. Two nozzle sizes were used: 1000 μm and 300 μm. No harmonics were seen with the 1000-μm nozzle since the confocal parameter of the laser was less than the width of the jet. Phase-matching conditions for harmonic generation require the interaction length to be less than the confocal parameter of the focused beam [9].

The backing pressure for the gas jet is approximately 1 atm. Xenon and krypton can form dimers at these high pressures resulting in a broadband fluorescent emission, which spans the wavelength range of the harmonics [1]. This signal cannot be detected with our spectrometer since its low collection efficiency reduces the signal-to-noise ratio to the point where the fluorescence light has an intensity at or below the noise level.

The spectrometer used in these experiments is shown in Fig. 1. It consists of a slit with approximate dimensions of 100 μm × 2.5 cm followed by a bare gold wire transmission grating. The slit is aligned to be parallel to the grating wires. The grating consists of 0.5-μm diam gold wires, which are separated by 1 μm (center to center). Following the grating is a microchannel plate (MCP) image intensified phosphor screen (Galileo model 8081). The MCP intensifier is not UV enhanced so it cannot detect harmonics lower than the ninth. The screen is positioned colinearly with the laser beam. The light incident on the slit and grating is dispersed by the grating and produces spectral lines on the phosphor screen. The spectral content of the light can be measured in the direction perpendicular to the grating lines and the angular distribution of the harmonic lines can be measured parallel to the slit. Thus we simultaneously obtain information about the spatial distribution as well as the spectral content of the light.

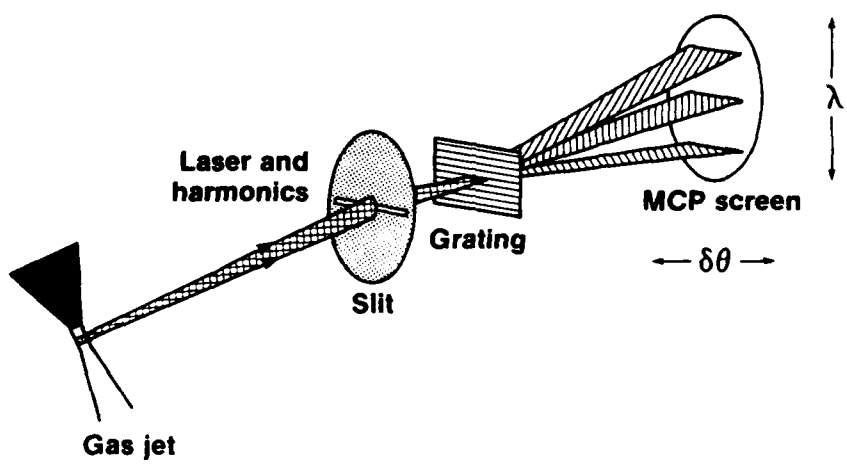

Figure 1. The spectrometer configuration. Laser and harmonic signals pass through a 100-μm slit and are dispersed by the gold wire transmission grating. The spectral lines are detected with an MCP intensified phosphor screen. The frequency spectrum is measured in the vertical direction and the angular distribution is measured in the horizontal direction.

Measurements of the harmonic distribution have also been done with the slit and the transmission grating removed so that the laser and harmonic beams directly strike the surface of the MCP. We were able to compare the spatial distribution of the harmonics to that of the laser by pulsing the gas jet on every other shot. Although the MCP is not sensitive to 1-μm wavelength light we were able to see a signal from the laser itself by increasing the bias voltage on the plates from 1.0 kV to 1.8 kV (a gain increase of ~1000). The extremely high intensity of the laser was sufficient to create a small signal. When the slit and transmission grating were in place, however, the laser beam alone would not create a signal on the MCP using comparable voltages. This is due to the large amount of 1.053-μm light, which is reflected by the grating.

A calibration of the gas pressure at the laser focus was performed by measuring the visible light emission perpendicular to the direction of laser propagation. The backing pressure of the jet was varied and the scattered signal measured. The entire chamber was then backfilled to various pressures, which produced similar signal levels. The spatial extent of the gas is clearly less in the case of the gas jet, which means there are fewer atoms from which the light can scatter. If low laser intensities are used, however, most of the scattered light will come from a very short region near the beam waist so the back-filled chamber should give only a slightly larger signal than the gas jet would at equal pressures. We estimate the output pressure of the gas jet at the laser focus to be ~5 ($\times 3^{\pm 1}$) Torr (particle density = ~10^{17} cm^{-3}).

The angular distributions of some harmonics is shown in Fig. 2. The peak heights have been normalized so that their widths can be compared. The small spatial structure could be due to many things such as defects in the grating or MCP, density variations in the gas jet, structure in the incident laser beam, or harmonic generation due to resonance effects. Some of these effects could be reduced by signal averaging, but the harmonics in Fig. 2 represent data from a single laser shot. We do not yet know if the structure is a significant feature of the data shown.

Fourier transform methods can be used to calculate the beam profile at the focal and detector planes [10,11] (if cylindrical symmetry is assumed, Hankel transforms are used). A comparison of the calculated and measured focal spot sizes suggests a nearly diffraction-limited spot size. If the harmonics are assumed to have an I^N dependence as predicted by LOPT, the spatial distribution of the harmonics at the focal plane can be calculated by raising the laser beam profile to the Nth power. The beam profile at the detector can then be calculated by performing an inverse Fourier transform. The results of these calculations are shown in Figs. 3–5, which assume (1) a Gaussian beam (Fig. 3); (2) a super-Gaussian (Fig. 4); and (3) a circular ring shape at the focus (Fig. 5), which would be the case for resonant harmonic production due to atomic levels being Stark shifted into resonance.

Clearly the LOPT prediction does not coincide with the experiment. Even though a Gaussian shape for the incident laser beam is not a realistic representation of the actual beam profile, almost identical results are obtained by using a super-Gaussian of the form: $exp\{-[a \times tan(\theta)]^4\}$. The "best-fit" width to the curve is obtained with the value $a = 50$. The super-Gaussian laser beam profile shown here is at the plane of the MCP detector approximately 60 cm from the focus.

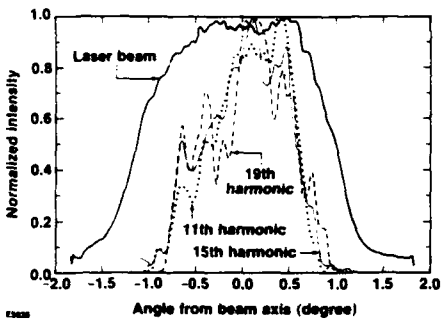

Figure 2. Experimental measurement of the spatial extent of high harmonics relative to that of the incident laser. The peak heights have been normalized so that their widths could be compared. Note that the laser beam profile represents a different laser shot from the other three curves.

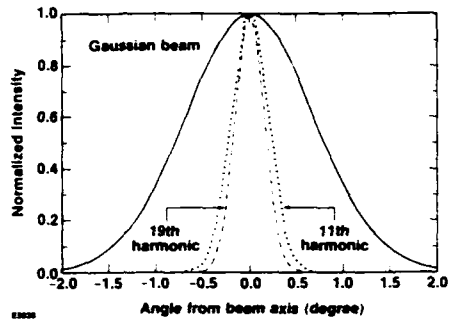

Figure 3. Lowest order perturbation theory prediction of the spatial extent of high harmonics relative to that of the incident laser. The width depends on harmonic order N as $N^{-1/2}$.

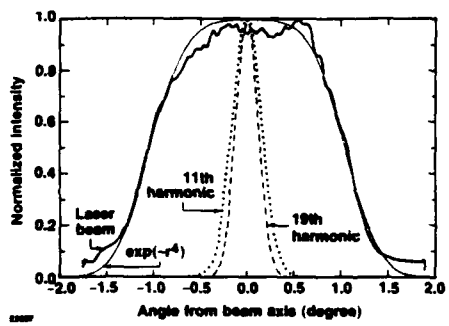

Figure 4. Comparison of the laser beam spatial profile to a super-Gaussian and the calculated harmonic widths using the super-Gaussian profile as described in the text.

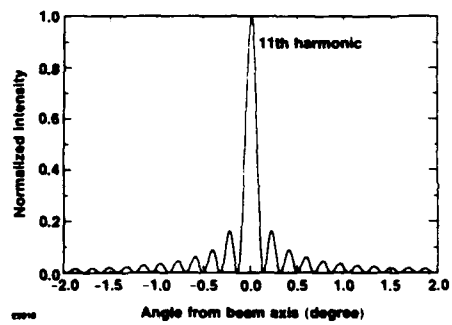

Figure 5. Angular distribution of the 11th harmonic assuming a circular ring distribution at the focus. A ring distribution might arise from resonant harmonic generation.

Harmonic production due to resonances would create harmonics in a circular ring at the focus. Figure 5 represents a calculation assuming a circular ring at the focal plane. Note that this calculation assumes a two-dimensional source whereas the actual source would more likely be some sort of ellipsoidal shell. Figure 5 is included for interest purposes only, and we do not suggest that this is the actual profile that would be expected from resonant harmonic production.

A recently proposed theoretical model of harmonic generation accounts for the presence of free electrons in the focal volume [12]. Those calculations do a good job of modeling the intensity dependence of the harmonics for large N. We are presently calculating the spatial profiles that are predicted by this model.

We wish to thank A. Hauer of LANL for the use of the transmission grating. This work was supported by the National Science Foundation under contract No. PHY 8822730. Additional support was provided by the U.S. Department of Energy Division of Inertial Fusion under agreement No. DE-FC03-85DP40200 and by the Laser Fusion Feasibility Project at the Laboratory for Laser Energetics, which has the following sponsors: Empire State Electric Energy Research Corporation, New York State Energy Research and Development Authority, Ontario Hydro, and the University of Rochester.

(a) Also Department of Physics and Astronomy, University of Rochester.
(b) Also Department of Mechanical Engineering, University of Rochester.

1. X. F. Li, A. L'Huillier, M. Ferray, L. A. Lompré, and G. Mainfray, "Multiple-harmonic generation in rare gases at high laser intensity," Phys. Rev. A 39 (11), 5751–5761 (1989).
2. L. A. Lompré, A. L'Huillier, M. Ferray, P. Monot, G. Mainfray, and C. Manus, "High-order harmonic generation in xenon: intensity and propagation effects," J. Opt. Soc. Am. B 7 (5), 754–761 (1990).
3. A. McPherson, G. Gibson, H. Jara, U. Johann, T. S. Luk, I. A. McIntyre, K. Boyer, and C. K. Rhodes, "Studies of multiphoton production of vacuum-ultraviolet radiation in the rare gases," J. Opt. Soc. Am. B 4 (4), 595–601 (1987).
4. N. Sarukura, K. Hata, T. Adachi, R. Nodomi, M. Watanabe, and S. Watanabe, "Coherent soft x-ray generation by the harmonics of an ultrahigh-power KrF laser," Phys Rev. A 43 (3), 1669–1672 (1991).
5. Y. H. Chuang, D. D. Meyerhofer, S. Augst, H. Chen, J. Peatross, and S. Uchida, "Suppression of the pedestal in a chirped-pulse-amplification laser," to be published in J. Opt. Soc. Am. B in July 1991.
6. P. Maine, D. Strickland, P. Bado, M. Pessot, and G. Mourou, "Generation of ultrahigh peak power pulses by chirped pulse amplification," IEEE J. Quantum Electron. QE-24 (2), 398–403 (1988).
7. S. Augst, D. Strickland, D. D. Meyerhofer, S. L. Chin, and J. H. Eberly, "Tunneling ionization of noble gases in a high-intensity laser field," Phys. Rev. Lett. 63 (20), 2212–2215 (1989).
8. S. Augst, D. D. Meyerhofer, D. Strickland, and S. L. Chin, "Laser ionization of noble gases by coulomb-barrier suppression," J. Opt. Soc. Am. B 8, 858 (1991).
9. J. Reintjes, C.-Y. She, and R. C. Eckardt, "Generation of coherent radiation in the XUV by fifth- and seventh-order frequency conversion in rare gases," IEEE J. Quantum Electron. QE-14 (8), 581–596 (1978).
10. A. E. Siegman, Lasers (University Science Books, Mill Valley, CA, 1986), p. 661.
11. J. W. Goodman, Introduction to Fourier Optics (McGraw-Hill, New York, 1988), Chap. 5.
12. A. L'Huillier, X. F. Li, and L. A. Lompré, "Propagation effects in high-order harmonic generation in rare gases," J. Opt. Soc. Am. B 7 (4), 527–536 (1990).

Resonantly Enhanced Harmonic Generation and Above-Threshold Ionization in Krypton

J. K. Crane, S. W. Allendorf, K. S. Budil, and M. D. Perry

Lawrence Livermore National Laboratory, P.O. Box 808, L-490, Livermore, California 94550

Abstract

We describe the results of experiments performed in Krypton to observe the effect of an isolated atomic level on harmonic generation at intensities above 10^{13} W/cm^2. We have measured the intensity of harmonics produced as a function of laser intensity and focal conditions as well as recorded the photoelectron energy spectra in complementary experiments. We discuss a simple model fit to our data that describes an atomic level ac Stark shifting through resonance.

In the search for an intense source of vacuum ultraviolet radiation, nonpertubative high-order harmonic generation (NHG) is being studied carefully by a number of experimental and theoretical groups.[1,2,3] This research followed closely the exploration of above threshold ionization (ATI), and more than one worker has suggested a strong connection between the two processes.[4,5] In this paper we present the results of our experimental investigation of the connection between NHG and ATI, focussing in particular on the effect of an intermediate state resonance on these two processes. We chose krypton for this work because it contains two atomic levels, the $4p^5(^2P_{3/2})5s$ and the $4p^5(^2P_{1/2})5s'$, that are isolated from the higher lying levels and can be expected to ac Stark shift into coincidence with five photons at 532 nm with intensities in the 10^{13} - 10^{14} W/cm^2 range (the $5s$ state lies 1.6 eV below the five-photon energy while the $5s'$ state is 1.0 eV below the energy of five photons).

Proceedings on Short-Wavelength Coherent Radiation, Vol. 11, Philip H. Bucksbaum and Natale M. Ceglio (eds.)
© 1991 Optical Society of America

The experimental conditions for observing ATI and NHG are quite different. ATI measurements are made with an electron spectrometer that operates at relatively low densities(~10^{10} cm^{-3}) so that space-charge effects on the electron flight times are minimized. In contrast, harmonic generation is proportional to the density squared and yields large signals at the high, localized densities(10^{15} - 10^{18} cm^{-3}) of a supersonic nozzle. To satisfy the quite different density requirements of ATI and NHG while maintaining all else the same, we used separate chambers with identical focussing conditions. The laser system consists of a mode-locked Nd:YAG laser that seeds a regenerative amplifier, which is frequency doubled to produce up to 125 mJ energy in a 75 ps pulse.[6] For the NHG experiments the laser is focussed at the output of a pulsed supersonic gas jet. The generated harmonics pass through the entrance slit of a normal incidence vacuum monochromator, are dispersed by a 1200 lines/mm grating, and are detected by a CsI-coated dual microchannel plate (MCP) detector. An identical lens is used to focus the laser between the pole pieces of a magnetic bottle photoelectron spectrometer for the ATI experiments. The use of 75 ps laser pulses means that the ponderomotive energy of the electrons in the intense field is completely recovered: the observed photoelectron time-of-flight is therefore independent of the laser intensity. To determine the laser intensity per pulse we simultaneously measure pulse energy, using a calibrated photodiode, and the beam profile at the focal plane, using a CCD-based beam profiling instrument. The focussed beam is Gaussian and slightly elliptical. In both experiments the signals are binned according to laser intensity and each recorded point is an average of 20-100 individual laser shots.

Figure 1 presents results from an NHG experiment where the laser was focussed with a 50 cm lens (the confocal parameter b=0.8 cm). The MCP signal is converted to photon number by correcting for the grating and MCP efficiencies at each harmonic wavelength and the fractional transmission of the monochromator input slit. We estimate this conversion is within a factor of five in absolute value but better than 50% when comparing the individual harmonics. We show data for the 3rd, 5th, and 7th harmonics. The higher orders were not observed above the background from the bright plasma formed at the laser focus. The 3rd harmonic was observed to increase as I^3 where I is the fundamental intensity. The 5th harmonic increases as I^5, but levels off at 3 x 10^{13} W/cm^2 then begins to rise again. The 7th harmonic shows a dip or step at the same intensity as the 5th. Harmonics measured with a shorter confocal parameter (b=0.3 cm) behaved similarly, with the exception that the 7th harmonic actually overtakes the 5th harmonic at the intensity near the step. With a shorter focal length lens we see the 9th harmonic above the background fluorescence. Figure 3 shows harmonic intensities from shorter confocal parameter NHG experiments (b=0.3 cm) for several peak laser intensities. At the lowest intensity we see the harmonic signal fall precipitously with order. At 2.8 x 10^{13} W/cm^2 the 5th and 7th harmonics have increased with respect to the 3rd, forming a small plateau where the 7th has actually surpassed the fifth. At the highest intensity the 9th harmonic is also beginning to catch up to the lower orders, causing the plateau to widen.

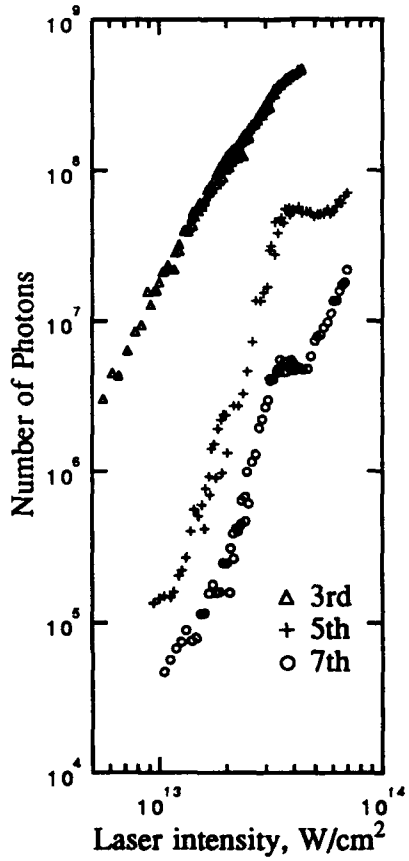

Figure 1. Number of harmonic photons detected, b=0.8 cm.

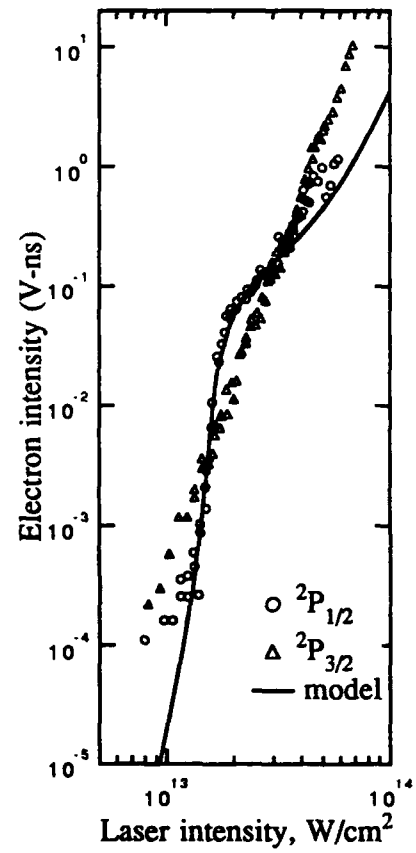

Figure 2. Integrated electron signal, seven photon ionization of Krypton, b=0.8 cm.

Figure 2 presents the results of ATI experiments using the longer focal length lens (b=0.8 cm). Each point is the integrated area of a peak in the time-of-flight photoelectron spectrum, corresponding to the production of Kr^+ in either the $^2P_{1/2}$ or $^2P_{3/2}$ spin states by absorption of seven photons. The $^2P_{3/2}$ signal rises as I^5, but otherwise displays no notable features. Conversely, the $^2P_{1/2}$ signal clearly shows a step similar to the feature observed in the harmonic data. A similar feature is also seen on the eight-photon $^2P_{1/2}$ ATI data. We do not see a similar step in the higher ATI peaks; however, the effect of a five-photon resonance may be washed out at the higher orders as was seen for the 9th harmonic. Additionally, we are unable to resolve the ion spin states for the higher ATI peaks, so the step is probably softened by the $^2P_{3/2}$ signal. The presence of the resonance feature in the $^2P_{1/2}$ ATI data but absence in the $^2P_{3/2}$ data suggests the resonant state has a $^2P_{1/2}$ core; we assign the $4p^5(^2P_{1/2})5s'$ excited state as the intermediate state at work in our ATI and NHG experiments.

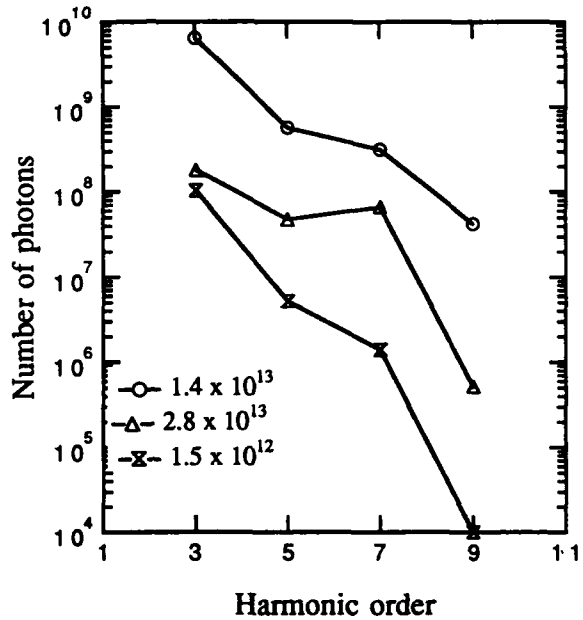

Figure 3. Relative harmonic production at selected laser intensities (W/cm^2) for b=0.3 cm confocal parameter.

To model the effect of this resonance, we calculate the total ions produced per laser shot when a state is nearly five-photon resonant.[7] The model is based on the five photon excitation to a level that is ac Stark shifted through resonance, followed by a two photon ionization to a continuum state. We integrated the following equation over the known temporal and spatial profile of our laser:

$$N_{ions} = \int dV \int dt \frac{\Omega^2}{4} \frac{\gamma_2}{(5\omega - \omega_o - \alpha_s I)^2 - \left(\frac{\gamma_2}{2}\right)^2} , \tag{1}$$

where Ω is the five photon Rabi rate given by $\Omega^2 = \alpha_5 I^5$, α_5 is the five-photon Rabi coefficient, γ_2 is the two-photon ionization rate and is given by $\gamma_2 = \sigma I^2$ (σ is the two-photon ionization cross section), α_s is the ac Stark coefficient, and $5\omega - \omega_o$ is the five-photon frequency offset. The fit results give α_5=2 x 10^{-137} cm^{10}-sec^3, γ_2=8 x 10^{-49} cm^4-sec, and α_s=6.5 x 10^{-14} eV-cm^2/W; the solid curve in Fig. 2 is the plot of Eq. (1) for these values of the three parameters. Clearly the better way to determine the ac Stark shift of this excited state is to record the ATI spectrum using short (1 ps) laser pulses; these experiments are currently underway.

In conclusion, we have shown the first direct evidence of the role that intermediate resonances play in producing the patently nonperturbative behavior that has become the trademark of high order harmonic generation in the regime of laser intensities greater than

10^{13} W/cm^2. In particular we showed a single, isolated level being ac Stark-shifted through resonance, causing the selective enhancement of the seventh harmonic and the beginning of plateau formation. In addition, by measuring the ATI spectra in a complementary experiment we have associated the state with a particular ion core state, which enabled us to identify the resonance as the $^2P_{1/2}$ $5s'$ state. Based on these results that show a single level being shifted through resonance to form a small plateau we suggest that the extended plateaus seen by several groups consist of many levels being shifted in and out of resonance as the atom is excited into the high density Rydberg and continuum states.

Acknowledgments

We would like to acknowledge the technical assistance of Ken Haney and thank K. Kulander, K. Schafer, J. Krause, and S. Dixit for valuable discussions. This work was performed under the auspices of the U. S. Department of Energy at Lawrence Livermore National Laboratory under contract number W-7405-Eng-48.

---

1. A. L'Huillier, L. Lompré, G. Mainfray, and C. Manus, "High-order harmonic generation in rare gases", Adv. Atom. Mol. Opt. Phys. (in press), 1991.
2. A. McPherson, G. Gibson, H. Jara, U. Johann, I. A. McIntyre, K. Boyer, and C. K. Rhodes, "Studies of multiphoton production of vacuum-ultraviolet radiation in the rare gases", J. Opt. Soc. Am. B 4, 595 (1987).
3. N. Sarukura, K. Hata, T. Adachi, R. Nodomi, M. Watanabe, and S. Watanabe, "Coherent soft x-ray generation by the harmonics of an ultra-high power KrF laser", Phys. Rev. A (in press), 1991.
4. K. C. Kulander, K. J. Schafer, and J. L. Krause, "Time-dependent numerical studies of multiphoton processes",Adv. Atom. Mol. Opt. Phys. (in press), 1991.
5. J. J. Eberly, Q. Su, and J. Javanainen, "Nonlinear light scattering accompanying multiphoton ionization", Phys Rev Lett. 62, 881-884 (1989).
6. M.D. Perry, O. L. Landen, J. Weston, and R. Ettlebrick, "Design and performance of a high-power, synchronized Nd:YAG-dye laser system", Opt. Lett. 14, 42-44 (1989).
7. M. D. Perry, "High-order multiphoton ionization of the noble gases", Ph. D Dissertation, University of California at Berkeley, 1987.

Photon accelerator: A novel method of frequency upshifting sub-picosecond laser pulses

Scott C. Wilks
Lawrence Livermore National Laboratory,
University of California, Livermore, CA 94550

Abstract

A novel method of frequency upshifting subpicosecond pulses of laser light, which makes use of relativistic plasma waves, is described in this paper. This method makes use of the fact that the response of a plasma to either a short laser pulse or a short relativistic electron beam is nearly identical. Thus, the wakefields, or electric fields, that are left behind in the plasma as either of these drivers pass, are also very similar. Since electron acceleration in plasma waves can effectively be thought of as the simple superposition of wakes, this analogy brings about the interesting question of whether the superposition of short laser pulse wakes would produce "acceleration" (or equivalently, frequency upshifting) of a trailing laser pulse. We estimate the rate of frequency upshift possible, and discuss some important physical limitations.

Two recent particle acceleration schemes, the plasma beat wave accelerator (PBWA)[1] and the plasma wake field accelerator (PWFA),[2] employ relativistic plasma waves to generate large electric field gradients (~ 1 GeV/cm)[3] for the acceleration of charged particles to ultra-relativistic energies. A third method, which was actually the proposed method in the original laser accelerator article by Tajima and Dawson [1] will be implicitly included in our references to the PBWA. This method relies on a short ($\leq \lambda_p/2$, where λ_p is a plasma wavelength) powerful laser pulse to create the plasma wave. Each scheme relies on using a finite-length, electrical disturbance (in the PBWA, an intense laser pulse; in the PWFA, a relativistic electron beam) propagating through a plasma to set up plasma waves that have a phase velocity of nearly the speed of light in vacuum. Once generated, one then injects a trailing bunch of electrons into the accelerating phase of the plasma wave, so that energy can be transferred from the wave to the trailing electrons (this is referred to as "beam loading.")[4,5,6]

We will discuss the results of replacing this trailing bunch of electrons with a short (less than 1/2 of a plasma wavelength) pulse of electromagnetic radiation. It will be shown that the frequency of the radiation is continuously upshifted, in analogy with the energy gain of the trailing bunch of electrons in the original concept of plasma accelerators. First, we will review the process of accelerating electrons with plasma waves. The acceleration of charged particles via plasma waves can be viewed in the following way. Consider it is as the superposition of the longitudinal electric fields (also referred to as wakefields) of an accelerating wave, which we take to have been generated some type of driving beam, and a trailing beam that lags the end of the driver by a few plasma wavelengths. We find that the density perturbation left behind by the driving beam is given by

$$n_1 = \delta n \sin k_p(z - ct),$$

where we have taken δn to be the amplitude of the disturbance in an otherwise homogeneous plasma of density n_0, and we have also assumed that the phase velocity of the wave is approximately the speed of light (c). The wavenumber, k_p, is related to the plasma frequency through the dispersion relation $k_p \approx \omega_p/c$; the plasma frequency being defined as $\omega_p^2 = (4\pi n_0 e^2)/m_e$. When a second bunch of electrons is then injected with te appropriate phase, we find that the field behind the trailing pulse is zero. This can be understood by saying that the driving beam

put energy into the plasma in the form of plasma waves, which we now call the accelerating field. As the trailing beam follows, it extracts this energy that was stored in the plasma waves. This energy finally shows up as an increase in the kinetic energy of the trailing beam electrons.

The idea of "loading" the plasma wave with a laser pulse can be explained in a manner similar to that of electron beam loading. This time we will assume that the driving beam is also a short laser pulse, although a driving electron beam would also create a suitable wake. As discussed above, this light pulse traveling through a plasma leaves behind it a "wake," or density perturbation given by the above equation. (The amplitude can be shown to be $\delta n/n_0 \approx (eE_0)/(m_e\omega_0 c)$, where E_0 is the amplitude of the electromagnetic wave associated with the laser pulse of frequency ω_p.) Now consider a second, identical, pulse placed $1\frac{1}{2}$ plasma wavelengths behind the first pulse. This second pulse will create an identical wake that is 180 degrees out of phase with the first wake. The superposition of the two wakefields behind the second pulse results in a lowering of the amplitude of the plasma wave. It is clear that the second laser pulse will absorb some fraction of the energy stored in the wake created by the first laser pulse. Assuming photon conservation, this increase in energy implies that the frequency of the second pulse can be upshifted, i.e.,

$$\Delta U = N\hbar\Delta\omega.$$

This follows from the fact that the energy of the pulse is $U = N\hbar\omega$, N being the total number of photons in the packet.

We obtain an estimate on the rate of frequency upshift possible in the presence of a relativistic Langmuir wave of amplitude δn in an otherwise homogeneous plasma with density n_0, that moves with the velocity of the driver, v_p. We first find that the laser pulse can be represented by an equivalent charge similar to our trailing electron beam discussed above. Once this is recognized, the electron beam loading formalism developed in previous section can be used to investigate the "acceleration" of the laser pulse. Computer simulations of both a short laser packet and a short trailing electron beam provides further evidence that this is a valid analogy. We find the rate of frequency upshift per unit distance to be

$$\frac{d\omega}{dz} \approx \frac{\omega_p^2 \epsilon k_p}{2\omega},$$

where ϵ is now the maximum density perturbation, normalized to the background plasma density; i.e., $\epsilon \equiv \delta n/n_0$. It is found that this increase in frequency of the accelerated laser packet exactly accounts for the loss in the energy of the accelerating plasma wave. Numerical examples will be given, assuming the initial laser pulses come from KrF and Nd :glass, or YAG lasers. Various physical limitations will begin to limit the upshift possible after the pulse has propagated some finite distance, and these will also be discussed.

Computer simulations have been performed with the plasma simulation codes WAVE [7] and ISIS, and they confirm this upshifting mechanism. We will now describe a simulation in which photon acceleration was observed. The plasma wave was set up by a wakefield driver [4] with initial $\gamma = 22$. The density perturbation, $\epsilon \sim 0.25$, set up by this driver produced a wake into which was injected a laser pulse of width $L_{pulse} \approx 2.5c/\omega_p$, the initial frequency $\omega_i = 18\omega_p$. After a distance of $237c/\omega_p$, we found that there was an upshift of 10% in the laser frequency, or a final frequency of $\approx 19.8\omega_p$. The above equation for the rate of frequency upshift predicts an upshift to $\approx 19.5\omega_p$. This slight difference is attributed to the fact that even at density perturbations of 25%, the wake shows nonlinear wave steepening.

In conclusion, we will present a novel method of continuously upshifting short ($L_{pulse} \leq \lambda_p/2$) pulses of electromagnetic radiation by use of relativistic electron plasma waves. By choosing the length of time the packet interacts with the plasma wave, any frequency between the initial frequency and the final frequency can be obtained. It is found that frequency increases of a factor of five may be possible. 1 and 2-D PIC simulations have confirmed the existence of this effect.

Acknowledgments

Work performed under the auspices of the United States Department of Energy by the Lawrence Livermore National Laboratory under contract number W-7405-ENG-48.

References

[1] T. Tajima and J.M. Dawson, Phys. Rev. Lett., **43**, 267 (1979), and W.B. Mori, IEEE Trans. Plasma Sci. **PS-15**, 88 (1987).

[2] R. Keinigs and M. E. Jones Phys. Fluids **30**, 252 (1987); P. Chen, R.W. Huff, and J.M. Dawson, *Bull. Amer. Phys. Soc.*, **29**, 1355, (1984); P. Chen, J.M. Dawson, R.W. Huff, and T. Katsouleas, Phys. Rev. Lett., **54**, 693, (1985).

[3] See for example, *Laser Acceleration of Particles*, edited by C. Joshi and T. Katsouleas, AIP Conference Proceedings No. 130 (American Institute of Physics, New York, 1985), also C. Joshi *et al.*, *Nature* (London), **311**, 525 (1984).

[4] R. Ruth, A. Chao, P. Morton, and P. Wilson, Particle Accelerators, **17**, 171 (1985).

[5] T. Katsouleas, *et al.*, Particle Accelerators, **22**, 81 (1987) and S. van der Meer, CLIC Note 3, CERN/PS/85-65 (AA) (1985).

[6] R.D. Ruth and P. Chen, SLAC-PUB-3906, March (1986).

[7] R.L. Morse and C.W. Neilson, Phys. Fluids, **14**, 830 (1971).

Generation of Ultrafast VUV Radiation by Reflection from a Relativistic Ionization Front

Henry C. Kapteyn and Margaret M. Murnane

Department of Physics, Washington State University, Pullman, Washington 99164-2814

Abstract

Tunable radiation can be produced by Doppler upshifting light from a laser-generated moving ionization front. We analyze this technique as a way of generating ultrashort tunable short-wavelength light pulses, and demonstrate the possibility of making pulses of duration ~1 femtosecond in the UV and XUV. The demonstration of this technique should be possible using the current generation of high power ultrashort-pulse (0.1 Joules in 100 fsec) laser systems.

1. Introduction

Herein we propose a method of producing short-wavelength radiation, which has the potential to produce optical pulses shorter than any that have been generated to date. This method is based on the process of upshifting light by reflecting it off a moving ionization front. Reflection from an ionization front has been considered in detail as a method for upshifting microwave radiation.[1] We show that by using an intense femtosecond light pulse to generate an ionization front through multiphoton ionization (MPI), it is possible to upshift a single-cycle far-infrared light pulse to optical and ultraviolet wavelengths. Since the ionization front created by MPI can be very sharp, the reflection process adds little dispersion to the pulse, making it possible to generate nearly single-cycle light pulses at wavelengths as short as 100-200 nm. This upshift process should be experimentally realizable using the current generation of high energy femtosecond (0.1 Joule in 100 fsec) lasers. We discuss several physics issues unique to the generation of short-wavelength light using this technique. In particular, more detailed calculations of MPI rates would be helpful to determine the efficiency of the reflection process, as will be discussed.

2. Fundamental physics

Consider an intense optical pulse (the "driver pulse") traveling through a gas. It can generate a sharply rising ionization front at the leading edge of the pulse through the

Proceedings on Short-Wavelength Coherent Radiation
Vol. 11, Philip H. Bucksbaum and Natale M. Ceglio (eds.)
© 1991 Optical Society of America

process of multiphoton ionization. To calculate the interaction of a counterpropagating pulse (the "probe pulse") with this "moving mirror", we shift to a reference frame moving at the velocity βc with the ionization front. In this reference frame, the frequency of the probe pulse will not change upon reflection. The frequency of the probe pulse before it encounters the ionization front is $\omega' = \omega_0 \gamma (1+\beta)$, where $\gamma = \left(1-\beta^2\right)^{-1/2}$, and ω_0 is the frequency of the probe in the lab frame. The plasma dispersion relation is invariant under Lorentz transformation, since $\left(\vec{k}, \frac{\omega}{c}\right)$ is a four-vector and thus $\omega_0^2 - k_0^2c^2 = \omega'^2 - k'^2c^2 = \omega_p^2$.[1] Therefore, in the moving reference frame the upshifted pulse will reflect off the ionization front for frequencies $\omega' \leq \omega_p$. After reflection, the probe frequency in the lab frame will be $\omega'' = \gamma\,\omega'(1 + \beta)$. In the absence of dispersion, the number of cycles in the pulse is unchanged, and the duration of the probe pulse is reduced by the same factor $\gamma^2 (1 + \beta)^2$ as the frequency upshift. This is exactly analogous to a mirror which is physically moving. However, in contrast to a real mirror, for the ionization front the electrons that make up the plasma are streaming away from the interface in the moving reference frame and thus can carry energy away with them. This reduces the energy in the reflected pulse by a factor of ω''/ω_0 independent of the details of the ionization profile.[1]

If the velocity of the ionization front is the group velocity of the driver pulse in the plasma, $\beta = \sqrt{1-\left(\omega_p/\omega_d\right)^2}$, the maximum reflected upshifted frequency will be $\omega'' < \gamma\,\omega_p(1 + \beta) = \omega_d(1 + \beta)$, while the maximum initial probe frequency ω_0 must be $\omega_0 \leq \omega_d\left(1 - \beta\right)$. For β close to 1, the maximum upshifted frequency corresponds to twice the frequency of the driver pulse. A UV driver pulse thus will allow the generation of VUV light. However, if the driver pulse is converging to a focus, the position of the ionization front relative to the peak of the pulse will advance. This effect can be used to obtain arbitrarily large upshifts. We have done simple simulations[2] which indicate that upshifts to a few times the driver frequency appear feasible. Thus the generation of VUV and XUV radiation should be possible even using visible-wavelength driver pulses.

3. Simulation

The initial wavelength of the probe pulse can be very long. If a single-cycle duration far-infrared (FIR) pulse[3,4] is used, it may be possible to create nearly single-cycle duration pulses at optical wavelengths. Since multiphoton ionization is a high-order process, it should readily be possible to create an ionization front which has a risetime much shorter than the length of the ionizing pulse, minimizing dispersion of the probe pulse. In order to investigate this dispersion, a model was developed. The simulation assumes a driver pulse of wavelength 400 nm, upshifting from a single-cycle far infrared pulse centered at 600 μm, with 1.2 psec pulse width, up to a pulse with a center wavelength of 250 nm. The gas density to provide the necessary upshift is 1.2×10^{19} cm^{-3}, and the gas was assumed to be hydrogen for simplicity. The light pulse was taken to be

100 fsec (FWHM), with a peak intensity of 2×10^{15} W cm^{-2}. Two models for multiphoton ionization (a Keldysh approximation[5,6], and a threshold approximation[7]) were used to model the ionization front. Given an ionization profile, group velocity dispersion of the pulse can be calculated in the moving reference frame using the WKB approximation, in which the phase function of the reflection process is given by $\varphi(\omega') = \int k' \, dx$.

The results of the simulation are shown in figure 1. Figure 1(a) shows the electric field of the incident FIR pulse as a function of time. Figure 1(b) and (c) show the electric field of the reflected pulse for each case. For the case of the Keldysh model, the ionization front risetime of ~20 fsec necessitates additional group-velocity pre-compensation in the form of a grating pair, which reduced the probe pulse width from 20 fsec to the shown 3 fsec. In the case of the threshold model with an ionization risetime of a few femtoseconds, nearly single-cycle pulses are produced without any GVD compensation.

To determine the experimental feasibility of this technique, the energy requirement for the driver pulse must be estimated. This energy requirement is determined by the time its takes the incident pulse to reflect from the ionization profile. If L_p is the length of the ionization front in the laboratory frame, in the moving reference frame this length is γL_p by relativistic length contraction. The velocity of the probe pulse in the moving frame is near c, so that the time required for reflection is $t_p = \frac{2\gamma L_p}{c}$. Shifting back to the laboratory frame, time dilation must be taken into account so that the interaction time will be $T_{lab} = \frac{2\gamma^2 L_p}{c}$.

The minimum confocal parameter of the driver pulse necessary to completely reflect the pulse will be given by $b = c\, T_{lab}$. Self-defocusing of the driver pulse due to plasma creation is the major factor limiting its confocal parameter; an effective plasma defocusing confocal parameter can be estimated to be $b = 2 r_0 / \sqrt{1-\beta}$. This yields an energy require-

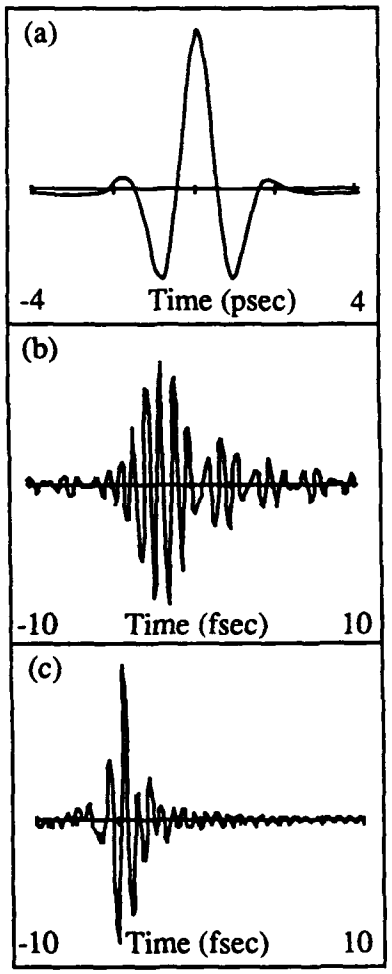

Figure 1: Simulation of reflection and upshifting of a FIR pulse.

ment of $E_d \approx \pi/4\, b^2(1-\beta)\, I_d\tau \approx \frac{\pi}{8}\frac{\omega''}{\omega_o} L_p^2\, I_d\tau$. Other considerations on the pulse energy, such as depletion of the driver pulse through ionization, and diffraction of the beam, are less stringent limitations. Dispersion of the driver pulse over the interaction length can also be shown to be small in comparison to the length of the driver pulse; thus the driver pulse and the ionization front can remain intact during the interaction process. For the simulation of Figure 1, the energy requirement of the driver pulse works out to 70 mJ--well within the range of technological feasibility using the current generation of high-energy femtosecond laser systems.

The amount of energy in the ultrashort pulse that one could obtain from this process can be estimated. Very large area photoconductive antennas[4] are in principle a feasible method of producing high pulse energies of FIR radiation. As was discussed previously, the reflection process has a theoretical maximum efficiency of ω_o/ω'', which for the simulation parameters is 4×10^{-4}. Collisional absorption can be shown to be insignificant compared with this factor. However, multiphoton absorption of the reflecting pulse is not negligible. An exact calculation of this absorption mechanism is difficult, but the magnitude can be estimated. Light with the maximum reflected frequency has a frequency of $\gamma\,\omega_p = \omega_d$ in the lab frame at the point of reflection. Thus, at this point the reflected light must have the same absorption depth as the driver photons, which is just $l = \frac{F}{R\,n\,n^*} = \frac{I\,L_p}{c\,n\,h\nu_i}$, where F is the driver photon flux, R is the ionization rate, n is the gas density, n^* is the average number of photons required to ionize an atom, and the final expression assumes that $R = c/L_p$ and $n^* = \frac{h\nu_i}{h\nu_d}$. For the above simulation, this results in a transmission coefficient of 0.044 over the interaction length. Thus, the total reflection efficiency of the ionization front would be expected to be about 10^{-5}. It should be possible to generate ultrashort light pulses with an experimentally useful energy of $\sim 10^{-6}$ - 10^{-7} Joules using this technique. A calculation of multiphoton ionization rates in the case of an intense pulse and a less intense pulse of differing frequency and polarization would be a useful theoretical extension of this analysis.

References

1. M. Lampe, E. Ott and J. H. Walker, "Interaction of electromagnetic waves with a moving ionization front," Physics of Fluids 21 (1), p. 42 (1978).
2. H.C. Kapteyn and M.M. Murnane, "Relativistic Pulse Compression," to be published in J. Opt. Soc. Am. B, August 1991.
3. P. R. Smith, D. H. Auston and M. C. Nuss, "Subpicosecond Photoconducting Dipole Antennas," IEEE Journal of Quantum Electronics 24 (2), p. 255 (1988).
4. J. T. Darrow, B. B. Hu, X.-C. Zhang and D. H. Auston, "Subpicosecond electromagnetic pulses from large-aperture photoconducting antennas," Optics Letters 15 (6), p. 323 (1990).
5. N. H. Burnett and P. B. Corkum, "Cold-plasma production for recombination extreme-ultraviolet lasers by optical-field-induced ionization," Journal of the Optical Society of America B 6 (6), p. 1195 (1989).
6. L. V. Keldysh, "Ionization in the field of a strong electromagnetic wave," Soviet Physics JETP 20 (5), p. 1307 (1965).
7. S. Augst, D. Strickland, D. D. Meyerhofer, S. L. Chin and J. H. Eberly, "Tunneling Ionization of Noble Gases in a High-Intensity Laser Field," Physical Review Letters

Section I: Sources of Short-Wavelength Radiation

Incoherent Generation

X-Ray Spectral Determination of Electron Density in Dense Laser-Excited Targets

T. S. Luk, A. McPherson, D. A. Tate, K. Boyer, and C. K. Rhodes

Laboratory for Atomic, Molecular, and Radiation Physics, Department of Physics, University of Illinois at Chicago, P.O. Box 4348, Chicago, Illinois 60680

V. L. Jacobs, P. G. Burkhalter, A. Zigler,†* D. A. Newman, and D. J. Nagel

U.S. Naval Research Laboratory, Washington, D.C. 20375-5000

ABSTRACT

The electron density of the x-ray emitting volume in a plasma produced by intense subpicosecond ultraviolet irradiation of UV-transparent targets is determined by measurement of the line ratio of dielectronic satellites from lithium-like ions.

I. DISCUSSION OF RESULTS

Plasmas produced by subpicosecond laser excitation of solid targets can produce powerful short duration x-ray pulses [1] for x-ray laser excitation [2]. X-ray spectroscopy can provide a simple and convenient diagnostic on the properties of these high-density plasmas. In this work, we explore the use of dielectronic satellite transitions from lithium-like (Li-like) ions for the determination of the electron density of the plasma. The experiments under discussion were conducted with intensities up to ~ 10^{17} W/cm^2 with a 248-nm source [3].

The dielectronic satellite transitions of interest are situated spectrally on the long-wavelength side of the resonance lines emitted by the He-like ions and are produced by spontaneous radiative decay from autoionizing states of the corresponding Li-like species. In the low density corona model for these satellite line intensities [4,5], one assumes that the autoionizing levels are populated either by inner-shell electron collisional excitation or by the radiationless electron-capture process which is the initial step in the two-step mechanism of dielectronic-recombination described by Burgess [5]. However, it has been demonstrated by Jacobs and Blaha [6] that, with increasing plasma density, the population of these autoionizing levels can be substantially and selectively altered from their low density values by collisional mechanisms. In particular, angular-momentum-changing collisions have high rates and can efficiently redistribute population among the metastable autoionizing states. This redistribution of excited state population gives rise to a dramatic density-dependent enhancement of the dielectronic satellite spectra that is particularly evident in the high-density region.

The sets of satellite lines under investigation are, following the notation of Gabriel [4], the $1s2p^2\ ^2D \rightarrow 1s^22p\ ^2P$ (j,k,l), $1s2p^2\ ^2P \rightarrow 1s^22p\ ^2P$ (a,b,c,d) and $1s2p(^1P)2s\ ^2P \rightarrow 1s^22s\ ^2S$ (q,r) transitions. The (j,k,l) lines, which depend only

†Currently at The Hebrew University, Jerusalem, Israel;

*Permanent Address: Sachs/Freeman Associates, Inc., Landover, Maryland 20785.

Proceedings on Short-Wavelength Coherent Radiation, 42
Vol. 11, Philip H. Bucksbaum and Natale M. Ceglio (eds.)
© 1991 Optical Society of America

on the He-like ion abundance, provide a convenient reference, since the intensity of these lines has been predicted [6] to vary quite weakly with electron density. On the other hand, the (a,b,c,d) lines, which are vanishingly weak at low density, exhibit dramatic enhancement [6] at high plasma densities due to the collisional mixing of the autoionizing states noted above. For Z = 12 – 14, this effect is significant at electron densities in the range of 10^{22} to 10^{24} cm^{-3}.

The KrF^* (248 nm) laser [3] employed in these experimental investigations has a pulse duration of ~ 600 fs and a pulse energy of ~ 150 mJ. The laser system was focused with a CaF_2 lens onto flat targets, composed of either SiO_2 and MgF_2, and produced intensities up to ~ 10^{17} W/cm^2 at the target surfaces.

High-resolution x-ray spectra were recorded on DEF film by flat potassium acid phthalate (KAP, 2d = 26.6A) and pentaerythritol (PET, 2d = 8.7A) crystal spectrometers. Each spectrum was generated by an integrated exposure derived from 25 laser shots. A question of particular concern in this work is the influence of a low density plasma potentially produced by the prepulse, since it could alter the nature of the interaction of the subpicosecond pulse with the dense target material. Independent measurements have shown [7], however, that for UV-transparent MgF_2 and SiO_2 targets, the prepulse plasma is not present for the range of intensities involved in these studies.

The dependence of the intensity ratio of the dielectronic satellite transitions to changes in this electron temperature has been experimentally investigated by varying the intensity of irradiation for the MgF_2 and SiO_2 targets over a factor of ~ 30. The x-ray spectra obtained by means of this procedure are shown in Fig. (1). No substantial variation can be seen in the relative intensities among the various satellite lines. This behavior is in agreement with the previous calculations of Jacobs and Blaha [6] which predict that the relative intensities of these transitions are weakly dependent upon the electron temperature. Conversely, with the same variation of focused laser intensities, the intensity ratios exhibited by the hydrogen-like 2p $\rightarrow$ 1s and the helium-like 1s3p $\rightarrow$ $1s^2$ resonance lines of Mg and Si are found to change by approximately a factor of ten. This observed behavior of the resonance lines reveals the existence of a strong temperature variation with laser intensity. Furthermore, the optical opacity for the satellite lines is estimated to be small, on the order of 0.1. This estimate takes into account only thermal Doppler broadening and assumes that the emission occurs from a plasma with an ion temperature of 0.5 keV, that the electron density is 5 x 10^{23} cm^{-3}, and that the path length [7] is 2500 Å.

The theoretical predictions [6] for the dielectronic satellite intensities have been made with the assumptions (1) that the electron-ion encounters involve electrons with a Maxwellian velocity distribution and (2) that the autoionizing level populations and charge state distributions are determined by the time-independent equilibrium balance established by the elementary atomic processes occurring in the plasma. A consideration of the collisional and radiative time scales, similar to that presented by Cobble et al. [8], reveals that electron-electron collisions are sufficiently rapid, even for subpicosecond excitation, to justify the assumption that the plasma electrons have a Maxwellian velocity distribution. However, the electron-ion collision times are generally not sufficiently short to satisfy the requirement for the establishment of the corresponding equilibrium values for the bound-state densities and charge state distributions. The <u>exception</u> to this for the ion levels is the case of the angular-momentum-changing electron-ion collisions that are responsible for the density enhancement of the satellite transitions [6,8]. These collisional rates are sufficiently rapid to fulfill the conditions for the establishment of a local statistical-equilibrium distribution of populations among the autoionizing levels. Since the rate coefficients for the (j,k,l) lines used in the model calculations are insensitive to <u>both</u> the electron

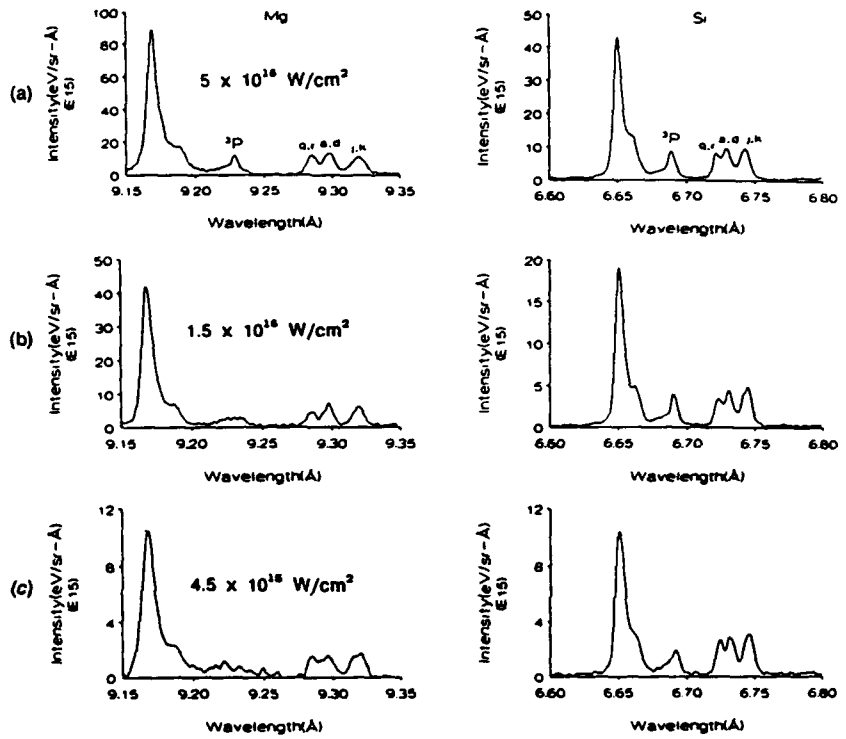

Fig. (1). Dielectronic spectra associated with the 1s2p $^1P \rightarrow 1s^2\ ^1S$ resonance lines of helium–like Mg and Si, obtained for various focused laser intensities. The alphabetical designation of the satellite transitions has been introduced by Gabriel [Ref. (4)]. The pair of spectra for sets (a), (b), and (c) have the intensity indicated in the Mg column.

temperature and density, these lines serve as a good reference for comparison with the density sensitive (a–d) lines.

The observed values of the intensity ratios I(a,b,c,d)/I(j,k,l) for both Mg and Si are 0.9. In addition, the intensity ratio between the $1s2p(^1P)2s\ ^2P \rightarrow 1s^22s\ ^2S(q,r)$ satellite lines and the $1s2p^2\ ^2D \rightarrow 1s^22p\ ^2P$ (j,k,ℓ) satellite lines is observed to be between 0.7 and 0.8 for both Mg and Si. This latter case also represents a substantial enhancement in comparison with the low density prediction. The comparison with the theoretical findings [6] obtained for the (a–d) satellite line in intensity ratio, shown for Si in Fig. (2), leads to the result that the electron density is on the order of 10^{23} cm^{-3}. A similar result is found for the (q,r) line.

Since the spectra are space–time integrated, it is necessary to understand the possible role of other mechanisms in producing $1s2p^2\ ^2P$ states which can result in a–d emission. Inner–shell excitation from the $1s^22p$ state of Li–like ions, which requires both a high temperature and a large Li–like ion abundance, is an alternative mechanism. At low electron temperature (<65 eV), Li–like ion ($1s^22p$) abundance is less than 10%, based on a Saha equilibrium estimate, until the electron density exceeds 10^{21} cm^{-3}. At such a low electron temperature, the inner–shell excitation rate for the $1s2p^2\ ^2P$ state is extremely low and, therefore, this process will give a negligible contribution to the a–d emission. As the electron temperature increases, the minimum density required to produce Li–like ions also increases rapidly reaching

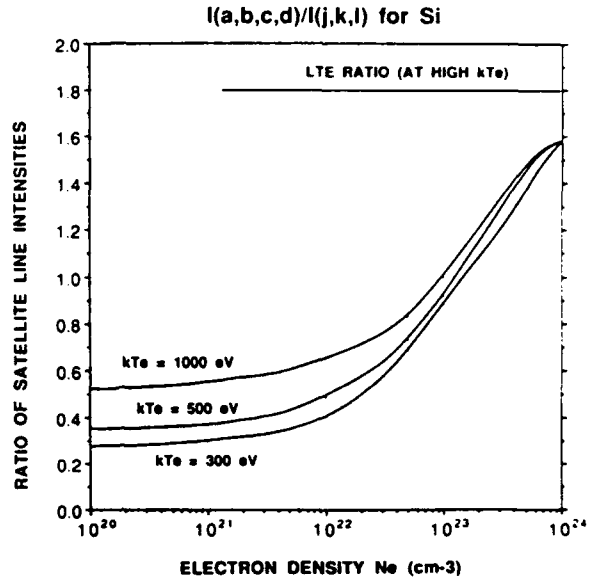

Fig. (2). The intensity ratio between the $1s2p^2\ ^2P \longrightarrow 1s^22P\ ^2P$ (a,b,c,d) satellite lines and the $1s2p^2\ ^2D \longrightarrow 1s^22p\ ^2P$ (j,k,ℓ) satellite lines for Si, as a function of the electron density N_e for various values of the electron temperature T_e.

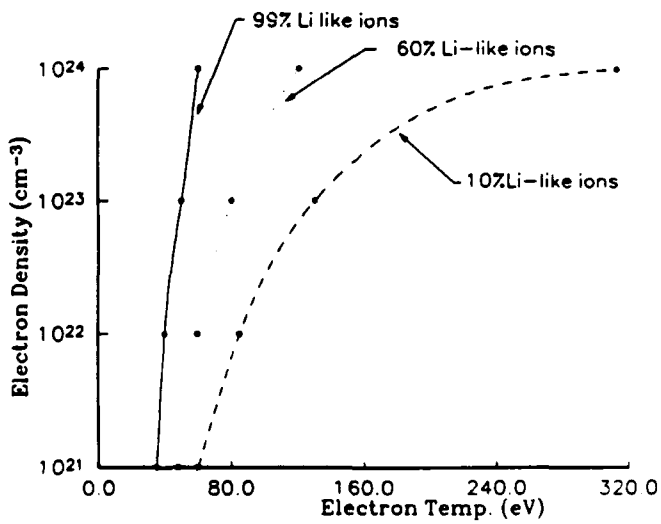

Fig. (3). Plot of the Saha relationship indicating the curves for 99%, 60%, and 10% abundance of Li-like ions.

~ 10^{22} cm^{-3} at 100 eV for 10% abundance. Furthermore, even a relatively high electron temperature (>300 eV), gives a Li-like ion abundance that is small unless the electron density is the order of 10^{24} cm^{-3}. These relationships are illustrated in Fig. (3). Therefore, significant a–d emission is only expected when the plasma is hot and dense.

Time integration does not change this conclusion. The time span during which the relevant plasma conditions are satisfied is expected to be very short due to rapid cooling by electron thermal conduction. Consequently, space–time–integration of the emission is not expected to change the results significantly. These conclusions are supported by comparison with the spectra observed with long pulse irradiation in which hot low density plasmas are generally produced. In this case [9], the strength of the a–d emission, relative to the (j,k,ℓ) transitions, is low, a finding in conformance with the picture described above.

II. CONCLUSIONS

In conclusion, the analysis of high–resolution satellite spectra of multi–charged lithium–like ions, produced by the interaction of high–intensity subpicosecond ultraviolet irradiation of solid surfaces, shows that the properties of these spectra can give a direct measure of the ambient plasma electron density in the radiating zone. In the case presented in this paper, it is found that the satellite transitions originate from a region having a plasma density on the order of 10^{23} cm^{-3}. It is the sensitivity of these spectral features to a selective collisional process, particularly active in the high density regime, that gives rise to the enhancement of their strength.

III. ACKNOWLEDGMENTS

The technical assistance of P. Noel and J. Wright and the helpful discussions with Dr. M. D. Rosen are acknowledged. This research has been supported by the Air Force Office of Scientific Research, the Department of Energy, the Office of Naval Research, and the Strategic Defense Initiative Organization.

IV. REFERENCES

1. M. M. Murname, H. C. Kapteyn, and R. W. Falcone, "High–Density Plasmas Produced by Ultrafast Laser Pulses," Phys. Rev. Lett. 62, 155–158 (1989).
2. M. A. Duguay and P. M. Rentzepis, "Some Approaches to Vacuum UV and X–Ray Lasers," Appl. Phys. Lett. 10, 350–352 (1967).
3. T. S. Luk, A. McPherson, G. Gibson, K. Boyer, and C. K. Rhodes, "Ultrahigh–Intensity KrF^* Laser System," Opt. Lett. 14, 1113–1115 (1989).
4. A. H. Gabriel, "Dielectronic Satellite Spectra for Highly–Charged Helium–Like Ion Lines," Mon. Not. R. Astron. Soc. 160, 99–119 (1972).
5. C. P. Bhalla, A. H. Gabriel, and L. P. Presnyakov, "Dielectronic Satellite Spectra for Highly–Charged Helium–Like Ions – II (Improved Calculations)," Mon. Not. R. Astron. Soc. 172, 359–375 (1975).
6. V. L. Jacobs and M. Blaha, "Effects of Angular–Momentum–Changing Collisions on Dielectronic Satellite Spectra," Phys. Rev. A 21, 525–546 (1980).
7. A. Zigler, P. G. Burkhalter, D. A. Newman, D. J. Nagel, T. S. Luk, A. McPherson, C. K. Rhodes, and M. D. Rosen, "Energy Penetration Depth and X–Ray Emission Density Interaction of Subpicosecond KrF Laser with Layered Targets," Bull. Am. Phys. Soc. 35, 1943 (1990).
8. J. A. Cobble, G. A. Kyrala, A. A. Hauer, A. J. Taylor, C. C. Gomez, N. D. Delamater, and G. T. Schappert, "Kilovolt X–Ray Spectroscopy of a Subpicosecond Laser–Excited Source," Phys. Rev. A 39, 454–457 (1989).
9. P. G. Burkhalter, M. J. Herbst, D. Duston, J. Gardner, M. Emery, R. R. Whitlock, J. Grun, J. P. Apruzese, and J. Davis, "Density and Temperature Profiles within Laser–Produced Plasmas in the Classical–Transport Regime," Phys. Fluids, 26, 3650–3659 (1983).

X-Ray Generation by High Irradiance Exawatt-Per-Square Centimeter Subpicosecond Lasers

G. A. Kyrala, R. D. Fulton, D. E. Casperson, E. K. Wahlin, L. A. Jones, G. T. Schappert, J. A. Cobble, and A. J. Taylor

Los Alamos National Laboratory, P.O. Box 1663, MS E526, Los Alamos, New Mexico 87545

Abstract

We have studied the interaction of 290-fsec, 308-nm laser pulses with Aluminum targets at irradiances exceeding 5×10^{18} W/cm^2 (5 EW/cm^2). The x-ray spectrum shows a hot electron component with a characteristic temperature of 30 keV, and a low temperature component of 1 keV. Imaging of the x-rays shows an emission region of few micrometers for the hot component and a larger region for the 1 keV emission. The x-ray spectrum is dominated by the hydrogen- and helium-like lines from Aluminum, with the brightest lines radiating 0.6% of the incident laser light energy. The spectral luminosity of the L_α line was measured to be 3×10^{14} W/cm^2/eV/sr.

Introduction

The interaction of ultrashort laser pulses with matter has become a significant method of generating very short x-ray pulses.[1,2] These x-ray pulses could be useful in the pumping of inner shell x-ray lasers where the instantaneous power requirements are very high. We have been advocating the use of selected x-ray lines to pump these inner shell x-ray lasers,[3] rather than using continuum radiation as has been suggested previously.[4,5] This selective method of ionization reduces the x-ray pump energy requirements as well as the extraneous heating that accompanies the pumping by broadband radiation.

In this present paper we investigate the effect of increased laser irradiance on the interaction of a short (290 fsec) laser pulse with an Aluminum target. We present data that shows that when the laser irradiance was increased from 1×10^{17} W/cm^2 to 5×10^{18} W/cm^2, the x-ray spectrum changed from a helium-like dominated spectrum to one where the hydrogen-like Aluminum lines became as intense. However, the peak x-ray conversion efficiency into each line did not change significantly.

These encouraging results lead us to believe that irradiating higher Z targets with higher irradiance, in the presence of amplified spontaneous emission (ASE) prepulse, will produce significant line emission at much shorter x-ray wavelengths permitting the pumping of shorter wavelength inner-shell x-ray lasers.

Proceedings on Short-Wavelength Coherent Radiation, Vol. 11, Philip H. Bucksbaum and Natale M. Ceglio (eds.)
© 1991 Optical Society of America

Experiment

The experiments were carried out at the Los Alamos Bright Source Laser-II. A detailed description of the laser system has been given elsewhere.[6] The laser (308 nm) produces 250 mJ in a 290 fsec pulse. A 10 ns long ASE prepulse with up to 15 mJ of energy precedes the main laser pulse. The pulse is focused, using a reflective f/1.9 off-axis parabola with 18 cm focal length, to irradiances (I) exceeding 5×10^{18} W/cm^2. A 10-mil thin flat plate made from Schlieren quality quartz and polished to $\lambda/20$ quality is used as a blast shield to protect the parabola from target debris. A planar diamond turned aluminum target was placed normal to the laser axis and the best focus of the laser was determined by adjusting the target axial position to maximize the x-ray emission. The x-rays generated in the interaction region were detected and analyzed using a variety of diagnostics as shown in Fig. 1. Filtered Silicon-pin-diodes were used to measure the broadband x-ray emission in various energy ranges. Other pin-diodes were used, with interference filters, to measure the scattered laser light and some of its harmonics. A flat pentaerythritol (PET) crystal spectrometer was used to record the hydrogen- and helium-like spectral emission from aluminum between 1.6 and 2.2 keV.

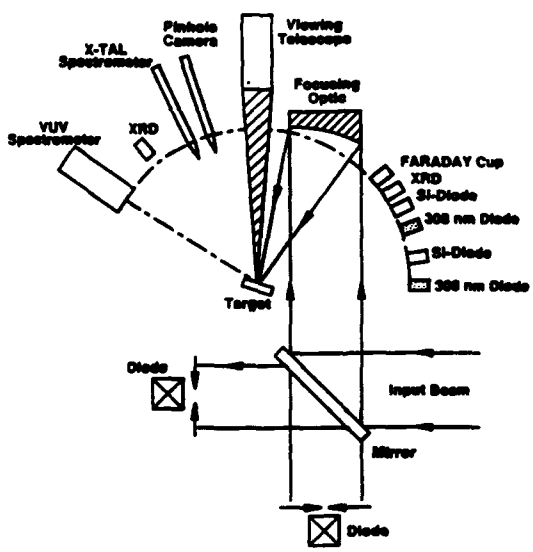

Figure 1. Schematic diagram of the target interaction region and the associated diagnostics.

The crystal spectrometer was also used in an imaging mode, Fig. 2. In this mode a knife edge was inserted in front of the spectrometer with its edge parallel to the dispersion direction. The spatial information was used to determine the size of the emission region for each recorded line. An imaging XUV grating spectrometer viewing the target parallel to the surface was used to look at the spectrum between 30 and 100 Angstroms. A vacuum ultraviolet spectrometer monitored the laser harmonics at 25 degrees to the target normal. Various diodes monitored the prepulse energy, the laser energy, and their relative timing. A 12.5-μm diameter pinhole camera with a 10-mil thick beryllium filter was used to image the x-ray emission region. A Faraday cup was also used to measure the speed of the ion expansion normal to the surface.

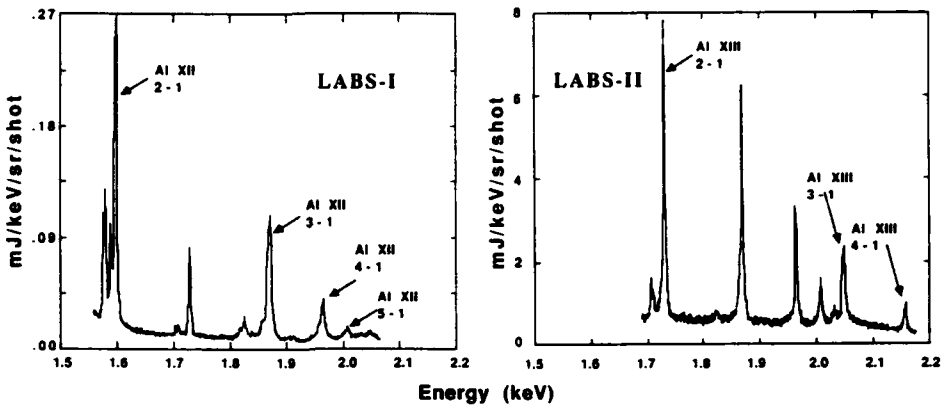

Figure 2. Comparison between the x-ray spectra from an aluminum plasma at 10^{12} W/cm^2 (LABS I) and 5×10^{18} W/cm^2 (LABS II).

Hot Electron Temperature

The hot electron temperature (T_H) was measured using two diagnostics. The first used filtered pin diodes to measure a temperature of 25-35 keV from the slope of the Bremsstrahlung spectrum above 8 keV.[7] This T_H agrees with previous[8,9] measurements at the same $I\lambda^2$ parameter.

The second method[10,11] relates T_H to the speed of the fastest ion. This was measured with a Faraday cup to be 2×10^8 cm/sec, resulting in a T_H of 22 keV.

X-Ray Line Spectra

The time-integrated line spectra from the target were observed using both crystal and grating spectrometers. A comparison of typical crystal spectrometer spectra from an aluminum target taken at irradiances of .1 and 5 EW/cm^2 are shown in Fig. 2. The low irradiance spectrum was obtained with a .7-ps 248-nm laser. Note that at higher irradiance the hydrogen-like emission increases relative to the helium-like emission, the energy per line increased with irradiance signifying constant conversion efficiency, and the ratios of the He_α satellites changed apparently due to the intercombination line. Curiously, the width of each line increases weakly with n, signifying that the plasma was formed at low density. Using the spectral line broadening code of R. W. Lee[12] for the 4-1 and 3-1 Helium like lines, we obtain an electron density of 6×10^{21} cm^{-3} corresponding to fully ionized aluminum at a density of 4.6×10^{20} cm^{-3}.

Other indications as to the density of the plasma come from the satellite and the intercombination line intensities.[13,14] The ratio of the a,b,c,d to the j,k,l component is sensitive to the electron density because the a-d emission is not normally allowed, except when electron collisions mix the autoionizing states. At high irradiance the ratio 2.5/3.5 gives an electron density of 6×10^{21} e/cm^3, below the critical density at 308 nm ($n_c=1.2\times10^{22}$ e/cm^3).

Imaging

The imaging of the plasma in the different x-ray spectral regions are indicative of the plasma behavior. We used a pinhole camera, with a 12.5 μm diameter aperture and

filtered with 10-mils thick Beryllium, to image the x-rays emitted from the target at energies above 4 keV. The emission region was found to be circular with a diameter of 11 μm at its base and with a FWHM diameter less than 3.5 μm. The emission region was thus a few times larger than the diffraction limit of the laser beam.

The spatial extent of the hydrogen- and helium-like lines emission regions were determined using the shadow of an edge in a crystal spectrometer, as shown in Fig. 3. Using the width of the penumbra of the image, the emission was found to come from a spot that has a full width at the base of 144 μm. This region is larger than the region from which the harder x-rays were emitted from.

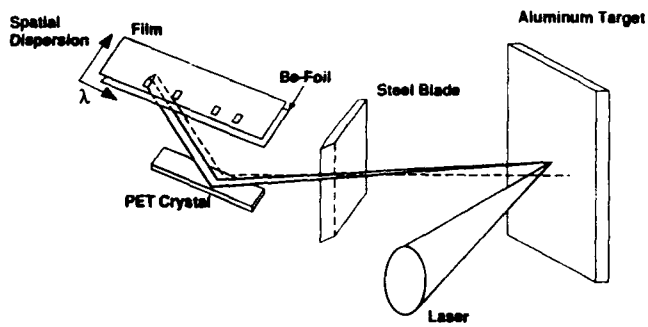

Figure 3. Schematic diagram of the PET x-ray crystal spectrometer used in the imaging mode.

Discussion

From the present data one can present a simple model that describes the method by which the laser energy is deposited and then converted into x-ray energy. The ASE prepulse energy from the laser is absorbed by inverse bremsstrahlung. A self-similar expansion of the resultant cool plasma ensues with a scale length that is determined by the ASE energy.[15] When the high irradiance main pulse arrives, it is partially absorbed by inverse bremsstrahlung and multiphoton ionization in the prepulse plasma. The electron density increases rapidly and a new critical density region is generated at some point in the prepulse plasma. This new critical density region is in front of the ASE generated critical density and may be well in front of the initial solid target interface. Resonance absorption then dominates. Hot electrons are generated and the region gets heated, emitting high energy bremsstrahlung.

The origin of the keV He- and H-like aluminum line radiation is not entirely clear. One can think of two limiting cases. If the electron temperature is sufficiently high for a long enough time to completely strip the aluminum, the line radiation is due to subsequent recombination. This mechanism favors emission at a lower temperature and hence at a later time to allow expansion and cooling. The line emission would come from a larger region over a longer time.

On the other hand, if the electron temperature is not sufficiently high over a long enough time to completely strip the aluminum, it may be enough to strip through Li-like aluminum and excite He-and H-like ions, leading to rapid radiative relaxation. In this case the line radiation would be emitted from the small absorption region for a short time prior to cooling and expansion. We suspect that experiments[15] on our 10^{17} W/cm^2 system were in the latter regime, and our present experiments at 5×10^{18} W/cm^2 in the former.

The data show that the hot electron temperature is close to what is expected given the input laser irradiance, and that the spot size is also close to what is expected. Thus we have no evidence for defocusing of the laser beam. Since electrons of 30 keV

temperature lose their energy primarily by ionization which causes atomic radiation,[16] one can use the spot size at low x-ray energies to infer an ion density. A continuous spectrum of electrons has a range of only 0.2 mg/cm^2 corresponding to a range of 0.7 μm of solid aluminum.[17] The observed image of the x-ray lines was, however, 72 μm in radius. This range corresponds to an aluminum density 0.01 solid density (6×10^{20} ion/cm^3) or an electron density 2/3 critical density. This electron density, 8×10^{21} e/cm^3, is consistent with that derived from the satellite ratio measurements.

Conclusions

We have investigated the effect of increasing the laser irradiance to 5×10^{18} W/cm^2 on the interaction of a 290 fsec laser pulse with an aluminum target. We found that the plasma heats up sufficiently to burn through to the hydrogen-like aluminum. We measured a hot electron temperature that is compatible with the predictions from measurements at lower irradiances and longer pulses. Though absorption occurs at low ion density, the energy conversion efficiency into individual hydrogen- and helium-like lines is close to the 0.6% that was measured at lower irradiance. However, at the current laser irradiance, higher ionization states are now observed. With faster (f/1) optics, irradiances in excess of 2×10^{19} W/cm^2 will soon be available to us, permitting the observation of H-like lines for even higher Z material with higher x-ray energies and hopefully similar conversion efficiencies.

Acknowledgments

We would like to acknowledge the valuable assistance of K. Stetler, J. Roberts, J. Studebaker, and B. Carpenter to the progress of this work. This work was done under the auspices of the United States Department of Energy.

References

1. J. A. Cobble et al., Phys. Rev. A39, 454 (1989).
2. M. M. Murnane, H. Kapteyn, and R. Falcone, Phys. Rev. Lett. 62, 155 (1989).
3. G. A. Kyrala, 16th IEEE/ICOPS, Buffalo, New York, poster session (1989).
4. M. A. Duguay and P.M. Rentzepis, Appl. Phys. Lett. 10, 350 (1967).
5. F. T. Arrechi, G. P. Banfi, and A. M. Malvezzi, Opt. Comm. 10, 214 (1974).
6. A. J. Taylor, C. R. Tallman, J. P. Roberts, C. S. Lester, T. R. Gosnell, P. H. Y. Lee, and G. A. Kyrala, Opt. Lett. 15, 39 (1990).
7. W. Priedhorsky, D. Lier, R. Day, and D. Gerke, Phys. Rev. Lett. 47, 1661 (1981).
8. G. A. Kyrala and D. Bach, LA-UR-82-305.
9. T. H. Tan, G. H. McCall, and A. H. Williams, Phys. Fluids 27, 297 (1984).
10. R. F. Schmalz, Phys. Fluids 28, 2932 (1985).
11. A. W. Ehler, F. Begay, T. H. Tan, J. Hayden and J. McCleod, J. Phys. D:Appl. Phys. 13, L29 (1980).
12. R. W. Lee, J. Quant. Spectroscopy Radiation Transfer 40, 561 (1988).
13. D. Duston, J. E. Rogerson, J. Davis, and M. Blaha, Phys. Rev. A 28, 2968 (1983).
14. V. A. Boiko, S. A. Pikuz, and A. Ya Faenov, J. Phys. B:Atom. Molec. Phys. 12, 1889 (1979).
15. J. A. Cobble et al., J. Appl. Phys. 69, 3369 (1991).
16. S. V. Starodubtsev and A. M. Romanov, "The Passage of Charged Particles Through Matter", AEC-TR-6468 (1965).
17. W. F. Libby, Phys. Rev. 103, 1900 (1956).

Soft-X-Ray Emission Characteristics of Line-Shaped, Laser-Produced Plasmas

Shisheng Chen, Xiaofang Wang, Aidi Qian, and Zhizhan Xu
Shanghai Institute of Optics and Fine Mechanics, Academia Sinica, P.O. Box 800-311, Shanghai 201800, China

Line-shaped plasmas produced by laser irradiating solid targets in line focus are of a large aspect ratio. Such plasmas are useful for x-ray laser demonstration and amplification and absorption spectroscopy as well. Soft x rays emitted from line-shaped plasmas can provide accurate information of such plasmas. Here, we report the studies of x-ray radiation transfer and spatial uniformity of line-shaped plasmas with a pinhole transmission grating spectrometer (PTGS), with a spectral resolution of 2–5 Å and a spatial resolution of 60 μm, and a soft-x-ray streak camera, with a time resolution of 30 ps.

The line-shaped plasmas were created by 1.05-μm laser beam with pulse width of 500–700 ps and an average power density of 10^{12}–10^{13} W/cm^2. Slab targets of low- and medium-Z elements such as Al, Si, and Cu were used.

The key element of the PTGS is a free-standing gold transmission grating with a period of 2000 lines/mm in a 25-μm-diameter pinhole. The PTGS was mounted along or off the plasma axis to measure axial or off-axis soft-x-ray spectra in the range 5–150 Å and the corresponding one-dimensional spatial images of the line-shaped plasmas at each wavelength.

Time-integrated spectra were recorded on film. Real emission spectra were obtained involving the response of the film used and the correction of the transmission grating's higher-order diffraction.

Comparisons of off-axis and axial spectra of different plasma length indicate that plasma opacity has a remarkable effect on resonance line radiative transfer. This effect may cause a detrimental influence on the realization of maximum x-ray laser gains in the case of long line-shaped plasmas.

Measurements of spatial uniformity along the line focus of different wavelength emission images show that spatial nonuniformity of higher-charged-state ions are more serious than that of lower-charged ones. With uniform and coherent laser illumination, the nonuniformity can be decreased but cannot be eliminated. Time-resolved measurements indicate that such nonuniformity occurs during optical laser heating. Various instabilities can be excited owing to long scale length in line-shaped plasmas to produce the nonuniformity.

Characteristics of Sub-100-ps Laser Irradiation of Cylindrical Cavities

J.E. Balmer, B. Soom, U. Ellenberger, and R. Weber

Institute of Applied Physics, University of Berne,
CH-3012 Berne, Switzerland

Laser irradiation of cylindrical cavities has attracted considerable interest in the context of soft x-ray laser experiments because the confined plasma may act as an x-ray waveguide.[1] Waveguiding requires a concave, radially symmetric density profile and thus uniform plasma ablation inside the cavity. In the case of transverse irradiation presented in this work, the uniformity of plasma ablation is primarily determined by the mechanisms which redistribute the energy from the initial location of plasma generation by the incident laser. Among the mechanisms to be considered are x-radiation, hot electrons, and laser light reflected at the primary spot. Experimentally, evidence was found that for short-pulse, long-wavelength, high-irradiance conditions, the redistribution of energy is dominated by reflected laser light.

In our continuing experiments, 300-μm diameter, 1-2 mm long Al cavities were irradiated at up to 10^{14} W/cm^2 with 1.05 μm/40 ps laser pulses directed through a 100-μm wide longitudinal entrance slit. Off-center slits were used to reduce direct reflection losses. A schematic of the irradiation geometry is shown in Fig. 1a. In order to study the basic characteristics of plasma ablation from the cavity walls, a point focus was chosen in most of the experiments. The distribution of the soft x-ray emission from the cavities was imaged onto the cathode of an x-ray streak camera by means of a 30-μm diameter pinhole. Alternatively, a Nomarski-type interferometer was used for diagnosing the density profiles.

A typical recording of the soft x-ray emission (0.1-6 keV) from an Al cavity with the streak camera in focus mode is shown in fig. 1b. Clearly, more than one region of strong x-ray emission is observed. A comparison with the result of the ray tracing calculation in Fig. 1a, shows the locations of plasma ablation to exactly coincide with the locations of (multiple) reflections of laser light at the cavity walls. Similar findings have been obtained in earlier work on time-resolved x-ray pinhole photography of laser-irradiated cylindrical cavities.[2] The area of brightest emission at the lower left

can be attributed to the directly irradiated spot (primary plasma). Along the upper wall of the cavity a less intense but larger region of emission is seen (secondary plasma). In addition, most of the cavity's interior as well as part of the slit region are seen to be filled with a third, rather inhomogeneous zone of emission which results from the collision and interpenetration of plasma streaming in from all sides.

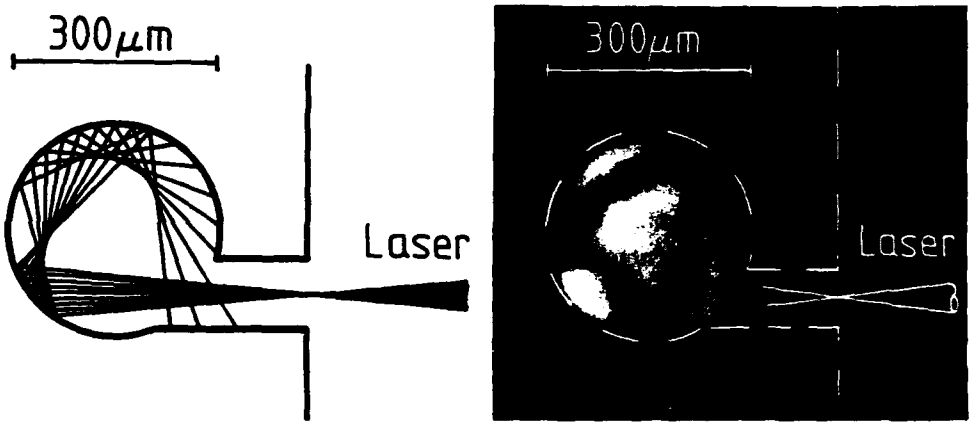

Fig 1a *Fig 1b*

The setup of the Nomarski interferometer used for diagnosing the density profiles has been described previously.[3] For the experiments to be reported here, the f-number of the imaging optics was changed from 3.5 to 2.4, with the consequence of higher plasma electron densities being diagnosed. An upper limit of about $n_e \cong 3 \cdot 10^{20}$ cm^{-3} is estimated for the present experimental conditions, mainly limited by the 527-nm probe beam wavelength. In addition, the shorter probe pulse duration (40 vs. 80 ps) results in reduced smearing of the fringes due to plasma motion.

The delay of the 2ω probe pulse was adjusted from 40 ps to 3 ns with respect to the main laser pulse. Fig. 2a shows a typical interferometer recording of an Al cylinder irradiated at $6 \cdot 10^{13}$ W/cm^2 and diagnosed 370 ps after the main laser pulse.

Later on in time (1.5 ns after the peak of the laser pulse, Fig. 2b), severe fringe distortion at the center indicates that the plasma is piling up near the axis of the cavity. The dark central region is the result of the corresponding probe beam missing the aperture of the imaging optics. Interesting features to be observed are jet-like structures protruding from the cylinder walls radially in towards the center. The origin of these jets is not clear to date; similar structures observed in short pulse experiments with spherical targets have been suggested to be caused by plasma instabilities.[4]

The information on the change in optical path length obtained from the interfero-

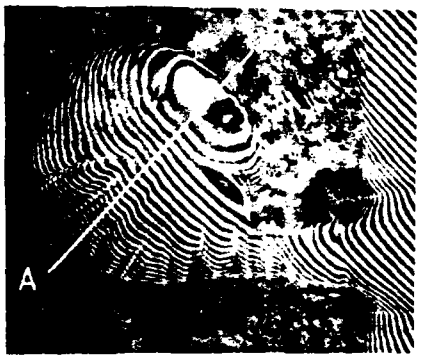

Fig 2a

Fig 2b

grams can be used to reconstruct the electron density distribution. A modified Abel inversion assuming an elliptical distribution of the refractive index was adopted to account for the nearly planar expansion typical of short pulse interactions.

Fig. 3 shows the temporal evolution of the underdense electron density along the line A-B for a series of shots as shown in Fig. 2. The plasma is seen to expand with slight asymmetry. The density scale length at a delay of 230 ps is about 17 μm for the primary (A) and 10 μm for the secondary (B) plasma. Interferograms at times when plasma collision has occurred could not be analyzed, since Abel inversion requires undisturbed fringes at the centre. Improvement of symmetry and the mechanisms of jet formation is a matter of further investigations.

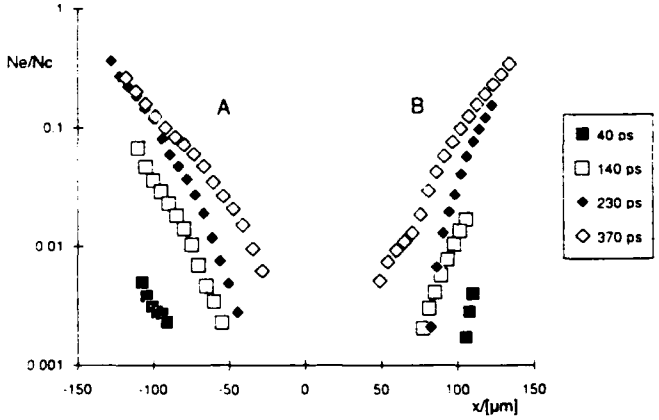

Fig 3.

References:

1) J.E. Balmer, R. Weber, P.F. Cunningham, and P. Lädrach, Laser Part. Beams 8, 327 (1990)
2) B. Soom, R. Weber, and J.E. Balmer, Opt. Commun. 79, 45 (1990)
3) P.F. Cunningham, R. Weber, P. Lädrach, and J.E. Balmer, Opt. Commun. 68, 412 (1988)
4) O. Willi, P.T. Rumsby, C. Hooker, A. Raven, and Z.Q. Lin, Opt. Commun. 41, 110 (1982)

Section I: Sources of Short-Wavelength Radiation

Short-Wavelength Lasers

Multiphoton Spectroscopy Using Tunable VUV Radiation from a Raman-Shifted Excimer Laser

Gregory W. Faris and Mark J. Dyer

Molecular Physics Laboratory, SRI International, 333 Ravenswood Avenue, Menlo Park, California 94025

Abstract

Raman shifting an ArF excimer laser in D_2 and HD, and applications to two-photon spectroscopy in the vuv and near-vuv are described. Preliminary results on generation of vuv by two-photon-resonant difference-frequency mixing of an ArF laser and frequency-doubled dye laser are reported.

Multiphoton spectroscopy has proved to be a valuable technique at visible and uv wavelengths, allowing access to high-lying states and the excitation of transitions not allowed for one photon excitation. Using vuv radiation for multiphoton excitation allows probing even higher states, but high powers are required to obtain reasonable signals. Two-photon excitation with vuv radiation has been performed using tunable excimer laser radiation[1] and by Raman-shifting a frequency-doubled dye laser.[2]

We are using the technique of Raman-shifting a tunable ArF excimer laser for the production of high powers in the vuv. Raman-shifting can provide relatively high efficiency for frequency conversion compared to non-resonant four-wave-mixing techniques. By Raman shifting an ArF laser, which provides high energy radiation tunable around 193.4 nm, anti-Stokes orders in the vuv can be obtained with low order Raman shifts. This allows high powers and lower power fluctuations than when using higher order Raman shifting. Raman shifting an ArF laser in H_2 for production of vuv radiation has been reported previously.[3] We have investigated Raman shifting in D_2 and HD. The use of different isotopes of hydrogen for Raman shifting allows greater spectral coverage, compensating in part for the limited tuning range of the ArF laser.

The apparatus used for our experiments is shown in Figure 1. The laser is a Lambda Physik EMG 150 dual discharge laser. Because the laser mode quality is very important for multi-wave mixing, we have made a number of modifications to the laser. The laser is operated as an oscillator triple-pass amplifier instead of an injection-locked amplifier. The output from the oscillator is passed through a spatial filter, which also magnifies the beam. The beam is then passed through the amplifier discharge in a vertical zigzag path, saturating the amplifier on the last pass. Optimum energies of over 60 mJ have been obtained through pressure optimization of the oscillator and amplifier discharge timing. We have found that depolarization of the beam can be reduced by careful alignment of the excimer laser's MgF_2

Proceedings on Short-Wavelength Coherent Radiation, 58
Vol. 11, Philip H. Bucksbaum and Natale M. Ceglio (eds.)
© 1991 Optical Society of America

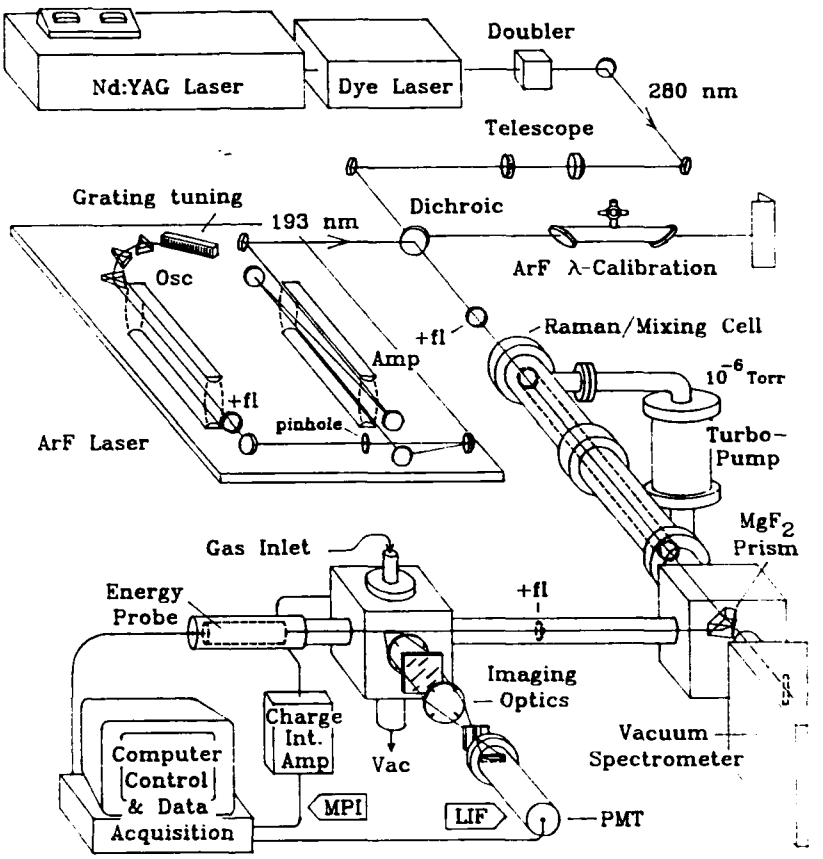

Figure 1. Experimental arrangement for multiphoton excitation using a Raman-shifted using a Raman-shifted excimer laser.

windows. This is performed by passing polarized light at 193 nm through the windows and rotating and tightening them to minimize the depolarization. Polarization of 200:1 has been obtained and the pulse-to-pulse amplitude stability is improved.

The laser is focused into a cell containing HD or D_2. To minimize absorption from the oxygen Schumann Runge bands, almost the entire beam path up to the cell is either evacuated or purged with argon. Because of the low Raman gain coefficient in HD, the Raman cell is cooled to liquid nitrogen temperature. This cooling increases the gain through redistribution of the HD ground state population, reduction of the Raman linewidth, and reduction of losses as impurities are frozen out. The Raman cell and surrounding liquid nitrogen jacket are contained in a vacuum for insulation and to avoid condensation on the cell windows. The different Raman orders exiting the Raman cell are separated using a MgF_2 prism.

Raman shifting in D_2 at room temperature, we have observed at least eight anti-Stokes orders (to 132 nm) and five Stokes orders. Up to 60% conversion into the first Stokes has

been obtained. In HD at room temperature, 10% conversion into the first Stokes, and low order anti-Stokes were seen. At liquid nitrogen temperature, four anti-Stokes and four Stokes orders have been observed using HD. Competition from rotational Raman scattering and phase matching effects lead to a well defined maximum density for anti-Stokes conversion. By optimizing the second anti-Stokes radiation in HD, we have obtained 1 mJ at 170 nm at a density of 3 amagat.

We have applied the Raman-shifted source to two-photon-resonant excitation of a number of states. Detection is through ions produced by absorption of a third photon. Using the first Stokes radiation in D_2 at about 205 nm, we have excited the $^1\Pi_g$ (v' = 3) state of F_2 from the ground X $^1\Sigma_g^+$ state. This is the central spectrum shown in Figure 2. The band heads correspond to the O and P branches. The top profile in the figure is the power of the first Stokes radiation. The dips in the power are due to Schumann Runge absorption of the fundamental ArF beam in the small length of beam path that is not purged. The bottom trace in the figure is a calibration spectrum for the fundamental ArF beam. It is obtained in a cell containing a mixture of H_2, HD, and krypton, all of which have two-photon resonances within the ArF tuning range. The accuracy of the calibration is limited by the ac Stark effect. We have also observed single lines for two-photon excitation of F atoms and H_2. Using radiation at about 169.67 nm produced as the second anti-Stokes line of ArF in HD we have excited the $^2D^o_{3/2}$ state in atomic fluorine from the $^2P^o_{3/2}$ ground state. A single rotational level of the H,$\bar{H}$ $^1\Sigma_g^+$ has been excited using two photons at about 173.53 nm produced as second anti-Stokes radiation using D_2.

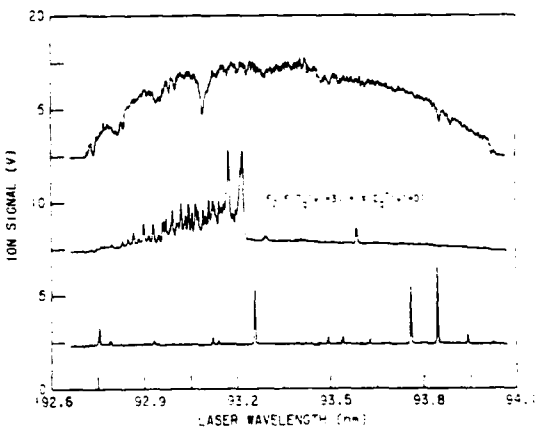

Figure 2. Two-photon resonant spectrum for excitation of the $^1\Pi_g$ (v' = 3) state of F_2. The x axis denotes the fundamental wavelength of the ArF laser.

Through understanding of the Raman process and optimization of the laser beam quality, Raman shifting an ArF excimer laser can provide large energies in the vuv even when shifting in D_2 and HD. The generated vuv power is more than adequate for two-photon spectroscopy.

To produce continuously tunable vuv radiation, we have begun to examine the capabilities of the ArF laser for two-photon-resonant difference frequency generation in krypton. By combining two ArF photons at ω_1 with a photon from a tunable laser at ω_T, vuv photons may be generated through the difference-frequency process

$$\omega_{vuv} = 2\omega_1 - \omega_T.$$

When the two photons at ω_1 lie near a resonance, this process is efficient, as has been shown for the 5p[5/2,2] ← $4p^6\ ^1S_0$ (Ref 4) and 5p[1/2,0] ← $4p^6\ ^1S_0$ (Ref 5) resonances. Two-photon resonances for the 6p ← $4p^6\ ^1S_0$ transitions in krypton lie within the tuning

range of the ArF laser. The high peak powers and good mode quality of the ArF make vuv generation using this technique attractive.

The apparatus for these experiments is also shown in Figure 1. A Nd:YAG-pumped frequency-doubled dye laser is used as the tunable laser. The pulse timing of two lasers is synchronized and they are overlapped using a dichroic mirror. A 1 m lens focuses the two beams into a cell containing krypton. The generated vuv is filtered with a vuv monochomator and detected with a solar blind photomultiplier. Light at 147 nm has been generated. The pressure dependence of the vuv radiation is shown in Figure 3. The optimum pressure is about 60 torr. By varying the input intensities, it is determined that both beams are saturating at the input energies of 6 mJ and 20 mJ for the ArF and frequency-doubled dye lasers, respectively. Experiments to measure the linewidth and energy of the vuv are in progress.

This work was supported by the AFOSR under contracts F49620-88-K-0003 and F49620-90-C-0044.

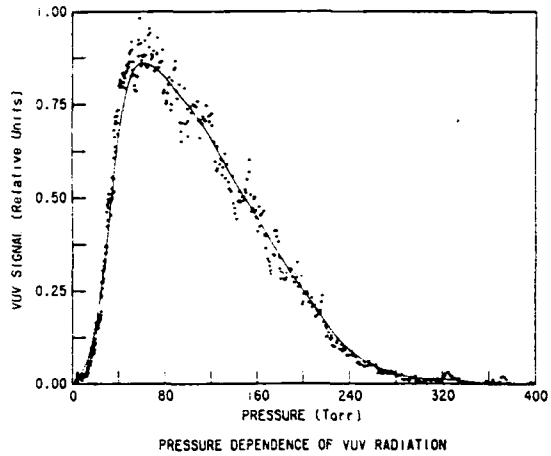

Figure 3. Pressure dependence of vuv radiation.

References

1. D. J. Kligler, J. Bokor, and C. K. Rhodes, "Collisional and Radiative Properties of the H_2 E,F $^1\Sigma_g^+$ State," Phys. Rev. A **21**, 607-617 (1980).
2. G. C. Herring, M. J. Dyer, L. E. Jusinski, and W. K. Bischel, "Two-Photon-Excited Fluorescence Spectroscopy of Atomic Fluorine at 170 nm," Opt. Lett. **13**, 360-362 (1988).
3. H. F. Döbele and B. Rückle, "Application of a Argon-Fluoride Laser System to the Generation of VUV Radiation by Stimulated Raman Scattering," Appl. Opt. **23**, 1040-1043 (1984).
4. G. Hilber, A. Lago, and R. Wallenstein, "Broadly Tunable Vacuum-Ultraviolet/Extreme-Ultraviolet Radiation Generated by Resonant Third-Order Frequency Conversion in Krypton," J. Opt. Soc. Am. B, **4**, 1753-1764 (1987).
5. J. P. Marangos, N. Shen, H. Ma, M. H. R. Hutchinson, and J. P. Connerade, "Broadly Tunable Vacuum-Ultraviolet Radiation Source Employing Resonant Enhanced Sum-Difference Frequency Mixing in Krypton," J. Opt. Soc. Am. B **7**, 1254-1259 (1990).

Recombination Lasers Pumped by Multiphoton Ionization

N. H. Burnett, F. Brunel, P. B. Corkum, and G. D. Enright

Steacie Institute, National Research Council of Canada, Ottawa, Ontario K1A 0R6, Canada

C. E. Capjack and R. Rankin

Department of Electrical Engineering, University of Alberta, Edmonton, Alberta T6G 2G8, Canada

ABSTRACT:

Recent advances in ultra-short pulse visible and uv laser technology make it practical for the first time to consider the production of multiply ionized laboratory plasmas in which ionization is moderated by an external optical field rather than by electron collisions. Such plasmas will be remarkable for the high degree of disequilibrium that can be achieved between the distribution of ionization and the electron energy distribution. In particular it should be possible to produce plasmas in which the electron energy distribution is much cooler (either locally or over a distance comparable to an electron mean free path) than the ionization temperature. This leads naturally to consideration of the use of these plasmas for short wavelength recombination lasers[1,2].

The laser intensity required to produce multiply ionized hydrogen or lithium like ions suitable for xuv recombination lasers in the 100Å wavelength range can be estimated from generalized tunnelling rates or more simply from the "over the barrier" intensity threshold[3] which is,

$$I_{app}=4\times10^{9}\frac{E_{ion}^{4}}{Z^{2}}\ \ (Watts/cm^{2}) \qquad (1)$$

where E_{ion} is the ionization potential in eV to produce the final ionization state Z. The above threshold energy of the photo-ionized electrons associated with multiphoton ionization in the tunnelling regime can be understood as originating from classical "half inverse-bremstrahlung" which predicts an excess electron energy of about 10% of the ponderomotive energy corresponding to the laser field into which the electrons are released in the case of a linearly polarized ionizing field and an excess energy about equal to the ponderomotive potential for a circularly polarized ionizing laser. Multiphoton ionization thus affords considerable control over the photo-ionized electron energy by varying the ionization potential of the candidate ion and the wavelength of the ionizing laser. Perhaps equally importantly for xuv laser plasmas, photoionization offers a means of controlling spatial gradients of electron temperature and ionization potential. In conventional plasmas where ionization is moderated by binary electron

Proceedings on Short-Wavelength Coherent Radiation, Vol. 11, Philip H. Bucksbaum and Natale M. Ceglio (eds.)
1991 Optical Society of America

collisions it is impossible to achieved large changes in ionization potential through distances which are small compared to the mean free path of the electrons responsible for ionization. In general, for xuv recombination lasers this means that it is probably impossible to cool these plasmas by diffusion of electrons from an external cold reservoir and that instead, recombination is strongly dominated by hydro-dynamic effects. In the case of optical field induced ionization, on the other hand, it is clear that spatial gradients in ionization potential are limited only by the wavelength of the optical driver. This can be seen most clearly by considering photo-ionization in a standing electromagnetic wave or some more general optical interference pattern.

The simplest (and perhaps most practical) conceptual geometry for an xuv laser pumped by multiphoton ionization is a filament of highly ionized plasma surrounded by a cold blanket of less highly ionized material. In the case of non self-terminating laser transitions, the central highly ionized region can be of sufficiently small diameter to cool rapidly by thermal diffusion with little or no hydrodynamic motion prior to recombination. The production of a suitable plasma filament may be complicated by refraction effects associated with multiphoton ionization itself. For a Gaussian pulse focused onto a partially ionized gas halfspace at an intensity only slightly above the threshold for ionization, this effect will be significant when the incremental electron density change introduced by multiphoton ionization is sufficient to cause a $\pi/2$ phase change upon propagation through its Rayleigh range, ie.,

$$\left(\frac{\delta n_e}{n_c}\right) \geq \left(\frac{1}{2\pi}\right)\left(\frac{\lambda^2}{\omega_0^2}\right) \tag{2}$$

Such refraction effects can be largely avoided by the axicon focusing of an intense short pulse laser into a volume of uniform density gas. More efficient use of the ionizing light might be possible if an axicon were used merely to preionize a column of gas which would be allowed to expand hydrodynamically to form a guiding structure for an axially injected ultra-intense pulse to produce the desired final ionization state[4].

The degree of cooling required to produce useful gain in a recombining plasma and the feasibility of a self terminating or ground state laser will depend on plasma heating effects associated with the optical frequency ionizing pump. Nonlinear inverse brehmsstrahlung, for example, appears to place an acceptable lower bound on electron temperature even for ground state lasers in the 100 Å range. Above threshold ionization (ATI) will in general produce low energy electrons for the initial stages of ionization but detrimentally high electron energies from the final ionization stages. For small diameter plasma filaments or rapid recombination schemes (ground state lasers) it appears possible to collisionaly decouple these final photo-electrons from those produced in earlier ionization stages so that they play no important role in the recombination kinetics. More severe constraints on the photo-ionized plasma temperature appear to come from collective plasma heating effects associated with the high field pump, in particular, various Raman modes.

We have used a one dimensional PIC simulation code to study several of the constraints imposed by plasma phenomena on the propagation of ultrashort high intensity laser pulses in uniform, low temperature underdense plasmas. We observe that pulses of duration much shorter than $\Delta t \approx 2\omega_{pe}^{-1}$ strongly couple to a plasma wake field[5] and that for v_{osc}/c in the range from .1 to .3, pulses of duration as long as twenty times ω_{pe}^{-1} undergo significant Raman backscattering. In the parameter range of interest for xuv laser plasma production we

generally observe electron heating associated with Raman scattering which, for sufficiently long driver pulses, saturates the instability by heating the bulk of the electron distribution to a temperature corresponding to the onset of strong Landau damping, ie. $2k_0\lambda_d \sim 1$, or $T_e \sim 1.1\times10^5\ n_e/n_c$ eV. A more comprehensive set of PIC simulations under conditions of relevance to ground state xuv lasers (and with lower initial electron temperatures than we have used) has been reported from researchers at LLNL[6]. Starting at a plasma temperature of 25 eV they observe that significant heating can be delayed for up to about 15 times the instability e-folding time[7] for backward Raman scattering and they conclude that this is probably sufficient to allow useful ground state population inversion in some systems in the 100Å wavelength range.

We have used a simple atomic kinetics computer code to model time dependent population inversion in the recombination of plasma filaments such as might be produced through multiphoton ionization of hydrogen or lithium like ions of ionization potential up to about 350 eV . An example of such a calculation for a lithium-like neon plasma is shown in figure 1. In this case we follow the population inversion on the 4f-3d transition of a 50 μm diameter filament at an initial electron density of 2×10^{18} cm^{-3}. The initially fully ionized central filament at temperature T_c is assumed to be surrounded by a constant temperature (T_b) cooling blanket of non-recombining plasma to which its temperature is tied by flux limited thermal conduction. That is, electrons in the recombining filament are heated by superelastic collisions associated with collisional recombination and cooled by thermal conduction to the surrounding reservoir. Such a plasma filament might be produced by multiphoton ionization in a 100fsec duration, .25 μm laser pulse which achieves a peak intensity of about 4×10^{17} W/cm^2. In this case, inverse bremstrahlung heating might be expected to produce a plasma temperature of 5-10 eV and stimulated Raman backscatter would be strongly damped at about the same temperature ($2k_0\lambda_d=1$ for T_e = 10 eV). The curves in

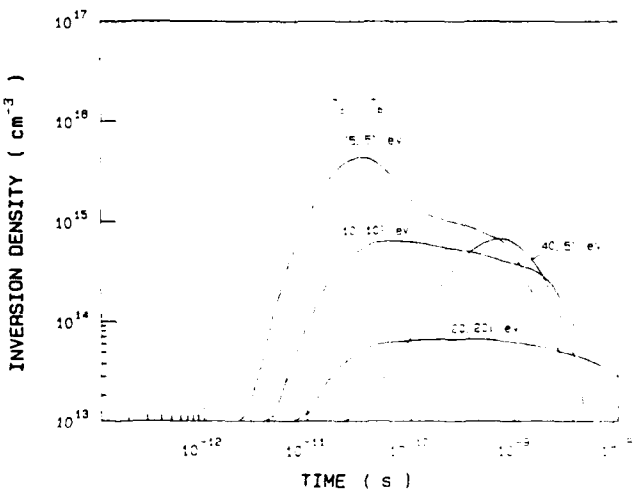

Figure 1. Inversion density $(N_u - (g_u/g_l)N_l)$ on 4f-3d transition in Ne IX.

Figure 1 show time dependent population inversion and estimated small signal gain on the 4f-3d transition (λ = 290Å) assuming various initial filament and cooling blanket temperatures. An inversion density of 7×10^{14} cm^{-3} corresponds to a gain of about 10 cm^{-1} under these conditions. It is clear that gain depends strongly on the assumed initial cooling blanket temperature. Although experiments to confirm collisional and other heating rates are clearly required, it seems possible that a useful xuv laser based on this transition could be made with a uv driver energy of a about a joule.

In order to scale such a thermal conduction cooled, quasi-steady-state recombination lasers to wavelengths shorter that about 100Å it is apparent from equation 1 that the required driver intensity would become relativistic even for a .25 µm ionizing laser. Relativistic driver intensities in conjunction with the higher electron density demanded by the recombination kinetics for shorter wavelength operation inevitably imply large ponderomotive force driven ion acceleration. This acceleration will occur on a time scale of ω_{pi}^{-1} and result in MeV ion kinetic energies. That is, at relativistic intensities most of the dissipated driver energy will likely go into ion kinetic energy rather than potential energy of ionization in contrast to the Li-like neon example cited above. The use of a self-terminating transition to the ground state principle quantum number of the stripped ion would be an alternative approach to short wavelength operation.

As an example of such a situation, we consider the achievement of population inversion on the resonance line of hydrogen-like boron at a wavelength of 48Å. The complete ionization of boron on a ~100fsec time scale would require a driver intensity of about 5×10^{18} W/cm^2. The maximum temporal duration of inversion on this transition is about equal to the radiative lifetime of the resonance level[8], ie, about 2psec. Achievement of significant gain requires an electron density of about 10^{20} cm^{-3} or greater. An example of the time dependent population inversion in the recombination of a fully stripped boron plasma with an initial temperature of 20 eV and electon density 1×10^{20} cm^{-3} is shown in Figure 2. An inversion density of 10^{16} cm^{-3} on the Lyman α line

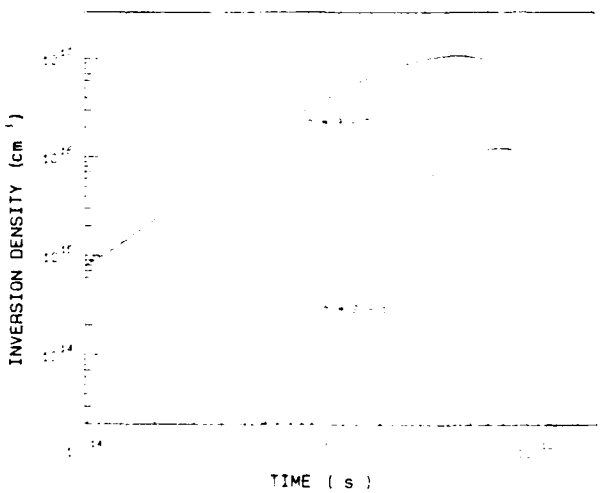

Figure 2. Inversion density on 3-2 and 2-1 transitions in B V.

corresponds to a gain of about 30 cm^{-1}. It is apparent that simultaneous gain on both the 3-2 and 2-1 transitions is possible in this case. This calculation includes reheating by super-elastic collisions but no thermal conduction. (Thermal conduction cooling on a psec time scale would require a filament of impractically small diameter.). The key to producing such a cold initial plasma lies in the suppression of plasma instabilities. An analysis of the constraints imposed by Raman backscatter on population inversion on the self-terminating 3s-2p transition in lithium like neon has been made by D. C. Eder et al[9]. This potential laser operates of necessity at a much higher electron density than the 4f-3d neon scheme discussed above.

1. N. H. Burnett and P. B. Corkum, JOSA B6, 1195 (1989).

2. N. H. Burnett and G. D. Enright, IEEE Jour. Quant. El. 26, 1797 (1990).

3. S. Augst, D. Strickland, D. D. Meyerhaufer, S. L. Hin and J. H. Eberly, Phys. Rev. Lett. 63, 2212 (1989).

4. R. Rankin, C. E. Capjack, N. H. Burnett, and P. B. Corkum, to be published.

5. F. Brunel, SPIE Vol. 664, p 35, *High Intensity Laser Processes* (1986)

6. S. C. Wilks, W. L. Kruer, A. B. Langdon, P. Amendt, D. C. Eder and C. J. Keane, SPIE Vol 1413, *High Power Lasers*, Los Angeles, 1991 (in press).

7. W. L. Kruer, *The Physics of Laser Plasma Interactions*, Addison-Wesley, New York (1988).

8. R. W. Waynant and R. C. Elton, Proc. IEEE 64, 1059 (1976).

9. D. C. Eder, P. Amendt, M. D. Rosen, J. K. Nash and S. Wilks, paper WA6, these proceedings.

Recent advances in soft-x-ray laser research

Brian J. MacGowan

University of California, Lawrence Livermore National Laboratory

L-483, P.O. Box 808, Livermore, Ca 94550, Tel (415) 422-2250

Soft x-ray laser experiments at the Lawrence Livermore National Laboratory, Nova laser will be described. Much of the work involves the study of collisionally pumped Ne-like and Ni-like lasers[1] although some studies of recombination pumped and resonantly photo-pumped x-ray lasers will be discussed. These experiments have produced nickel-like collisionally pumped x-ray lasers at wavelengths near to, and below that of the K absorption edge of carbon (43.76-Å)[2]. Recent work has concentrated on the development of the Ni-like Ta amplifier as a high power source at 44.83-Å. Amplification occurs in a laser produced plasma created by irradiating a thin foil of Ta with two beams of the Nova laser. Up to 8 gainlengths have been demonstrated so far, with a gain coefficient of 3 cm^{-1} and a gain duration of 250 psec. The Ni-like Ta amplifier at 44.83-Å lies at the edge of the water window, and provides the basis for the design of an x-ray laser source that should fulfill some of the requirements for holography of living cells. It remains to optimize the coherent output power of the amplifier to use it as a source for future x-ray holography experiments. Experiments utilizing normal incidence x-ray optics to enhance the power output from this laser will be described.

Ne-like experiments have been investigating the utility of Ne-like Y which lases at 155-Å as a high power laser at a wavelength where high reflectivity normal incidence optics are currently available and hence laser applications are easier. Experiments with both solid and exploding foil Ne-like amplifiers will be described.

Recently a laser has been discovered in collaboration with LLE, Rochester that may be driven by resonant photo-pumping[3]. The laser operates at 326.5-Å in Ne-like Ti and is believed to be pumped by resonances between 2p - 4d and C- and N-like 3d - 2p transitions. This laser exhibits very narrow divergence (~ 4 mrad) and may be a useful testbed for studies of soft x-ray laser coherence.

References

[1]R.C.Elton, *X-ray Lasers* (Academic, New York, 1990), and references therein.

*This work was performed under the auspices of the U.S. Department of Energy by Lawrence Livermore National Laboratory under contract No. W-7405-Eng-48.

[2]B. J. MacGowan *et al.., Demonstration of x-ray amplifiers near the carbon K edge,* Phys. Rev. Lett. 65, 420 (1990).

[3]T. Boehly *et al., Demonstration of a narrow divergence x-ray laser in neon-like titanium,* Phys Rev A, (in press) and UCRL-JC-104656 (Aug 1990).

Temperature Determination in X-Ray Laser Plasmas by Thomson Scattering

D. M. Villeneuve, B. La Fontaine, H. A. Baldis, J. Dunn, and G. D. Enright

National Research Council of Canada, Ottawa, Ontario K1A 0R6, Canada

M. D. Rosen, P. E. Young, and D. L. Matthews

Lawrence Livermore National Laboratory, Livermore, California 94550

Abstract

Thomson scattering diagnostics were used to measure electron and ion temperatures in plasmas similar to those used for x-ray lasers. These measurements were compared with predictions of a hydrodynamic simulation.

1 Introduction

One of the outstanding uncertainties in modelling x-ray laser experiments lies in determining the actual plasma parameters which crucially affect the prediction of laser performance. Electron temperatures are commonly inferred experimentally from x-ray emission spectra or from the Landau damping cutoff of stimulated Raman scattering, neither of which directly measures the temperature with sufficient precision at the location where lasing occurs.

Therefore hydrocodes are usually used to estimate the plasma conditions, but there is still uncertainty in their predictions. Experimental measurements which can test the accuracy of the codes' predictions can be used to "calibrate" the codes, and hence lead to either code improvements or an increased confidence in the codes' accuracy.

Experiments were performed with plasmas produced from a laser spot focussed on solid targets of carbon, germanium and tantalum. The electron temperature could be measured as a function of time at different locations in the plasma, for various laser intensities.

2 Thomson Scattering

Thomson scattering is the very weak scattering of an optical probe beam by individual electrons in a plasma. Depending on the arrangement, the scattered light spectrum can be used to determine the parameters of the electron and ion distribution functions, such as electron and ion temperatures (T_e, T_i) and drift velocities (v_e, v_i).

The LP2 Nd:glass laser system was used to produce plasmas with parameters typical of x-ray laser conditions. A 500 mJ, 355 nm probe pulse was focussed into the plasma and the 90° scattered light was dispersed in a spectrograph and recorded on a streak camera. The plasma volume being probed was a cube of approximately 80 μm on each side. This volume could be moved around within the plasma between shots to determine the spatial

Proceedings on Short Wavelength Coherent Radiation, 69
Vol. 11, Philip H. Bucksbaum and Natale M. Ceglio (eds.)
© 1991 Optical Society of America

variation of parameters. The temporal history was recorded by the streak camera on each shot. The plasma density profile was measured by means of a 20 ps interferometer.

3 Results

Figure 1 shows a streak photograph of the Thomson scattered light spectrum. The plasma was produced with about 100 J of 1.064 μm light in a 1.5 ns pulse, focussed onto a solid germanium target. The peak laser intensity was about 2×10^{14} W/cm^2. The measuring volume was at an electron density of about 10^{20} cm^{-3}, 100 μm from the target surface.

Two peaks are seen in the spectrum, and since their separation is approximately proportional to the square root of the sound speed, T_e may be determined. The width of the peaks and the depth of the valley are related to T_i. Lineouts of the spectrum taken at different times were fitted to theoretical spectra and four fitting parameters were determined, namely T_e, T_i, v_e, v_i.

Figure 2 shows such a fit and the parameters which were deduced. One additional parameter to the fit is the electron density n_e. In principle this may be determined from the intensity of the scattered light, but this is very difficult to measure. Instead the interferograms are used to determine the density of the scattering volume, although this varies during the pulse. Fortunately, for the scattering geometry used, the fitting parameters are quite insensitive to density.

Fig. 1. A typical streak record of the Thomson scattered light spectrum for a germanium target. Two peaks can be seen which increase in separation as the plasma temperature increases.

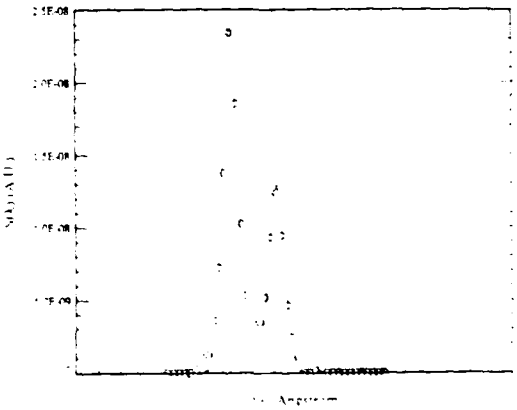

Fig. 2. A lineout of the data (o) at one time fitted to a theoretical spectrum (—). The inferred temperature is $T_e = 130 \pm 15$ eV.

Figure 3 shows the temporal evolution of the electron temperature of germanium targets for two intensities. Figure 4 shows the temporal evolution of the measured T_e for carbon targets in comparison with 1D and 2D LASNEX simulations. It can be seen that the simulations over-estimate the temperature, although the 2D results are quite close at the peak of the pulse. Ion temperature measurements shown in Fig. 5 are in very good agreement with the 2D simulations.

L-shell x-ray spectra were recorded with a flat crystal spectrometer. Figure 6 shows such a spectrum from a germanium target. Figure 7 shows a spectrum recorded from a line-focus germanium plasma during a separate x-ray laser experiment. It was found that the pump laser intensity had to be sufficient to produce fluorine-like emission in order for laser gain to be observed. The Thomson scattering experiments with a spot focus produce a similar x-ray spectrum, suggesting that the plasma conditions are quite close to those of a line-focus plasma.

Part of this work was performed under the auspices of the U.S. Department of Energy by the Lawrence Livermore National Laboratory under Contract No. W-7405-ENG-48.

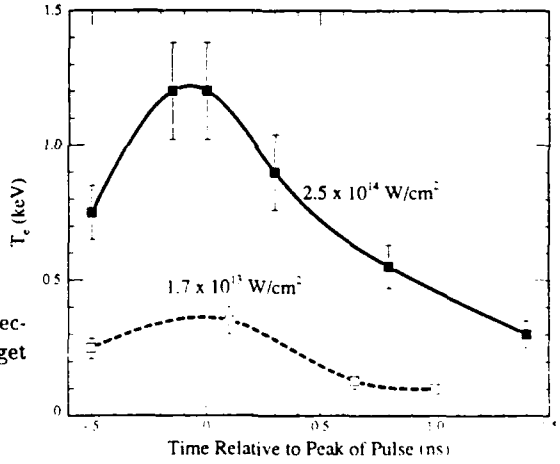

Fig. 3. Temporal evolution of the electron temperature of a germanium target for two shots with different intensities.

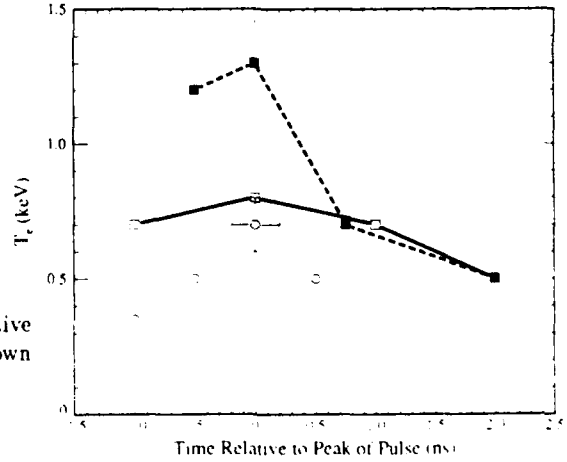

Fig. 4. Measured evolution of T_e relative to the peak of the pulse (o). Also shown are 1D and 2D LASNEX simulations.

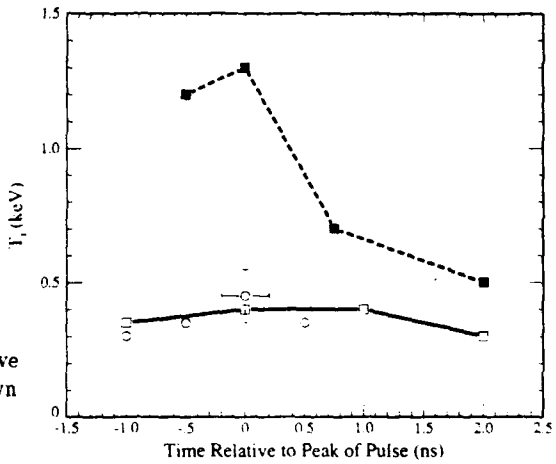

Fig. 5. Measured evolution of T_i relative to the peak of the pulse (o). Also shown are 1D and 2D LASNEX simulations.

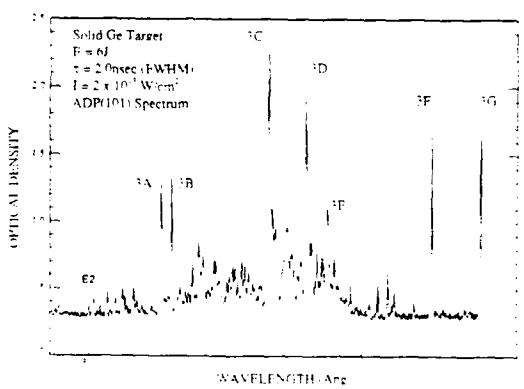

Fig. 6. X-ray spectrum from germanium target with a spot focus at 2×10^{13} W/cm^2.

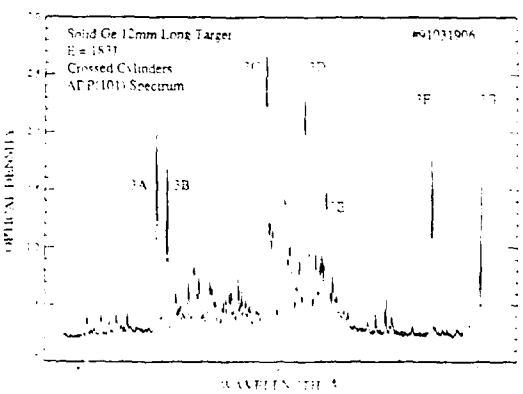

Fig. 7. X-ray spectrum from a germanium target with a line focus at 2×10^{13} W/cm^2. This plasma achieved an x-ray laser gain of 4 cm^{-1} on the 232 and 236 Ålines. The presence of the fluorine-like emission was a necessary condition to observe gain. Thus the conditions of Fig. 6 during the Thomson scattering experiments simulate actual line-focus conditions.

Future Directions of Laboratory X-Ray Laser Research

Mordecai D. Rosen

Lawrence Livermore National Laboratory, P.O. Box 5508, L-477, Livermore, California 94550

Abstract

We explore ways to make laboratory x-ray lasers and their applications more accessible to a wider community of users. This includes optical pump facilities that are affordable due to progress in optical laser technologies, from nsec 1KJ sources, to 100 fsec 1J tabletop sources. Based on these possibilities, the future for x-ray lasers seems bright.

Introduction

X-ray lasers(XRLs) produced in the laboratory hold great promise for applications such as holography of wet biological samples, probing of high density plasmas, and non-linear x-ray optics. Many current XRLs are pumped by very high power, high energy optical lasers. An important example is the recent achievement of gain-length products exceeding 8 with the Ni-like (Ta and W), 4d-4p x-ray laser scheme [1] at wavelengths just inside and just outside the water window, near the carbon K edge at 43.7 Å which are optimal for x-ray holography [2]. This achievement required the utilization of two of the ten arms of Nova, the world's most powerful laser, to pump the exploding foils [3] that served as the amplification medium. This is a costly facility, and relatively inaccessible to most potential users. If applications of x-ray lasers are to become a reality, we must devote some thought and effort to schemes that can produce such short wavelength lasing using more user friendly and less costly facilities. It is the purpose of this paper to explore some of those possibilities.

Schemes in the 1 nsec regime

The current Ni like success is achieved with a pump duration of about 1/2 nsec. In principal, the nsec regime allows for multipassing of the beam through the amplification medium via the use of synthetic multilayer mirrors. This increases the signal exponentially without requiring further pump power. Moreover, by proper placements of mirrors and pinholes, more coherent output can be achieved. These methods of increasing the efficiency of the XRL will be attempted in the very near future. However these still use two arms of Nova.

Proceedings on Short-Wavelength Coherent Radiation, Vol. 11, Philip H. Bucksbaum and Natale M. Ceglio (eds.)
© 1991 Optical Society of America

The first important point we wish to make in this paper, is that the technology of high energy glass lasers has progressed significantly in recent years. While the cost of laser energy on Shiva (late 70's) was about $2,000/J, it dropped to $500/J for Nova (late 80's) , and is projected to be about $150/J for the Nova Upgrade (late 90's). Thus a several kJ facility should be rather affordable (few million $ level, including the cost of a classroom sized building) and could serve as a dedicated, stand alone, user friendly facility for XRL applications [4]. By using 1.06 μm light, which heats an exploding foil amplifier medium more efficiently than the currently used 0.5 μm light [5], we believe we can achieve the conditions necessary for Ni-like lasing using only 1 KJ of laser- pump light. This belief is based on calculations [6] using our most sophisticated modeling tools, which have been successful to within about a factor of two in predicting the performance of our Ni like XRLs to date. This then, is our lowest risk path to successful XRLs in a laboratory conducive to users and dedicated to applications.

Schemes in the 10 psec regime.

A further substantial savings in required optical pump energy can be achieved by considering a double pulse method for creating the amplification medium [7]. Typically the single optical laser pulse explodes a foil to create the relatively uniform plasma gain medium that heats the plasma to the requisite high temperature (typically about 1 keV) so that the target element is ionized to the proper state and inverted as well. For an optimized Ni-like W target, requiring 5×10^{14} W / cm^2 irradiance, with a predicted gain coefficient of 5 cm^{-1}, a 200 μm line focus height , a 1/2 nsec pulse, and a 4 cm line focus length in order to achieve saturation (gl of 20), this implies 20 KJ of required optical (0.53 μm) pump energy.

We propose a double pulse method that delivers only the requisite energy when it is needed. A 1 nsec pulse of only 40 J of green light irradiates the same foil (of thickness 100 μg/cm^2) focussed somewhat better to 100 μm high by 2 cm long. The irradiance of 2×10^{12} W / cm^2 is predicted to heat the foil only moderately, to about 100 eV. By the peak of the 1 nsec pulse, we predict that the foil will have expanded to about a 100 μm scale size, with an electron density of about 10^{21} cm^{-3}. These energy and power requirements are quite modest and commercially available. In fact, we can probably achieve these conditions by using any number of alternative technologies such as gas jets or capillary discharges.

Having created the proper density for the amplifier medium, we then bring in a very short pulse, of about 20 psec duration, with an even better line focus of about 50 μm in height, at the required irradiance of 5×10^{14} W / cm^2. This corresponds to an energy requirement of 40 J for the plasma forming pulse, and 100 J for this short pulse pump, a savings of over 2 orders of magnitude in required pump energy. In many laboratories around the world, by using chirping techniques, such high power short pulse facilities are being built on "tabletops," thus making this approach accessible and feasible for applications. Under that irradiance , and despite the short pulse length, we predict that the plasma temperature will rise to over 1 keV, that about 25% of the ions will be in the proper, Ni-like state, and that some of those ions will be inverted, leading to a predicted gain of about 10 cm^{-1}. These predictions are based on the same modeling tools mentioned above, and are shown explicitly in Fig. 1 a)-d). Thus the 2 cm foil will achieve saturation (gl of about 20). Of course it takes 60 psec for the x-ray laser beam to propagate the full 2 cm, while the gain is predicted to last only on the order of the 20 psec pulse duration. Thus, the 20 psec pump pulse will have to be phase driven down the 2 cm length. There are well known techniques to accomplish that [8].

The two-pulse scheme mentioned above has not been demonstrated to date in a line focus, XRL amplification geometry. However, a proof of principle experiment has been performed [9], and within the usual factor of two of the predicted required irradiances,

Ni-like and Co-like Yb has been produced and has shown sensible sensitivities to the relative timings of the long pulse (2 nsec) plasma-former vs. the short pulse (10 psec) ionizer/inverter. Thus there is good reason for optimism that this scheme could work, leading to substantial drops in the pump energy requirements and possibly bringing XRLs to the table top regime.

Schemes in the sub psec regime

Space limitations do not allow a full discussion of some of the more exotic sub psec approaches to tabletop XRLs. These include femtosecond, multiphoton ionized gas targets that lase in a transient recombination mode, and femtosecond laser irradiated solid targets that serve as radiation sources for inner shell photoionizing schemes. In both cases the exciting developments of 1J / 100 fsec tabletop lasers allow us to consider these as real possibilities. A systematic study [10] of the transient recombination mode, multiphoton approach reveals that efficiencies as high as 0.01% can be achieved at 98Å, though extrapolating to shorter wavelengths may be very difficult due to plasma instabilities heating the medium and interrupting the rapid recombination required for inversion.

The scheme using fsec radiation to pump K shell vacancies depends critically on the efficiency of creating the radiation. This scales favorably with absorbed irradiance [11]. Moreover, recent success at increased absorption at high irradiance has been

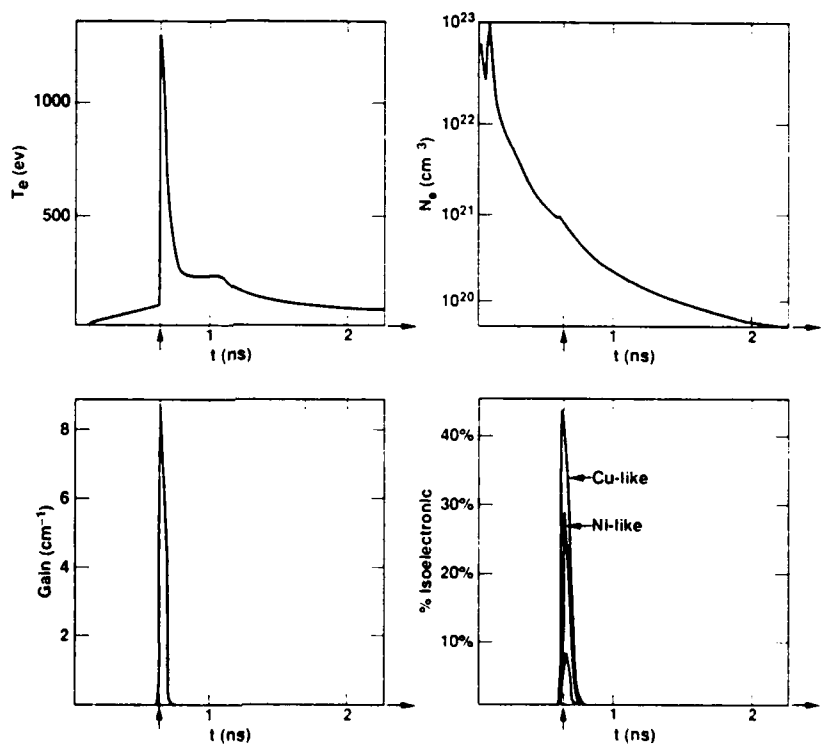

Figure 1. Time history, at foil center, of a) electron temperature, b) electron density, c) gain coefficient, and d) fraction of ions in Ni-like and Co-like ionization states. Arrow indicates onset of high irradiance short pulse.

reported by groups at Berkeley and Stanford by using roughened surfaces. Thus , if the radiation from the roughened surface targets still proves to be of short duration, this approach also holds out great promise for table top XRLs.

Summary

We have shown that there are a wide variety of approaches for future XRLs that utilize pumps that are either room size or smaller ("true tabletop"). In either case the age of useful XRLs that are accessible and dedicated to the user interested in applications is rapidly approaching.

Acknowledgments

This work could not have been performed without the dedicated efforts of my many colleagues both within LLNL and beyond its gates. These include: R. London, D. Eder, S. Maxon, and P. Amendt for target design; J. Scofield, A. Hazi, M. Chen, J. Nash, Y. Lee, S. Dalhed, R. Walling, C. Cerjan, W. Goldstein, A. Osterheld, and J. Nilsen for atomic physics support; D. Matthews, B. MacGowan, J. Trebes, C. Keane, R. Stewart, T. Phillips, G. Shimkaveg, B. Young, R. Shepard, L. DaSilva, D. Fields, and M. Carter for experiments; R. Falcone, M. Murnane, H. Kapteyn, A. Zigler, H. Tom, A. Szoke, R. More, S. Harris, J. Kmetec, B. Penetrante, N. Bardsley, S. Wilks and W. Kruer for fsec physics; and J. Lindl, B. Tarter, J. Nuckolls, M. Campbell, E. Storm, J. Davis, M. Eckart, D. Novak, D. Fortner, and G. Miller for support and encouragement. This work was performed under the auspices of the U.S. Department of Energy by the Lawrence Livermore National Laboratory under contract No. W-7405-ENG-48.

References

1. B.J.MacGowan , S. Maxon, L. Da Silva, D. J. Fields, C. J. Keane, D. L. Matthews, A. L. Osterheld, J. H. Scofield, G. Shimkaveg, and G. F. Stone, "Demonstration of X-ray Amplifiers near the Carbon K Edge," *Phys. Rev. Lett.* **65**, 420 (1990).
2. R.A.London, M.D.Rosen, and J.E. Trebes, "Wavelength Choice for Soft XRL Holography of Biological Samples," *Applied Optics* **28**, 3397 (1989).
3. M. D. Rosen, P. L. Hagelstein, D. L. Matthews, E. M. Campbell, A. U. Hazi, B. L. Whitten, B. MacGowan, R. E. Turner, R. W. Lee, G. Charatis, Gar. E. Busch, C. L. Shepard, P. D. Rockett, and R. Johnson, "Exploding Foil Technique for Achieving a Soft X-Ray Laser," *Phys. Rev. Lett.* **54**, 106 (1985).
4. J.T.Hunt and D. L. Matthews, private communication, LLNL, 1991.
5. R. A. London and M. D. Rosen, "Hydrodynamics of Exploding Foil XRLs," *Phys. Fluids*, **29**, 3813 (1986).
6. M.S. Maxon, "Calculations of a Ta soft x-ray laser using a sub-Kilojoule pump," *Appl. Phys. Lett.* **58**, 10 (1991).
7. M.D. Rosen and D. L. Matthews, "Photo-Resonant Boosting of Gain in Ne-like and Ni-like X-ray Laser Systems," *Bull. Am. Phys. Soc.* **33**, 2042 (1988).
8. Z. Bor, S. Szatmari, and A. Muller, "Picosecond Pulse Shortening by Travelling Wave Amplified Spontaneous Emission," *Appl. Phys. B*, **32**, 101 (1983).
9. L. DaSilva, B. MacGowan, M. Rosen and H. Baldis, "Short Pulse / Long Pulse Ni-like Laser schemes: Experiment and Analysis" *SPIE proceedings of Femtosecond to Nanosecond High Intensity Lasers and Applications*, E.M. Campbell, Editor (L.A. 1990) SPIE Volume **1229** pg. 153, (1990).
10. P. Amendt, D. Eder, and S. Wilks "X-ray Lasing by Optical Field Induced Ionization" *accepted for publication in Phys. Rev. Lett.* (1991).
11. M. Murnane, H. Kapteyn, M. D. Rosen, and R. Falcone "Ultra fast X-ray Pulses From Laser Produced Plasmas," *Science*, **251**, 531 (1991).

Recent Progress in Soft-X-Ray Laser Research at the Institute of Laser Engineering

H. Daido, Y. Kato, H. Azuma, K. Murai, H. Shiraga, K. Yamakawa, T. Togawa, E. Miura, Y. Gang, T. Kanabe, M. Takagi, H. Takabe, K. Tanaka, M. Yamanaka, and S. Nakai

Institute of Laser Engineering, Osaka University, 2-6 Yamada-oka, Suita, Osaka 565, Japan

C. Lewis, D. O'Neill, D. Neely, G. Pert, S. Ramsden, and M. Key

X-Ray Laser Consortium, Central Laser Facility, Rutherford Appleton Laboratory, Chilton, Didcot, Oxfordshire OX11, UK

Abstract

Extension of the Na Balmer-alpha recombination laser to larger gain-length product has been made with a simultaneous lasing of F Balmer-alpha line under short pulse pumping. Up-to-date report including the collisional excitation Ge laser is also presented.

We present recent progress in soft x-ray laser research at the Institute of Laser Engineering. Detailed characterization of the explosive mode Balmer-alpha soft x-ray laser has been made. Extension of the Balmer-alpha laser to a larger gain length product has been tested. We also tested the collisional excitation Ge laser with large gain length product and good beam quality.

The Recombination Pumped Balmer-Alpha Lasers

In our previous experiment[1,2], a stripe target coated with NaF and MgF_2 were irradiated with a 351 nm, 130 ps laser pulse with the maximum energy of 150 J, line-focused to a 7 mm length and 50 um width. In this "long pulse" experiment, a time-integrated gain of 1.2 cm^{-1} on Na XI Balmer-alpha at 5.42 nm was obtained. Since the pulse width in this experiment was long compared with the required characteristic expansion time of 30 ps for Na, we have implemented a revised "short pulse" experiment where a foil target was irradiated with a 28 ps, 23 J laser pulse. The measured time integrated gain of 4 cm^{-1} was 3 times higher than the value obtained in long pulse experiment[3].

In order to characterize the explosive mode Balmer-alpha laser in more detail, space and time resolved measurements were made on the Na XI Balmer-alpha line. The intensity of the Balmer-alpha line increases ex-

Proceedings on Short-Wavelength Coherent Radiation, Vol. 11, Philip H. Bucksbaum and Natale M. Ceglio (eds.)
© 1991 Optical Society of America

ponentially with the gain length. The peak gain of 5.3 cm^{-1} is located at 60 μm from the original target surface.

Based on these results we have done an experiment using Gekko XII to demonstrate a larger gain length product in NaF thin foil target which was composed of 0.4 μm thick 50 μm wide NaF stripe coated on the 0.2 μm thick CH substrate. A laser beam of 30 J energy in 20 ps at 0.53 μm was focused on to a thin foil target with a 6 mm long, 50 μm wide line focusing optics. The focused intensity on the target was 5 x 10^{14} W/cm^2. Typical space resolved on-axis spectra are shown in Fig. 1. We can see the two lasing lines of Na and F Balmer-alpha transitions(5.4 nm and 8.09 nm). The time- and space-integrated Na and F Balmer alpha gain coefficients of 6.8 cm^{-1} and 6.0 cm^{-1}, respectively were obtained from the calibrated on- and off-axis spectra. The gain-length products of 4.1 and 3.6 were obtained for these lines. The peak gain of the F line is located 150 μm from the original target position while that of Na is 60 μm from the original position. These values are reasonable considering the atomic number dependence of the temperature and density, i.e., F gain occurs in lower temperature and density region compared to Na gain.

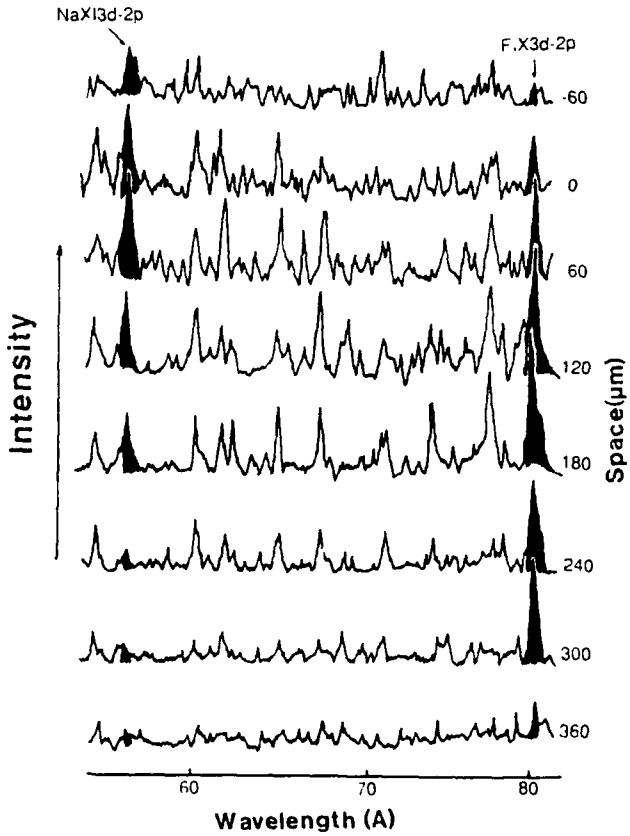

Fig.1 The space resolved on axis spectra of a NaF thin stripe target under short pulse pumping.

The Collisional Excitation Ge Lasers

The collisional excitation soft x-ray lasers including Ne-like and Ni-like isoelectronic sequences have been investigated extensively at LLNL[4,5]. Several papers on Ne-like Ge lasers have also been published by other groups[6,7] where the relatively small lasers produced a definitive gain length product. To investigate the properties of the gain medium having large gain length product of the order of ten, we tested the Ne-like Ge laser whose gain length was up to [illegible] cm. The schematic diagram of the experimental setup is shown in Fig. 2. Two arms of the

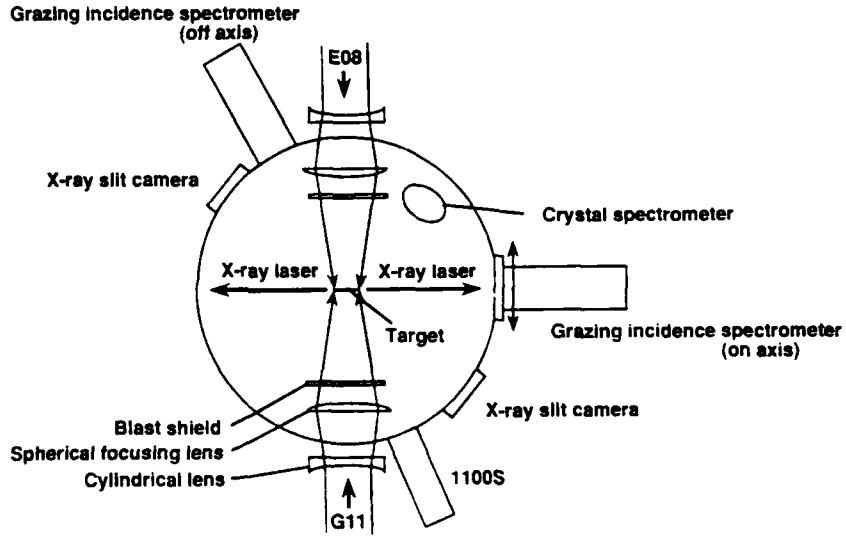

Fig. 2 Schematic diagram of the experimental setup of the collisional excitation lasers using Gekko XII laser.

Gekko XII laser (E08, G11) irradiated the target with a line focusing optics delivering the energy of 1.1 kJ per beam in 1 ns duration at 1.05 μm wavelength. The line focusing length of 6 cm with the average width of 100 μm gives an intensity of 1.7×10^{13} W/cm^2 per beam. The on-axis spectrometer was translated in a plane perpendicular to the soft x-ray laser beam axis in order to measure the intensity distribution of the x-ray laser beam. We also installed the two off-axis grazing incidence spectrometers and a crystal spectrometer which can measure the ionization balance of the medium. Two x-ray slit cameras were installed to monitor the line focusing condition of each beam at each shot.

We tested three kinds of targets as shown in Fig. [illegible] slab target, a double target[8] and an exploding foil target. The gain coefficients of five lasing lines in these target have been measured by changing the length of the targets. Note that the amplified soft x-ray beam was significantly deflected, approximately 10 mrad. Due to the refractive effect especially for the long slab target. We also measured the polar distribution of the beam in a horizontal plane with the on-axis grazing incidence spectrometer.

We describe more precisely on the exploding foil target. For sym-

metric expansion, Ge layer was located between the two 120 nm thick CH substrates. At first, the optimum thickness of the target was investigated using the hydrodynamic simulation code with the NLTE atomic physics package under the irradiation condition of 1.7×10^{13} W/cm^2 in 1 ns duration at 1.05 μm wavelength. Desired plasma conditions of the medium include the electron density of 5×10^{20} cm^{-3} for J=2-1 transition [9] and the electron temperature of around 1 keV considering the ionization balance and the monopole excitation rate. According to the simulation, Ge thickness of around 100 nm was suitable because of the density matching. Actually we found the most intense amplified beam was produced
with 120 nm thick Ge target experimentally when we tested the thin foil targets with various Ge layer thickness. Then we fixed the thickness of

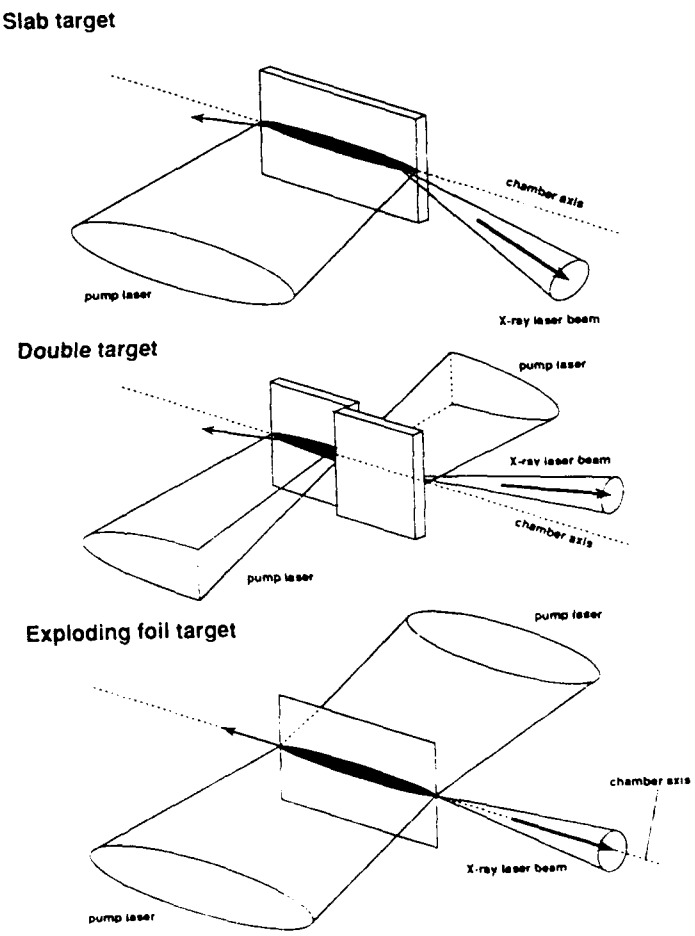

Fig. 3 Three types of soft x-ray targets. The slab and the double targets are composed of [illegible]-1 μm thick Ge stripe coated on the 1.[illegible] mm thick glass plate. The exploding target is composed of 50-140 nm thick Ge stripe between the 120 nm thick CH substrates.

the foil target and measured the gain coefficient with irradiating the targets with various lengths. An example of the on- and off-axis spectra are shown in Fig. 4. Five lasing lines are clearly visible.

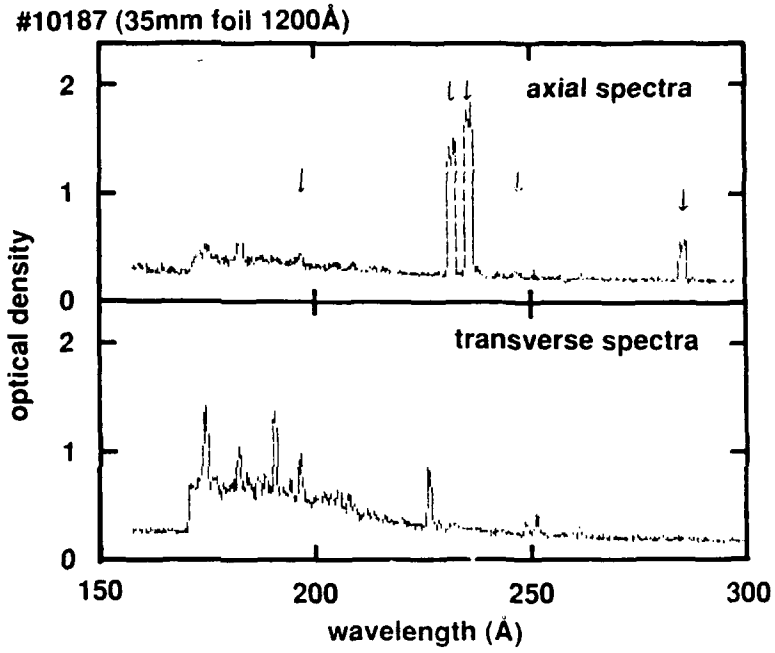

Fig. 4 Typical on-axis(upper) and off-axis spectrographs of the Ge exploding foil target with Ge thickness of 120 nm and the length of 3.3 cm.

Up to 45 mm, the intensity of the lasing lines increased exponentially. However, a 50 mm long target gave weaker signals compared to the exponential growth due to weaker illumination intensity at the ends of the line focus. The gain coefficient and the maximum gain length product of approximately 3 cm^{-1} and 12, respectively have been obtained.

References

1. Y. Kato et al., OSA Proc. Short Wavelength Coherent Radiation: Generation and Applications, Vol.2(Opt. Soc. Am., Washington, DC 1988)pp.47-51.
2. Y. Kato et al., Appl. Phys. B50, 247(1990).
3. H. Azuma et al., Opt. Lett. 15, 1011(1990).
4. C. J. Keane et al., J. Phys. B22, 3343(1989).
5. R. A. London et al., J. Phys. B22, 3363(1989).
6. T. N. Lee et al., Phys. Rev. Lett. 59, 1185(1987).
7. D. M. O'Neill et al., Opt. Commun. 75, 406(1990).
8. C. L. S. Lewis et al., Proc. 2nd Int. Coll. on X-Ray Lasers (IOP Publishing, 1990).
9. R. C. Elton, X-RAY LASERS (Academic, New York 1990) p.133.

Coherent X-Ray Generation Through Laser Pumping of a Relativistic Ion Beam: Feasibility Assessment

S. A. Bogacz

Accelerator Physics Department, Fermi National Accelerator Laboratory, P.O. Box 500, Batavia, Illinois 60510

The efficiency of most popular approach to generating short wavelength radiation involving particle beams, FEL[1], is limited by the Thomson scattering cross section. If one were to use a beam of particles having a resonant scattering cross section for some frequency, a greatly enhanced gain might be expected. A natural candidate is a hydrogenic positive ion, having $Z > 2$, with a single bound electron. The fact that the ion is charged allows the beam to be accelerated to relativistic energies ($\gamma >> 1$), therefore one can exploit the properties of relativistic kinematics which dictate that the back scattered radiation will have its wavelength shortened by a factor $(2\gamma)^2$.

Introduction – General Configuration

Suppose the ion beam encounters a laser beam traveling in the *opposite* direction. In the rest frame of the ions the frequency of the light is enhanced by a factor 2γ (extreme relativistic case, $\gamma >> 1$). Assume that the rest frame frequency matches, say, the 1s–2p transition frequency, and that the interaction path length in the lab frame corresponds to a time in the rest frame necessary to invert the level population (a so-called π pulse). If we subsequently apply a different wave, traveling *parallel* to the ion beam, we may achieve stimulated emission. The wavelength of this signal would be reduced by a factor 2γ from that of the resonant radiation in the rest frame, and by a factor $(2\gamma)^2$ from the original laser wavelength. If the ions were at rest, there is no reduction in the wavelength since the frequencies of the pump and the stimulated emission would be identical; for a relativistic beam with $\gamma = 50$ the frequency of the stimulated radiation is higher by a factor 10^4! Feasibility, of course, rests on whether the necessary pump power is achievable and whether the gain is sufficient to overcome the losses associated with typical x-ray mirrors; both of these are governed by the spontaneous emission rate.

Pumping – Population Inversion

One can derive expressions for the time evolution of the 1s and 2p level occupations (in the rest frame) as a function of an applied oscillatory electric field strength E and frequency ω for some initial occupation of the levels. The time dependence of a two-by-two density matrix, N, (in the interaction picture) is governed by the following equation[2]:

Proceedings on Short-Wavelength Coherent Radiation, Vol. 11, Philip H. Bucksbaum and Natale M. Ceglio (eds.)
1991 Optical Society of America

$$\frac{\partial}{\partial t}\mathbf{N} = i\hbar\,[\mathbf{U}, \mathbf{N}] - \frac{1}{\tau}(\mathbf{N} - \mathbf{N}_{eq})\,. \tag{1}$$

where **U** denotes the perturbing Hamiltonian given by:

$$\mathbf{U} = |U| \begin{bmatrix} 0 & e^{i\varepsilon t} \\ e^{-i\varepsilon t} & 0 \end{bmatrix}. \tag{2}$$

Here $|U| = eE|\langle 1s|z|2p\rangle|/2$, $\langle 1s|z|2p\rangle = 4\sqrt{2}(2/3)^5(a_o/Z)$, $\varepsilon = \omega_{1s\to 2p} - \omega$, and $\hbar\omega_{1s\to 2p} = E_{2p} - E_{1s} = (3/4)RZ^2$, where R and a_o are the Rydberg and Bohr radius respectively. The last term in Eq.(1) accounts for spontaneous emission[2], where τ is the lifetime and N_{eq} is the equilibrium density matrix (at zero temperature).To describe the pumping stage we solve Eq.(1) with the initial population entirely in the ground state. The required evolution of the excited state population is given by the first diagonal element of the density matrix[3]

$$N_{\uparrow\uparrow}(t) = \frac{1}{2}\,\frac{(\Omega\tau)^2}{1 + (\Omega\tau)^2}\left\{1 - e^{-t/\tau}\left[\frac{\sin \Omega t}{\Omega\tau} + \cos \Omega t\right]\right\}, \tag{3}$$

$$\Omega \equiv \sqrt{\Omega_o{}^2 + \varepsilon^2}\,,$$

where $\Omega_o = 4|U|/\hbar$. Therefore population inversion, $N_{\uparrow\uparrow} = 1 - O(\Omega\tau)^{-1}$, requires $\Omega\tau >> 1$ (strong field limit) and occurs after a time $T_{rest} = \pi/\Omega$; (this corresponds to the π-pulse in NMR). Evaluating τ from the Einstein relation[4],

$$\tau = \frac{3\hbar c^3}{4e^2\omega_{1s\to 2p}{}^3}\,|\langle 1s|z|2p\rangle|^{-2} = 1.59 \times 10^{-9}\,Z^{-4}\,\mathrm{s}. \tag{4}$$

and using the explicit expression for Ω,

$$\Omega = 4\sqrt{2}(2/3)^5\,\frac{eEa_0}{3\hbar Z}\,; \tag{5}$$

one can rewrite the strong field condition ($\Omega\tau >> 1$) as an inequality on the required electric field (rest frame value):

$$E_{rest} >> 0.349 \times Z^5 \text{ st. V cm}^{-1}. \tag{6}$$

In the lab-frame the E-field is reduced by a factor 2γ and the pulse width , $T^{\pi}_{rest} = \pi/\Omega$, translates to an interaction length

$$L = \gamma c\, T^{\pi}_{rest} = 2.61 \times 10^1\, Z/E_{lab} \tag{7}$$

and a power flux, $\langle S \rangle = (c/8\pi)\, E_{lab}{}^2$, of

$$\langle S \rangle >> 3.64 \times Z^{10}/\gamma^2 \text{ W/cm}^2 , \tag{8}$$

which is readily achievable in steady state for low Z. Were one to operate in the fundamental Gaussian mode of an optimized confocal resonator, the condition on the *total power flux*, P, can be written as

$$P >> 10^{-2} \times Z^4 \text{ [W]} \tag{9}$$

and may be enhanced over the drive power by a factor involving the Q of the resonator. Finally, the Doppler-shifted resonance condition $2\pi c/\lambda = \omega_{1s\to 2p}/(2\gamma)$ relates γ and λ as follows

$$\gamma = 4.12 \times 10^4 Z^2 \lambda . \tag{10}$$

Stimulated Emission – Lasing

We now examine the second stage of our model, where the inverted population ion beam is subjected to an incoming electromagnetic wave, which is to be amplified by stimulated emission. The field strength will be assumed small, i.e. $\Omega'\tau << 1$, where we use Ω' for the precession frequency associated with the amplified wave.

To introduce the gain mechanism we note that the rate of production of coherent photons, N_{coh}, is given by a solution of Eq.(1) with the assumed population inversion as the initial condition.

$$N_{coh}(t) = \frac{1}{2}\left(\frac{\Omega'_o}{\Omega'}\right)^2 \Omega' \left\{ e^{-t/\tau} \sin \Omega'\tau + \frac{1 + (\Omega'\tau)^2}{e^{-t/\tau}(\sin \Omega'\tau + \Omega'\tau \cos \Omega'\tau) - 1} \right\}.$$

$$\Omega' \equiv \sqrt{\Omega'^2_o + \varepsilon^2} . \tag{11}$$

The above solution describes a general "off resonance" situation ($\varepsilon \neq 0$) which reflects frequency spread , $\Delta\omega/\omega = \Delta\gamma/\gamma$, due to a longitudinal momentum spread in the incoming ion beam ($\Delta\gamma$). Note that this effect could be neglected in the discussion of the pumping stage where the strong field limit ($\Omega_o\tau >> 1$) applies. However, the lasing stage is in the weak field regime and the off resonance frequency broadening has to be considered.

Coherent Gain

The total number of coherent photons emitted during some time t (to be discussed shortly) results in an increment to the energy density of the initial wave, ΔE, given by

$$\Delta E = \hbar n\, \omega_{1s\to 2p} \langle \int_0^t N_{coh}(t')dt' \rangle_\varepsilon ; \tag{12}$$

here n is the ion density (in the rest frame) and

$$\langle \ldots \rangle_\varepsilon \equiv \frac{1}{\Delta\varepsilon} \int_{-\Delta\varepsilon/2}^{\Delta\varepsilon/2} \ldots d\varepsilon \tag{13}$$

defines the ensemble average over momenta in the incoming beam. The right hand side of Eq.(12) is evaluated in two asymptotic regions: (a) cool beam limit ($\Delta\varepsilon\tau << 1$); (b) hot beam limit ($\Delta\varepsilon\tau >> 1$).

Evaluating appropriate ε–averages in the above two regimes, one can rewrite Eq.(12) as follows:

$$\Delta E = \frac{\hbar}{2} n\, \omega_{1s\to 2p} (\Omega_0'\tau)^2 A\ , \tag{14}$$

where

$$A = \begin{cases} 0.17 & ;\ \Delta\varepsilon\tau << 1 \\ 0.39\pi/\Delta\varepsilon\tau & ;\ \Delta\varepsilon\tau >> 1. \end{cases} \tag{15}$$

The relationship between Ω'_o and the energy density E ,

$$(\Omega'_o)^2 = 2^5\pi^3 e^2 |\langle 1s|z|2p\rangle|^2 E/h^2\ , \tag{16}$$

allows us to rewrite Eq.(14) as

$$\Delta E = (2\pi)^2 A n\, e^2\, \omega_{1s\to 2p}\, \tau^2 E/h\ . \tag{17}$$

The total gain, G, is defined as

$$G = (E + \Delta E)/E \tag{18}$$

and lasing requires $GR^2 > 1$; here R is the mirror reflectivity of the second (lasing) cavity. Finally the gain coefficient can be written as :

$$G = 1 + (2\pi)^2 A n\, e^2\, \omega_{1s\to 2p}\, \tau^2/h\ . \tag{19}$$

Feasibility

Assuming mirrors with an intensity reflection efficiency of 50% and a longitudinal momentum spread in the incoming ion beam of 1% ($\Delta\gamma/\gamma = 10^{-2}$) one can estimate the ion concentration required for lasing as

$$n_{rest} = 6.84 \times 10^9 \, Z^8 \, cm^{-3} . \tag{20}$$

In the lab frame this requires an ion beam current density of

$$j_{lab} = (Z - 1)e \, n_{rest} \, c\gamma . \tag{21}$$

For the case of Li^{++} ions the threshold current density would be

$$j_{lab} = 4.31 \times 10^5 \, A \, cm^{-2} . \tag{22}$$

Particle beams having the requisite current density, momentum spread and energy are within the scope of present generation high current storage rings. The discussion in this paper centers on the 1s–2p transition in a hydrogenic atom. However, other types of transitions may also be of interest; particularly those with longer lifetimes (eg., transitions to various dipole-forbidden or metastable states). It may also be possible to exploit a nuclear transition as well as various multilevel systems.

References

1. J.M.J. Madey, J. Appl. Phys. **42** (1971) 1906.
2. R. Karplus and J. Schwinger, Phys. Rev. **73** (1948) 1020.
3. S.A. Bogacz, *Ph.D. Thesis*, Northwestern University, Evanston (1986).
4. L.I. Schiff, *Quantum Mechanics*, 3rd ed. (McGraw-Hill, 1986) 414.

Search for Gain on 2p–2s Transitions in a Collisionally Excited Ge Plasma

G. D. Enright, H. A. Baldis, J. Dunn, B. La Fontaine, and D. M. Villeneuve

Steacie Institute, National Research Council of Canada, Ottawa, Ontario K1A 0R6, Canada

J. C. Kieffer, H. Pépin, and M. Chaker

INRS-Énergie, Varennes, Québec J3X 1S2, Canada

Abstract

Population inversion is expected on 2p-2s transitions in Ne-like Ge in the 60-80 Å region. The feasibility of observing gain on these transitions is explored.

Soft x-ray amplification in collisionally excited Ne-like Ge plasmas has been extensively studied in a number of laboratories[1-3]. Gains in excess of 4 cm^{-1} have been reported for the 3p-3s transitions and significant gains have been inferred over a wide range of irradiance conditions. In our laboratory we have made use of a novel focusing arrangement[4] that employs a segmented wedge array to overlap several line foci to produce a more uniform linear plasma. The reproducibility of the XUV spectra was improved allowing gain to be inferred on a core-excited $2s2p^63d$-$2s2p^63p$ J=2-1 transition[3]. The 3d-2s quadrupole (E2) emission from the upper state of this core-excited transition was also identified in the L-shell emission spectrum.

In this paper we report preliminary results of experiments designed to extend Ne-like systems to shorter wavelengths. The observation of gain on a core-excited transition has led us to consider the possibility of observing gain on 2p-2s inner-shell transitions of the form $2s2p^63s$-$2s^22p^53s$ and $2s2p^63d$-$2s^22p^53d$. In the case of Ne-like Ge the n = 3-3 transitions for which gain has been observed occur at wavelengths of ~200 - 250 Å. The 2p-2s transitions which are expected to have gain are in the 65 - 80 Å region. The gains for these transitions will be somewhat lower than that inferred for the 3-3 transitions. If the inversion densities and oscillator strengths are similar to that observed on 3-3 transitions, the gain would be reduced by the square of the ratio of the wavelengths. In the present experiment this would suggest that gains ≤ 0.5 cm^{-1} on the 2p-2s transitions. Higher gains would be possible if reduced refractive effects allow observation of higher density plasma regions.

The experiments were performed with the LP2 Nd:glass laser system operating at 1.06 μm. The laser pulse had a fast (200 ps) risetime with a full width of ~1.5 ns. Optically polished Ge slabs were aligned to an accuracy of 2 mr with respect to the laser axis. The width of the line focus was ~80 μm and the length was fixed at 12 mm. The present results were obtained with incident energies of 140±10 J/cm of line focus which corresponds to ~1.5×10^{13} W/cm^2.

Proceedings on Short-Wavelength Coherent Radiation
Vol. 11, Philip H. Bucksbaum and Natale M. Ceglio (eds.)
1991 Optical Society of America

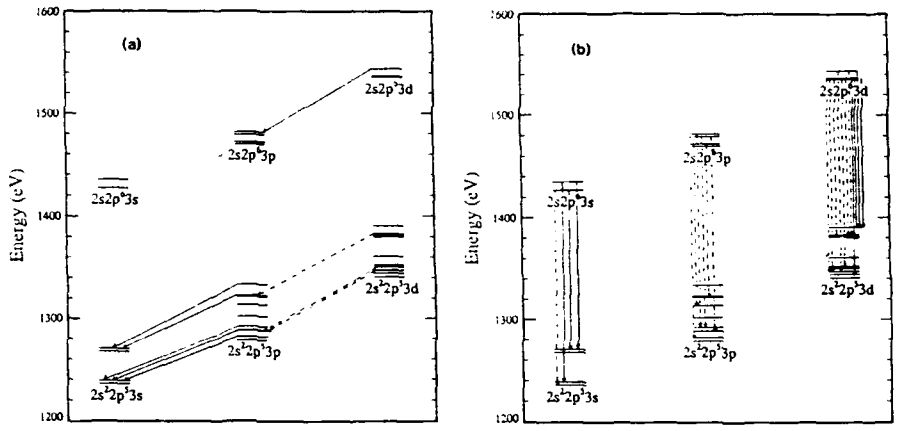

Figure 1. Grotrian diagrams showing the observed n=3-3 transitions (a) and the 2p-2s transitions (b).

The diagnostics include two flat field XUV spectrometers[5], one of which was accurately aligned (±5 mr) with respect to the line focus axis. The second spectrometer was aligned at 45 degrees to the line f$xus axis in the plane of incidence. For the 3-3 transitions the spectrometers were equipped with 3000 Å thick Al foil filters which transmit from ~175 Å to greater than 300 Å. For the present experiments the Al filters were replaced with 1100 Å thick Ag filters which transmit between 35 and 110 Å. The XUV spectra were recorded on Kodak 101-01 film. The off-axis spectrometer employed a 300 μm wide slit approximately midway between the plasma and film to spatially resolve the emission along the line focus. An ADP crystal spectrograph was used to observe the L-shell emission from the plasma.

In our previous experiments we have measured the wavelengths of nine 3-3 transitions in the 200 Å region. This included five 3p-3s and one 3d-3p (core-excited) transitions for which gain was inferred and three 3d-3p optically thin transitions. In addition, accurate wavelengths have been determined for the seven resonance (3-2) transitions and one E2 (3d-2s) transition. These experimentally determined transition energies have allowed a more precise determination of the excited state energies for Ne-like Ge. The computed energy levels are based on the calculations of Zhang and Sampson[6] with corrections to agree with the experimentally determined levels. The corrections are generally small except for the J = 0 and core excited-levels. Fig. 1(a) shows a Grotrian diagram showing all the observed 3-3 transitions with the solid lines representing transitions for which gain has been inferred. Fig 1(b) is the same diagram showing the strong 2p-2s dipole transitions. The solid lines represent possible lasing transitions since the lower level can decay by a dipole transition to the ground state. The calculated wavelengths for these transitions are given in Table 1, and are expected to be accurate to within ~0.10 Å. These 2p-2s transitions will appear as Ne-like satellites of F-like resonance lines at 79.75 and 65.90 Å.

Table I. Computed and observed wavelengths of 2p-2s transitions in Ne-like Ge. transitions marked with an asterisk are possible lasing transitions. Lines appearing as blends are noted ([b]).

$2p_{1/2}$-2s	Calculated (Å)	Observed (Å)	$2p_{3/2}$-2s	Calculated (Å)	Observed (Å)
2s3s-$2p_{1/2}$3s			**2s3s-$2p_{3/2}$3s**		
$^3S_1$-$^3P_1^*$	79.10	79.00	$^3S_1$-$^3P_2$	64.82	64.85[b]
$^1S_0$-$^3P_1^*$	75.14	75.00	$^1S_0$-$^1P_1^*$	63.10	63.06[b]
2s3p-$2p_{1/2}$3p			**2s3p-$2p_{3/2}$3p**		
$^3P_1$-$^3D_2$	83.00	83.05[b]	$^3P_2$-$^3D_3$	67.37	67.45
$^3P_1$-$^1P_1$	78.24	78.14	$^3P_2$-$^3P_2$	66.30	66.33
			$^1P_1$-$^3P_2$	65.07	65.09
			$^3P_2$-$^1D_2$	62.93	63.06[b]
2s3d-$2p_{1/2}$3d			**2s3d-$2p_{3/2}$3d**		
$^3D_1$-$^3F_2$	79.75	79.75[b]	$^3D_3$-$^3F_4$	65.33	65.26
$^3D_3$-$^1F_3$	80.54	80.52 (3rd)	$^3D_2$-$^3F_3$	65.71	65.68
$^1D_2$-$^1F_3$	77.10	77.08 (3rd)	$^1D_2$-$^3F_3$	63.08	63.06[b]
$^3D_2$-$^1P_1^*$	85.28	85.18	$^3D_3$-$^3D_3$	64.72	64.85[b]
$^3D_1$-$^1P_1^*$	85.58	85.55	$^3D_1$-$^3P_1^*$	64.92	64.85[b]
$^1D_2$-$^1P_1^*$	80.91	80.75 (3rd)			

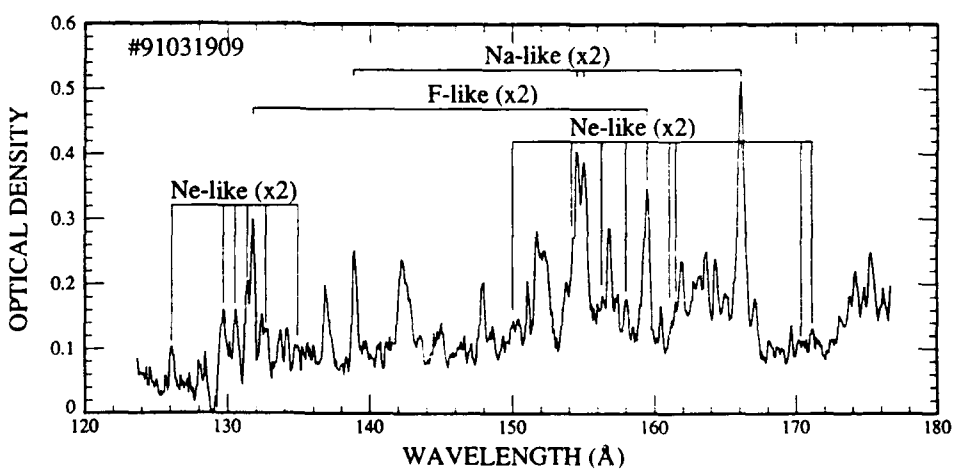

Figure 2. Axial XUV spectrum of the Ge plasma. The F-like and Na-like resonance lines and Ne-like 2s-2p lines are in second order.

Fig. 2 shows an axial XUV spectrum of the Ge plasma. The Ag filter does not transmit above ~110 Å so the lines appear mostly in second order (although 3rd and 4th order lines have been identified). F-like and Na-like resonance lines are clearly visible and have been used to accurately determine the wavelength scale. The instrumental resolution, as determined by the width of the narrowest lines is less than 0.1 Å. In this spectral region, the off-axis spectrum consisted only of the Na-like and F-like resonance lines. The spatially-resolving slit on this spectrometer limited the field of view of this instrument (in the film plane) to ~0.6 mm of plasma length, too short to observe the weak, optically thin lines. A number of lines in the axial spectrum have been tentatively identified as 2p-2s transitions in Ne-like Ge. Table 1 compares the observed wavelengths to the calculated values. The asterisk identifies the possible lasing transitions. The 2p-2s transitions around 66 Å are easily identified. Unfortunately the possible lasing transitions at 63.06 and 64.05 Å are seen to blend with other (probably stronger) 2p-2s transitions. In the region of 80 Å the Na-like resonance lines complicate the spectrum. Nevertheless it is possible to identify several potential lasing transitions. In some cases the 3rd order spectrum has been used to more accurately determine the wavelength.

In summary we have used the L-shell emission spectra and the observed 3-3 transitions in the 200 Å region to calculate more accurate wavelengths for 2p-2s transitions in Ne-like Ge. A number of optically thin lines have been identified in the axial XUV spectra that correspond to these transitions. Transitions for which gain is expected have wavelengths of 63.06, 64.85, 75.00, 79.00, 80.75, 85.18, and 85.55 Å.

References

1. T. N. Lee, E. A. McLean, and R. C. Elton, "Soft x-ray lasing in neonlike germanium and copper plasmas," Phys. Rev. Lett. **59**, 1185 (1987).
2. D. M. O'Neill, C. L. S. Lewis, D. Neely, J. Ohomoibhi, M. H. Key, A. MacPhee, G. J. Tallents, S. A. Ramsden, A. Rogoyski, and E. A. McLean, "Characterisation of soft x-ray amplification observed in Ne-like germanium," Opt. Comm. **75**, 406 (1990).
3. G. D. Enright, D. M. Villeneuve, J. Dunn, H. A. Baldis, J. C. Kieffer, H. Pépin, M. Chaker, and P. R. Herman, "X-ray laser gain measurements in a collisionally excited Ge plasma," to be published, J Opt. Soc. Am. B (1991).
4. D. M. Villeneuve, G. D. Enright, H. A. Baldis, and J. C. Kieffer, "Novel line focus geometry applied to x-ray lasers," Opt. Comm. **81**, 54 (1991).
5. N. Nakano, H. Kuroda, T. Kita, and T. Harada, "Development of a flat-field grazing-incidence XUV spectrometer and its application in picosecond XUV spectroscopy," Appl. Opt. **23**, 2386 (1984).
6. H. L. Zhang and D. H. Sampson, "Relativistic distorted wave collision strengths for excitation to the 88 n = 3 and n = 4 levels in all 71 neon-like ions with 22 ≤ Z ≤ 92," At. Data Nucl. Data Tables **42**,1 (1989).

Modal Study of Refractive Effects on X-Ray Laser Coherence

Peter Amendt and Richard A. London

Lawrence Livermore National Laboratory, University of California, Livermore, California 94550

Moshe Strauss

Nuclear Research Centre-Negev, P.O. Box 9001, Beer Sheva, Israel

Abstract

The role of smoothly varying transverse gain and refraction profiles on x-ray laser intensity and coherence is analyzed by modally expanding the electric field within the paraxial approximation. Comparison with a square transverse profile reveals that smooth-edged profiles lead to: (1) a greatly reduced number of guided modes, (2) the continued cancellation of local intensity from a loosely guided mode by resonant free modes, (3) and the absence of extraneous (or anomalous) free mode resonances. These generic spectral properties should enable a considerable simplification in analyzing and optimizing the coherence properties of laboratory soft x-ray lasers.

1. Introduction

Current X-ray laser (XRL) designs rely on amplifying spontaneous emission in a high temperature plasma.[1] An important issue in the study of XRL's is the degree of transverse spatial coherence necessary for holographic applications.[2] Longitudinal coherence appears to be satisfactory, but transverse coherence remains problematic and requires further optimization study.

Recently, London *et al.*[3] have undertaken a study of transverse coherence based on a modal decomposition of the electric fields in an amplifying medium. With this ansatz for the laser fields, the paraxial wave equation is transformed into two equations which separately govern the longitudinal and transverse behavior. The longitudinal equation describes the usual longitudinal amplification from a distributed noise source, whereas the transverse equation is of the Schrödinger-type with complex "potential" arising from the gain or imaginary part of the atomic susceptibility. The analysis of this latter equation leads to a spectrum of eigenmodes which determines the possible transverse profiles of intensity and coherence.

Proceedings on Short-Wavelength Coherent Radiation, Vol. 11, Philip H. Bucksbaum and Natale M. Ceglio (eds.)

© 1991 Optical Society of America

The above mathematical characterization for the fields has formed the basis in the literature for the predicted phenomenon of "excess noise" in an amplifying medium.[4] In particular, the inherent non-self-adjoint property of a general amplifying medium presumably allows for the possibility that loosely guided or bound transverse eigenmodes may dominate the profiles at large transverse distances from the lasant medium. Such a prospect has serious implications for coherence and intensity studies since the predicted profiles will be overly sensitive to the precise value of gain used, and which we argue cannot be physical.

Previous use of the modal approach to understand XRL phenemena has been restricted to the bound or discrete portion of the transverse eigenmode spectrum. For sufficiently large values of gain-length product this restricted analysis can obtain accurate transverse profiles of intensity and coherence. Unfortunately, most gain-length products observed in the present generation of amplified spontaneous emission (ASE) XRL experiments are not sufficiently large to justify use of this truncated approach in general.

More recently, Amendt *et al.*[5] have reexamined the modal approach by appending the continuum or free modes to the bound mode portion of the transverse spectrum for the particular example of transverse square gain and refraction strength profiles. The primary motivation for including the continuum is that by virtue of the non-orthogonality of the eigenmodes, sufficient cancellation from cross-terms in the expression for the modal intensity may occur and possibly eliminate to a large extent the "excess noise" phenomenon. It is found that for small and moderately large gain-length products the anomalously large intensities associated with one loosely bound transverse mode are significantly reduced by the inclusion of neighboring free eigenmodes. This feature has the two-fold effect of greatly reducing the level of "excess noise" and of removing the source of undue sensitivity of previous modal modelling to the exact value of the gain parameter adopted.

Amendt *et al.*[5] address some fundamental problems arising in a general ASE XRL environment, but they do not determine the degree of transverse coherence relevant for an ASE XRL experiment. In particular, the square gain and refraction strength profiles explored in that analysis were intended mostly for analytic ease and conceptual clarity. What remains to be shown is whether the effective modal intensity cancellation persists as effectively for rounded profiles which now allow for the beneficial effect of refractive defocussing. In this paper we continue our analysis of modal XRL coherence by considering some consequences of rounded gain and refraction strength profiles in a finite geometry.

2. Modal Analysis

Our starting point is the paraxial equation for the slowly varying wave electric field amplitude E:[3]

$$\left[\frac{1}{k}\nabla_\perp^2 - 2i\partial_z - h(x) + ig(x)\right] E(x, z) = -4\pi k\, P_{sp}(x, z)\,, \tag{1}$$

where k is the free-space longitudinal (or parallel to z-axis) wavevector, $\nabla_\perp^2$ is the transverse Laplacian, $h=\omega_{pe}^2(x)/kc^2$ is the refraction strength, ω_{pe} is the electron plasma frequency, g(x) is the atomic gain of the medium, and P_{sp} is the random (in x and z), spontaneous atomic polarization. Upon writing $E(x, z) = \Sigma c_n(z)u_n(x)$ we find a transverse mode equation:

$$\left[\partial_{xx}^2 - F_e(\eta\, h(x) - i\, g\,(x))\right] u_n(x) = -\, E_n u_n(x)\,, \tag{2}$$

and a longitudinal transfer equation:

$$\sum_n \left[u_n\, \partial_z c_n - \frac{i}{2} E_n c_n u_n\right] = -i\, P_{sp}\,, \tag{3}$$

where $F_e = kg_0a^2$ is an effective Fresnel number, a is the lasant half-width, E_n is the eigenvalue, $x \to xa$, $z \to zka^2$, $P_{sp} \to P_{sp}/2\pi(ka)^2$, $\eta = h_0/g_0$, and $h = h/h_0$ and $g = g/g_0$ are normalized transverse profiles. Since eq. (2) is non-self-adjoint, the eigenvalues are generally nonreal and the eigenfunctions are *biorthonormal*: $\int u_n u_m dx = \delta_{nm}$ ($\neq \int u_n u_m^* dx$). This feature specifically gives rise to the problem of "excess noise" where a "loosely" bound mode may dominate the field intensity $<|E|^2>/8\pi$ at large transverse distance ($x >> a$).[4] Amendt *et al.*[5] have previously shown that free modes ($\lim_{x\to\infty} u_n < \infty$) contained in the spectrum of eq. (2) tend to compensate for "excess noise" arising from marginally bound modes ($\lim_{x\to\infty} u_n = 0$) for the particular example of a square gain and refraction strength profile. However, the case of a hard-edged profile is not a realistic feature of XRL's that are based on amplifying spontaneous emission.

3. Modal Study with Refraction

A useful method for considering smooth transverse profiles in the modal approach is to numerically relax the square profile into a hyperbolic secant squared profile as follows: $h(x), g(x) \to (1-\varepsilon)\, f(x,\varepsilon) + \varepsilon\, \mathrm{sech}^2(x)$, where $\varepsilon \to 1$ and

$$f(x,\varepsilon) = \begin{cases} 0 & ;|x| > 1+\varepsilon \\ \sin^2\left[\dfrac{\pi(\,|x| - 1 - \varepsilon)}{4\varepsilon}\right] & ;\, 1-\varepsilon < |x| < 1+\varepsilon \\ 1 & ;|x| < 1-\varepsilon \end{cases}\,, \tag{4}$$

and then solving (by shooting methods) the transverse eigenvalue equation (2) at each incremental step in ε using the eigenvalue for the previous ε as a guess. The $\mathrm{sech}^2(x)$ profile is a convenient choice because: 1) $h(0)$ equals unity as for the square profile, (2) the integrated area under h coincides with the square profile, and (3) the bound mode eigenvalues are analytically known for the case of an unbounded geometry:

$$E_n = -\left[\frac{1}{2}(1 + 4iF_e(1 + i\eta))^{1/2} - (n + \frac{1}{2})\right]^2 \qquad , n=0, 1, 2, \ldots . \tag{5}$$

The general requirement for a bound mode is that $\mathrm{Im}\,(E_n) < 0$, leading to only three bound modes for a Ni-like Se XRL, where typically $F_e = 1500$ and $\eta = 59$.[3] By contrast, the number of modes n_g in a hard-edged laser scales as:[3] $2F_e/\{\pi \ln[F_e/(1+\eta)]\}$, giving nearly 300 bound modes for the Ni-like Se XRL. Clearly, the coherence length (or distance at which the normalized correlation function $<E(0,z)E^*(x,z)>\cdot 1/[<|E(0,z)|^2><|E(x,z)|^2>]^{1/2}$ is reduced to 0.85) is far greater for a smooth profile than for a square profile, if we consider only the bound mode contribution. The key question becomes whether the inclusion of free modes can affect this conclusion.

To consider this question, we first show how the free mode portion of the spectrum compensates for anomalous intensities arising from loosely bound modes as in the square profile case. The free modes are obtained by using a reflecting boundary condition at $x = \pm A$, where $A >> 1$. Figures (1a-b) display the compensated

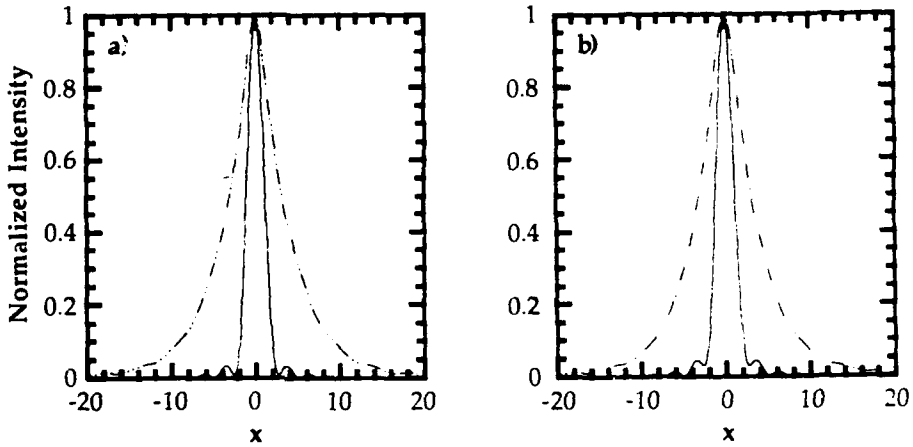

Figs. (1a-b): Normalized compensated (solid line) and uncompensated (dash-dotted line) intensity for the square profile (a) and the $sech^2(x)$ profile (b) for F_e=0.5, η=0, and geometric half-width A=25.

intensity for one loosely bound mode compared to the uncompensated or "bare" intensity. Note how the bound mode intensity dramatically cancels beyond $x \sim \pm 2$ for the uncompensated case, while in the absence of resonant free modes a considerable surplus of energy resides outside the lasant medium ($|x| \geq 1$). This example illustrates the "excess noise" phenomenon for a smooth profile, but with a significant degree of reduction occurring due to cross-correlations between neighboring (in $Re(E_n)$) free modes and the one marginally bound mode.

In fig .(2) we show the point (or bound mode) and continuum spectra for both square and $sech^2(x)$ profiles. Note the absence of continuum resonances beyond the

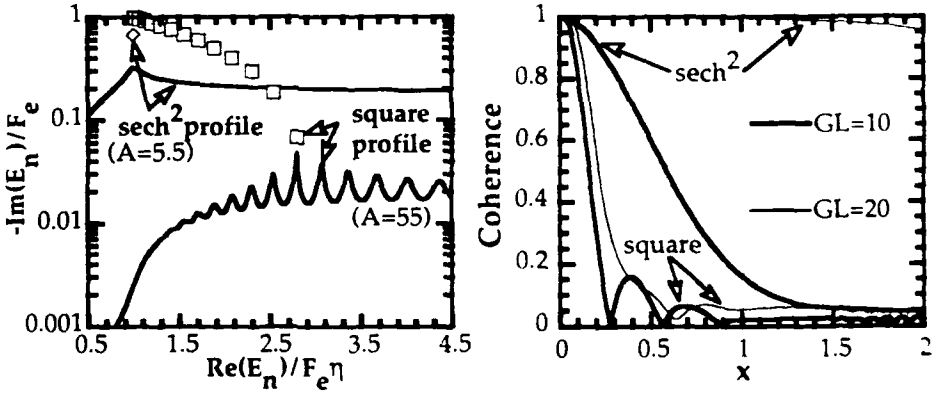

Figs. (2, 3): In fig. (2) (left) are shown the point and free mode (even parity) spectra for square and $sech^2(x)$ profiles with F_e=100 and η=10. Note the larger value of A (10x) used for the square profile. In fig. (3) (right) are shown coherence profiles for A=5.5, F_e=100, and η=10 with gain-length parameter GL=10, 20.

one (even parity) bound mode for the $\mathrm{sech}^2(x)$ profile; such resonances effectively act as loosely bound modes in the case of the square profile. This generic feature of the smooth profile is seen to simplify the analysis: relatively more free states behave as high or nearly orthogonal modes which happen to depend only weakly on the details of the gain and refraction profiles. In fig. (3) we compare coherence profiles for the square and $\mathrm{sech}^2(x)$ gain profiles by considering, for example, the first 74 (even parity, bound plus free) modes. The improved coherence for the $\mathrm{sech}^2(x)$ profile is due mainly to the fewer number of bound modes in the system which is attributed to refractive defocussing in a smoothly varying medium. This phenomenon actually consists of two parts: (1) the usual bending of rays away from the lasant medium when $\eta \neq 0$ and (2) the effectively reduced region of maximum gain giving rise to fewer high-gain transverse modes in general. Both effects contribute significantly in discarding many of the bound modes responsible for degraded transverse coherence.

4. Discussion

Realistic coherence modelling of current XRL experiments must include the role of refractive defocussing arising from non-trivial gain and refraction profiles. We have begun to study this phenomenon from a modal viewpoint with the aim of both clarifying the role of "excess noise" in such a system and optimizing the degree of coherence for eventual holographic applications. The generally large values of F_e and η found in current XRL experiments require a streamlined use of the modal approach as outlined above in order to compare with existing numerical wave propagation codes.[6] We have shown that the role of free modes in a smoothly varying media appears not to be as complex as for the square profile by virtue of the far fewer number of bound mode resonances and the absence of additional continuum resonances.

Acknowledgments

We thank J. Milovich, M. Rosen, and E. Williams for many stimulating discussions. This work was performed under the auspices of the U.S. Department of Energy by the Lawrence Livermore National Laboratory under Contract W-7405-ENG-48.

References

1. M.D. Rosen *et al.*, *Phys. Rev. Lett.* **54**, 106 (1985); D.L. Matthews *et al.*, op. cit. **54**, 110 (1985).
2. R.A. London, M.D. Rosen, and J.E. Trebes, *Appl. Optics* **28**, 3397 (1989).
3. R.A. London, M. Strauss, and M.D. Rosen, *Phys. Rev. Lett.* **65**, 563 (1990).
4. K. Petermann, *IEEE J. Quantum Electron.* **QE-15**, 566 (1979); H.A. Haus and S. Kawakami, *IEEE J. Quantum Electron.* **QE-21**, 63 (1985); C.H. Henry, *J. Lightwave Tech.* **LT-4**, 288 (1986); A.E. Siegman, *Phys. Rev.* **A39**, 1253 (1989); A.E. Siegman, *Phys. Rev.* **A39**, 1264 (1989).
5. P. Amendt, R.A. London, and M. Strauss, UCRL-JC-106071, submitted to *Phys. Rev.* A.
6. M.D. Feit and J.A. Fleck, *JOSA* **B7**, 2048 (1990).

Saturation and Kinetic Issues for Optical-Field-Ionized Plasma X-Ray Lasers

D. C. Eder, P. Amendt, M. D. Rosen, J. K. Nash, and S. C. Wilks

Lawrence Livermore National Laboratory, Livermore, California 94550

Abstract

Lasing between excited states and the ground state following optical-field ionization is studied. Saturation of an x-ray laser when the lower lasing level is a ground state of a H-like or Li-like ion is discussed. Efficiencies of 10^{-5} to 10^{-4} are calculated for the $3d_{5/2} - 2p_{3/2}$ transition at 98 Å in Li-like Ne. The assumption that the fine-structure levels are populated according to their statistical weights is shown to be justified through comparisons with calculations using a detailed atomic model. The effect of saturation by a given fine-structure transition on the populations of the fine-structure levels is analyzed.

I. Introduction

Optical-field ionization by a high-intensity/short-pulse UV laser allows the possibility of x-ray lasing between excited states of an ion and the ground state.[1,2] We calculate efficiencies in Li-like Ne, for the $3d_{5/2} - 2p_{3/2}$ transition at 98 Å, to be in the range of 10^{-5} to 10^{-4}. These relatively high efficiencies are obtained despite the short lifetime of this self-terminating laser and the reduced saturation intensity associated with the lower lasing state being the ground state of the ion. In this proceeding we discuss saturation issues for lasing down to the ground state in H-like and Li-like ions. A common assumption in modeling these ions is that the fine-structure levels are populated according to their statistical weights. We discuss the validity of this approximation by comparing shell-averaged results with those obtained using a detailed atomic model. We also study the effects of saturation on the relative population of the fine-structure levels.

II. Saturation Issues for Lasing to Ground State

The large energy difference between the ground state and the first excited state of an ion makes the idea of lasing down to the ground state an attractive one. The small populations that can be achieved in excited states require that the ground state be emptied to a very high degree (of order 0.1%) to obtain population inversion and gain. Such complete ionization appears possible by using high-intensity lasers where the electric field associated with the laser field is

Proceedings on Short-Wavelength Coherent Radiation, 96
Vol. 11, Philip H. Bucksbaum and Natale M. Ceglio (eds.)
© 1991 Optical Society of America

larger than the Coulomb field binding the ground-state electrons, of a given ionization stage, to the nucleus.[1,3] If the electron temperature following ionization is sufficiently low, there is rapid collisional recombination to the upper levels followed by collisional cascade giving large population inversions and gains between the first excited state and the ground state. The ground state is populated on a time scale associated with the radiative lifetime of the first excited state which is of order a picosecond. The short lifetime of these self-terminating lasers reduces the energy that can be obtained. An additional aspect of lasing down to the ground state that limits the output energy is the relatively low intensity required to saturate.

As the length of the lasing medium is increased the output increases exponentially until the intensity associated with the lasing transition starts to affect the kinetics. The intensity at which the gain is reduced to 1/2 the small-signal-gain value is referred to as the saturation intensity I_{sat}. For transitions between excited states, one can often neglect the effect of the intensity on the lower laser state population in calculating saturation.[4] In this case, I_{sat} is the intensity that causes the upper laser state to be reduced by a factor of 2. This is found by equating the stimulated rate out of the upper laser state with the total exit rate γ_{out} excluding stimulated processes. For lasing down to the ground state, one cannot neglect the effect of the intensity on the lower laser state for two reasons. First, electrons stimulated out of the upper laser state accumulate in the lower state. Second, the population inversion at the time of maximum gain is not large which results in the gain being sensitive to the population in the lower laser state. We first show how to calculate I_{sat} neglecting fine-structure levels and then discuss the role of fine structure in H-like and Li-like ions.

In treating the situation where the lower laser state cannot be neglected, we introduce a parameter α whose value will depend on the populations and statistical weights of the lasing levels. We equate the net stimulated emission out of the upper laser state to α times γ_{out},

$$\frac{c^2}{2h\nu^3}A_{ul}\left(1-\frac{N_l' g_u}{N_u' g_l}\right)J_{sat} = \alpha\gamma_{out}, \tag{1}$$

where $(1 - N_l' g_u/N_u' g_l)$ is the population inversion factor, primes denote saturated values, g_u and g_l are the statistical weights of the upper and lower states, respectively, A_{ul} is the spontaneous emission rate, and J_{sat} is the specific (or per unit frequency) mean saturation intensity. The population of the upper level is reduced as a result of saturation because of the additional exit channel via stimulated emission. By equating the population outward flow without stimulated emission $N_u\gamma_{out}$ to the outward flow after saturation $N_u'\gamma_{out} + N_u'\alpha\gamma_{out}$, the saturated population can be expressed in terms of the population in the absence of stimulated processes as $N_u' = N_u/(1+\alpha) = \beta N_u$, where $\beta \equiv 1/(1+\alpha)$. Assuming that electrons that arrive in the lower state accumulate there, the saturated population in the lower state is $N_l' = N_l + (1-\beta)N_u$. This is usually a good approximation when the lower laser state is a ground state of the ion. We can solve for β by requiring that the gain calculated using N_u' and N_l' be 0.5 times the small-signal gain giving

$$\beta = \left[\frac{1}{2}\left(1+\frac{N_l g_u}{N_u g_l}\right)+\frac{g_u}{g_l}\right] / \left(1+\frac{g_u}{g_l}\right). \tag{2}$$

Using this expression for β and then α from $\alpha = 1/\beta - 1$, we obtain J_{sat} from Eq. (1). The saturated intensity is then given by $I_{sat} = \Delta\nu J_{sat}(2\pi^3/ln2)^{1/2}$, where $\Delta\nu$ is the FWHM of the atomic line profile.

As an example of the effect of including the lower state, the choice $N_l g_u/N_u g_l = 1/2$ and $g_u/g_l = 2.25$ gives $\alpha = 0.09$. This results in a factor of 11 decrease in I_{sat} as compared with neglecting the role of the lower state in determining the intensity sufficient to saturate the laser. This ratio of the statistical weights corresponds to the $n = 3$ to $n = 2$ levels in a Li-like

ion neglecting fine structure. For lasing down to the ground state of a H-like ion from the first excited state, $g_u/g_l = 4$ and $\alpha = 0.05$ for the same amount of inversion. In general, the spacing between fine-structure levels is greater than the line widths and the effects of fine structure must be included in calculating saturation.

The assumption that the fine-structure levels are populated according to their statistical weights allows an easy estimate of the role of fine structure on saturation. We address the validity of this approximation in the next section. In Li-like ions, the $3d_{5/2} - 2p_{3/2}$ is the fine-structure transition between the $n = 3$ and $n = 2$ levels with the largest gain and therefore it reaches saturation first. The A_{ul} rate used in Eq. (1) is for this fine-structure transition, but we continue to use the shell-averaged or total exit rate γ_{out}. The population outward flow without stimulated emission is $N_{n=3}\gamma_{out} = 3N_u\gamma_{out}$, where N_u is the population of the $3d_{5/2}$ level which has 1/3 of the $n = 3$ population if the sublevels are populated according to their statistical weights. Equating this to the outward flow after saturation, $3N'_u\gamma_{out} + N'_u\alpha\gamma_{out}$, one obtains an expression for N'_u given by $N'_u = N_u/(1+\alpha/3) = \tilde{\beta}N_u$, where $\tilde{\beta} \equiv 1/(1+\alpha/3)$. Assuming the $n = 2$ levels are populated according to their statistical weights, 1/2 of the electrons stimulated out of the upper laser level accumulate in the $2p_{3/2}$ lower laser level. This gives $N'_l = N_l + 1/2(1-\tilde{\beta})N_u$ and solving for $\tilde{\beta}$ one obtains

$$\tilde{\beta} = \left[\frac{1}{2}\left(1 + \frac{N_l g_u}{N_u g_l}\right) + \frac{1}{2}\frac{g_u}{g_l}\right] / \left(1 + \frac{1}{2}\frac{g_u}{g_l}\right). \tag{3}$$

For $N_l g_u/N_u g_l = 1/2$ and $g_u/g_l = 6/4 = 1.5$, appropriate for the $3d_{5/2} - 2p_{3/2}$ transition, $\alpha = 0.5$. If the lower state is neglected in calculating saturation, $\alpha = 3$ because the stimulated rate acts only on the $3d_{5/2}$ population. Thus, including the lower state results in a factor of 6 decrease in I_{sat} for $N_l g_u/N_u g_l = 1/2$.

In H-like ions, the $2p_{3/2} - 1s_{1/2}$ transition has the largest gain and saturates first. The $2p_{3/2}$ level has 1/2 of the $n = 2$ population if the sublevels are populated according to their statistical weights and we have $N'_u = N_u/(1+\alpha/2) = \beta N_u$ and $N'_l = N_l + (1-\beta)N_u$. These are the same expressions as for the first case where fine structure is neglected with $\tilde{\beta}$ replacing β. The expression for β, Eq. (2), can be used for $\tilde{\beta}$ with $\alpha = 2(1/\beta - 1)$. For $N_l g_u/N_u g_l = 1/2$ and $g_u/g_l = 2$, appropriate for the $2p_{3/2} - 1s_{1/2}$ transition, $\alpha = 0.18$ which is a factor of 11 decrease as compared with neglecting the lower state population. For comparable population inversions, the $2p_{3/2} - 1s_{1/2}$ transition in H-like ions has a greater reduction in I_{sat}, associated with including the lower laser state, than the $3d_{5/2} - 2p_{3/2}$ transition in Li-like ions.

We calculate reasonable efficiencies for the $3d_{5/2} - 2p_{3/2}$ transition in Li-like Ne despite the short duration of lasing and the reduction in I_{sat} associated with the lower laser state being the ground state. In Fig. 1 we show the calculated efficiencies (output energy/input energy) at an electron density of 2.5×10^{20} cm^{-3} as a function of electron temperature T_e for three laser focal radii. The increase in efficiency as T_e decreases is because of more rapid recombination and collisional cascade to the upper laser level. The increase in efficiency with increasing radius comes from the assumption that the length of the lasing region is given by the confocal length $z = 4\pi a^2/\lambda ln2$, where λ is wavelength of the driving laser and a is the half-intensity focal radius. Refraction arising from transverse ionization gradients can limit the length of the laser and we are studying the effects of a preionized channel and imposed density gradients to control refraction. We have calculated efficiencies as high as 10^{-4} by using an electron density of 1.0×10^{21} cm^{-3} and an electron temperature of 50 eV.[2] A driving pulse with a duration of only 50 fs is required at this density to keep stimulated Raman scattering from heating the plasma above 50 eV.

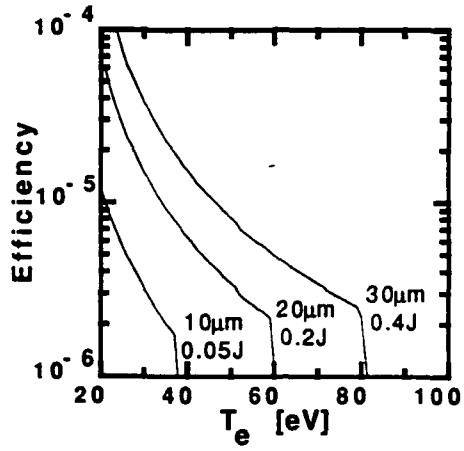

Figure 1: Efficiency versus temperature at an electron density of 2.5×10^{20} cm^{-3} for several values of focal radius and the corresponding input energy.

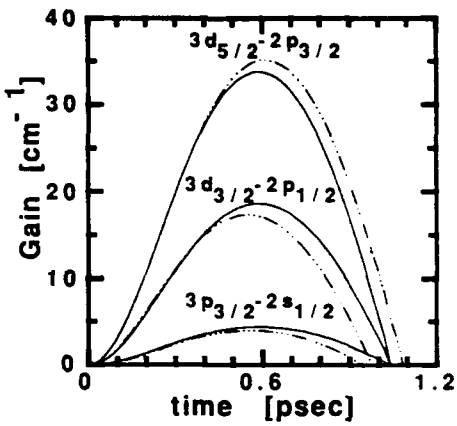

Figure 2: Small-signal gains calculated with independent sublevels (dashed curves) and with sublevels populated according to their statistical weights (solid curves).

III. Kinetic Issues for Lasing to Ground State

The efficiencies calculated for the $3d_{5/2} - 2p_{3/2}$ transition in Li-like Ne use a shell-averaged atomic physics model. The populations of the sublevels, in a given shell corresponding to a principle quantum number, are assumed to be proportional to the statistical weights of each sublevel. We discuss two issues that can affect the validity of this approximation for the $n = 2$ levels in Li-like Ne. (These issues also affect the $n = 3$ sublevels but to a lesser amount.) The first arises when the energy differences between the sublevels is not much less than the electron temperature. The second occurs when a given fine-structure transition becomes saturated and a large fraction of the population flow between shells is carried by that transition. We study these issues by comparing shell-averaged results with those obtained using a detailed atomic model that allows independent sublevels.

The assumption that the sublevels are populated according to their statistical weights assumes that $\Delta E_{\max} \ll kT_e$, where $E_{\max}$ is the maximum energy difference between any of the sublevels. In the collisional limit, the ratio of populations is $n_j/n_i = (g_j/g_i)\exp(-\Delta E_{ij}/kT_e)$. The $2p_{3/2}$ and $2p_{1/2}$ levels have energies approximately 16 eV greater than the $2s$ level giving a Boltzmann factor $e^{-\Delta E/kT}$ between the $2p$ levels and the $2s$ level of 0.7 for a representative temperature from Fig. 1 of 40 eV. The $n = 2$ shell is primarily populated by radiative transitions into the $2p$ sublevels from the $3d$ sublevels. The $2s$ sublevel is populated radiatively from the $3p$ sublevels and collisionally from the $2p$ sublevels. These $\Delta n = 0$ collisions try to keep a Boltzmann population distribution among the sublevels. The electron collision rate between $2p_{3/2}$ and $2s$ is approximately a factor of 2 larger than that between $2p_{1/2}$ and $2s$. Ion collisions are included in our calculations but do not play an important role. The result of all these processes is that at the time of maximum gain the $2p_{3/2}$ level is slightly underpopulated compared with the other $n = 2$ levels accounting for statistical weights but not as much as predicted by the Boltzmann factor. The effect of this on gains is shown in Fig. 2 where gains

for three fine-structure transitions are shown for an electron density of 2.5×10^{20} cm^{-3} and an electron temperature of 40 eV. The dashed curves are for independent sublevels and the solid curves are the gains if the sublevels are populated according to their statistical weights. The $3d_{5/2} - 2p_{3/2}$ transition has a slightly higher gain when sublevels are treated independently primarily because of the reduced $2p_{3/2}$ population giving a larger inversion ratio.

Saturation by the $3d_{5/2} - 2p_{3/2}$ transition selectively populates the $2p_{3/2}$ level because a large fraction of the population flow between the $n = 3$ and $n = 2$ levels to pass through this transition. We find that the saturated gain using independent sublevels is often slightly smaller than the saturated gain obtained by assuming levels are populated statistically. Thus, the two effects we describe act in different directions on the $2p_{3/2}$ sublevel. The general conclusion is that the assumption of statistical population between the sublevels is appropriate.

IV. Summary

We have shown the importance of including the lower laser level in calculations of saturation when that level is the ground state of an ion. We have calculated efficiencies of 10^{-5} to 10^{-4} for the $3d_{5/2} - 2p_{3/2}$ transition at 98 Å in Li-like Ne. The assumption that the fine-structure levels are populated according to their statistical weights is shown to be justified.

Acknowledgments

This work was performed under the auspices of the U.S. Department of Energy by the Lawrence Livermore National Laboratory under contract number W-7405-ENG-48.

References

1. N. H. Burnett and G. D. Enright, "Population Inversion in the Recombination of Optically Ionized Plasmas", IEEE J. Quant. Electron. **QE-26**, 1797 (1990).

2. P. Amendt, D. C. Eder, and S. C. Wilks, " X-Ray Lasing by Optical-Field-Induced Ionization", Phys. Rev. Lett. (in press).

3. B. M. Penetrante and J. N. Bardsley, "Residual Energy in Plasmas Produced by Intense Subpicosecond Lasers", Phys. Rev. A **43**, 3100 (1991).

4. R. A. London, "Beam Optics of Exploding Foil Plasma X-Ray Lasers", Phys. Fluids **31**, 184 (1988).

Radiation Cooling in Photopumped C VI Inversion

Ricardo A. Pakula

Department of Physics, Lehigh University, Bethlehem, Pennyslvania 18015

Abstract

Radiation cooling as a means to reach inversion in photoionized C VI is analyzed in the context of energy transfer between excited ions and free electrons.

Introduction

The idea of generating inversion and gain by photo-ionization followed by three-body recombination was first stated by Bunkin [1] et al., and further analized by Goodwin and Fill [2]. The application of this scheme for the specific case of a hydrogen-like C VI plasma, exposed to the soft x-ray emission of a titanium-laser-produced plasma was considered in Refs. 3 and 4. Necessary conditions for the achievement of inversion are a low plasma temperature ($\sim$ 10 eV), and a high electron density ($\sim 10^{19}$ cm^{-3}). Both are required for the establishment of a strong collisional-recombination regime, favouring the cascading of electrons towards the upper excited levels, leaving the lower levels almost unpopulated. Radiative cooling was originally proposed as a means to reach the desired temperature in similar recombination schemes [5], however posterior work has shown that this regime was not attainable for low-Z materials [6]. In this paper we consider in detail the hypothesis of radiative cooling for the case of C VI pumped by the Ti-plasma.

We have developed a numerical code that solves the rate equations for all ionization stages, electron temperature and density, and the first 6 excited levels of C VI for an initially cold carbon-gas in the presence of the Ti-emission. The x-ray emission is assumed to have the same spectral distribution as in Ref. 7, with a temporal dependence in the form of $[\sin(\pi \frac{t}{\tau})]^2$, τ = 20 ns, and normalized to an average laser intensity of 10^{12} W/cm^2. The rate coefficients were taken from published data and hydrogen-like models and the linewidth for the lasing transitions were estimated from values given in Refs. 2, 8 and 9.

Proceedings on Short-Wavelength Coherent Radiation, 101
Vol. 11, Philip H. Bucksbaum and Natale M. Ceglio (eds.)
© 1991 Optical Society of America

Perfect coupling between radiation and electron temperature

In order to simulate the behavior of radiative cooling, we have first assumed that each radiative transition modifies directly the free electron temperature: every time a photon is absorbed by the C-ions, its energy is added to the electron energy, and every time a photon is emitted, the electron energy is decreased by this amount. This model seems reasonable in quasi-equilibrium regimes, where population unbalances are rapidly compensated through inelastic collisions, and the free electrons act as an energy reservoir. On the other hand, under the extremely nonequilibrium conditions of this problem, it is not clear *a priori*, if this model can be considered a good approximation.

The results following this assumption are presented In Figs. 1 and 2. It can be seen that after 10 ns the plasma is almost fully stripped and the electron temperature reaches a maximum of 65 eV. With the decay of the laser intensity, radiative cooling sets in, and after the laser is switched off, the temperature drops so fast, that a transient inversion of almost 10^{16} cm^{-3} is predicted for the $3 \rightarrow 2$ transition, in less than 1 ns, generating a gain of more than 10 cm^{-1}.

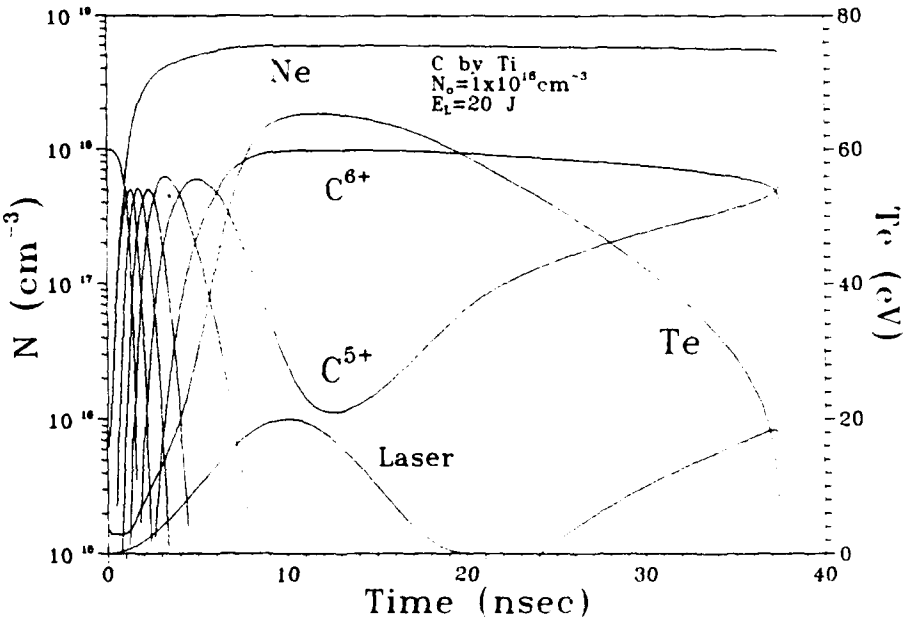

Figure 1. Density N for the different ionization stages of carbon; electron density Ne; electron temperature Te; and pumping pulse for an initial neutral carbon density of 1×10^{16} cm^{-3}. Radiative processes are directly coupled to the energy equation.

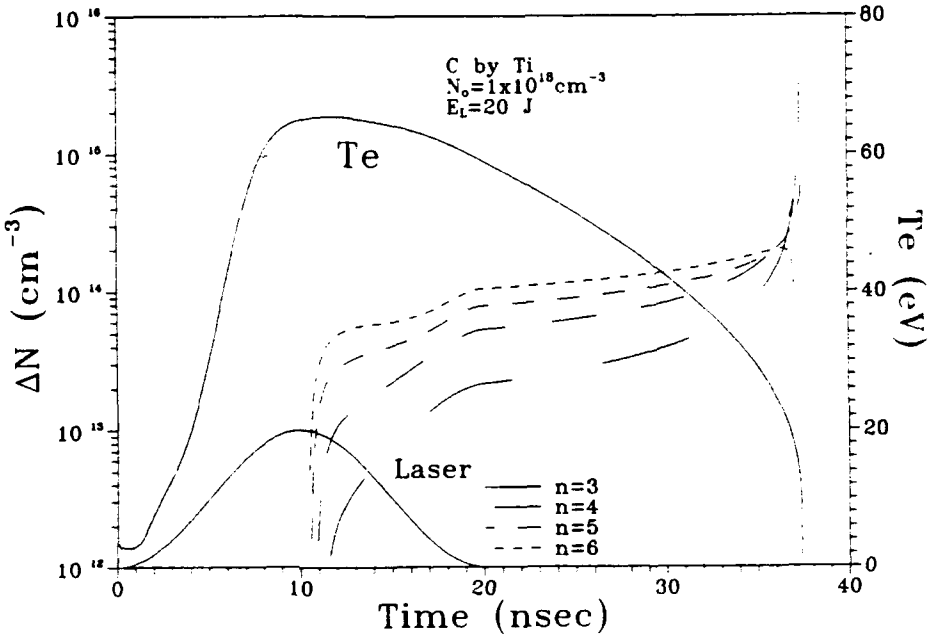

Figure 2. Inversion density ΔN between upper excited states of C VI respect to the n = 2 level; and electron temperature Te for the same case as Fig. 1.

Collisional coupling between electrons and ions

As a second step we have solved the more realistic case where changes in the free electron energy are allowed only through inelastic collisions with the ionic species. This has the effect of producing a weaker coupling between radiative transitions and changes in the electron temperature. The energy difference remains as excitation (or potential) energy of the ionic systems. As can be seen in Figs. 3 and 4, the cooling effect is less pronounced, and stops around 10 eV, when the population of excited levels of C VI disappears. However, the same decoupling is responsible for the decrease in the electron temperature to a maximum of 15 eV, even while the laser is on. Due to the overall lower temperature, a steady inversion is generated with a value of 10^{16} cm^{-3} (and a gain of 10 cm^{-1}) over more than 5 ns, which is more suitable for practical purposes.

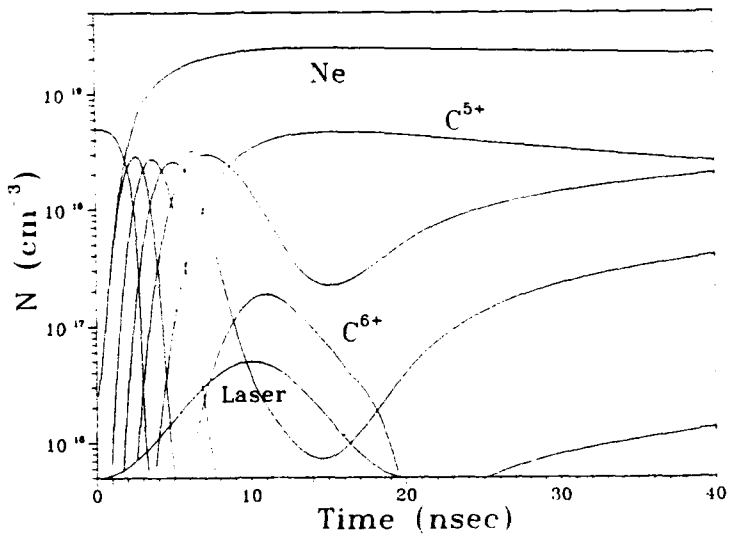

Figure 3. Density N for the different ionization stages of carbon; electron density Ne; and pumping pulse for an initial neutral carbon density of 5×10^{18} cm^{-3}. Only collisional transitions are coupled to the energy equation. After Ref. 4.

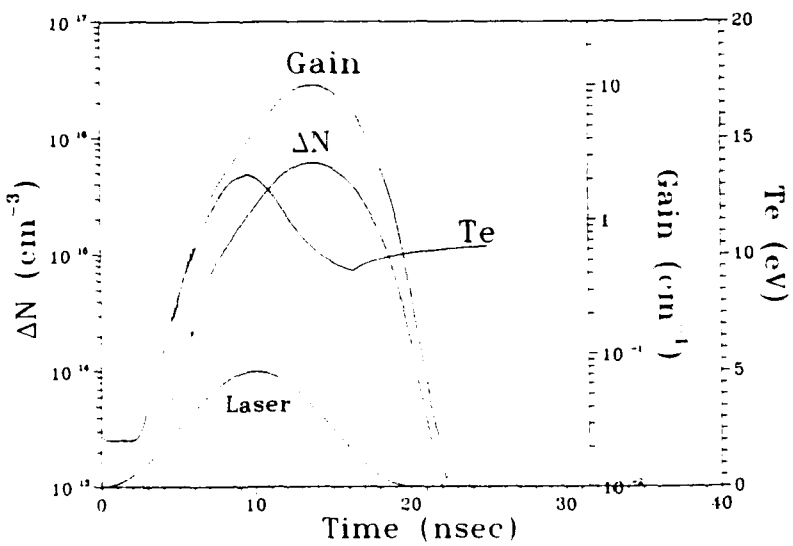

Figure 4. Inversion density ΔN between the second (n = 3) and first (n = 2) excited states of C VI; electron temperature Te; and gain for the 182 Å line for the same case as Fig. 3. After Ref. 4.

Conclusions

We conclude that radiative cooling is not effective for this scheme, but at the same time is not needed. Indeed the inertia associated with the energy transfer to free electrons, allows the plasma to remain at the desired temperature for all times.

References

1. F.V. Bunkin, V.I. Derzhiev, and S.I. Yakovlenko, "Specification for pumping x-ray laser with ionizing radiation," Sov. J. Quant. Electron. 11, 971 (1981).

2. D. Goodwin and E. Fill, "Inversion and gain in hydrogenic levels induced by photoionization pumping," J. Appl. Phys. 64, 1005 (1988).

3. R.A. Pakula, "Radiation-pumped C VI population inversion," Bull. Am. Phys. Soc. 34, 1915 (1989).

4. R.A. Pakula, "Radiation pumped C VI lasing scheme," J. Optical Soc. Am. 8, 639 (1991).

5. S. Suckewer and H. Fishman, "Conditions for soft x-ray lasing action in a confined plasma column," J. Appl. Phys. 51, 1922 (1980).

6. C. Keane and S. Suckewer, "Soft x-ray population inversions in radiatively cooled carbon/aluminum plasmas," preprint UCRL 102111 (Lawrence Livermore National Laboratory, Livermore, Calif., 1989).

7. K. Eidmann and T. Kishimoto, "Absolutely measured x-ray spectra from laser plasmas with targets of different elements," Appl. Phys. Lett. 49, 377 (1986).

8. D. Oza, R. Greene, and D. Kelleher, "Stark broadening of Hα and Hβ lines of C^{5+}," Phys. Rev. A 34, 4519 (1986).

9. H.R. Griem, "Line profiles of soft x-ray laser gain coefficients," Phys. Rev. A 33, 3580 (1986).

Progress Toward the Development of a Compact Capillary Discharge Soft-X-Ray Laser

J. J. Rocca, M. C. Marconi, B. T. Szapiro, and J. Meyer

Department of Electrical Engineering, Colorado State University, Fort Collins, Colorado 80523

ABSTRACT

The possibility of developing a soft X-ray recombination laser in a capillary discharge plasma is being investigated. Soft X-ray emission spectra of highly ionized carbon plasmas generated by two excitation regimes in 1 mm diameter polyethylene capillaries are discussed. A 50 kA, 108 ns FWHM discharge produced a dense ($1*10^{19}$ cm^{-3}) plasma in which intense CVI emission is only observed shortly after the peak of the current pulse. In contrast, the first time resolved spectra from a fast 25 ns FWHM, 90 kA discharge pulse, showed strong CVI 18.2 nm emission also at the end of the first half cycle of the current pulse. This new fast discharge, which is capable of generating 150 kA current pulses through 2 cm long capillaries was designed to produce larger CVII density and shorter excitation fall time, to explore the possible occurrence of soft X-ray amplification.

INTRODUCTION

Significant success has been achieved in the last several years in pumping soft X-ray lasers with high energy lasers [1-3]. We have proposed the development of smaller soft X-ray recombination lasers based on direct discharge excitation of a capillary plasma with a fast current pulse [4,5]. Capillary discharges are known to generate dense highly ionized plasmas [6-9] with good axial uniformity due to the stabilizing effect of the capillary walls. In this laser scheme a dense and highly ionized plasma core with a large length-to-diameter ratio is created by a fast discharge pulse. Subsequent rapid plasma cooling by electron heat conduction to the capillary walls and plasma radiation results in the recombination of highly ionized species into ions of lower charge, and could possibly create population inversions and amplification of soft X-ray radiation.

Proceedings on Short-Wavelength Coherent Radiation, 106
Vol. 11, Philip H. Bucksbaum and Natale M. Ceglio (eds.)
© 1991 Optical Society of America

Of particular interest are the 3-2 transitions in hydrogenic ions in which large amplification has already been demonstrated in laser created plasmas [1,10,11]. In previous experiments with a 5 J lithium hydride capillary discharge, we observed increased excitation of the 3-2 transition in LiIII at 72.9 nm towards the end of the current pulse, an indication that this transition was excited by collisional recombination [9]. Scaling of the experiment to carbon is predicted to produce gains of the order of 5 cm^{-1} in the 18.2 nm line of CVI [4]. Recently, Steden and Kunze studied the emission of low energy, low voltage (≤12 J, ≤16 kV) polyacetal capillaries and reported the observation of short bursts of radiation at 18.2 nm coincident with the peak of the second half cycle of the current pulse. This phenomenon was attributed to amplified spontaneous emission [12]. Our experiments with a similar polyacetal discharge have not been able to detect these burst of radiation. Weak CVI emission was observed only during the first half cycle of the current pulse.

In this paper we discuss the results of soft X-ray emission spectroscopy experiments in carbon plasmas created by a 40 kV capillary discharge having a FWHM pulsewidth of 108 ns, and present the first results obtained with a fast, high voltage (25 ns, ≤800 kV) capillary discharge designed to produce the initially hot and rapidly cooled plasmas required to investigate the possible occurrence of soft X-ray recombination lasing.

CVI SOFT X-RAY EMISSION FROM A 40 kV, 100 ns POLYETHYLENE DISCHARGE

The soft X-ray emission from 0.5-1 mm diameter polyethylene capillaries excited by discharge current pulses of up to 60 kA and 108 ns FWHM pulsewidth was studied using the compact capacitive discharge setup shown in figure 1.

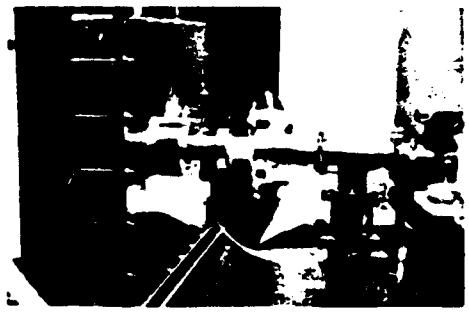

Figure 1. Photograph of 100 nF, 40 kV capillary discharge setup.

It consists of a disk of thirty two 40 kV ceramic capacitors of 3.3 nF each placed in the perimeter of a rectangle having as center the capillary axis. The capacitors are directly connected to the capillary electrodes by a parallel plate transmission line forming a circuit with a total inductance of 23 nH. The discharge switch is the capillary itself, and discharge initiation is achieved by flashover on the capillary inner walls when a secondary trigger discharge is fired in the proximity of the cathode. The soft X-ray emission exiting one of the hollow discharge electrodes was analyzed with a 1 m grazing incidence vacuum spectrograph utilizing either a 1200 lines per mm or a 300 lines per mm gold coated grating. The instrument contains a multichannel plate intensified array detector which can be gated to obtain temporally resolved spectra with 5 ns resolution.

For excitation currents above 35 kA, CVI lines are observed to dominate the soft X-ray spectra. Strong 18.2 nm CVI emission is observed in the time integrated spectra of figure 2, which corresponds to the axial emission from a 1 mm diameter polyethylene capillary excited with a 50 kA current pulse.

A collisional-radiative ionization balance calculation based on the rate coefficients of Kolb and Lupton [13] shows that for CVI to be the dominant specie, as is observed in the higher current discharges, the electron temperature must reach a value of more than 70 eV in the hottest region of the plasma, located in the axis of the discharge. This hot plasma core is likely to be surrounded by a cooler and denser plasma region near the capillary walls, which act as a heat sink and introduce cold ablated material into the discharge.

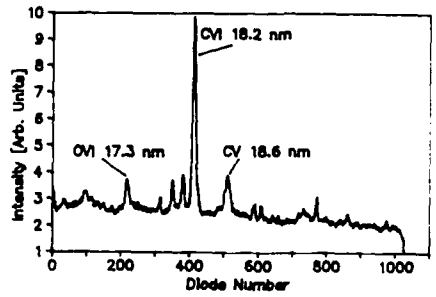

Figure 2. Time integrated spectrum of a 1 mm diameter, 1cm long polyethylene capillary excited by a 50 kA, 108ns FWHM current pulse. A 300 lines/mm grating was used.

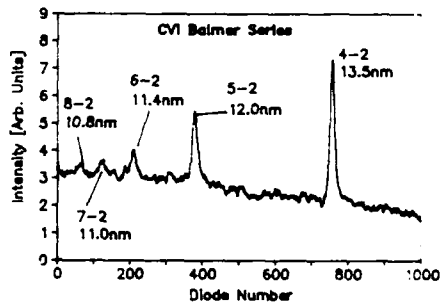

Figure 3. Spectrum of the CVI Balmer series of a 1mm diameter polyethylene discharge excited by a 50 kA, 108ns FWHM current pulse. A 1200 lines/mm grating was used.

Figure 3 shows the lines of the CVI Balmer series originated from levels n=4 to n=8 for the same discharge conditions of fig.2. The increased linewidth of the shorter wavelength transitions is caused by Stark broadening. The corresponding electron density was calculated to be approximately $1*10^{19}$ cm^{-3}. This value of the electron density is close to the optimum required for amplification of the 18.2 nm line of CVI by collisional recombination.

The temporal evolution of the intensity of the axial emission in the 14-24 nm spectral region was also studied and is shown in figure 4. The maximum intensity of the CVI Balmer α transition occurs shortly after the peak of the current pulse and its intensity rapidly decreases as the current drops. The maximum intensity of the CV lines occurs later in time, as it might be expected from collisional recombination of CVI ions. The emission of CVI transitions observed during the current pulse can be attributed, in principle, to collisional excitation. However, it is possible for part of the observed CVI emission to be created following the collisional recombination of CVII ions that diffuse from the hot plasma core into the cooler and denser boundary plasma. The low electron temperature (10-16 eV) that results from a Boltzmann plot of the intensities of the CVI Balmer series lines of fig.3 supports this possibility, since it is significantly lower than the temperature required to excite the observed CVI transitions. Nevertheless, no gain has been observed in comparing the intensity of the 18.2 nm line with other CVI transitions for 1cm and 2cm long capillaries in this device.

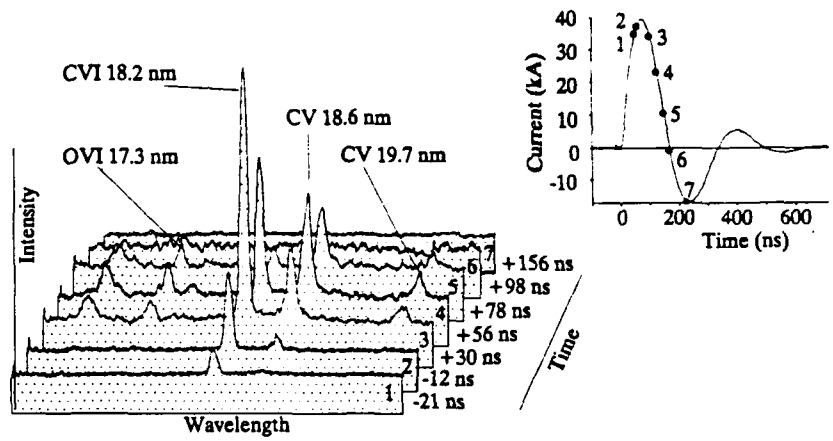

Figure 4.Time resolved 14-24nm spectra of a 1mm diam. polyethylene capillary excited by a 40 kA, 108ns FWHM current pulse. The time of each spectrum relative to the peak of the current pulse is indicated.

HIGH POWER DENSITY, SHORT PULSE CAPILLARY DISCHARGE

To generate initially hotter and more rapidly cooled plasmas, we have developed a fast high power density discharge. This new discharge consists of a circular plate transmission line charged by a 800 kV Marx generator and connected to the capillary load through a SF_6 switch. The setup is schematically illustrated in figure 5. When ethylene glycol is used as dielectric, the capacitance is 3 nF and peak currents in excess of 150 kA can be generated through 1 mm diameter, 1-2 cm long capillaries, with a first half cycle FWHM pulsewidth of 25 ns. The device has so far been

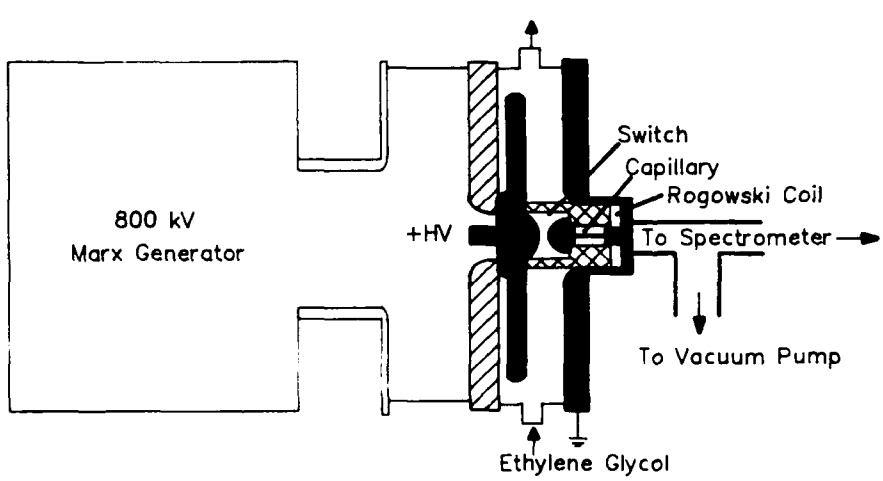

Figure 5.Diagram of high power density fast capillary discharge.

tested at voltages up to 600 kV, producing a current pulse of 140 kA through the capillary load.

The first experiment with such high power density capillary discharge has been conducted in a 1 mm diameter polyethylene capillary. Figure 6 is a time resolved spectrum of a 92 kA discharge corresponding to the end of the first half cycle of the current pulse. In contrast with the slower discharge discussed in the previous section, the current pulse decay time is shorter than the CVII recombination time and intense CVI emission at 18.2 nm is detected at the end of the first half cycle of the current pulse. Gain measurements for different capillary geometries and excitation conditions will be conducted changing the capillary length.

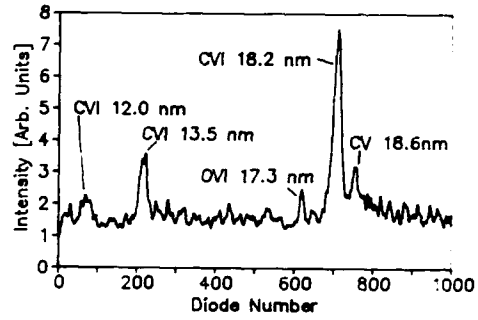

Figure 6.Time resolved spectrum of a 1mm diam., 1cm long, polyethylene discharge at the time of the end of a 25 ns FWHM current pulse.

ACKNOWLEDGMENTS

We acknowledge the collaboration of D.Cortazar,O.Buccafusca and K.Richardson in the design and construction of the capillary discharges. This work was supported by the U.S. D.O.E. Advanced Energy Projects of Basic Energy Sciences Grant DE-F602-91ER12110 and by the National Science Foundation Grant ECS 9013372.

REFERENCES

1. S.Suckewer, C.H.Skinner, H.Milchberg, C.Keane and D.Voorhes. Phys. Rev. Lett., 55, 1753, (1985).
2. D.L.Matthews et al.Phys. Rev. Lett. 54, 110, (1985).
3. T.N.Lee, E.A.McLean and R.C.Elton, Phys. Rev. Lett. 59, 1185, (1987).
4. J.J.Rocca, D.C.Beethe and M.C.Marconi. Opt. Lett., 13, 565, (1988).
5. J.J.Rocca, M.C.Marconi, D.C.Beethe and M.Villagran Muniz. OSA Proc. on "Short Wavelength Coherent Radiation: Generation and Applications". Ed. R.W. Falcone and J.Kirz. Vol.2, pag. 99, (1989).
6. P.Bogen,H.Conrands,G.Gatti and W.Kohlhaas. J. Opt. Soc. Am. 58, 203, (1968).
7. R.A. McCorkle, Appl. Phys. A, 26, 261, (1981).
8. S.M. Zakharov, A.A. Kolomenskii, S.A.Pikuz and A.I.Samokhin. Sov. Tech. Phys. Lett. 6, 486, (1980)
9. M.C.Marconi and J.J.Rocca. Appl. Phys. Lett., 54, 2180, (1989).
10. C.Chenais-Popovics, R.Corbett, C.J.Hooker, M.H.Key, G.P.Kiehm, C.L.S. Lewis, G.J.Pert, C.Regan, S.Sadaat, T.Tomie and D.Willi. Phys. Rev. Lett., 59, 2161, (1987).
11. H.Azuma, Y.Kato, K.Yamakawa, T.Tachi, M.Nishio, H.Shiraga, S.Nakai, S.A.Ramsden, G.J.Pert and S.J.Rose. Opt. Lett. 15, 1011, (1990).
12. C.Steden and H.Kunze. Physics Letters A, 151, 534, 1990.
13. In "Spectral Intensities" by R.W. McWirter, pag.222 in Plasma Diagnostic Tech. Ed. R.Heddlestone and S.Leonard. Acad. Press,New York, (1965).

Longitudinal Pumping by an Ellipsoidal Reflector for Short-Wavelength Lasers

Katsumi Midorikawa and Hideo Tashiro

Riken, The Institute of Physical and Chemical Research, 2-1 Hirosawa, Wako-shi, Saitama 351-01, Japan

Toshihisa Watabe and Minoru Obara

Department of Electrical Engineering, Keio University, 3-14-1 Hiyoshi, Kohoku-ku, Yokohama 223, Japan

Abstract

We have designed and tested an ellipsoidal reflector to pump short-wavelength lasers by broadband soft-x-ray radiation from laser-produced plasmas. Xenon gas supplied by a pulsed gas valve with a slit nozzle, which was placed in the vicinity of the second focus, was irradiated longitudinally along the optical axis. Soft x-ray absorption and VUV emission resulted from the 4d inner-shell excitation was investigated.

Introduction

A wide variety of excitation schemes for short-wavelength lasers operating below 1000 Å have been investigated extensively. Photoionization pumping through inner-shell processes is one of the promising methods to produce a spatially uniform gain.[1] In this method, being different from the plasma

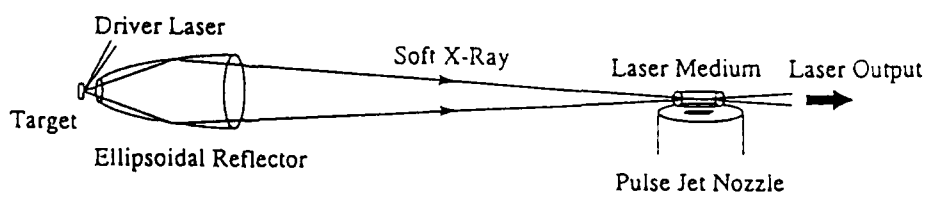

Fig. 1 Schematic drawing of longitudinal pumping by an ellipsoidal reflcetor.

Proceedings on Short-Wavelength Coherent Radiation, 111
Vol. 11, Philip H. Bucksbaum and Natale M. Ceglio (eds.)
© 1991 Optical Society of America

method accompanied with high density and highly ionized plasmas, it can create population inversion in low ionized or neutral atoms[2,3] if a sufficient pumping radiation is supplied. A laser-produced plasma is excellent as a soft-x-ray source because of high energy conversion efficiency and short time duration. An important issue in the optical pumping scheme is how to collect and focus the incoherent soft x-ray to a lasing medium. The end-pumping geometry using an ellipsoidal reflector,[4,5] of which schematic drawing is shown in Fig.1, have some advantages for the short wavelength laser pumping. First, it can separates a lasing medium from the plasma source so that the harmful collisional interaction with particles out of the plasma source can be avoided. Secondly, it also allows a traveling wave excitation which is essential for short wavelength lasers.[6]

In this paper we describe experimental results on soft-x-ray pumping by an ellipsoidal reflector. The reflectivity and focusability of the reflector were measured with soft-x-ray radiation from a laser produced plasma. The absorption spectrum of Xe gas was also investigated from 100 to 300 Å region. Feasibility of longitudinally pumped short wavelength laser by means of an ellipsoidal reflector is discussed.

Design and Performance of an Ellipsoidal Reflector

There are no materials which have high reflectivity at a normal incidence in soft-x-ray region. At a grazing angle of incidence, however, high reflectance can be achieved on some metal surfaces. In the case of gold surface, reflectivity more than 30% for the 100 Å radiation is achieved at a grazing angle smaller than 25 degree.[7] In addition to high reflectivity, a grazing incidence reflector using a metal surface provides superior properties than multilyer reflectors: 1) damage resistance of a metal surface to the optical radiation is much higher, 2) no wavelength selectivity results in broadband reflection, which is suitable for photoionization pumping, 3) fabrication by means of diamond turning can supply relatively large reflector.

The collection efficiency of an ellipsoidal reflector is dependent on its configuration expressed by the ratio of the minor to the major axis. The magnification of the plasma source is also directly related to the ratio of the axes. Considering these factors into account, the ratio of the minor to the major axis was determined to be 0.1. A focal length, that is, dimen-

Table 1 Design parameters of an ellipsoidal refrector for wavelength longer than 100 Å

Base Material	Al
Surface Material	Au(Ni)
Major Axis	40 cm
Minor Axis	4 cm
Foal Length	79.6 cm
Surface Roughness	< 30 Å
Reflectivity (at 100 Å)	30%

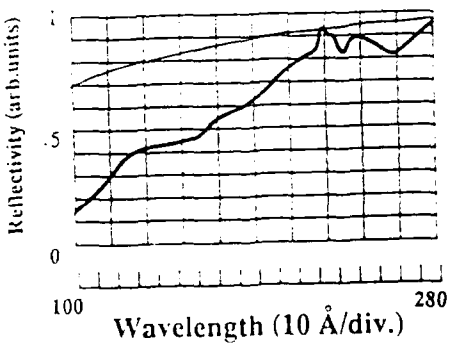

Fig. 2 Relative reflectivity of an Ni reflector for soft-x-ray region.

sions of the reflector was imposed restriction due to both a diamond turning machine and the space for a plasma source and was fixed at 80 cm. A useful region of the reflector is the sections shorter than a quarter of the focal length measured from the first focus. Moreover, in order to introduce a plasma source at the first focus, the edge section surrounding the focus should be removed. After all, the section from 9.5 mm to 200 mm measured from the edge of the reflector along the major axis was used. These positions correspond to the grazing angles of 25 to 6.6 degrees, respectively. For the designed configuration, relectivityof more than 30% was estimated for wavelength longer than 100 Å by using the straight-line approximation to the data taken from Ref.7

For nonimaging application, surface accuracy is not so important, compared to surface roughness which affects scattering of the radiation. Rayleigh's criterion gives requirement of the roughness of less than 30 Å or the 100 Å radiation. Table 1 lists the design parameters of the ellipsoidal reflector for wavelength longer than 100 Å radiation.

Although a gold surface has high reflectivity for wavelength longer than 100 Å,[7] problems caused by evaporation process degraded the surface quality. Therefore, we changed the surface material for Ni because it could be directly manufactured by diamond turning. Direct measurement of the surface roughness of the Ni reflector fabricated by diamond turning showed that averaged and peak-to-valley values of the surface roughness were 30 and 150 Å, respectively. The measurement of the reflectivity in soft-x-ray region was done by a laser-produced-plasma source, of which setup is described below. Shown in Fig.2 is the relative reflectivity from 100 to 280 Å. Compared to the theoretical value for Au surface, the measured reflectivity for Ni surface rapidly deceases for wavelength shorter than 200 Å. This is mainly due to difference of the material.

Experimental

The experimental arrangement for soft-x-ray aborption measurement of Xe is shown in Fig.3. The laser plasma was produced by introducing a 100-ps, 60-mJ Nd:YAG laser pulse onto gold rotating-disk target. The target was set close to the edge of the reflector so that the laser pulse was focused at the first focus of the ellipsoid. The focal spot size was 100 μm, which gave the intensity of 2 x 10^{11} W/cm^2. Black body radiation from the laser produced plasma was collected and focused to the second focus of the ellipsoid where a pulsed Xe gas was supplied

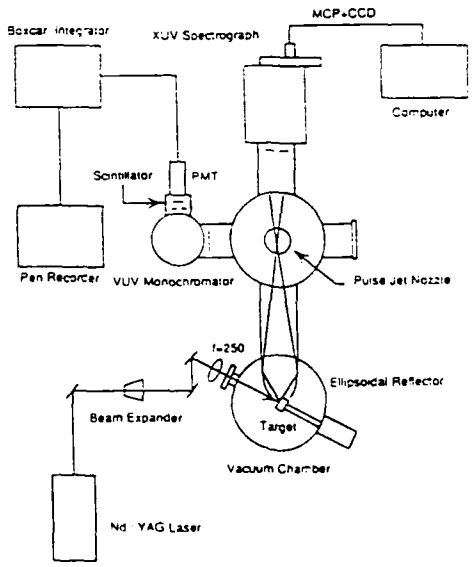

Fig. 3 Experimental setup for soft-x-ray pumping by an ellipsoidal reflector.

from a slit nozzle. The nozzle locates at 5 mm below the second focus and has a .5 x 50 mm^2 aperture. When Xe gas was supplied synchronously with the YAG laser pulse, visible fluorescence colored dark blue was observed through a window of the chamber. By taking a picture of this fluorescence, a focused column volume was estimated to be 2 mm diameter x 50 mm length

The time integrated absorption spectrum was monitored by an XUV spectrograph set along the optical axis. The XUV spectrograph consists of a variable-spacing grating, microchannel plates and CCD. The results are shown in Fig.4. Figure 4(c) shows the absorbed spectrum, which is obtained by subtracting the spectrum with Xe (Fig.4(b)) from without Xe(Fig.4(a)). The large peak around 150 Å is due to the 4d innershell absorption.[8] The absorption due to the 5s electorn gradually increases from 200 Å. Two peaks at 185 and 190 Å correspond to the resonant absorption to the Rydberg states, $4d^9 5s^2 5p^6 6p(^2D_{3/2})$ and $(^2D_{5/2})$, respectively.[9,10] Number density of Xe in the interaction region was calculated by the absorbed spectrum and photo absoption cross sections taken from Ref.4. The density was 5 x 10^{16} cm^{-3}.

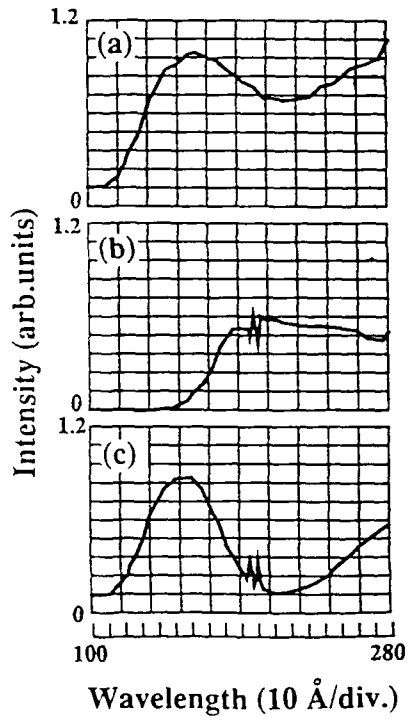

Fig. 4 Photoabsorption spectrum of Xe: (a) without Xe, (2) with Xe, (c) absorbed spectrum.

VUV fluorescence from the excited colum was measured by VUV monochromator which was placed perpendicular to the optical axis. The VUV fluorescence was converted to UV light by a P-terphenyl scintilator and detected by a photomultiplier. The fluorescence signal is shown in Fig. 5. The peak locates at 109 nm, which corresponds to the XeIII $5s^0 5p^{61}s_0$-$5s^1 5p^{51}p_1$ transition resulted from the Auger decay of the 4d electron removal.[11-13] Although we investigated gain of the 109 nm line by replacing the axial XUV spectrograph by VUV spectrograph covering from 80 to 120 nm, a conspicuous peak did not appear around 109 nm so that we could not obtain the gain.

Discussion

In this scheme, black body radiation from a plasma source so strong that the signal line along the optical axis is buried. Intensity of the 109 nm radiation from the plasma source was estimated to be 3 x 10^5 kW/cm^2 in 5 Å bandwidth, assuming the conversion efficiency of 3% and a black body temperature of 20 eV. This intensity level is same as the signal intensity obtained for the gain-length product of 9, which is close to the theoretically estimated vale of 10. Another reason why we could not measure the gain seems to be the lack of

pumping power of soft x-ray, because lower reflectivity of the Ni surface below 200 Å region and lower soft-x-ray generation efficiency for a 100-ps YAG laser would decrease the pumping flux.[14,15] Annular focusing pattern also makes it difficult to find the gain direction along the optical axis. Therefore, to obtain uniform gain column, we tried quartz optical guide[16,17] of which diameter and length were 2 and 50 mm, respectively. However, little improvement was recognized.

In summary we have investigated longitudinal pumping of Xe inner-shell excitation by an ellipsoidal reflector. The reflectivity in the soft-x-ray region and focusability were measured by a laser produced plasma. The 109 nm fluorescence resulting from the soft-x-ray absorption by the 4d electron was observed. Use of gold surface for the reflector and increase of a pumping laser energy will increase soft-x-ray power, which will result in a large gain-length product. The soft x-ray filter cutting VUV radiation will be also useful.

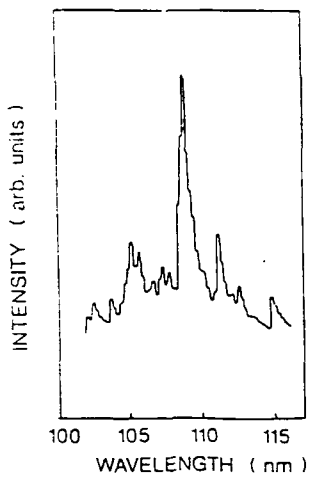

Fig. 5 VUV fluorescence from Xe by soft-x-ray pumping.

References

1. R. C. Elton, *X-ray Laers*, (Academic Press, Sandiego, London, 1990) Capt. 5.
2. W. T. Silfvast and O. R. Wood II, J. Opt. Soc. Am B4, 609(1987).
3. H. C. Kapteyn and R. W. Falcone, Phys. Rev. A37, 2033(1988).
4. J. S. Pearlman and R. F. Benjamin, Appl. Opt. 16, 94(1977).
5. J. F. Young, J. J. Macklin, and S. E. Harris, Opt. Lett. 12, 90(1987).
6. M. H. Sher, J. J. Macklin, J. F. Young, and S. E. Harris, Opt. Lett. 12, 891(1987).
7. R. F. Malina and W. Cash, Appl. Opt. 17, 3309(1978).
8. J. Berkowitz, *Photoabsorption, Photionization, and Photelectron Spectroscopy*, (Academic Press, New York, London, 1979) Chap. V.
9. G. C. King, M. Tronc, F. H. Read, and R. C. Bradford, J. Phys. B: At. Mol. Phys. 10, 2479(1977).
10. W. Eberhardt and G. Kalkoffen, Phys. Rev. Lett. 41, 156(1978).
11. H. Hertz, Z. Physik A, 289(1975).
12. J. E. Hansen, F. G. Meijer, M. Outred, W. Persson, and H. O. Di Rocco, Physica Scripta. 27, 254(1983).
13. H. C. Kapteyn, R. W. Lee, and R. W. Falcone, Phys. Rev. Lett. 57, 2939(1986).
14. G. Yu. Yin, C. P. J. Barty, D. A. King, D. J. Walker, S. E. Harris, and J. F. Young, Opt. Lett. 12, 331(1987).
15. O. R. Wood, II, W. T. Silfvast, H. W. K. Tom, W. H. Knox, R. L. Fork, C. H. Brito-Cruz, M. C. Downer, and P. J. Maloney,Appl. Phys. Lett. 53, 654(1988).
16. D. Mosher and S. J. Stephanakis, Appl. Phys. Lett. 29, 105(1976).
17. M. Watanabe, T. Hidaka, H. TaninoK. Hoh, and Y. Mitsuhashi. Appl. Phys. Lett. 45, 725(1984).

Designs for Coherent X-Ray Lasers

R. A. London, P. Amendt, M.R. Carter, M. D. Feit, J. A. Fleck,

D. L. Matthews, S. Maxon, R. E. Stewart, J. E. Trebes

University of California, Lawrence Livermore National Laboratory

Livermore, CA 94550

and M. Strauss

Nuclear Research Centre-Negev, Beer Sheva 84190, Israel

The property of coherence is important for many suggested applications of x-ray lasers. For x-ray holography, the longitudinal coherence length is required to be larger than the pathlength difference between the object beam and the reference beam, estimated to be about 5 μm in a Fourier transform holography system. The longitudinal coherence length is related to the line width by $L_\ell = \lambda^2/\Delta\lambda$, where λ is the laser wavelength. Using the thermal Doppler width for an estimate we get $L_\ell = 37\,\mu m$ for a 45Å laser. This estimate is supported by a measurement at 206Å. We therefore expect that longitudinal coherence will not be a problem. The transverse coherence length must be larger than the extent of the sample, typically $\approx 10\,\mu m$, and a certain amount of energy must irradiate the sample in order provide a high signal to noise hologram. The coherence length is obtainable straightforwardly by placing a pinhole in front of the laser, or by placing the object far from the laser. The combined requirement of energy and coherence is, however, much more difficult, requiring efficient production of coherent radiation.

A simple model using the Van Cittert-Zernike theorem to calculate the development of coherence from an incoherent disk source at one end of the laser yields estimates for the degree of coherence. The number of modes in each transverse direction scales as the Fresnel number ($F=ka^2/L$, where k is the wavenumber, a is the width and L is the length). Applying this simple model to current exploding foil x-ray lasers such as neon-like selenium (206Å) and nickel-like tantalum (45Å), of order 10^4 modes are estimated. We are therefore interested in designs for more coherent x-ray lasers.

Recently several methods have been developed to model the buildup of coherence in x-ray lasers in detail, including such effects as gain and electron density variation. These methods are based on the paraxial wave equation, with a spontaneous emission source term. The observables of the laser (the intensity and coherence) are represented by the mutual coherence function (MCF) – the ensemble averaged electric field complex product. The methods include modal analyses (London, Strauss and Rosen 1990, and Amendt, London and Strauss 1990), numerical split-operator methods (Feit and Fleck 1990), and propagator methods (Hazak and Bar-Shalom 1989).

In the modal analysis, the electric field is written as a sum over modes, each having a longitudinal and transverse factor. The substitution of this sum into the paraxial equation gives rise to a transverse eigenvalue equation and a longitudinal amplification equation for each mode. We have solved these equations for the MCF for several types of transverse profiles. For the case of square gain and density profiles, the Fresnel number scaling of the simple model is reproduced. For rounded profiles, more typical of an exploding foil x-ray laser, the effects of gain-guiding and refractive defocusing are found to have two important consequences. They improve the degree of coherence by limiting the number of strongly amplified modes and they complicate the analysis because of the non-orthogonality of the modes. We have derived a general scaling law giving the design parameters to obtain good coherence through the guiding effects. To address the mode non-orthogonality, we find that it is important to include both discrete "guided" modes as well as a continuum of "unguided" modes in a complete analysis.

A split-operator numerical code (WAVE, Feit and Fleck, 1990) has also been applied to the design of coherent x-ray lasers. This code solves the paraxial equation using numerical difference methods on a Fourier representation of the electric field. It is allows for general gain and refractive index profiles and gain saturation. Calculations with WAVE agree closely with those of the modal method for several simple test problems. For typical current x-ray lasers, WAVE calculations predict somewhat better coherence than the simple incoherent disk model, but still not good enough for holography.

Several methods for improving the coherence of x-ray lasers are suggested. From the simple model, we infer that increasing the amplification factor, through the gain-length product, is the most direct way to increase the coherent energy output. This must be achieved in a way that avoids gain saturation, so that

unwanted modes do not saturation the laser and rob gain.

The first method is to utilize the gain guiding and refractive defocusing inherent in a exploding foil laser to improve coherence. These effects act as a distributed spatial filter to eliminate unwanted modes. This will improve the coherent fraction of the output radiation, and more importantly, delay the onset c saturation until a larger gain-length is achieved. Estimates of the parameters to achieve good coherence have been made. Calculations with WAVE confirm the validity of this concept.

The second method is to use a normal incidence mirror to re-inject the x-ray laser radiation into the plasma for a second pass, thereby achieve higher gain-length. Several possible forms of spatial filtering involving distant placement of the mirror, pinholes, and convex mirrors are suggested to improve the coherenc and avoid saturation with unwanted modes.

The third method is to use a oscillator-amplifier architecture similar to those used in high power optical lasers (Rosen, Trebes and Matthews 1987). This involves using two separate lasing plasmas. The first plasma would, by virtue of small cross-section and spatial filtering, produce a coherent x-ray output. These rays would be injected into a second stage designed as an amplifier.

Detailed designs of several x-ray laser configurations are in currently being explored. Experiments to characterize the physics needed for these designs and t measure the power output, angular beam pattern and coherence of these lasers are in progress.

This work was supported by the U. S. Department of Energy, Lawrence Livermore National Laboratory under contract number W-7405-ENG-48.

References

Amendt, P. A., London, R. A. and Strauss, M. 1990, submitted to Phys. Rev. A

Feit, M. D. and Fleck, J. A. 1990, JOSA-B, **7**, 2048.

Hazak, G. and Bar-Shalom,A., 1989, Phys. Rev. A, **40**, 7055.

London, R. A., Strauss, M. and Rosen, M. D. 1990, Phys. Rev. Lett., **65**, 563.

Effects of Illumination Uniformity Improvement on X-Ray Lasing Plasmas

J. C. Kieffer, M. Nantel, M. Chaker, and H. Pépin

INRS-Energie, C.P. 1020, Varennes, Québec J3X 1S2, Canada

H. Baldis, J. Dunn, G. D. Enright, and D. M. Villeneuve

Steacie Institute, National Research Council, Ottawa, Ontario K1A 0R6, Canada

ABSTRACT

A beam smoothing technique (SWA) was used to produce a linear Ge plasma (12 mm x 100 μm). The plasma parameter uniformity along the amplification axis was studied with various X-ray diagnostics. Time resolved monochromatic images of the 3d-2s quadrupole emission (E2) regions have been obtained giving informations on the dynamics of 3d-3p core excited lasing.

1. INTRODUCTION

An accurate knowledge and an efficient control of the plasma conditions are required for gain optimization and development of compact X-ray lasers [1]. It was recently pointed out that local perturbations in the plasma parameters along the amplification axis could strongly affect the gain buildup [2-4]. We investigate the dependence of line focus plasma conditions and gain on irradiation non-uniformity. We recently showed that laser non-uniform irradiation could drive large scale density inhomogeneities which could be highly critical for population inversions by recombination [5]. For electron collisional excitation scheme our results [6,7] indicate that laser intensity modulations are above all critical for amplification of 3d-3p core excited Ne-like transitions. In the present work we characterize the uniformity of a plasma produced with a novel focussing arrangement which gives a nearly uniform illumination. In particular we present a preliminary study of the dynamics of the 3d-2s emission which is a potential density diagnostic [8] and which can also give us some indications on the core excited lasing.

The experiments were performed with the LP2 laser system (1.06 μm) at the National Research Council of Canada. Intensities of about 10^{13} W/cm^2 were available

Proceedings on Short-Wavelength Coherent Radiation, Vol. 11, Philip H. Bucksbaum and Natale M. Ceglio (eds.)
© 1991 Optical Society of America

with 1.5 ns pulse (FWHM) and 12 mm long line focus. The line focus was formed with either a pair of f/10 cylindrical lenses or the SWA arrangement [9]. Time resolved (or integrated) monochromatic images (Kev range) have been obtained with a Johann spectrometer working in imaging mode [10] and coupled to an X-ray streak camera (or a film).

2. RESULTS

The Fig. 1a shows a time integrated image of a 8 mm long plasma obtained with the SWA system. The detection wavelength window was 20 mÅ wide and adjusted on the 3C Ne-like transition at 8.92 Å. The detection axis was in the target plane at 90° from the laser axis and at 30° from the horizontal line focus axis. The Fig. 1b presents a line out along the line focus axis taken at 100 μm from the target plane. This result indicates that an improved large scale plasma uniformity is obtained with the SWA focussing arrangement. The Ne-like emission contrast is about 0.4 for a laser intensity contrast of 0.2. With a conventional focussing system (incident laser beam contrast equal to 0.65) the 3C emission contrast is about 0.83. However the interferences of adjacent beams produce high spatial frequency structures as observed in figure 1b. Similar intensity profiles along the line focus have been obtained for detection wavelength window adjusted on the 3A Ne-like transition at 8.371 Å and with pinhole camera pictures. Large gains have been measured in these conditions on five 3p-3s transitions and also on a J=2-1 3d-3p core excited transition at 199A [7]. This last amplification is only observed with the most uniform plasma. One possible explanation is that the gain is confined to a very narrow region in space. In order to understand the dynamics of this amplification, which could allow the scaling of the Ne-like inner shell transitions

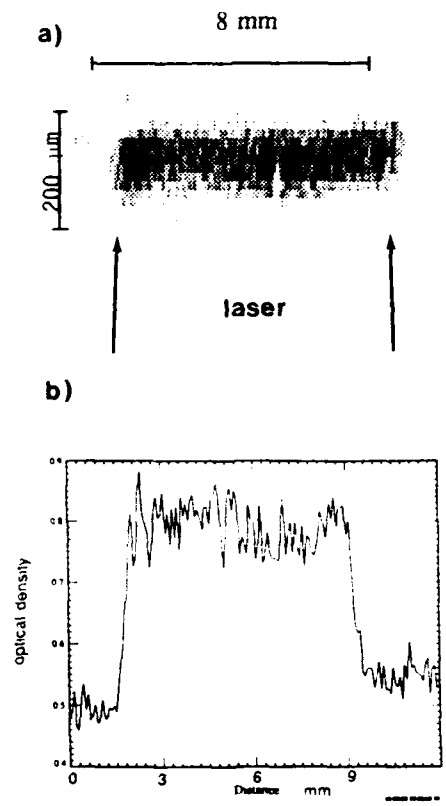

Fig. 1: Time integrated image of the SWA produced plasma at the 3C line emission wavelength.
a) 2D space resolved image
b) Line out along the line focus, at 100 μm from the target plane.

systems to very short lasing wavelengths [7], we study the 3d-2s quadrupole emission which shares the same upper level as the 3d-3p transition. Furthermore the ratio of this emission to the 3A Ne-like emission is a potential density diagnostic [8]. The Fig. 2 shows a high resolution spectrum of the Ne-like L emission near 8 Å obtained with the Johann spectrograph for incident energy of 90 J/cm. The spectrometer was calibrated with various Kα emissions and the accuracy of the wavelength determination was ± 2 mÅ around 8 Å. The emission line at 8.031 Å has been identified as a Ne-like E2 decay of the upper state of the 199A lasing transition [7]. At higher intensities this line blended with F-like 3p-2s transition. The Fig. 3 presents the space and time resolved E2 emission. The spectrometer detection axis is in the target plane and the detection wavelength window is 30 mÅ wide adjusted on the 8.031 Å wavelength. This result obtained with the SWA system shows the E2 emission distribution along the line focus vs time at 100 μm from the target plane. A very good plasma uniformity is detected along the amplification axis. Similar results have been obtained at various distances from the target plane along the incident laser axis indicating that the E2 emission region is about 100 μm wide and is very uniform. Results obtained with two cylindrical lenses indicate that the E2 emission regions are strongly affected by non-uniform irradiation. Strong variations along the line focus of the ion velocity is observed in these conditions. Preliminary results with SWA indicate a strong improvement of the uniformity of the emission zones.

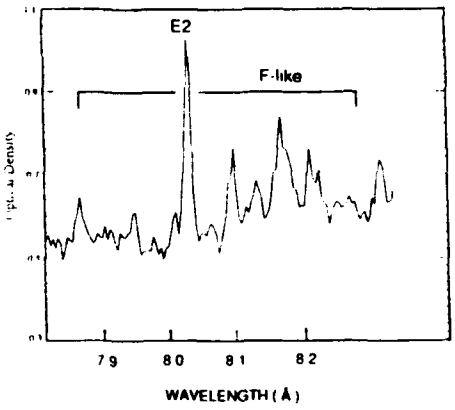

Fig. 2: High resolution spectrum of Ge near 8 Å showing the 3d-2s quadrupole emission line (E2) at 8.031 Å.

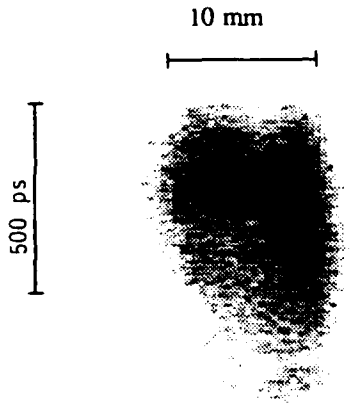

Fig. 3: Space and time resolved monochromatic image at the wavelength of the E2 line with a 30 mÅ detection wavelength window.

3. CONCLUSION

The plasma uniformity along the 3p-3s and 3d-3p amplification axis was studied with time resolved monochromatic imaging diagnostic. Time resolved images of the 3d-2s Ge quadrupole emission regions have been obtained for the first time. These data gives informations on the dynamics of the 3d-3p core excited lasing and can also be useful to see the density fluctuations induced by the non-uniform irradiation. A very uniform plasma is necessary to relax energy requirements for lasing at short wavelength by using Ne-like inner shell transitions.

REFERENCES

1. M.D. Rosen, "Plasma physics issues in laboratory X-ray lasers", Phys. Fluids B2, 1461-1466 (1990).
2. R.W. Lee, and K.G. Estabrook, "Simulations of laser produced cylindrical carbon plasmas", Phys. Rev. A35, 1269-1274 (1987).
3. H. Griem, "Line profiles of soft X-ray laser gain coefficients", Phys. Rev. A33, 3580-3583 (1986).
4. G. Jamelot et al., Appl. Phys. B50, 239-243 (1990).
5. J.C. Kieffer et al., "Large scale structures in line focussed plasmas", Phys. Fluids B3, 463-467 (1991).
6. J.C. Kieffer et al., "Effects of beam non-uniformities on line focus plasma conditions, in Proceedings of second Int. Conf. on X-ray lasers (1991).
7. G.D. Enright et al., "X-ray gain measurements in a collisionally excited Ge plasma", in Proceedings of second Int. Conf. on X-ray lasers (1991).
8. B.K.F. Young et al., "Measurements of density - sensitive electric quadrupole transitions", Phys. Rev. Lett. 62, 1266-1269 (1989).
9. D.M. Villeneuve et al., "Novel laser line focus geometry applied to X-ray lasers", Opt. Comm. 81, 54-58 (1991).
10. J.C. Kieffer et al., "Monochromatic X-ray imaging of a laser produced plasma", Appl. Opt. 28, 4333-4336 (1989).

Evidence of X-Ray Laser Gain Cancellation Due to Plasma Inhomogeneity

P. Jaegle, P. Dhez, A. Klisnick, A. Carillon, G. Jamelot, B. Gauthé, and J. P. Raucourt

Laboratoire de Spectroscopie Atomique et Ionique, Université Paris Sud F, 91405 Orsay, France

P. Goedtkindt

CBNM, Steenweg op Retie, B-2440 Geel, Belgium

J. C. Kieffer

INRS-Energie, 1650 Montée St. Julie, CP 1020, Varennes, Quebec J3X 1S2, Canada

Abstract

Influence of Random Phase Plates on homogeneity of long plasma columns is studied by X-ray imaging. Consequence on laser gain at 105.7Å is discussed.

I. Introduction.

Compared to the collisional pumping scheme, the recombination scheme in lithium-like ions is an attractive way to carry out a small-scale X-ray laser because it is known to be potentially the cheapest way of soft X-ray pumping [1,2]. With the gain values actually reported, 1 cm^{-1} to 4 cm^{-1}, a long plasma column, of about 5 cm, would make soft X-ray lasers using lithium-like ions already available in laboratories. However some difficulties are associated with large gain production in long plasma columns ($L \geq 2$ cm). The observation of a rather low gain coefficient (0.5 cm^{-1}) seems to be the general fact for plasmas of such length[3,4].

To explain the gain reduction observed in long plasmas compared to the short ones, three phenomena are invoked: i) deflection of the amplified beam owing to refraction, ii) radiation trapping which would result in population inversion reduction and iii) plasma non uniformity. The first phenomenon has to be considered mainly for the collisional pumping scheme, but much less for the quite low electronic densities needed in the recombination scheme in lithium-like ions. The second phenomenon has been demonstrated to have a small part in our experiments[2]. That led us to investigate the role of plasma inhomogeneities because not only they can affect both schemes, but also because recombination pumped inversions are known to be strongly dependent on the local state of the plasma and of the dynamic of the recombination. Local perturbations in the plasma parameters along the line focus can produce spatial and temporal local changes in the plasma hydrodynamics. That does affect the time history of the lasing action by detuning of the gain regions[5], leading to reduce the maximum values for the overall obtained gain. A few experiments on thin and thick planar targets have been done, but their results show

© 1991 Optical Society of America

small and large scale inhomogeneities in plasmas produced by line focus illumination. These experiments used pinhole camera[6] interferometry or shadowgraphy[7].

Here we would like to illustrate how a simple polychromatic imaging method helps to prove plasma inhomogeneities which can be correlated to gain measurements.

II. Experimental results.

Inhomogeneities along the focal line prepared for making a long plasma column can evidently be induced by inhomogeneities of the incident laser beam. In the case of the LULI laser, the non uniformity of the intensity through the beam cross section has been observed at the entrance of the interaction chamber by using infrared filters and photographic films. That demonstrated a pronounced illumination inhomogeneity with a minimum at the center of the beam and a contrast as large as about 0.75 between maxima and minima of flux densities. Such a spatial variation of incident laser beam intensities drives strong plasma density and temperature perturbations. These perturbations will affect the emissivity of spectral lines, some of which are of special interest in the recombination scheme. This is what has been seen when imaging the plasma column at the wavelength of the He_α line in aluminum. This diagnostic made use of a bent crystal spectrometer combined with a pinhole camera[8].

Polychromatic pinhole X-UV images of hot plasmas, just filtered by an absorbing thin film, can be obtained easily by using windowless CCD detector[9]. On the long line focus, in spite of the quite large band pass, they showed plasma inhomogeneities similar to those seen on monochromatized images. Figure 1a shows such a CCD pinhole image from a 9 mm long plasma which demonstrates the presence of inhomogeneities.

One of the method proposed to smooth the plasma inhomogeneities along the line focus is to place a Random Phase Plate (RPP) prior to the final focusing lens[10]. A RPP is a random array of transmitting areas which induces a phase shift of either 0 or π in view to produce a far field distribution containing a multiple beam, high spatial frequency interference pattern. We tested the effect of inserting a RPP after the focusing lens as schematically indicated in figure 2a. The used RPP was kindly provided by C.N. Danson from the Rutherford Laboratory. The effect observed on the X-UV image is shown in figure 1b, in the case of a laser beam similar to the one used to get image 1a. On the contrary to our hope we observed a quite periodic row of hot spots whose characteristic scalelength is not small enough to be smoothed by plasma hydrodynamics.

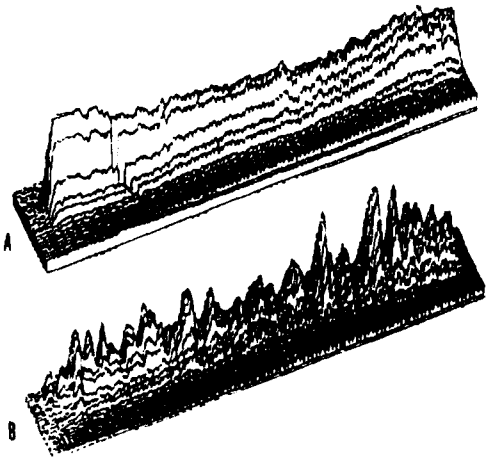

Figure 1: Examples of polychromatic pinhole camera images obtained with a CCD detector. The pinhole camera is set as shown in figure 2. The intensity received is proportional to the vertical size. a) The top figure corresponds to an image of a 9 mm long plasma without Random Phase Plate (RPP). Large scale variations of the X-UV emissivity along the line focus are observed. b) The bottom image corresponds to the case where a RPP (1 cm long, 20 µm elementary zones) is set after the focusing lens. In this case one observes a series of hot spots indicating how the laser beam has been modulated by the RPP.

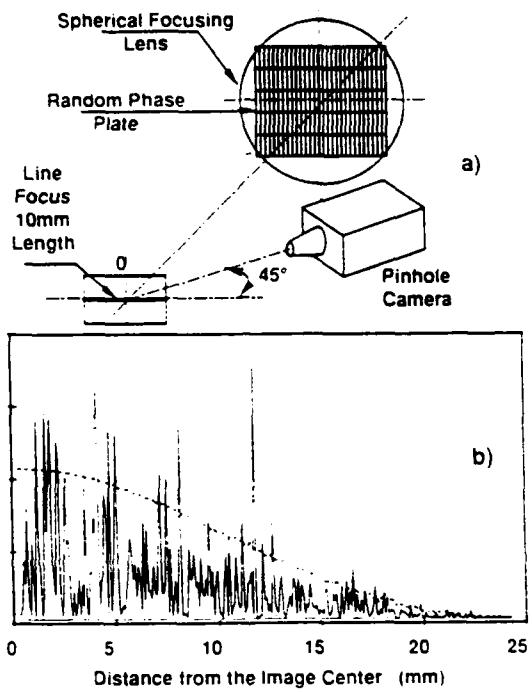

Figure 2:a) Scheme of the experiment showing the relative position of the used elements to get the images shown on figure 1. b) Calculated intensity on the focal line in the case of a Random Phase Plate (RPP) having 5 rows of 1 cm height and 6 cm length; each row contains 3000 zones of 20 µm width. The origin in abscissa is the center of the RPP; the indicated smooth dashed line corresponds to the diffraction pattern of a single zone. In our experiment the used target was 9 mm length to get a more uniform mean density along the focus. This calculated intensity distribution is to be compared to the image b in figure 1.

Although this result is opposite to the desirable goal, it gives an interesting way to correlate the gain and plasma inhomogeneities. That is why we have compared the gains obtained with and without RPP on the lithium-like aluminum ionic line (5f -> 3d) at 105.7Å we are commonly studying. Such a gain measurement achieved in both cases confirms that inhomoge-neities exhibited in figure 1b have strong negative consequence on the gain.

Faced to the failure of the first tested RPP we have developed a computer program able to simulate the laser flux density produced on our line focus by such a system. Figure 2a is the scheme of the optical system we used in the experiment. Figure 2b is an example of laser flux density calculated in the case of a 5x6 cm RPP having 5 rows of 1x6 cm, each row containing 3000 zones of 20 µm width. One can observe how this flux density modulation mimics the X-UV emissivity shown on 2a.

III. Conclusions.

We have demonstrated that plasma inhomogeneities affect the gain obtained with long plasma columns presently produced to make X-UV lasers. That confirms the importance of plasma inhomogeneity on the overall gain which could be obtained from the recombination scheme in lithium-like ions. Monochromatic imaging of long plasma columns is certainly the best method to track plasma inhomogeneities connected to gain decreasing observed in long plasma. It is especially interesting to choose a spectral line giving direct information on the population of interest for the lasing action. Such an information offers the easiest way to model the plasma conditions and to progress on test of 1D and 2D codes. Although a polychromatic X-UV image is not sufficient for a modeling, we have demonstrated it is a convenient way to evaluate the homogeneity along the plasma focus as indicated by our comparison between monochromatic and polychromatic images.

Pinhole camera equipped with a windowless CCD detector is a very compact system which can be set very close to the plasma. The linearity of CCD detector over several orders of magnitude of flux variation and the possibility to get an image directly on a computer screen is advantageous for a shot to shot test. In addition of homogeneity test along the focus, such a system in our experiment appears as the more reliable indication about laser focusing quality versus distance from lenses to target.

The clear correspondence experimentally observed between the calculated flux density modulations produced by our RPP and the observed polychromatic X-UV plasma images is interesting. On the one hand our RPP simulations are verified, proving to be able to predict the main effects at least qualitatively, at the scale we tested. On the other hand, the pinhole-plus windowless-CCD combination appears as a tool not only to progress on the fabrication of RPP, but also to control the systems proposed to cure the effect of incident laser inhomogeneities. Finally, at the scale we were able to observe, it seems that no smoothing of the detected inhomogeneities can be expected from plasma hydrodynamics.

Authors acknowledge the financial support of DRET.

References.

1. P. Jaegle,G. Jamelot, A. Carillon, A. Klisnick, A. Sureau and H. Guennou, JOSA B4, 4, 563 (1987).
2. P. Jaegle, A. Carillon, P. Dhez, B. Gauthé, G. Jamelot, A. Klisnick and J.P. Raucourt , Proceedings of the 2nd Int. Colloquium on X-Ray Lasers, 17-21 Sept. 1990, York University (UK). To be published.
3. C. Jamelot, A. Carillon, A. Klisnick and P. Jaeglé, Appl. Phys. B 50, p.239, (1990).
4. LLE Review 1990 (January-March) 42, p.76, Laboratory for Laser Energetics, University of Rochester, Rochester, N.Y.
5. A. Klisnick, A. Sureau, H. Guennou, C. Moller and J. Virmont, to be published in Annales de Physique (1991).
6. T.N. Lee, W.A. Molander, J.L. Ford and R.C. Elton, Rev. Sci. Instrum. 57,.2052 (1986).
7. Z.Z. Xu, P.M.Y. Lee, Li h. Yen, W.Q. Zhang, Z.M. Jiang, S.X. Meng, J.J. Yu and A.D. Qian, Opt. Com. 61,.199 (1987).
8. J.C. Kieffer, M. Chaker, H. Pepin, D.M. Villeneuve, J.E. Bernard and H.A. Baldis, Appl. Opt. 28, p 4333 (1989).
9. R. Benattar, J. Godart and E. Houbebine, SPIE Vol.831, 129 (1987).
10. C. Danson, R. Bann, J. Exley, D. Pepler and I. Watson, Proceedings of the 2nd Int. Colloquium on X-Ray Lasers, 17-21 Sept. 1990, York University (UK). To be published.

OPTICAL WIGGLER FREE-ELECTRON X-RAY LASER AS A TWO-LEVEL QUANTUM GENERATOR WITH FULLY INVERTED MEDIUM

E.M.Belenov, S.V.Grigoriev, A.V.Nazarkin, I.V.Smetanin
P.N.Lebedev Physics Institute, Ac.Sci.USSR, Moscow 117924,
Leninsky prospect 53

Recently the possibility was widely discussed of creation of an X-ray free-electron laser (FEL) using a high-power laser pulse as the undulator (optical wiggler FEL) [1]. Optical wiggler FEL is characterized by relatively small energy of the used electrons ($\varepsilon \sim 1 \div 10$ MeV). In order to achieve high values of the gain for X-rays it is necessary to use rather monoenergetic electron beams ($\Delta\gamma/\gamma \sim 10^{-4}$) and the wigglers with a large number of periodic elements ($N \geq 10^4$). In such FEL the energy of X-ray quantum can exceed the induced emission (absorption) linewidth: $\omega_X > \max(\varepsilon\Delta\gamma/\gamma, \varepsilon(4N^{-1}))$. We have shown that in this case the electrons interacting with the fields in FEL behave as two-level particles (the energies of these two levels are defined by energy and momentum conservation laws in an elementary act of stimulated Compton backscattering). The electron beam injected into the region of interaction with the energy close to the energy of the upper level represents a fully inverted medium for the amplified X-ray emission. The possibility is shown of FEL lasing with full extraction of inversion.

[1] J.Gea-Banacloche, G.T.Moore, R.R.Schlicher, M.O.Scully, H.Walter IEEE J.QE, vol.23, p.1558 (1987).

Section II: Applications of Short-Wavelength Radiation

X-Ray Holographic Microscopy Using Photoresists: Recent Developments

C. Jacobsen and S. Lindaas

Department of Physics, State University of New York at Stony Brook, Stony Brook, New York 11794

M. Howells

Advanced Light Source, Lawrence Berkeley Laboratory, Berkeley, California 94720

Abstract

X-ray holography using photoresists is a method of x-ray microscopy which may be well-suited to flash imaging of radiation-sensitive specimens if suitable sources are developed. We describe our results of imaging dried samples using a synchrotron x-ray source, and our efforts at imaging hydrated biological specimens.

Introduction

X-ray microscopes are used to image thick, hydrated biological specimens at 50 nm resolution. This resolution is nearly an order of magnitude better than that obtained in full-field or confocal optical microscopes, and further developements can be expected. As image resolution (and thus photon density on sample) improves, radiation damage effects must be considered more carefully. Gilbert *et al.* have shown that initially live chick DRG fibroblasts appear structurally intact for more than 0.5 but less than 3 hours following exposure to a 2×10^4 Gy dose resulting from a 95 nm resolution soft x-ray image[1]. Bennett *et al.* have found that a 3×10^3 Gy soft x-ray radiation dose will stop contraction in active myofibrils[2], and Williams *et al.* have observed gross shrinkage in hydrated, fixed *v. faba* chromosomes following soft x-ray radiation doses of $> 10^3$ Gy[3]. The timescale for biological damage resulting from these dose levels is thought to be at the msec level[4]. This timescale is considerably shorter than the few-second exposure time of synchrotron-based transmission x-ray microscopes. In scanning transmission x-ray microscopes, the per-pixel dwell time can be 1–10 msec which may be acceptable for short-range radiation damage effects like diffusion of radiolysis products; however, if a specimen to be studied is sensitive to > 50 nm range radiation damage effects, the few-minute full image exposure time may prove problematic. These and other considerations make the possibility of flash imaging using x-ray laser sources attractive[5].

Gabor holography using photoresists may be well-suited to high resolution flash x-ray imaging of sufficiently sparse samples. No prefocussing of the specimen is required

Proceedings on Short-Wavelength Coherent Radiation, Vol. 11, Philip H. Bucksbaum and Natale M. Ceglio (eds.)

© 1991 Optical Society of America

(the focussing is done in the hologram reconstruction stage), and a limited amount of 3D information can be obtained from a single exposure (simultaneous exposures from several viewing angles can also be contemplated[6]). The technique also makes good use of partially coherent or multimode sources; monochromaticity requirements are eased compared to longer focal length zone-plate based x-ray microscopes, and multiple spatially coherent modes can be used to record a hologram of a large field (although the image resolution will be limited by the width of one mode). X-ray photoresists such as PMMA are thought to be capable of recording holograms at 20 nm or better resolution with soft x-ray exposures of ~ 300 mJ/cm^2. One unanswered question is the survivability of PMMA to such an intense flash exposure; at present, the only experience we are aware of[7] is the successful use of PMMA in contact microscopy using a laser plasma source of 2.4–3 nm x-rays with a resist exposure of 5–10 mJ/cm^2 in 0.5 ns.

Previously reported results: dried specimen imaging

Our present efforts are based on using synchrotron sources of soft x-rays. Using a 35 period soft x-ray undulator and beamline at the National Synchrotron Light Source at Brookhaven National Laboratory[8], we have a source brightness of 10^{17} photons/(sec, mm^2, mrad^2, 0.1% BW) in the 1.5–5 nm wavelength range. When optical system losses are included, this is sufficient for us to record 300 mJ/cm^2 hologram exposures in vacuum in 1–3 minutes. The exposed hologram is then developed in MIBK:IPA 1:5 for 0.2–1 minutes, metal shadowed, and enlarged in a transmission electron microscope (TEM). The TEM negatives can then be digitized using a scanning microdensitometer, or a contact print of the negative can be digitized using an inexpensive PC-based image scanner. By numerically reconstructing the digitized holograms, we have obtained images of rat pancreatic zymogen granules and test objects at 56 nm resolution[9]. X-ray holographic images of these samples show similar structure to what is seen in a 1.5 MeV transmission electron microscope[10].

Gabor holograms are known to suffer from the fact that light from the virtual image appears out-of-focus but superimposed upon the real image. We have studied the use of iterative computer algorithms[11] to reduce this twin-image noise. In Gabor holography, the object plane must be largely empty in order to allow the reference wave to reach the hologram plane. At the hologram plane, the hologram records the magnitude of the mixture of sample plus reference wave. By iteratively propagating a wavefield between these two planes in the computer and inserting at each plane the known information (a uniform plane wave in the specimen-free regions at the object plane, and the measured optical magnitude at the hologram plane), we are able to greatly reduce the twin image noise[12]. We are currently studying the application of this image reconstruction technique to larger samples.

Wet specimen imaging

A primary appeal of x-ray microscopy is the ability to image thick, hydrated specimens. Accordingly, our efforts have shifted from imaging dried specimens in vacuum to imaging wet specimens in air. Using silicon nitride vacuum and sample chamber windows, we bring the coherent soft x-ray beam out of the UHV undulator beamline into a wet sample chamber[13], past the specimen, and onto the photoresist[12]. A visible light microscope is used to align the desired specimen into the beam. Recently, we have had success using a phosphor-coated avalanche photodiode with an aluminized silicon nitride entrance window (which transmits x-rays but reflects visible light) as an in-air flux monitor. With this system, we are able to reliably obtain high resolution holograms of dried specimens in air. Progress in wet specimen imaging has been complicated by the fact that a non-uniform water layer tends to build up around the sample due to surface tension. As a result, the x-ray transmission through the sample is often reduced by a factor of two or three compared to an area ~ 5 μm away; this leads to a non-uniform reference wave and a non-uniform exposure of the photoresist. By using UV pre-exposure on the photoresist[14], we have advanced to the point of imaging the boundaries of cells at 100 nm resolution (see Fig. 1), but we have not yet been successful at imaging intracellular structure at high resolution. We expect that the use of thicker photoresists (with greater dynamic range) and extracellular solutions with varied viscosity will allow us to make further progress in this area.

Figure 1. Reconstructed image from an x-ray hologram of a hydrated, fixed hippocampal cell provided by J. Pine. The cell body is clearly outlined, but intracellular structure cannot be seen partly because of the thickness of these cell bodies and partly because hologram formation has been complicated by uneven attenuation of the in-line hologram reference beam in non-uniform water layers surrounding the cell. Present efforts are aimed at imaging thinner cells and at controlling the water layer thickness.

Scanning force microscope readout

The TEM used to enlarge the holograms is the weak point in our current system. The photoresist must be metal-coated for use in the TEM (precluding any further resist development), and the resist suffers from radiation damage during examination. Because the high resolution fringes needed for a good hologram are not visible in an optical microscope, this means that we presently develop resists in a somewhat blind fashion. In addition, the TEM image contrast is dominated by the metal shadowing pattern, which is nonlinearly related to the hologram pattern we wish to measure. Finally, the commercial TEMs we have used suffer from spiral distortion so that the edges of a 45 mm field of view on the film plane are typically displaced by ~ 0.05 mm. At the 1400× magnification we typically use to match the film resolution with the required hologram field of view, this corresponds to a ~ 36 nm displacement over a hologram radius of 32 μm. If we assume that wavefront aberrations of $\lambda/4$ set the limit to image resolution in reconstructing a hologram, and note that the reconstructed image resolution should be half a fringe width, we see that our currently demonstrated image resolution of 56 nm could well be limited by the TEM readout rather than by the quality of the hologram. In fact, power spectra of our photoresists suggest that hologram information is present with good signal to noise at the 32 nm fringe width level[9].

To overcome these limitations, we have explored the use of scanning force microscopes (SFM) to read out the developed resist surface. These microscopes are able to look at molecular detail on resists in a semi-nondestructive fashion, and we have obtained low resolution reconstructions by this means. However, commercial SFMs suffer from severe image field non-linearities due to the use of uncorrected piezoelectric scanners. We are therefore building an SFM with a linear image field and the capability of producing a digital map of a 70 μm × 70 μm hologram sub-field. This system should allow us to fully extract the information recorded in photoresist holograms.

Acknowledgments

We gratefully acknowledge many helpful conversations with J. Gilbert, J. Kirz, D. Sayre, and S. Williams, the support of the NSF under grant DIR-9006893 (C.J., S.L.), and the Office of Health and Environmental Research of the Department of Energy under subcontract 431-3378A of grant DE-FG02-89ER60858 (M.H.).

References

1. J. R. Gilbert *et al.*, "Soft x-ray absorption imaging of whole wet tissue culture cells", in A. G. Michette, G. R. Morrison, and C. J. Buckley, eds., **X-ray Microscopy III** (Springer, Berlin, to be published in 1991).
2. P. M. Bennett, C. J. Buckley, G. F. Foster, and P. A. F. Anastasi, "Radiation damage studies on active myofibrils", in A. G. Michette, G. R. Morrison, and C. J. Buckley, eds., **X-ray Microscopy III** (Springer, Berlin, to be published in 1991).

3. S. Williams, Department of Physics, SUNY at Stony Brook, Stony Brook, NY 11794 (personal communication).
4. K. Shinohara and A. Ito, "Factors affecting the observation of hydrated mammalian cells by soft x-ray microscopy", in A. G. Michette, G. R. Morrison, and C. J. Buckley, eds., **X-ray Microscopy III** (Springer, Berlin, to be published in 1991).
5. J. C. Solem, "Imaging biological specimens with high-intensity soft x rays", *J. Opt. Soc. Am. B* **3**, 1551–1565 (1986).
6. J. Trebes *et al.*, "X-ray holography at Lawrence Livermore National Laboratory—high and ultra-high resolution x-ray imaging", in A. G. Michette, G. R. Morrison, and C. J. Buckley, eds., **X-ray Microscopy III** (Springer, Berlin, to be published in 1991).
7. T. Tomie *et al.*, "Three-dimensional readout of flash x-ray images of living sperm in water by atomic-force microscopy", *Science* **252**, 691–693 (1991).
8. H. Rarback *et al.*, "Coherent radiation for x-ray imaging—the Soft X-ray Undulator and the X1A beamline at the NSLS", *J. X-ray Sci. Tech.* **2**, 274–296 (1990).
9. C. Jacobsen, M. Howells, J. Kirz, and S. Rothman, "X-ray holographic microscopy using photoresists", *J. Opt. Soc. Am. A* **7**, 847–1861 (1990).
10. C. Jacobsen, M. Howells, S. Rothman, and J. Bastacky, "X-ray holography: early experience in microimaging", in D. Attwood and B. Barton, eds., **X-ray Microimaging for the Life Sciences** (Lawrence Berkeley Laboratory report LBL-27660, 1989), pp. 69–73.
11. G. Liu and P. D. Scott, "Phase retrieval and twin-image elimination for in-line Fresnel holograms", *J. Opt. Soc. Am. A* **4**, 159–165 (1987).
12. C. Jacobsen, S. Lindaas, and M. Howells, "X-ray holographic microscopy using photoresists: high resolution lensless imaging" in A. G. Michette, G. R. Morrison, and C. J. Buckley, eds., **X-ray Microscopy III** (Springer, Berlin, to be published in 1991).
13. J. Pine and J. Gilbert, "Live cell specimens for x-ray microscopy", in A. G. Michette, G. R. Morrison, and C. J. Buckley, eds., **X-ray Microscopy III** (Springer, Berlin, to be published in 1991).
14. F. Pollack, A. Bernstein, and D. Joyeux, "Hints for a proper use of photoresists as optical recording media for x-ray holography", *Proc. SPIE* **1140**, 367–372 (1989).

Broadband Diffractive Lens

N. M. Ceglio, A. M. Hawryluk, D. P. Gaines,† R. A. London, and L. G. Seppala

Lawrence Livermore National Laboratory, University of California, P.O. Box 808, Livermore, California 94550

Abstract

Significant progress has been made toward solving the century-old problem of chromatic aberrations in diffractive optics. Our approach exploits modern materials and microfabrication technology and is very different from the "purely diffractive strategy", which is commonly employed and which results in multiple diffractive elements separated by a finite distance. We have developed a Fresnel zone plate lens comprised of a serial stack of patterned minus-filters which allows broadband radiation to be focussed (or imaged) without longitudinal or transverse chromatic aberrations.

Introduction

Diffractive optics, such as the Fresnel zone plate shown in Figure 1, are commonly used for imaging and focussing radiation at wavelengths for which refraction is not a viable option. For example, Fresnel zone plates have been used extensively as narrowband imaging elements for soft x-rays.[1] In these applications the zone plate is used as a thin lens with focal length,

$$f = \frac{r_1^2}{\lambda} \tag{1}$$

where r_1 is the radius of the central zone, and the radii of the other zones is given by,

$$r_n^2 = n r_1^2 + \frac{n^2\lambda^2}{4} \quad . \qquad n = 2, \ldots N \tag{2}$$

(in cases where $n^2 < \frac{2f}{\lambda}$, the last term in equation (2) can be neglected.)

†Brigham Young University

1991 Optical Society of America

There is a growing interest in diffractive optics for applications at visible wavelengths. This results from the fact that a diffractive optic is in essence a symmetric pattern of obstacles (in amplitude or phase). As such, it can be very thin, lightweight, and amenable to modern techniques of microfabrication–allowing the possibility for inexpensive mass production. The primary limitation on the growth of visible light applications for diffractive optics is the well-known problem of chromatic aberrations. As indicated in equation (1), the focal length of a diffractive optic depends not only on its geometry, but also on the wavelength (color) of illumination. Indeed, the spread in focussing power (diopters = $\frac{1}{f\,(\text{meters})}$) across the visible spectrum (4500Å - 6500Å) for a 20 diopter (@ 5500Å) zone plate lens is greater than 6 diopters. The typical human eye can accommodate a spread of about 1.5 diopters over the same spectral range.[2] As such, a diffractive lens would not be a viable substitute for the natural refractive lens of the human eye.

There has been a great deal of work on the problem of chromatic aberration correction in diffractiive optics.[3-6] All this previous work pursues a purely diffractive strategy for chromatic aberration correction. It uses multiple, separated diffractive components to achieve "dispersion compensation" – (i.e. the dispersion of a second diffractive lens is designed to compensate for the dispersion of the first diffractive lens). Invariably these 'solutions' result in an imaging system which is color corrected over a narrow spectral range and over a very limited field of view. Indeed, many of the advantages of diffractive optics are compromised in the attempt to achieve color correction by such conventional means. In particular, such an imaging system with spatially separated components hardly qualifies as a diffractive lens.

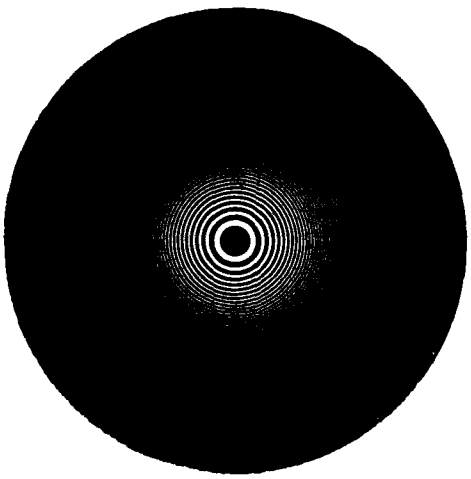

Figure 1 A Fresnel zone plate pattern

A New Idea

In our development of a color corrected diffractive lens we chose not to employ a fully diffractive strategy. Instead, we chose to explore the construction of such a lens using novel materials and technologies. In particular, we explored the use of what engineers call a "Minus-Filter"[7], and what physicists call a multilayer, quarter-wave, high reflectivity coating. The idealized performance of a minus-filter is illustrated in Figure 2(a). Its more realistic embodiment and performance as a quarter wave stack is shown in Figure 2(b). The ideal minus filter has the property that it will stop radiation in a narrowband, $\Delta\lambda$, around λ_0, and let radiation outside that bandwidth pass without loss. The resonant wavelength, λ_0, and the bandwidth, $\Delta\lambda$, can be engineered to meet the requirements of the application of interest. In a multilayer, quarter-wave stack this performance is achieved by arranging for a resonant reflection at

$$\lambda_0 = 4\, n_A d_A = 4\, n_B d_B \tag{3}$$

where n_A, d_A are the refractive index thickness of the "A" layer, and n_B, d_B are the refractive index and thickness of the "B" layer in the periodic stack.

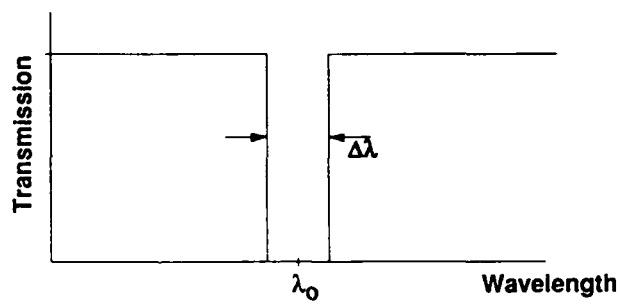

Figure 2(a) The spectral distribution of transmission for an idealized minus-filter. It stops radiation within a narrowband around λ_0, but lets radiation at other wavelengths pass without loss.

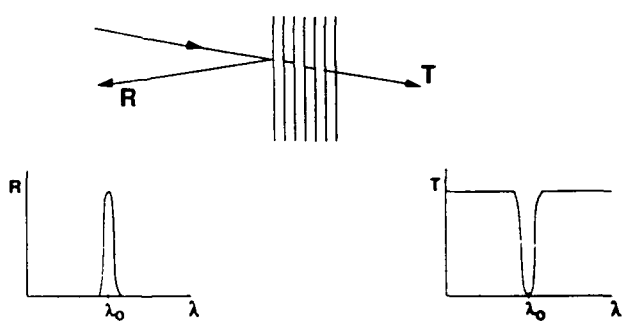

Figure 2(b) The multilayer, quarter wave stack–a practical means for achieving minus-filter performance.

The fundamental concept of the Broadband Diffractive Lens is illustrated in Figures 3(a), 3(b), 3(c). Figure 3(a) shows a Fresnel zone plate patterned into a minus-filter with its stop band in the red (i.e. $\lambda_o = \lambda_R$). The structure is illuminated with collimated broadband radiation (blue, green, red), but only the red light is modulated, and focussed by the minus-filter zone plate. The red light focuses at a focal distance given by

$$f = \frac{r_{1R}^2}{\lambda_R} , \tag{4}$$

but the incident blue and green light are passed without loss.

In figure 3(b) a second zone plate structure patterned into a minus filter with a stop band in the green (i.e. $\lambda_o = \lambda_G$) is overlaid on the red minus-filter zone plate. The green minus-filter zone plate is scaled so that its focal length for green light is equal to that given in equation (4), i.e.

$$f = \frac{r_{1R}^2}{\lambda_R} = \frac{r_{1G}^2}{\lambda_G} . \tag{5}$$

In this way the green minus-filter modulates only the green light and focuses it to the same point as the red light.

The logical extension of this process is illustrated in Figure 3(c) in which a zone plate patterned blue minus-filter is overlaid atop the first two filter patterns. The blue minus-filter is scaled so that it's focal length for blue light is the same as given in equation (5), i.e.

$$f = \frac{r_{1R}^2}{\lambda_R} = \frac{r_{1G}^2}{\lambda_G} = \frac{r_{1B}^2}{\lambda_B} \tag{6}$$

Expanding this concept, a serial stack of minus-filters, each patterned with an appropriately scaled zone plate structure, can be used to focus (or image) light of virtually any chosen bandwidth without lateral or longitudinal chromatic aberrations.

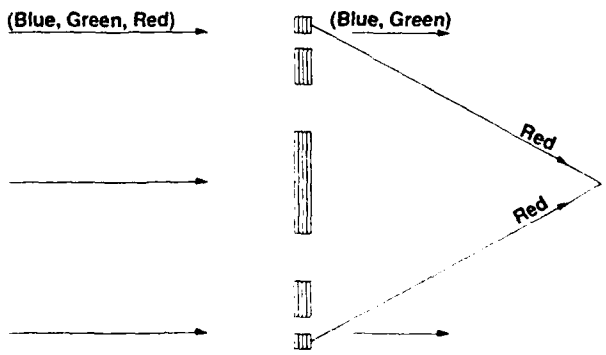

Figure 3(a) A zone plate is patterned in a minus-filter with its stop band in the red.

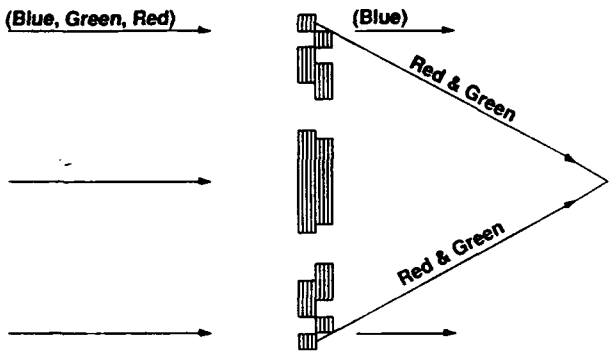

Figure 3(b) Two zone plate patterned minus-filters with stop bands in the red and green are used serially.

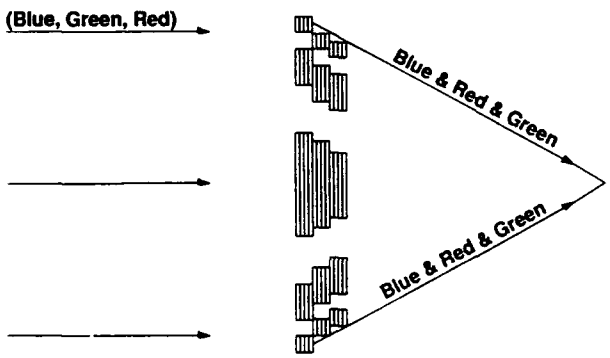

Figure 3(c) The extension of the concept to three (or more) zone plate patterned minus filters.

A further extension of this concept can be achieved by considering the spectral and spatial distribution of light transmitted by the serial stack of patterned minus-filters. (Since this color image cannot be shown in this black and white printing, it is not presented). Any filter technology that achieves the same spatial and spectral modulation of the incident light will also accomplish the sought after chromatic aberration correction.

An example of the above is presented in Figure 4, in which appropriately scaled zone plate patterns were printed onto a tri-layer color film and used as a diffractive lens to image a test pattern illuminated with white light. Shown side by side are images of the test pattern imaged by zone plate lenses–one without chromatic aberration correction, and one with chromatic aberration correction.

More sophisticated imaging tests are being conducted along with analyses for the development of a "phase minus-filter", which allows for phase (instead of amplitude) modulation of the incident light leading to an improved diffraction efficiency for the color corrected lens. This work will be presented in a subsequent publication.

Test pattern image using conventional diffractive optic

Test pattern image using Broadband Diffractive Lens

White light illumination

Figure 4 Demonstration of the imaging performance of the color corrected diffractive lens. The test pattern was illuminated with white light.

Acknowledgments

The authors wish to acknowledge the professional laboratory contributions of Horst Bissenger, Ralph Hostetler, Sherry Hill and John Blunden. This work would not have been possible without the encouragement and support of Drs. Michael Campbell and Erik Storm of LLNL.

References:

1 See for example, N. M. Ceglio, "Revolution in X-ray Optics", Journal of X-ray Science and technology 1, 7-78 (1989).

2 R. E. Bedford and G. Wyszecki, "Axial Chromatic Aberration of the Human Eye", Journal of the Optical Society of America 47, 564 (1947).

3. S. J. Bennett, "Achromatic Combinations of Hologram Optical Elements", Applied Optics 15, 542 (1976).

4. M. Kato, S. Maeda, F. Yamagiski, H. Ikeda, and T. Inagaki, "Wavelength Independent Grating Lens System", Applied Optics 28, 682 (1989).

5. R. Ferriere and J. P. Goedgebuer, "Achromatic System for Far-Field Diffraction with Broadband Illumination", Applied Optics 22, 1540 (1983).

6. I. Weingartner, "Real and Achromatic Imaging with Two Planar Holographic Optical Elements", Optics Communications 58, 385 (1986).

7 A. Thielen, Design of Optical Interference Coatings, Chapter 7 (Mc Graw Hill, New York, 1989).

Differential Phase Contrast Imaging in the Scanning Transmission X-Ray Microscope

J. R. Palmer and G. R. Morrison

Department of Physics, King's College, Strand, London WC2R 2LS, UK

Abstract

Calculations of the contrast transfer functions for differential phase contrast imaging are presented and compared to those for absorption imaging in the x-ray microscope.

Introduction

In the scanning transmission x-ray microscope (STXM) the specimen is scanned in a raster by an x-ray probe formed with a Fresnel zone plate. To achieve near diffraction limited resolution it is necessary to have a coherent source, even when forming an incoherent brightfield image by measuring the x-ray intensity transmitted by the object. This has so far been the only imaging mode used in the STXM and for hydrated biological specimens is well suited to soft x-ray wavelengths within the "water window" (2·33 to 4·36 nm) where carbon absorbs much more strongly than water. However, by the use of phase contrast rather than amplitude contrast, it is possible to form images at wavelengths where the absorption is low, resulting in lower radiation dose for the same level of contrast. Calculations made by Howells [1] and Rudolph and Schmahl [2] have demonstrated very clearly the advantages of phase contrast imaging at wavelengths outside the water window.

In essence, absorption contrast in an image arises from attenuation of the beam as it passes through the specimen, whilst phase contrast arises from changes in the beam direction. By the use of a large area detector with an antisymmetric response function it is possible to form a system which is sensitive to changes in the beam position. This has previously been demonstrated in the STEM and scanning optical microscope with a detector split into two halves about the optical axis [3,4] and with one split into four quadrants [5]. The ideal detector would be one which responds in some way to the first moment of the intensity distribution [6,7]. An image formed by such a system is said to be in differential phase contrast (DPC) and will respond to the phase gradients in the specimen transmittance. It is the theory of DPC

Proceedings on Short-Wavelength Coherent Radiation, 141
Vol. 11, Philip H. Bucksbaum and Natale M. Ceglio (eds.)
© 1991 Optical Society of America

imaging as applied to the STXM which is considered in the remainder of this paper and the performance of such a system is compared to the usual form of amplitude contrast imaging.

Theory

If the detector lies in the far-field then the complex amplitude of the scattered wave in the detector plane is related by a Fourier Transform to that immediately after the specimen. When the probe is centred about a point $\mathbf{r}_0$ the complex amplitude at $\mathbf{r}$ in the specimen exit plane is $\psi(\mathbf{r},\mathbf{r}_0)$ and the signal from a detector with response function $R(\mathbf{k})$ will be

$$s(\mathbf{r}_0) = \int |\Psi(\mathbf{k},\mathbf{r}_0)|^2 R(\mathbf{k}) d\mathbf{k}, \tag{1}$$

where $\Psi(\mathbf{k},\mathbf{r}_0)$ is the Fourier Transform of $\psi(\mathbf{r},\mathbf{r}_0)$ and $\mathbf{k}$ is the spatial frequency vector.

If the specimen can be represented by a simple multiplicative transmittance, $h(\mathbf{r})$, then for a weak-phase, weak-amplitude object,

$$h(\mathbf{r}) = 1 - a(\mathbf{r}) - i\phi(\mathbf{r}), \tag{2}$$

with a and ϕ both real and $\ll 1$. The Fourier Transform of this is

$$H(\mathbf{k}) = \delta(\mathbf{k}) - A(\mathbf{k}) - i\Phi(\mathbf{k}), \tag{4}$$

where $\delta(\mathbf{k})$ is the Dirac function. For a complex amplitude at the specimen entrance plane $\psi_0(\mathbf{r},\mathbf{r}_0)$ the Fourier Transform of the image intensity is

$$S(\mathbf{k}) = \iint \Psi_0(\mathbf{k}_1)\Psi_0^*(\mathbf{k}_1+\mathbf{k})H(\mathbf{k}_2-\mathbf{k}_1)H^*(\mathbf{k}_2-\mathbf{k}_1-\mathbf{k})R(\mathbf{k}_2)d\mathbf{k}_1 d\mathbf{k}_2. \tag{5}$$

Using the abbreviated notation

$$C(m,n,\mathbf{k}) = \int \Psi(\mathbf{k}_1 - m\mathbf{k})\Psi^*(\mathbf{k}_1 - n\mathbf{k})R(\mathbf{k}_1)d\mathbf{k}_1, \tag{6}$$

then to first order the Fourier Transform of the image intensity will be

$$\begin{aligned} S(\mathbf{k}) = \delta(\mathbf{k})C(0,0,\mathbf{k}) - A(\mathbf{k})\big(C(1,0,\mathbf{k}) + C(0,-1,\mathbf{k})\big) \\ - \Phi(\mathbf{k})\big(C(1,0,\mathbf{k}) - C(0,-1,\mathbf{k})\big). \end{aligned} \tag{7}$$

The amplitude contrast transfer function (ACTF) can be identified from Eq. (7) as $C(1,0,\mathbf{k}) + C(0,-1,\mathbf{k})$ and the phase contrast transfer function (PCTF) is $C(1,0,\mathbf{k}) - C(0,-1,\mathbf{k})$. These can be evaluated for any detector response function, but if $R(\mathbf{k})$ is an odd function then the ACTF is zero for an aberration-free probe, giving a purely phase contrast image.

Results

The PCTF has been calculated for three types of detector configuration: the split detector, a quadrant detector using the difference signal from two diagonally opposite quadrants and the one-dimensional first moment detector where $R(\mathbf{k}) = k_x$. These have been calculated previously for the case of an unobstructed probe-forming aperture [6], but when using a zone plate it is necessary to prevent undiffracted zero order radiation from reaching the detector by means of a central stop. For a zone plate with a central stop obstructing a fraction a of its radius, then the function $\Psi(\mathbf{k})$ takes the form of an annulus. For simplicity we take the outer radius $k = 1$ and inner radius a.

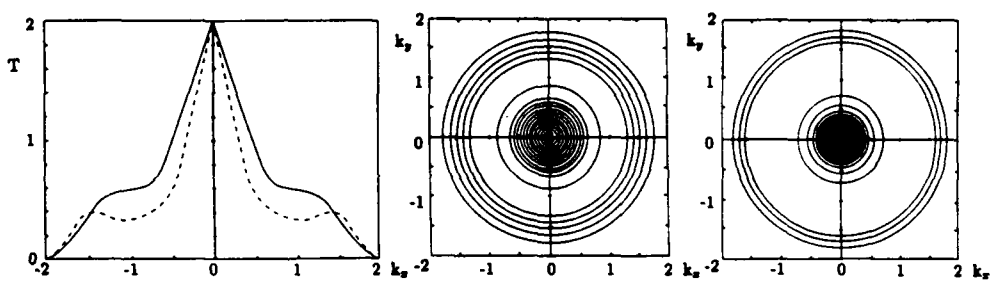

Figure 1. ACTF shown in the k_x direction and as two-dimensional contour plots for central stop sizes a=0·4 (full line and centre) and a=0·6 (dashed line and right); contour interval = 0·1.

At high spatial frequencies the PCTF in the direction of differentiation for the split and opposite quadrant detectors is identical to the ACTF for incoherent brightfield imaging (see figs. 1 and 2). At low frequencies the PCTF drops to zero, as would be expected since such a system only responds to differences in the phase shift induced by the specimen. However our main interest lies with the small detail in the specimen so the loss of the low frequency information is not so significant. The PCTF is of course also zero in a direction perpendicular to the axis of differentiation but if the signals from all four quadrants of a quadrant detector are recorded simultaneously it will be possible subsequently to form a DPC image for four different directions of differentiation, and also form the amplitude contrast image from the sum of the signals.

For high spatial frequencies the choice between absorption and phase contrast imaging can be based on the relative magnitude of phase shift to amplitude change between the feature of interest and the background medium. If the complex refractive index is $n(\mathbf{r}) = 1 - \delta(\mathbf{r}) - i\beta(\mathbf{r})$, the real and imaginary parts can be found from the Henke data [8,9] and will give the amplitude and phase transmittance,

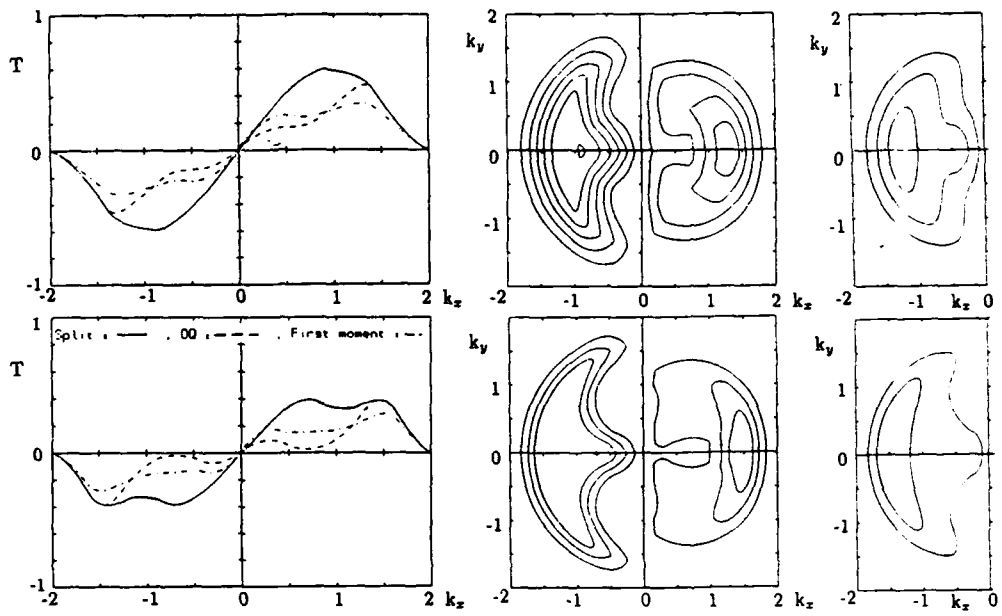

Figure 2. PCTF for central stop sizes a=0·4 (top) and a=0·6 (bottom). Shown in the direction of differentiation (left) and as two-dimensional contour plots for (left to right) the split detector, the quadrant detector where the image is formed by the difference between the signal on opposite quadrants, and the first moment detector. In each case only one half of the function is shown as it is anti-symmetric about k_y=0. Contour interval = 0·1.

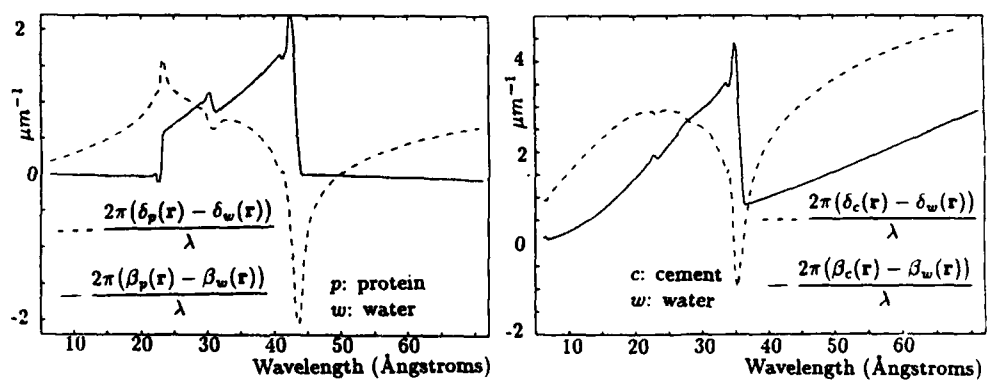

Figure 3. Amplitude and phase shifts for protein and cement in water.

$a(\mathbf{r}) = 2\pi\beta(\mathbf{r})/\lambda$ and $\phi(\mathbf{r}) = 2\pi\delta(\mathbf{r})/\lambda$. Figure 3 shows phase contrast to be significantly better than amplitude contrast at many wavelengths, especially outside the water window.

Conclusions

DPC imaging in the STXM by the use of an appropriately configured detector will allow both the amplitude and the phase contrast images to be recorded simultaneously, making prior choice of the imaging mode unnecessary. The lack of circular symmetry in the PCTF is not a disadvantage when using a quadrant detector where any of four different directions of differentiation can be chosen. The calculations presented above show the transfer characteristics for the high spatial frequencies to be as good for DPC imaging in the direction of differentiation as for amplitude imaging. However, since we will be measuring the small difference between two large signals it will be necessary to have a high brightness source to achieve satisfactory image acquisition times. Phase contrast will in many cases be greater than amplitude contrast for wavelengths shorter than in the water window, where the higher transmission and greater depth of focus will allow thicker specimens to be imaged; lower absorption can also result in less radiation dose to the specimen.

References

1. M.R. Howells, in "Synchrotron Radiation and Biophysics", Ed. S. Hasnain, Ellis Horwood, (1990), p295
2. D. Rudolph, G. Schmahl, B. Niemann, in "Modern Microscopies", eds. A.G. Michette and P. Duke, Plenum, New York, (1990), p59
3. N.H. Dekkers and H. de Lang, Philips Technical Review, **37**, 1, (1977)
4. D.K. Hamilton and C.J.R. Shephard, J.Microscopy, **133**, 27, (1984)
5. P.W. Hawkes, J. Optics (Paris), **9**, 235, (1978)
6. G.R. Morrison and J.N. Chapman, Optik, **64**, 1, (1983)
7. E.M. Waddell and J.N. Chapman, Optik, **54**, 83, (1979)
8. B.L. Henke, P. Lee, T.J. Tanaka, R.L. Shimabukuro and B.K. Fujikawa, At. and Nucl. Data Tables, **27**, 1, (1982)
9. A.R. Hare, King's College Henke Data Program, Internal document, (1987)

Real World Issues for the New Soft-X-Ray Synchrotron Sources

Brian M. Kincaid

Lawrence Berkeley Laboratory, University of California, 1 Cyclotron Road, Berkeley, California 94720

Abstract

A new generation of synchrotron radiation light sources covering the VUV, soft x-ray and hard x-ray spectral regions is under construction in several countries. They are designed specifically to use periodic magnetic undulators and low-emittance electron or positron beams to produce high-brightness near-diffraction-limited synchrotron radiation beams. An introduction to the properties of undulator radiation is followed by a discussion of some of the challenges to be faced at the new facilities. Examples of predicted undulator output from the Advanced Light Source, a third generation 1–2 GeV storage ring optimized for undulator use, are used to highlight differences from present synchrotron radiation sources, including high beam power, partial coherence, harmonics, and other unusual spectral and angular properties of undulator radiation.

Introduction

The properties of undulator radiation and undulator magnets dominate the design of the electron storage ring and the experimental apparatus planned for the new synchrotron light sources.

In a typical undulator magnet, the magnetic field on-axis can be written as $B_y(z) = B_0 \cos kz$, where $k = 2\pi/\lambda_u$. For permanent magnet systems, B_0 is proportional to the magnetization strength of the polarized magnetic material, and can be as high as 2 Tesla. An electron of energy $E = \gamma m_0 c^2$ has a sinusoidal trajectory given by $x(z) = a \cos kz$, where $a = K\lambda_u/2\pi\gamma$. The maximum deflection angle K/γ. The undulator parameter K is $\lambda_u e B_0/2\pi m_0 c^2$, having the value $0.934\, B_0(T)\lambda_u(cm)$, usually of the order of unity. For the ALS, $\gamma \simeq 3000$, so a is of the order of 10μ, which is much smaller than the electron beam dimensions of $\sigma_x = 330\mu$ and $\sigma_y = 63\mu$.

The radiation produced by a single electron is essentially that of a moving dipole. The Doppler effect for such a moving source results in an angle dependent observed wavelength, given by $\lambda = \lambda_u(1-\beta_z \cos\theta)$. Here β_z is v_z/c, with v_z being the electron's

This work was supported by the Director, Office of Energy Research, Office of Basic Energy Sciences, Materials Sciences Division, of the U. S. Department of Energy, under contract DE–AC03 – 76SF00098.

© 1991 Optical Society of America

average velocity in the z direction. The speed of the electron is constant travelling through the undulator magnetic field, so the transverse deflection of the trajectory results in a slowing down of the average z motion. This can be expressed as a reduced γ, given by $\gamma^* = \gamma/(1 + K^2/2)^{\frac{1}{2}}$. The radiation pattern is strongly peaked in the forward direction, with an opening angle of the order of $1/\gamma$, about 0.3 milliradians for the ALS. The small angle approximation may therefore be used, resulting in $\lambda = \lambda_u(1 + K^2/2 + \gamma^2\theta^2)/2\gamma^2$. Hence, the shortest wavelengths are radiated in the forward direction, with longer wavelengths radiated off-axis.

For an undulator of length $L = N\lambda_u$, the electron radiates a Doppler-compressed wave train of length $N\lambda$, resulting in a transform limited sinc^2 spectrum, with fractional linewidth $1/N$. For undulators at the new light sources, $N \simeq 100$, resulting in a one percent spectral bandwidth for each observation angle. Near the forward direction, energy within this bandwidth is radiated into a central cone with an opening angle of $\theta = 1/\gamma^*\sqrt{N} = (1+K^2/2)^{\frac{1}{2}}/\gamma\sqrt{N}$, a small fraction of $1/\gamma$, approximately 0.1 milliradian for the ALS. This is the same as the diffraction limited angular width of the radiation pattern from a line source of length L, given by $\theta \simeq (\lambda/L)^{\frac{1}{2}}$. This is because, classically, a single electron radiates a completely deterministic coherent wave field, which must obey the rules of diffraction. The peak intensity, or energy/unit solid angle, in the forward direction scales as N^2. The total energy radiated into the central cone therefore goes as N, resulting in roughly N times more spectral flux than from a bend magnet source.

If an optical system is used to form an image of the source of the central cone radiation, the diffraction limited 1-σ source size and angular divergence are $\sigma_r = \sqrt{\lambda L}/4\pi$ and $\sigma_{r'} = \sqrt{\lambda/L}$, resulting in a phase space (emittance) of $\lambda^2/4$. This is the same expression as for a single Gaussian laser mode[1]. These properties are in marked contrast to the broad spectral and angular features of bend magnet radiation.

Brightness, Flux, and Coherence

Brightness. Higher source brightness is the major performance improvement for the new light sources. Brightness is defined as source photon flux divided by the product of source area and emission solid angle[2]. It is the figure of merit for microimaging systems since it determines how much flux can be focussed onto a small target. Using a high-brightness light source, the entire central-cone undulator output can be focussed through a small entrance slit into a high-resolution grating monochromator, something not possible using present day sources. The source brightness is significantly higher for the new sources because of the small beam emittance (about a factor of ten) and the use of undulators (about another factor of N).

Flux. The total power radiated by the electron beam is proportional to $B^2\gamma^2 IL$. B is dependent on magnet technology, and is about the same for all synchrotron radiation sources. Since storage ring beam emittance grows with increasing γ, the electron beam energy must be kept relatively low (1-2 GeV) to achieve the small emittance and energy spread necessary for high brightness undulator sources. Beam current is limited by the low beam energy and the small beam size. This means that the new light sources will produce about the same flux as present sources.

Coherence. Some of the work at the forefront of x-ray optics involves the use of Fresnel zone plate lenses for microscopy and the use of the coherence of present day undulator sources for x-ray holography[3][4]. Both these techniques depend on spatial and temporal coherence. One of the major benefits expected from the new light sources is an increase in the amount of spatially coherent light, and hence an improvement in performance.

The random distribution of electrons within a stored bunch of electrons results in classical, non-laserlike, chaotic light [5]. The angular and energy spreads of the electron beam broaden the radiated spectrum. The non-zero electron beam size further reduces the brightness of the source. Spatial coherence is produced by the small electron beam, combined with the intrinsic properties of undulator radiation. Temporal coherence is strictly first order[5], determined by the combination of beam emittance, energy spread, and $1/N$.

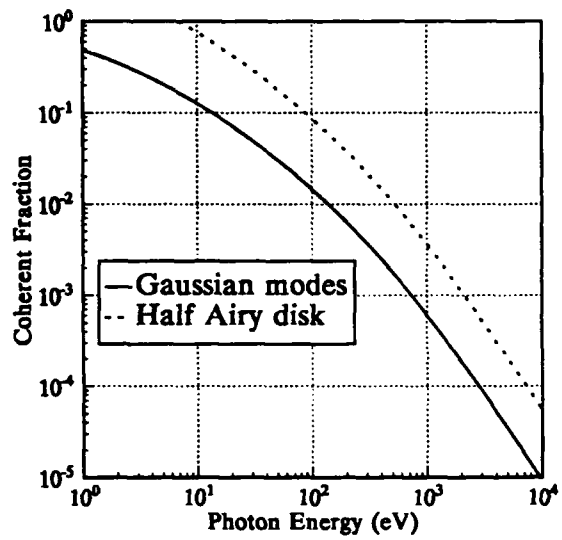

Figure 1. The coherent fraction f.

The amount of spatially coherent light is proportional to source brightness[1]. The fraction of the central-cone radiation that is spatially coherent (i.e. within a single gaussian mode) is given by[1] $f = (\lambda/4\pi)^2/\sigma_{Tx}\sigma_{Ty}\sigma_{Tx'}\sigma_{Ty'}$. Here $\sigma_{Tx} = (\sigma_x^2 + \sigma_r^2)^{\frac{1}{2}}$, $\sigma_{Ty} = (\sigma_y^2 + \sigma_r^2)^{\frac{1}{2}}$, $\sigma_{Tx'} = (\sigma_{x'}^2 + \sigma_{r'}^2)^{\frac{1}{2}}$, and $\sigma_{Ty'} = (\sigma_{y'}^2 + \sigma_{r'}^2)^{\frac{1}{2}}$. For the ALS, $\sigma_x = 330\mu$, $\sigma_y = 63\mu$, $\sigma_{x'} = 30\mu rad$, and $\sigma_{y'} = 16\mu rad$. This ratio involves only the photon wavelength, the electron beam emittance, and the undulator length. For practical optical systems using the coherence properties of the light, it is possible to use several radiation modes without significantly losing resolution, as reflected in the half-Airy-disk criterion [6]. This allows the acceptance of about six times more flux than the Gaussian mode criterion, although, at the diffraction-limited end of the spectrum it becomes unphysical, allowing more than 100% of the radiation to be coherent.

Consequences of Large K.

High Power Loading. To maximize light source performance, the longest possible straight sections and the largest N should be used, since both flux and brightness increase with N. Usually the size and number of straights in the machine are fixed, and hence the length L of the undulator. This means λ_u must decrease for N to

increase. For a fixed machine energy (γ) and operating wavelength λ, this means K must increase, requiring an increase in B. A large value of K_{max} means that a single undulator can cover a large tuning range by varying K, a desirable feature. Unfortunately, this also drives up the total power that must be handled by the first optical element in the beam line. For the ALS this can be several kW.

Harmonics. The undulator spectrum is rich in harmonics, with even harmonics forbidden by symmetry on-axis[1]. The number of significant harmonics is $n_c = (3/4)K(1 + K^2/2)$, increasing as K^3 for large K, and, the fraction of total radiated power in the first harmonic is $P_1/P_{tot} = 1/(1 + K^2/2)^2$. The maximum useful harmonic limited by undulator quality and the electron beam emittance and energy spread, so the higher harmonics are just extra heat to deal with. In addition, harmonics can pass through grating monochromator systems and show up in the output beam, and may have to be filtered out. For the ALS, undulators have been designed to produce useful output up to the 5th harmonic. So, the optimization of undulator performance can lead to difficult optical engineering problems: how to remove extra heat with thermal distortions kept to a minimum to preserve brightness

Optics Contamination. The extra power produced when central brightness and flux are maximized can pose a serious mirror contamination problem. Synchrotron radiation hitting mirror surfaces generates an intense photoelectron flux, which can lead to deposition of carbonaceous contamination, reducing the mirror reflectivity. The contamination deposition rate may be reduced by improved vacuum, but, in-situ cleaning systems probably will be necessary.

Effects on the Storage Ring. In an undulator magnet the peak mid-plane field depends on the gap between pole tips or magnet blocks, $B_y \simeq \exp(-\pi g/\lambda_u)$[7]. If the λ_u is decreased, as desired, g must decreased also to increase B and K. This means that the electron beam must pass through an increasingly long and narrow vacuum chamber. Such a small gap may make it difficult or impossible to inject beam into the storage ring or have a long stored beam lifetime.

Strong undulator fields, combined with the relatively low energy of the electron beam required, result in significant electron beam focussing effects, making it necessary to re-tune the machine when the undulator gap is varied. This may have an adverse effect on electron beam lifetime, position, or size around the ring.

Off-axis Radiation. The potential problems arising from changing the undulator gap may make it seem more practical to use off-axis radiation, using the Doppler shift to vary the wavelength rather than the undulator gap. This approach, while tempting, is fraught with difficulties. As L and N are increased, the fact that the observer of the undulator output is not infinitely far away becomes increasingly important. Typical undulator to experiment distances are of the order of 10 meters, while L can be as large as 5 meters. This places the experiment in the Fresnel region, where the variation of observation angle θ from one end of the undulator to the other results in a chirped radiation pulse. Furthermore, since the upstream end of the undulator is farther away from the observer than the downstream end, the inverse square law results in significant amplitude modulation of the chirped wave. An analysis leads to the result that if the off-axis observation angle α is greater than $\sigma_{r'}\sqrt{D/L}$, then the chirp effect broadens the narrow undulator spectral peaks[8]. For larger off-axis angles, the broadening is large enough to overlap different harmonics, and all the spectral advantages of using undulators are lost. The apparent source size $\Delta x = L \sin\alpha$ increases off-axis, decreasing source brightness. These effects might be useful, however, in lithographic imaging, where too much spatial coherence causes speckle. A better method of broadening the undulator peaks to avoid gap adjustments is to taper the undulator gap, again producing a chirped wave, but without as serious a brightness penalty.

Tuning for Spatial Coherence.

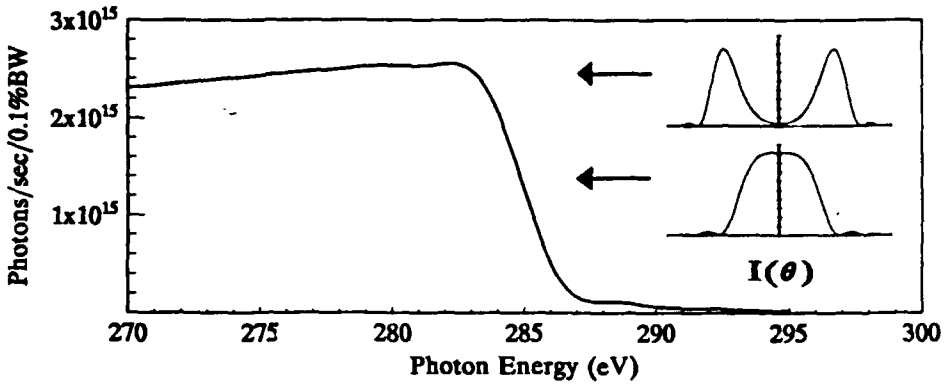

Figure 2.

The amount of spatial coherence is a sensitive function of wavelength. Figure 2. shows the angle integrated spectrum for the first harmonic of ALS undulator U5 with $K = 1$, for photon energies near the carbon K-edge. This spectrum is what might be observed after opening up the entrance slits of a high-resolution monochromator in an attempt to coordinate the undulator gap, the beam position, and the monochromator setting to maximize spatially coherent light output. The best spatially coherent flux is produced at the exact fundamental photon energy, indicated by the lower arrow. Even though the total flux is greater at the peak of the curve at slightly lower photon energy, the radiation pattern has a hole in the center, and a larger total opening angle, certainly not well described by a Gaussian mode. This results in a significantly smaller coherence fraction.

More work is needed in the area of imaging undulator radiation and the spatial coherence of undulator radiation. The theory of brightness propagation using Wigner distributions in principle includes all of above, but the theory has not been developed beyond its initial formulation[1].

Conclusions

To make use of the improved performance promised for the new light sources, users needing spatially coherent light must have adjustable gap, long length, short period undulators. This leads to the requirement for high quality, high heat load optics, and for the control of surface contamination. Beam position stability is a must, and beam position feedback and thermal stability systems should be built in from the outset. To be able to adjust a beam line for desired coherence properties, the user must have control of electron beam position and angle in the undulator, as well as the alignment of optical elements in the beam line. Accurate and reproducible calibration of both the undulator and monochromator is mandatory Techniques must be developed for dealing with small, high-power beams of invisible radiation. The use of off-axis radiation to avoid changing the undulator gap should be eschewed, although undulatory tapering may have its uses. These requirements will have a major impact on the design and operation of the new soft x-ray light sources.

References

1. K.-J. Kim "Characteristics of Synchrotron Radiation", in AIP Conference Proceedings 184, Physics of Particle Accelerators, Vol. 1, M. Month and M. Dienes, eds. (American Institute of Physics, New York, 1989).
2. M. Born and E. Wolf Principles of Optics, 4th Ed. (Pergamon Press, Oxford, 1970).
3. J. Kirz and D. Sayre "Soft x-ray microscopy of biological specimens", in Synchrotron Radiation R search, H. Winick and S. Doniach, eds. (Plenum Press, New York, 1980).
4. C. Jacobsen, M. R. Howells, J. Kirz, and S. Rothman, "X-ray holographic microscopy using photoresists" JOSA A 7,1848 (1990).
5. R. Loudon, The Quantum Theory of Light, 2nd Ed. (Clarendon Press, Oxford, 1983)
6. J. W. Goodman, Statistical Optics, (Wiley, New York, 1985), p. 227.
7. K. Halbach, "Permanent Magnet Undulators" in Proceedings of the 1982 Bendor FEL Conference, Journal de Physique 44, C1-211 (1983).
8. R. P. Walker "Near field effects in off-axis undulator radiation", Nucl. Inst. and Meth. A267 (1988).

High-Performance Multilayer X-Ray Optics

D. G. Stearns and R. S. Rosen

Lawrence Livermore National Laboratory, P.O. Box 808, Livermore, California 94550

S. P. Vernon

Vernon Applied Physics, P.O. Box 10469, Torrance, California 90505

ABSTRACT

We review the state-of-the-art in multilayer (ML) coatings for high normal incidence reflectivity at soft x-ray wavelengths. In particular, Mo-Si ML and Ru-B_4C ML grown by magnetron sputtering have demonstrated normal incidence reflectivities as high as 64% at 130 Å and 20% at 70 Å respectively. A strong dependence of the Mo-Si layer morphology on the sputtering gas pressure is observed, and is directly correlated with the normal incidence x-ray reflectivity. We consider issues relevant to the deposition of multilayers on figured imaging optics, and describe recent measurements of the normal incidence reflectivity of spherical substrates coated with Mo-Si ML.

INTRODUCTION

Multilayer x-ray optics are becoming increasingly important in diverse applications such as x-ray projection lithography[1], x-ray laser cavities[2], x-ray microscopy[3], astronomy[4] and spectroscopy[5]. In this paper we focus on the current development of normal incidence reflective optics for the soft x-ray spectrum of ~45 - 130 Å. The ultimate goal is to develop a soft x-ray imaging system capable of high throughput and diffraction-limited performance over an appropriate image field.

The fundamental requirements of high performance multilayer coatings include high reflectivity and long term stability in potentially hostile environments. Furthermore, the development of a practical x-ray imaging system requires the controlled deposition of multilayer coatings on large-area figured optics. Achieving success in these areas is extremely challenging due to the nature of x-ray multilayer coatings. The structures are composed of ultrathin (~10 -100 Å), alternating layers of dissimilar materials such as Mo and Si, chosen to have the greatest possible difference in the index of refraction at the wavelength of interest, while at the same time minimizing absorption. The multilayer stack can consist of anywhere from ~10 to several hundred bilayers.

Proceedings on Short-Wavelength Coherent Radiation, 152
Vol. 11, Philip H. Bucksbaum and Natale M. Ceglio (eds.)
© 1991 Optical Society of America

A net reflectivity of order unity is achieved by the constructive interference of the fields reflected at each interface, resulting in a dispersion condition analagous to Bragg diffraction from a one-dimensional crystal lattice. The x-ray wavelength λ is related to the multilayer period Λ (the bilayer thickness) and the angle of incidence θ (as measured from the normal) by Bragg's law: $\lambda \cong 2\Lambda\cos\theta$. To achieve optimum reflectivity the interfaces at the layer boundaries must be smooth and abrupt. Any average composition variation across the interface, due to either roughness, interdiffusion or compound formation, can result in significantly reduced reflectivity[6].

We have established a comprehensive research program at Lawrence Livermore National Laboratory (LLNL) to develop high performance reflecting optics for the soft x-ray regime. In view of the important issues discussed above, we believe that progress towards the goal of developing efficient, diffraction-limited x-ray optics requires a thorough understanding of the fundamental physics underlying the growth and structure of the multilayer films. To this purpose we have assembled a broad range of capabilities, both at LLNL and in collaboration with other institutions, which includes thin film deposition, structural characterization, x-ray optical characterization and computer modeling of the multilayer performance.

HIGH REFLECTIVITY ML COATINGS

The ML are deposited onto polished substrates using dc magnetron sputtering in an Ar plasma discharge[7]. The substrates are mounted on a rotating platter and are alternately exposed to two large rectangular (12 x 25 cm) sources. The source-to-substrate separation is typically 6 cm. The rotation speed of the platter is adjusted to control the layer thicknesses. In addition, the substrates are spun at ~4 Hz to average out any spatial inhomogeneities in the flux of the depositing species.

A typical Mo-Si ML coating deposited onto a [100] single-crystal Si wafer is shown in Fig. 1. The ML consists of 40 layer pairs with period Λ=68Å and a ratio of the Mo layer thickness to the period of γ=0.5. A high resolution electron micrograph[8] of the ML microstructure is shown in Fig. 1a, where the dark and light bands correspond to Mo and Si respectively. The Mo layers are polycrystalline, having a [110] texture in the growth direction, and the Si layers are amorphous. The pure layers are separated by thin, asymmetric interfacial regions[9] of mixed composition. It has been suggested[10] that the intermixing at the interfaces is the major limitation to achieving the theoretical highest reflectivity in the Mo-Si system. The normal incidence reflectivity of this Mo-Si ML, measured using synchrotron radiation[11], is shown in Fig. 1b. The ML exhibits a peak reflectivity of 64% at 130 Å and has a bandwidth defined as the full-width-at-half-maximum of 5.6 Å. The theoretical reflectivity, calculated using optical constants from Henke et al.[12] and assuming ideally smooth and abrupt interfaces, is shown as the dashed curve and has a maximum value of 72%.

It has been found that the ML morphology has a striking dependence on the sputtering gas pressure, exhibiting a transition from layer growth at lower pressures to columnar growth at higher pressures. This effect can be seen in

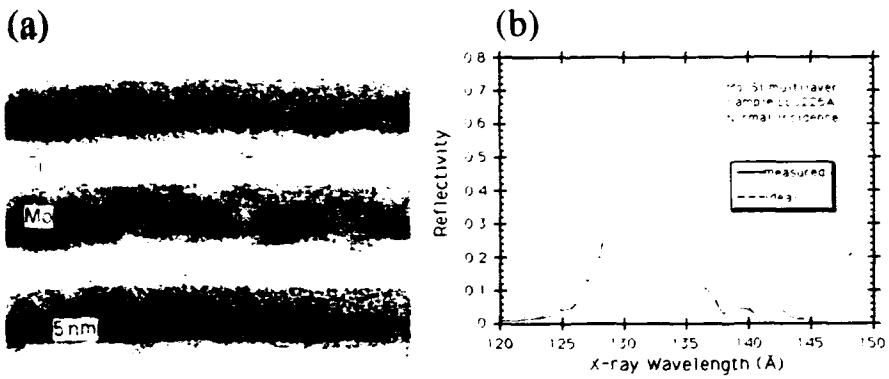

Figure 1. (a) HREM cross-sectional image of a Mo-Si ML having a period of Λ=68 Å. The substrate is oriented below the figure. (b) Measured normal incidence reflectivity (solid curve) and reflectivity calculated (dashed curve) assuming ideal interfaces.

Fig. 2 where we show a sequence of HREM images of ML grown at Ar pressures ranging from 2.5 to 20 mtorr. As the pressure is increased amplifying roughness is observed thoughout the ML stack, eventually leading to columnar growth and complete disruption of the layer structure at the highest pressures. We attribute this behavior to the variation with gas pressure of the energy deposited at the growth surface[7]. At lower pressures there is less thermalization of the sputtered atoms and reflected Ar neutrals so that they are incident on the substrate with greater kinetic energy, thereby locally heating the substrate surface. The increased surface temperature enhances the surface mobility of the adatoms, accomodating an approach to the equilibrium configuration which corresponds to layer formation in this system. The variation in the normal incidence reflectivity is found to strongly correlate with the observed variation in layer morphology. The peak reflectivities, plotted in Fig. 3, range from over 60% at 2.5 mtorr to less than one percent at 20 mtorr. It is evident that the optimal reflectivity is achieved at the lowest sputtering gas pressures.

Our efforts are currently directed at developing high-performance multilayer coatings for normal incidence reflectivity throughout the x-ray wavelength range of 45 - 130Å. One promising material combination for x-ray wavelengths below 124 Å (where Mo-Si is no longer viable due to increased absorption in the Si) and above 65 Å (the boron K-edge) is Ru-B_4C[13]. A typical Ru-B_4C ML coating, deposited onto a [100] Si wafer at a sputtering gas pressure of 1.5 mtorr, is shown in Fig. 4. The ML consists of 150 layer pairs with a period of Λ=36.4 Å and γ=0.4. An HREM image of the microstructure, shown

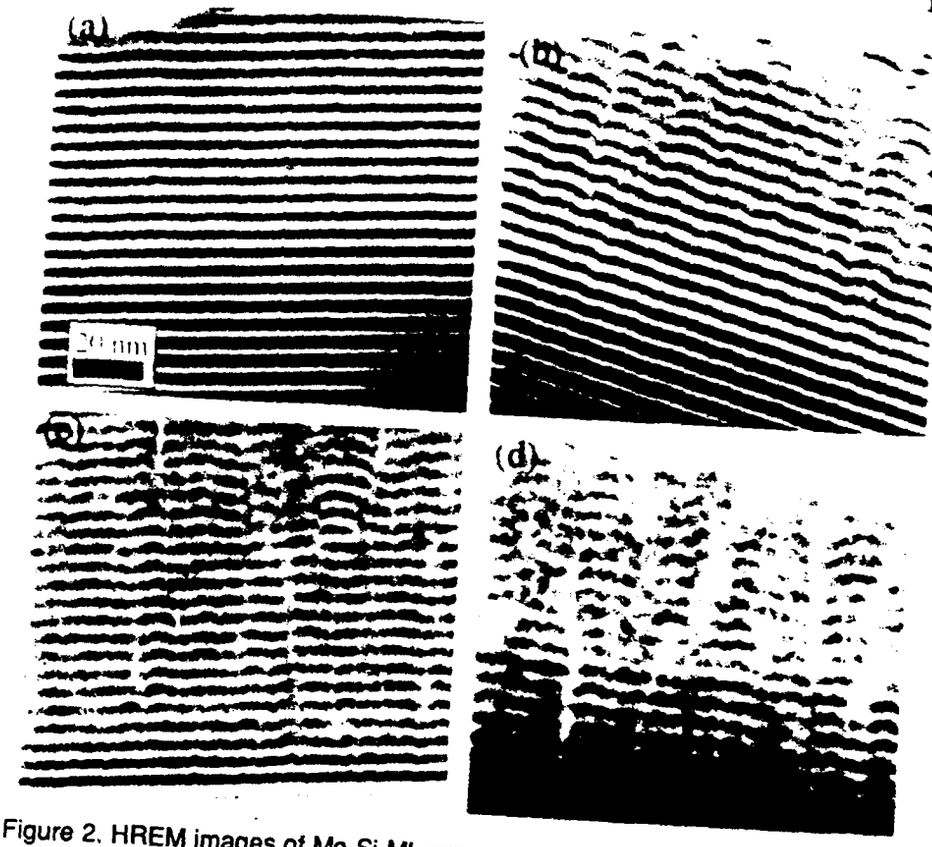

Figure 2. HREM images of Mo-Si ML grown at different sputtering gas pressures: (a) 2.5 mtorr, (b) 5.0 mtorr, (c) 10 mtorr, (d) 20 mtorr. The substrate is oriented below each image.

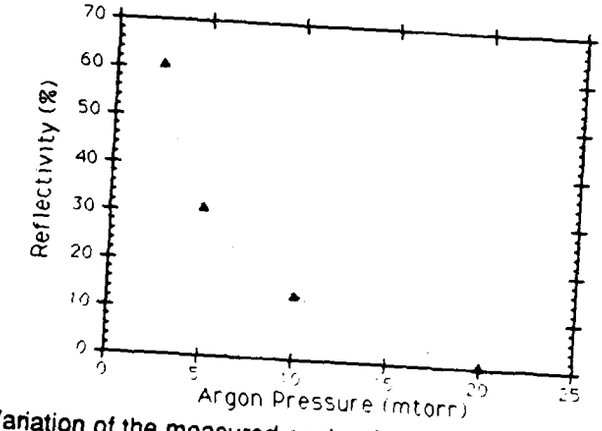

Figure 3. Variation of the measured peak reflectivity of Mo-Si ML as a function of the sputtering gas pressure.

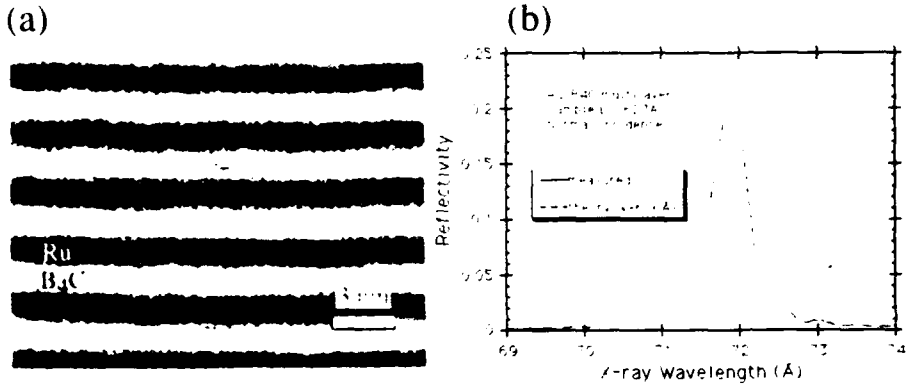

Figure 4. (a) HREM cross-sectional image of a Ru-B_4C ML having a period of Λ=34 Å. The substrate is oriented below the figure. (b) Measured normal incidence reflectivity (solid curve) and reflectivity calculated (dashed curve) assuming an RMS interface roughness of σ=6.9 Å.

in Fig. 4a, indicates that the layers are fairly smooth and compositionally abrupt. Both the Ru and B_4C are in amorphous phases. The measured normal incidence reflectivity is shown in Fig. 4b. The ML reflectivity has a maximum value of 20% at 72 Å and a bandwidth (FWHM) of 0.55 Å. The dashed curve in the figure represents the best fit to the data, and was calculated assuming an RMS interface roughness of σ=6.9 Å. The theoretical peak reflectivity of a ML having ideally smooth and abrupt interfaces is 48%.

ML-COATED FIGURED OPTICS

Perhaps the greatest challenge in fabricating multilayer x-ray optics involves the controlled deposition of a designed coating onto a large-area figured substrate. For normal incidence optics, the operational x-ray wavelength will dictate the period of the multilayer structure according to $\Lambda \cong \lambda/2$. Depending on the angular dispersion of the optical system, it might also be necessary to grade the coating, i.e. vary the multilayer period across the surface of the substrate in some well-defined manner. In order to maintain high throughput at the wavelength of interest, the relative error in the multilayer period $\Delta\Lambda/\Lambda$ must be less than the bandpass of the multilayer $\Delta\lambda/\lambda$. Furthermore, to achieve diffraction-limited x-ray imaging, figure errors introduced by variations in the total thickness of the multilayer coating are not allowed to exceed $\lambda/4$. Together these requirements impose severe tolerances on the uniformity of the multilayer coating.

To derive a simple estimate of the uniformity requirements, let us assume that the goal is to deposit a uniform ML coating on a perfectly figured substrate, to yield a maximum normal incidence reflectivity at wavelength λ across the

entire surface. We expect that due to deposition error the actual period of the ML coating will vary from point to point on the surface. An error $\delta\Lambda$ in the ML period will degrade the imaging properties of the optic in two ways. First, the ML bandpass will shift so that the reflectivity at the operating wavelength λ is reduced. This effect we call "detuning". We require that the shift of the bandpass $\delta\lambda=2\delta\Lambda$ be less than one fourth of the full width of the bandpass $\Delta\lambda$. This is given approximately by $\Delta\lambda=\lambda/N$, where N is the number of bilayers. Hence to avoid detuning the fractional error in the ML period must be held to within $\delta\Lambda/\Lambda < 1/4N$.

The second detrimental effect of an error in the ML period is to locally distort the figure of the optical surface, resulting in a change of the phase of the reflected field. This effect we call "dephasing". The position of the surface of the ML-coated optic changes by an amount $N\delta\Lambda$, causing a change in the phase of the reflected field of $4\pi N\delta\Lambda/\lambda$. However, this change in phase is partially mitigated by a phase shift associated with the detuning of the ML bandpass. It can be shown that the period error $\delta\Lambda$ results in a phase shift of $-2\pi N\delta\Lambda/\lambda$, which is opposed to and just half of the value of the change in phase caused by the altered figure. We require the net change in phase of the reflected field to be less than an eighth wave (a typical error budget for a single optic in a compound system). Hence we conclude that the fractional error in the ML period must be held to within $\delta\Lambda/\Lambda < 1/4N$. It is interesting to note that in this simplistic treatment the requirements for avoiding detuning and dephasing are identical.

The implication of the uniformity requirements on the ML deposition can be illustrated in a few examples. Consider a Mo-Si ML coating operating at 130 Å with Λ=67 Å and N=40. Using the criteria derived above, the tolerance on the ML period error is $\delta\Lambda$<0.4 Å. In simple terms, the period of the ML coating must be held constant across the entire surface of the optic to within a fraction of an angstrom. As the x-ray wavelength decreases, the tolerance becomes more severe for two reasons: the ML period must decrease *and* the number of periods increases rapidly as the index of refraction approaches unity. For example, a Ru-B_4C ML coating operating at 70 Å, where Λ=34 Å and N=150, requires a tolerance in the ML period error of $\delta\Lambda$<0.06 Å! It is possible to somewhat relax the tolerance by decreasing the number of periods at the expense of the peak reflectivity. However, it is evident that fabrication of diffraction-limited imaging optics for wavelengths less than ~100 Å will require extremely precise control of the ML deposition.

We have studied the issue of ML uniformity in a series of recent experiments. A variety of figured substrates have been coated with Mo-Si ML (Λ~67 Å, N=40) designed to provide a maximum normal incidence reflectivity at λ~130 Å. Our strategy for achieving uniform coatings was to use large targets (12 x 25 cm) located in close proximity (6 cm) to the substrates, and to spin the substrates to average out spatial variations in the deposition rate. In this way we have avoided the inconvenience of tailoring the spatial distribution of the

deposit for a particular substrate by incorporating baffles or masks. The normal incidence reflectivity of the ML-coated figured optics has been measured using synchrotron radiation at the BESSY facility. A vacuum reflectometer was modified to allow measurements on curved surfaces within ~0.8° of normal incidence, providing excellent spectral resolution ($\lambda/\Delta\lambda$ ~ 100-1000) and spatial resolution (spot size ~ 150-um-diameter). The normal incidence reflectivity was measured as a function of x-ray wavelength for an array of points across the surface of the optic.

The reflectivity measured on a 2-inch-diameter spherical optic composed of zerodur and having a 60 cm radius of curvature is presented in Fig. 5. The measurements were made for an array of points across a diameter of the optic to within a few millimeters of the edges. The peak reflectivity, shown in Fig. 5a, has an average value of 62% at 138 Å and is uniform to within ±1.6% across the entire surface. By fitting the reflectivity versus wavelength data we were able to determine values for the ML period Λ at the different test points and these are plotted in Fig. 5b. The ML period has an average value of 70.1 Å and is uniform over the central 40 mm section to within ±0.5%. The dashed horizontal lines represent the ±0.4 Å uniformity requirment for achieving diffraction-limited performance. The variation in the ML period is well within the tolerance except near the very edge of the optic. We attribute the decrease in the period at the edge to shadowing by the mounting fixture during deposition.

As another example, Fig. 6 presents the results for a 3-inch-diameter spherical, fused silica substrate having a 100 cm radius of curvature. The peak reflectivity, shown in Fig. 6a, has an average value of 57% at 129 Å and is uniform to within 5.6% across the surface. We believe that the lower reflectivity is associated with an increased surface roughness of the substrate. The ML period is 65.4 Å and is uniform to within 0.6%. Once again the period is found to be well within the ±0.4 Å uniformity requirement over the entire diameter of the optic (>60 mm), except near the edges. These initial results demonstrate the feasibility of depositing ML coatings on precision substrates for optimum normal incidence reflectivity at λ~130 Å without compromising the diffraction-limited imaging performance of the optics.

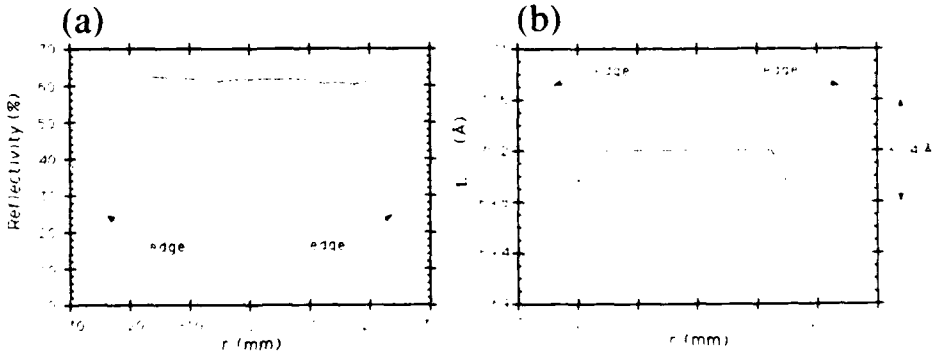

Figure 5. Characterization of a 2-inch-diameter spherical optic (R=60 cm) coated with Mo-Si ML. (a) Normal incidence reflectivity measured across the diameter of the optic. (b) Variation of the ML period.

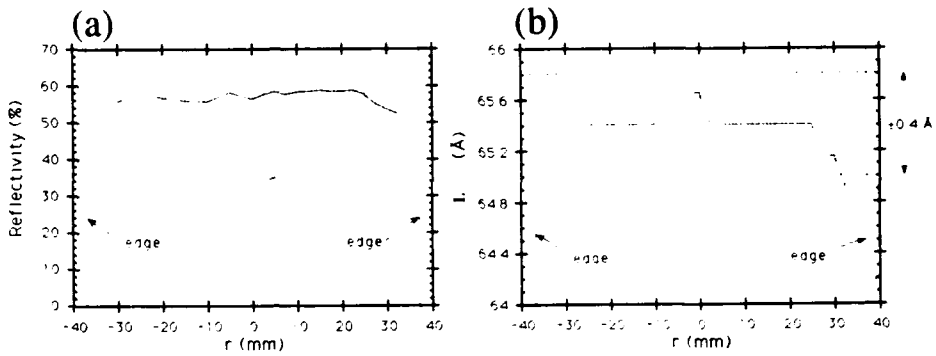

Figure 6. Characterization of a 3-inch diameter spherical optic (R=100 cm) coated with Mo-Si ML. (a) Normal incidence reflectivity measured across the diameter of the optic. (b) Variation of the ML period.

ACKNOWLEDGMENTS

We thank J. Hayes, B. Cook and M. Viliardos for their assistance in the ML deposition. The HREM results were obtained at the Facility for High Resolution Electron Microscopy within the Center for Solid State Scince at Arizona State University. The HREM samples were prepared by Y. Cheng and were viewed by D. J. Smith. The normal incidence x-ray reflectance measurements were accomplished through a collaborative association with the VUV Radiometric Laboratory of the Physickalisch Technische Bundesanstalt (PTB) at the Berlin Electron Storage Ring (BESSY). The principal collaborators were M. Kuhne and P. Muller from the PTB, D. Gaines from Brigham Young University and N. Ceglio from LLNL. This work was performed under the auspices of the U. S. Department of Energy by LLNL under contract No. W-7405-Eng-48.

REFERENCES

1) J. E. Bjorkholm, J. Bokor et al., J. Vac. Sci. Technol. B, **8**, 1509 (1990).
2) N. M. Ceglio, D. G. Stearns et al., Opt. Lett., **13**, 108 (1988).
3) J. A. Trail and R. L. Byer, Opt. Lett., **14**, 539 (1989).
4) A. B. C. Walker, Jr., T. W. Barbee, Jr. et al., Science, **241**, 1781 (1988).
5) M. Finkenthal, A. P. Zwicker et al., Appl. Opt., **29**, 3467 (1990).
6) D. G. Stearns, J. Appl. Phys., **65**, 491 (1989).
7) D. G. Stearns, R. S. Rosen and S. P. Vernon, to be published in J. Vac. Sci.Technol. A.
8) A. K. Petford-Long, M. B. Stearns et al., J. Appl. Phys., **61**, 1422 (1987).
9) D. G. Stearns, N. M. Ceglio et al., Proc. SPIE, **688**, 91 (1986).
10) D. L. Windt, R. Hull and W. K. Waskiewicz, in this proceedings.
11) M. Kuhne, K. Danzmann et al., Proc. SPIE, **688**, 76 (1986).
12) B. L. Henke, J. C. Davis et al., Lawrence Berkeley Laboratory Internal Report LBL-26259, (November, 1988).
13) D. G. Stearns, R. S. Rosen and S. P. Vernon, Mat. Res. Soc. Symp. Proc. (Boston, Fall, 1990) in press.

Soft X-ray Optic For An Efficient Laser Plasma Spectrometer

S.C.Davey[a], *R.R.Freeman*[a], *T.J.McIlrath*[b], *L.D.vanWoerkom*[c], *W.K.Waskiewicz*[a] and *T.Lucatorto*[d]

a AT&T Bell Laboratories, Murray Hill, NJ
b IPST, University of Maryland, College Park, MD
c Lawrence Livermore National Laboratory, Livermore, CA
d NIST, Gaithersburg, MD

ABSTRACT: A soft x-ray figured optic has been incorporated into a spectrometer with a multi-channel detector to enhance signal levels from short pulse laser produced plasmas.

Laser produced plasmas are a source of soft x-rays but their usefulness is limited by their relatively small time averaged fluxes. To increase the utility of these sources a spectrometer has been designed which incorporates a figured multilayered soft x-ray optic and a multi-channel detector.

The x-ray optic is used to collect the plasma emission and focus it onto the input slit of a grazing incidence monochromator. The portion of the radiation that can be collected with the x-ray optic is much greater than can be collected by the input slit alone of a conventional monochromator. The Mo/Si multilayer optic used was matched to the input f/50 acceptance of the spectrometer. Figure one shows the increased signal level of the emission from a gold plasma obtained with the optic. A soft x-ray linear detector and amplifier from NIST has also been installed on the spectrometer. Figure two shows a typical reflected spectrum measured with the multi-channel detector. Spectra acquisition times have been dramatically reduced with the x-ray optic and the linear detector.

Another important feature of this system is that since entire spectra are obtained at one time data can be discriminated by plasma emission variations. This enables that some shot-to-shot type variations can be normalized out. A demonstrated of this is in the measurements of the soft x-ray absorption of Kr. Figure three shows the spectrum of the emission of a gold plasma reflected from a near normal incidence spherical multilayer optic when the target chamber has been filled with a low pressure of Kr. The signal with gas has been normalized to the signal without gas and is shown in figure four. These results will be compared to synchrotron based measurments of absorption features.

The use of a x-ray optic and linear detector have enhanced signal levels, decreased acquisition times and enabled single shot spectra acquistions which will make the short pulse laser plasma emission a viable source for a broader range of experiments.

Fig. 1 Gold plasma soft x-ray emission spectra measured with a conventional single slit detector. The top graph shows the direct signal from the plasma and lower graph shows the signal level of the beam that has been collected and focused with the multilayer optic.

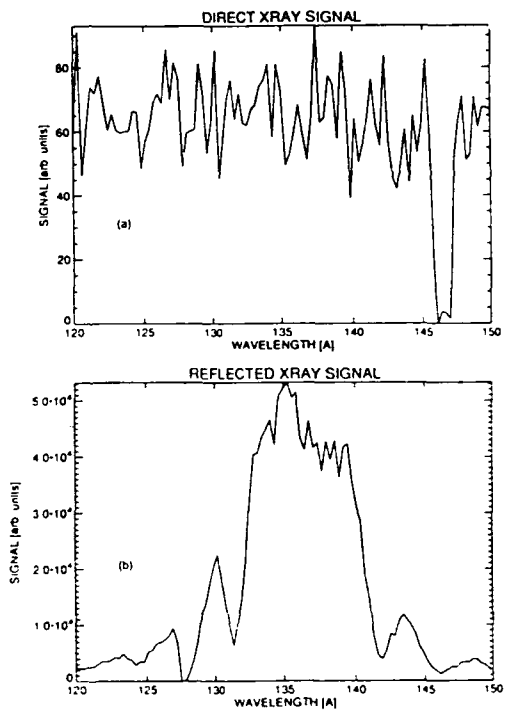

Fig. 2 Reflected spectra measured with a multi-channel detector.

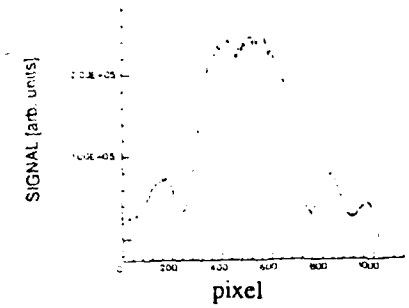

Fig. 3 Reflected spectra with Kr absorption features.

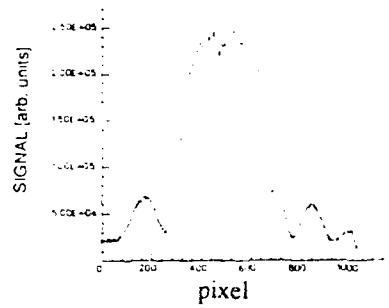

Fig. 4 Normalized Kr absorption, data in figure 3 divided by the data in figure four.

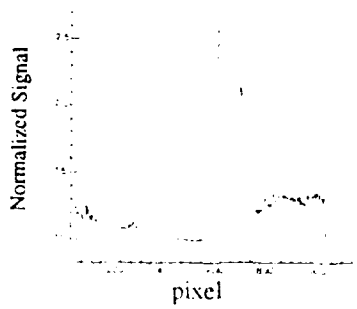

Feasibility of X-Ray Nonlinear Resonant Effects in Plasma

P. L. Shkolnikov and A. E. Kaplan

Department of Electrical and Computer Engineering,
The Johns Hopkins University, Baltimore, Maryland 21218

Abstract

We demonstrate the feasibility of the experimental observation of saturation related third-order X-ray nonlinear resonant effects in plasma.

Recent developments in X-ray laser (XRL) research resulted in the experimental observation of laser amplification at many wavelengths in the soft X-ray domain [1] ranging from $\lambda = 28$ nm to $\lambda = 4$ nm. Within the next few years powerful sources of coherent XRL radiation at those wavelengths will also be available. This sets a stage for the research on the interaction of intense coherent X-ray radiation with matter, in particular on X-ray nonlinear optics.

The first obvious choice of the environment for the X-ray resonant nonlinear effects (XRNE's) to occur and to be experimentally observed, is the plasma consisting of the same ions that give rise to the laser action itself. XRNE's in these situations are expected to be essentially similar to nonlinear effects due to other resonantly-enhanced nonlinear interaction of light with matter in a visible optical domain. In this paper we present evaluation of the saturation intensity and nonlinear refractive index for the soft X-rays in the Se XXV and Mo XXXIII XR laser and laser-like plasmas.

The strongest nonlinear X-ray interactions may occur in the active XRL plasma e. g. in the neonlike Se or Mo plasma, during X-ray lasing. However, from the point of view of studying XRNE's as such, i. e. in a situation in which they do not intervene with the lasing process, it would be more instructive first to investigate plasma which consists of the same ions as the respective XRL, but with electron density N_e not high enough to excite laser action. This assumption also significantly simplifies [2] the problem. In particular, it allows us to neglect collision rates for the transitions near the neonlike ground state, and to take into account only the levels coupled by X-ray radiation of interest. The stability of neonlike plasmas in a wide range of N_e assures that the fraction of the neonlike ions f_{Ne} in the plasma will remain almost unchanged. In the absence of any external pumping radiation between ground level and 3p-3s levels, such low electron density cannot provide any significant 3s-3p levels population (see e. g.. [3] for Kr), and therefore no interaction with the XRL radiation resonant to 3s-3p

Vol. 11, Philip H. Bucksbaum and Natale M. Ceglio (eds.)
© 1991 Optical Society of America

transitions can be observed. However, XRNE's can be made feasible if the 3s level is populated, e. g. by the powerful radiation resonant to the transition between 3s and the ground levels. This radiation is conveniently originated from the radiative decay of the 3s level in the XRL.

As a result, our model could be restricted to only three levels: the upper (u) and the lower (l) XRL levels, and the neonlike ground level (g). Levels u and l in this low density plasma will be coupled by the XRL radiation with the resonant frequency; we will be interested in the absorption saturation and nonlinear refraction at that transition. Level l will be populated by sufficiently strong (incoherent) pumping radiated as a "side product" by the respective XRL as a result of the decay of its level l into its ground level g. Two examples will be considered: Se XXV as the medium of the most successful XRL so far [1], [4] (the line with the wavelength $\lambda_{ul}=20.638$nm), and Mo XXXIII where gain for the X-ray with one of the shortest wavelengths in the neonlike sequence has been recently reported [4] ($\lambda_{ul}=10.64$nm).

The first important problem to be solved is the choice of the electron temperature T_e. To have a meaningful estimate, we choose $T_e \simeq \frac{1}{2}\lambda$ (the temperature of the lasing plasmas [5-7]). The ion temperature $T_i=0.4T_e$ [5], yielding $T_i \simeq 400$eV for Se and 800 eV for Mo). For these temperatures , f_{Ne} may be assumed to be 0.3 and 0.1 for Se and Mo, respectively [5]. Dividing f_{Ne} by the average ion charge, one obtains the ratio α of neonlike ion density N_i to N_e equal to 0.02 for Se and to 0.005 for Mo. Collision rates can be neglected if $N_e << A_{ik}/C_{ik}$ where A_{ik} and C_{ik} are the radiative and downward collisional rate coefficients for transitions of interest [2], respectively. The atomic data from [5-8] as well as the principle of detailed balance (required to obtain downward collisional rate coefficients from upward ones [9]) yield $N_e \simeq 10^{18}\text{cm}^{-3}$ for Se plasma and $N_e \simeq 10^{19}\text{cm}^{-3}$ for Mo plasma.

Two-level models [10,11] modified to take into account the level degeneracy [12] and the inhomogeneous broadening [13], result in the following set of equations. At first, for the dimensionless $l-$ level population in the absence of the XRL radiation $\beta \equiv N_l/N_i$ (N_l denotes the population density of the $l-$ level) we have:

$$\beta=(\pi\ln 2)^{1/2}(1+g_l^{-1})^{-1}\Delta_{lg}r_{lg}(1+r_{lg})^{-1/2}, \tag{1}$$

where Δ_{lg} is the ratio of the Lorentzian full width on half maximum $\Delta\nu_{lg}$ to the Doppler width, $\Delta\nu_{lg}^D \equiv 2\nu_{lg}[(2kT_i/M_ic^2)\ln 2]^{1/2}$, for the $l-g$ transition, ν_{lg} being the central frequency; M_i is the mass of the ion; $r_{lg}\equiv I_{lg}/I_{lg}^s$ is the dimensionless pumping intensity with $I_{lg}^s=4\pi^2hc\,\Delta\nu_{lg}\lambda_{lg}^{-3}(1+g_l)^{-1}$ being the $l-g$ "saturation intensity"; g_l is the statistical weight of the level l. This equation is valid unless r_{lg} is large enough (>50) to destroy the implied Doppler broadening predominance. It is worth noting that no significant absorption of the pumping photons with the energy $h\nu_{lg}$ by the <u>excited</u> neonlike ions is expected, since the energy $2h\nu_{lg}$ is significantly higher than the ionization potential of these ions.

For the absorption coefficient $\gamma(\nu)$ of the incident radiation with the frequency ν one obtains:

$$\gamma(\nu)=\gamma_0\frac{\text{Re}\ w(x+ib)}{\sqrt{1+r}},\ \gamma_0\equiv\frac{\sqrt{\pi\ln 2}}{4\pi^2}\frac{\lambda_{ul}^2A_{ul}}{\Delta\nu_{ul}^D}\frac{g_u}{g_l}\beta\alpha N_e, \tag{2}$$

where λ_{ul} is the central wavelength of the transition; $b\equiv(\ln 2)^{1/2}\Delta_{ul}(1+r)^{1/2}$ describes the degree of homogeneous broadening; $r\equiv I/I_{ul}^s$ and $x=2(\ln 2)^{1/2}(\nu_{ul}-\nu)/\Delta\nu_{ul}^D$ are the dimensionless XRL radiation intensity and detuning , respectively; $I_{ul}^s=4\pi^2hc\,\Delta\nu_{ul}\lambda_{ul}^{-3}$; $w(x+ib)$ denotes the complex error

function (see e. g. [13]). Finally, the nonlinear correction $\Delta n^{NL}(r) = n(r) - n(r=0)$ to the refractive index n(r) can be written as:

$$\Delta n^{NL} = (4\pi)^{-1}\lambda_{ul}\gamma_0[\mathrm{Im}\ w(x+ib) - \mathrm{Im}\ w(x+ib_0)],\ b_0 \equiv b(r=0) = \sqrt{\ln 2}\,\Delta_{ul}, \quad (3)$$

In our calculations we assume that the homogeneous linewidths are determined mainly by the lifetime of the $l-g$ transitions (similar to [14]), so that $\Delta\nu_{ul} = \Delta\nu_{lg} \simeq A_{lg}/2\pi$. Given the transitions probabilities $A_{lg} \simeq 3.9\times10^{12}(1.1\times10^{13})$ and $A_{ul} \simeq 7.7\times10^{9}(7.2\times10^{10})$, and plasma conditions, one can obtain following estimations for Se (Mo) plasma. Pumping intensity $I_p \simeq 10^{13}(10^{14})\mathrm{W/cm^2}$ is required to attain $\beta = 0.1$. Such population yields the absorption coefficient at the central u-l frequency $\gamma(\nu_{ul}) \simeq 1.5(0.5)\mathrm{cm}^{-1}$, with the "saturation intensity" $I^s_{ul} \simeq 6\times10^7(10^9)\mathrm{W/cm^2}$. The nonlinear part of refractive index is $\Delta n^{NL} \simeq 3\times10^{-8}(10^{-8})$ for $I = 3\times I_s$ and dimensionless detuning $x = 0.8$ (such detuning corresponds to the frequency ν being within the kernel of the Doppler lineshape).

Our calculations of nonlinearities in the laser active medium show that at least for Se XRL they should be very large; this conclusion does not depend on any specific model. Indeed, the power of the order of 1 MW per line and the source size $\simeq 200\mu$m [4] mean that the intensity $I \simeq 2\times10^9\mathrm{W/cm^2} \simeq 35\times I^s_{ul}$ has been reached in the Se plasma. According to Eq. (2), this decreases the gain coefficient γ by factor up to 20. (This result remains almost the same even if in addition to the lifetime of the $l-g$ transitions, as above, the collision dephasing time $\simeq 4\times10^{-13}$sec [15] is taken into account). Therefore, the discrepance between the calculated ($38\mathrm{cm}^{-1}$) and measured ($5\mathrm{cm}^{-1}$) small-signal gain coefficients [5] could be attributed at least in part to the gain saturation. Furthermore, even assuming the measured small-signal gain coefficient for γ_0, one obtains from Eq. (3) that for the intensities existing inside the Se XRL, the nonlinear correction to the refractive index can become fairly large in the X-ray domain, $\Delta n^{NL} \simeq 8\times10^{-8} - 2\times10^{-7}$. This nonlinear refractive index may result in the significant change ($\simeq 2\pi$ across the beam) in the phase front of the wave at the length $L_{NL} = \lambda/\Delta n^{NL} \simeq 5 - 10$cm.

Our choice here of the same ions as in the XRL plasma has been justified by the advantage of perfect frequency match between the XRL radiation and the transition of interest. In such a case, however, we have to deal with a still very hot plasma, and to use additional X-ray irradiance (pumping) , since the nonlinear transition occures between two excited levels. It would be greatly desirable, therefore, to identify also some alternative (i. e. non-XRL) plasmas, for which (i) the degree of ionization (and therefore, the required temperature) is significantly lower than that of the XRL plasma, and (ii) the XRL radiation is matched (not necessarily perfectly) to some direct transition from their ground level. A number of such "XRL line-plasma " couples have been found by us; some of the examples are: Se XXV 209.78 Å line and Fe X or Cl XIII plasma; Al XI 150.7 Å or C VI 182 Å line and Na IV plasma. Our preliminary evaluations show that significant XRNE's can be feasible for $T_e \simeq 35 - 300$eV and $N_e \simeq 10^{17} - 10^{18}\mathrm{cm}^{-3}$. Such plasma can be readily produced by relatively simple and well controlled electrical discharge [17].

All these estimates indicate a significant potential for third-order XRNE's in plasma XRL as well in some other plasmas. Self-action effects based on the resonant nonlinear effects such as self-(de)focusing, self-trapping, and self-bending, can be observed rending themselves as either desirable effects for enhancing of laser action, or the effects to be avoided or inhibited. Other effects of the same group, e. g. four-wave mixing, may be efficiently used for plasma diagnostics and for phase-conjugation amplification. Since the intensities significantly

exceeding the saturation intensity have apparently been achieved in experiment, it may also be possible that self- transparency and related 2π-solitons can be attained similar to that in the optical domain [16]. As a next step, high-order harmonics generation in the X-ray domain can be natural extension of the similar optical effect. Our future plans include investigation of XRNE's in metallic vapors and, what may be the most promising, — in condensed matter.

This work is supported by AFOSR.

References

[1] B. J. MacGowan et al., in *Short Wavelength Coherent Radiation: Generation and applications,* R. W. Falkone and J. Kirz, Eds. (OSA, Washington, DC) 2, 2 (1989).

[2] B. N. Chichkov and E. E. Fill, Opt.Comm. 74, 202 (1989); Phys.Rev. A 42, 599 (1990).

[3] U. Feldman, J. F. Seely, and A. K. Bhatia, J. Appl. Phys. 56, 2475 (1984).

[4] C. J. Keane et al., J. Phys. B22, 3343 (1989).

[5] B. L. Whitten, R. A. London, and R. S. Walling , J. Opt. Soc. Am. 5, 2537 (1989).

[6] M. D. Rosen et al., Phys. Rev. Lett. 54, 116 (1985).

[7] B. J. MacGowan et al., J. Appl. Phys. 61, 5243 (1987).

[8] P. L. Hagelstein and R. K. Jung, ADNDT 37, 121 (1987).

[9] H. Van Regemorter, Astrophys. J. 136, 906 (1962).

[10] A. Yariv, *Quantum Electronics* , John Wiley & Sons, NY, 1989, Ch. 8.

[11] D. H. Close, Phys. Rev., 153, 360 (1967).

[12] A. Corney, *Atomic and laser spectroscopy* , Clarendon Press, Oxford, 1977, Ch. 13.

[13] P. W. Millony and J. H. Eberly, *Lasers,* John Wiley & Sons, NY, 1988, Ch. 3.

[14] Y. T. Lee, W. M. Howard, and J. K. Nash, J. Quant. Spectrosc. Radiat. Transfer 43, 335 (1990).

[15] G. Hazak and A. Bar-Shalom, Phys. Rev. A 38, 1300 (1988).

[16] S. L. McCall and E. L. Hann, Phys. Rev. Lett. 18, 908 (1967).

[17] K. H. Finken and U. Ackerman, Phys. Lett. 85A, 278 (1981); A. W. DeSilva and H.-J. Kunze, J. Appl. Phys. 39, 2458 (1968).

NORMAL INCIDENCE MULTILAYER REFLECTORS FOR SUB-10 nm REGION

Tai D. Nguyen, Eric Gullikson, and Jeffrey B. Kortright

Center for X-Ray Optics, Accelerator and Fusion Research Division, Lawrence Berkeley Laboratory, University of California, Berkeley, California 94720.

An preliminary investigation of the performance and quality of Ru/C, Ru/B_4C, Ru/B, and Ru/BN multilayers is presented. The purpose of the study is to determine the choice of material combinations that yields the highest normal incident reflectance for application such as soft x-ray projection lithography at energies above the Si L edges. Measurements of relative reflectivities of the multilayers from an electron-impact source (Henke tube) with Boron K emission at 183 eV are presented. As the operating wavelength decreases, the period or the layer thicknesses inside the multilayers also decrease. Imperfections and fabrications of high quality multilayers then play a more dominant role in the performance of the multilayers. Correlation between the performance of these multilayers and uniformity of the layers inside the multilayers is discussed.

This work was supported by the Director, Office of Energy Research, Office of Basic Sciences, Materials Sciences Division, of the U.S. Department of Energy under Contract No. DE-AC03-76SF00098 and by the Air Force Office of Scientific Research, of the U.S. Department of Defense under Contract No. F49620-87-K-0001.

Section III: High-Intensity Laser Sources

High-Damage-Threshold Gratings Using Coated Silicon Substrates

H. W. K. Tom, M. H. Sher, O. R. Wood II, W. M. Mansfield, U. Mohideen, R. R. Freeman, and J. Bokor

AT&T Bell Laboratories, Holmdel, New Jersey 07733

Abstract

High damage threshold gratings can be made by putting suitable coatings on silicon grating blanks. We expect several times improvement in the damage threshold for nanosecond laser pulses and similar improvements for 100 femtosecond laser pulses.

We are currently investigating the manufacture of high damage threshold gratings using a novel idea. We are placing high reflectivity coatings on holographically patterned Silicon grating blanks. This approach provides three principle advantages compared to current gratings made by placing a thin metallic layer over holographically patterned photoresist on glass substrates. First, advanced lithographic and processing techniques for Si make possible the fabrication of arbitrary grating groove profiles with holographic registration across large areas. Second, metal-Si gratings should not be limited by damage at the metal-silicide interface because Si is an efficient thermal conductor and the damage threshold of metal-silicide is > 400°C. This is in great contrast to metal-photoresist gratings which damage at the metal-photoresist interface when temperatures exceed 100−200°C. Third, extremely efficient gratings can be fabricated using enhanced metallic and dielectric coatings (~99% reflectivity) on blazed gratings (ie., triangular groove profiles). These advantages make us believe damage thresholds comparable to those of bulk metals (~300 mJ/cm^2) are obtainable. For dielectric enhanced metallic coatings, several times the bulk metal damage threshold should be possible.

In Fig. 1 we show examples of the groove profiles one can achieve with lithographic techniques. With suitable etching, one can obtain square, triangular, or sinusoidal profiles. In Fig. 1a we show a triangular profile with apex angle of 72° and period of 5000 Å. The apex angle is determined by the angle between (111) planes and the Si(100)

Proceedings on Short-Wavelength Coherent Radiation. 170
Vol. 11, Philip H. Bucksbaum and Natale M. Ceglio (eds.)
© 1991 Optical Society of America

surface and is produced by an etching process that preferentially exposes (111) faces. In Fig. 1b we show the groove profile of a grating we have made that has reasonably high diffraction efficiency (80%) at 810 nm, and is the one used for damage threshold measurements described below. The profile is trapezoidal with apex angle = 72° as in Fig. 1a. We note that height to period ratios of ~ 30-40%, similar to those that might be used for chirped-pulse amplication schemes, can be readily fabricated. Clearly one approach to the problem of damage threshold is to increase the Au film thickness until the bulk damage threshold is reached. In principle, we could control the Si groove profile to allow for modification of the profile after a relatively thick deposition of Au.

Fig. 1. Scanning electron micrograph of grating groove patterns on Si(100). The rectangular silicon nitride "caps" are removed before metal deposition. a) triangular grating exposing (111) planes. b) trapezoidal grating with (111) and (100) faces.

Once optical energy has been deposited into the thin metal overlayer of a grating, there are three mechanisms for damage: 1) the lattice temperature at the metal-substrate interface exceeds damage threshold, 2) the electron temperature at the metal-substrate interface exceeds damage threshold, and 3) either the lattice or electron temperature at the metal-air interface leads to ablation of metal.

Here we use the standard approach to characterizing the excitation of solids with optical pulses as short as 100 fsec.[1,2,3] Light is coupled to the electrons in the solid, and we assume that coupling between the electrons and the lattice excitation modes (vibrations) is relatively slow. Assuming equilibrium among the electrons and the lattice modes, individually, we then characterize the electrons and lattice excitations by temperatures T_e and T_L. These evolve in time by the coupled differential equations:

$$\gamma T_e \partial T_e/\partial t = \kappa \nabla^2 T_e + g(T_L - T_e) + S(x,t)$$

$$C_L \partial T_L/\partial t = g(T_e - T_L)$$

where γT_e is the temperature-dependent electron specific heat, κ is the thermal conductivity, g is the electron-lattice coupling constant, and C_L is the lattice heat capacity. S(x,t) is the absorbed energy source term: in this term one includes the usual Fresnel-Drude calculation of the absorbed energy as well as enhanced absorption due to the grating profile (local field effects), due to plasma formation above the surface, and due to changes in the optical dielectric constant from electron heating effects. For gold,

$\gamma=6.2\times10^5$ J/cm^3−K^2[4], $\kappa=3.1T_e/(T_L+1.16\times10^{-5}T_e^2)$ W/cm^2−K (with T_e in K),[5] $g=4\times10^{10}$ W/cm^3−K[6], and $C_L=2.47$ J/cm^3−K. The equilibration of electron and lattice temperatures implied by the value of g is approximately 1-5 psec. For nanosecond optical pulses, the electron and lattice temperatures are in equilibrium and one only has to consider lattice mechanisms for damage.

When the damage mechanism is due to lattice temperature, it is clear that the Au-Si gratings can have higher damage thresholds than Au-photoresist gratings. Si is a better substrate than glass, first, because the Au-silicide damage threshold at >400°C is higher than the damage threshold of photoresist at 100−200°C. Secondly, Si is a good thermal conductor and can lower the peak temperatures reached at the front Au surface and the Au-substrate interface. The nsec pulse multishot damage threshold for many metals is around 500 mJ/cm^2 for normal incidence in the near IR depending on surface preparation. The nsec pulse damage threshold for the best Au/photoresist gratings have been reported (Jobin-Yvon, France) as high as 200 mJ/cm^2 with 1.06 μm excitation.[7] Assuming a reflectivity of 97%, 6 mJ of absorbed energy would raise a 200 nm film of Au to 150°C. The actual absorption and Au film thickness on the grating are probably less favorable, but it is reasonable that 150°C is sufficient to damage the Au-photoresist interface. On the other hand, since Si is a good thermal conductor and Au-Silicide is stable to >400°C, one would expect for Au thicknesses >200 nm, the damage threshold at the Au-silicide interface is higher than 500 mJ/cm^2 and that the damage threshold of the grating should be determined at the front surface as for bulk Au.

We tested whether or not damage is occurring at the Au-silicide interface vs. the front face by measuring the damage threshold as a function of Au thickness. The results are summarized in Fig. 2. The samples were Si flats overcoated with a 30 nm Ti binding layer followed by Au of the specified thickness. The data were taken with 810 nm laser pulses of pulse durations 145 fsec, 450 fsec, and 4.5 psec, and at 0° and 62° angle of incidence. The 0° data are almost exactly twice the values of the 62° data, consistent with the 2 times more absorption due to Fresnel reflection at the two angles. The damage threshold is defined here as the peak fluence incident on the sample surface (beam fluence times cos(θ)) for which the sample survives for 10 minutes at 10 Hz in the pulsed laser beam. Survival occurred if no visible change in the surface could be detected (as evidenced by scattered light from the illuminated spot). The shot-to-shot energy fluctuation was ±10%. Absolute fluence resolution was limited to 15% by the neutral density filters used to attenuate the beam.

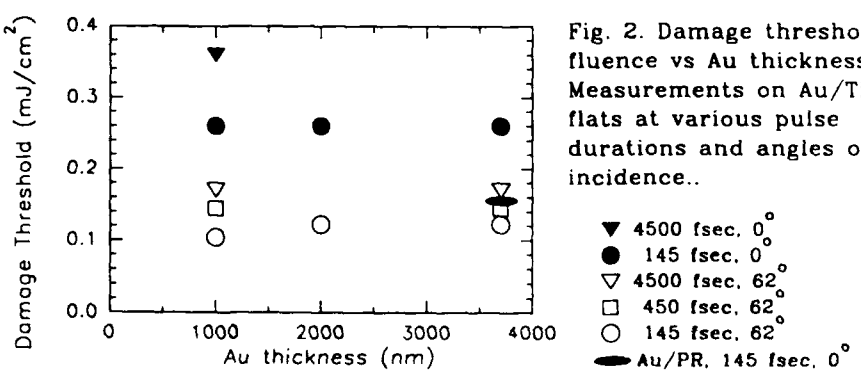

Fig. 2. Damage threshold fluence vs Au thickness. Measurements on Au/Ti/Si flats at various pulse durations and angles of incidence..

The absence of Au thickness dependence on all but the 145 fsec data taken at 62° angle of incidence shows clearly that the damage does not take place at the Au/Ti/Si interface, and that the damage threshold is that of bulk Au (ie., front face induced damage). The data for a 3700 nm flat film of Au on photoresist excited at 0° incidence is shown as the solid ellipse in Fig. 2. The Au film was provided by American Holographic (MA). The damage threshold is 60% of the corresponding Au/Ti/Si flat.

Laser-induced damage of bulk materials often occurs at thresholds below what would be necessary for lattice melting assuming a constant reflection coefficient. This is because excited state effects such as enhanced optical absorption in the electronically excited bulk material and absorption in the plasma above the target surface, can lead to more than the nominal deposition of optical energy. The optical dielectric constant for a metal is roughly given by the Drude model (disregarding interband transitions): $\varepsilon(\omega)=1-[\omega_p^2/(\omega^2+\nu_{ei}^2)](1+i\nu_{ei}/\omega)$. Here ω_p is the plasma frequency and ν_{ei} is the electron-ion collision frequency. The latter represents the free carrier absorption of the electrons near the Fermi level. In the free electron model when $T_e \leq h\nu$, the free carrier absorption increases with electron temperature as $(1+0.3T_e(eV)/1.5)$ where the factor of 0.3 comes from a numerical calculation of the joint density of states assuming the free electron model. Changes of a factor of 3 in the normally small $\mathrm{Im}(\varepsilon(\omega)) \propto \nu_{ei}/\omega$ can drastically change the optical reflectivity especially at non-normal incidence. The increase in the electron-ion collision frequency with electron temperature was invoked to explain the decrease in reflectivity observed for Ag(111) from nearly 100% to 20%, as the incident intensity is changed from 5×10^{12} to 5×10^{13} W/cm^2 in 90 fsec pulses.[8] For gold at several 100's of mJ/cm^2 irradiance, the change in free carrier absorption should be small, however, a large increase of $\mathrm{Im}(\varepsilon(\omega))$ occurs because electronic excitation to $T_e \sim 0.5$ eV opens up the possibility of the 810 nm light (1.5 eV) exciting the strong d-sp interband transition (2 eV). The oscillator strength of the interband channel is 10 times that for the conduction band electrons near the Fermi energy. Once enough energy is absorbed, the surface will also expand to create a plasma gradient of critical thickness which will further increase the absorption. For extremely intense laser pulses, the absorption may also be enhanced by multiphoton absorption.

To test these effects, we measured the the damage threshold fluence as a function of optical pulse duration. In Fig. 3a we show the results for Au/Ti/Si flats. The data clearly show that the damage threshold is lower for pulses shorter than 500 fsec and confirms that excited state effects increase absorption. The damage thresholds at 0°C incidence were 260 mJ/cm^2 at 145 fsec and 360 mJ/cm^2 at 4.5 psec. It is unlikely that electronic heating without enhanced absorption leads to plasma ablation damage in this case because the electron temperature reached on the front face with 145 fsec excitation assuming 2.5% linear absorption is only 5400K. If on the other hand, one assumes 10% absorption, which might occur for electron temperatures in excess of 0.5 eV due to d-band absorption or sufficient increase in the free electron ν_{ei}, then the peak lattice temperature of the front surface can exceed the bulk melting temperature of 1060°C. It is unlikely that enhanced absorption in a plasma layer plays a role for 145 fsec excitation because the electron temperature is too low (~1.5 eV for 10% absorption) to generate an absorbing plasma layer in 145 fsec. For longer optical pulses, enhanced absorption in the plasma layer probably plays a substantial role. The damage even for 145 fsec pulses is probably not due to multiphoton absorption since there is no substantial difference

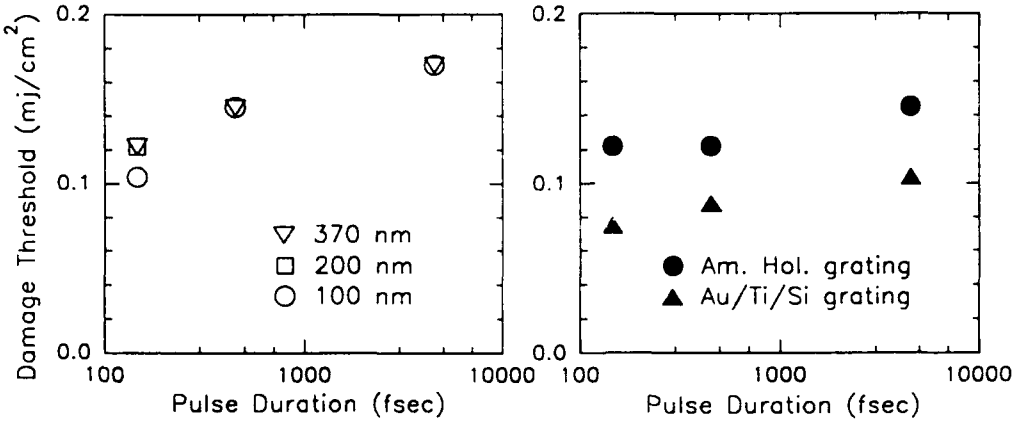

Fig. 3. Damage threshold fluence vs laser pulse duration. 3a) (left) Measurements performed on Au/Ti/Si flats for various Au thicknesses at 62° angle of incidence. 3b) (right) Measurements on American Holographic grating and Au/Ti/Si grating with groove profile of Fig. 1b and with 30 nm Ti and 100 nm Au overlayer.

between the 145 and 450 fsec pulse damage threshold even though the intensity is 3 times higher in the 145 fsec case.

We also observe that for 145 fsec excitation, the damage threshold on the 100 nm thick Au flat is about 30% lower at 62° angle of incidence than at 0° angle of incidence after allowing for a factor of 2 change in nominal absorption. This is shown in the data of Fig. 2. Such a result is consistent with a change in the Au dielectric constant due to electronic excitation causing a larger increase in absorption at 62° than at normal incidence. Although resonance absorption is also a maximum at 62° angle of incidence, we believe there is inadequate time to generate a critical thickness plasma and to get significant resonance absorption in 145 fsec. The fact that this difference is not observed for thicker Au films may be explained by a coincidence that the Au/Ti/Si interface at 100 nm deep reaches its damage threshold temperature of ~ 500°C at a lower fluence than required to heat the front surface to the melting temperature of 1060°C. One can only speculate that the dynamics of the nonlinear change in absorption and optical attenuation depth makes this occur on the sample irradiated at 62° incidence but not on the sample irradiated at normal incidence.

We have fabricated a Au/Ti/Si grating with trapezoidal profile as in Fig. 1b and with Au thickness of 100 nm. In our first efforts, a height/d-spacing ratio of ~32% gave the best diffraction efficiency 80 (±5) % at 810 nm. The period is 5000 Å. The best American Holographic grating (on photoresist) was 90 (±2) % efficient. In Fig. 3b we show the damage thresholds for these two gratings for different optical pulse durations. The damage thresholds for gratings scale with pulse duration the same way the damage thresholds for flats do, ie., ~20-30% lower damage threshold for short pulses. In all cases, the Au/Ti/Si gratings had lower damage threshold than the commercial grating or even

flats irradiated at 62°. This strongly suggests that the nominal absorption of the grating is slightly larger than that for flats at 62°. Part of this may be due to fabrication defects, and part may be due to local field effects that may enhance the absorption at specific places in the groove profile. We believe that one should be able to increase the grating efficiency and decrease the absorption with proper choice of the grating profile. One obvious direction is to try groove profiles approaching the blaze condition, eg., where the effective incidence angle approaches 0°. The sharp corners may have to be smoothed to diminish local field enhancements, but a factor of two improvement over the commercial holographic gratings should then be possible.

For triangular profiles approaching the blaze condition, it becomes reasonable to apply dielectric coatings to the metal surface. By limiting the nominal absorption to 99%, one can improve diffraction efficiency and raise the damage threshold further. It is of course uncertain how dielectric coatings act in grating geometries where the lateral dimensions are less than the optical wavelength. We plan to explore this possibility.

In conclusion, we have fabricated Au/Ti/Si diffraction gratings. In experiments on flats, we have shown that with Au thickness >100 nm, we obtain the damage threshold of bulk Au, eg., 260 mJ/cm^2 in 150 fsec and 360 mJ/cm^2 in >500 fsec at normal incidence. This is approximately 2 to 3 times better than the best Au gratings on photoresist. Our experimental results on Au/Ti/Si flats show that the damage for 145 fsec pulse excitation occurs because the laser pulse heats the electron temperature enough to dramatically increase the optical absorption so that the front surface lattice temperature eventually (1-5 psec later) exceeds the melting temperature.

References and Notes

1. S.I Anisimov, B.L. Kapeliovich, and T.L. Perel'man, Sov. Phys.-JETP 39, 3754 (1974).
2. J.G. Fujimoto, J.M. Liu, E.P. Ippen, and N. Bloembergen, Phys. Rev. Lett. 53, 1837 (1984).
3. P.B. Corkum, F. Brunel, N.K. Sherman, and T. Srinivasan-Rao, Phys. Rev. Lett. 61, 2886 (1988).
4. N.W. Ashcroft, N.D. Mermin, Solid State Physics (Holt, Rinehart and Winston, NY) 1976, p. 48.
5. this temperature dependent form for κ follows from the free electron model and a choice of electron-electron screening length of 2500 Å at 0.55 eV consistent with S.M. Sze, J.L. Moll, and T. Sugano, Sol. St. Electronics 7, 509 (1964).
6. H.E. Elsayed-Ali, T. Juhasz, G.O. Smith, and W. E. Bron, "Femtosecond Thermomudulation of Single-Crystalline and Polycrystalline Gold Films", in Ultrafast Phenomena, VII, C.B. Harris, *et. al.*, eds. (Springer-Verlag, New York, 1990) p. 315.
7. private commun., L.A. Lompre, CEN Saclay, France, 1991.
8. W.C. Banyai, D.C. Anakcer, X.Y. Wang, D.H. Reitze, G.B. Focht, M.C. Downer, "Femtosecond Photoemission and Reflectivity Measurements of High Temperature Electron Dynamics in Solid Density Plasmas", in Ultrafast Phenomena, VII, C.B. Harris, *et. al.*, eds. (Springer Verlag, New York, 1990), p. 116.

0.5-TW, 125-fs Ti:Sapphire Laser

J. D. Kmetec, J. J. Macklin, and J. F. Young*

Edward L. Ginzton Laboratory, Stanford University, Stanford, California 94305

Abstract

We report the design and construction of a compact 0.5 terawatt, 125 femtosecond laser system based upon chirped pulse amplification in Ti:sapphire. The final output beam contains 60 millijoules and is 1.2 times diffraction limited. A saturable absorber reduces the pre-pulse intensity to 10^{-9} that of the main pulse. Frequency doubling the output to 403 nm has been achieved in KDP with a peak conversion efficiency of 45%, and a whole beam conversion of 25%.

Recent progress has been reported in the development of femtosecond, terawatt laser systems.[1-4]. Such novel light sources, when tightly focused, can produce an intensity exceeding 10^{18}W/cm^2 One interest in such a source is for the generation of femtosecond x-ray pulses emitted from a solid target placed at the focus of such a laser. Calculations[5] have shown that laser energy to 3.5 Å x-ray conversion efficiency can exceed 0.1%, while preserving the ultrashort duration of the laser pulse. To obtain this laser power, we have constructed a system based on Ti:sapphire amplifiers and the technique of chirped pulse amplification. A key feature of chirped pulse amplification is the very large reduction in necessary amplifier aperature for the safe, linear propagation of the pulse. This allows the use of small (0.2 cm^2) aperature amplifiers and optics. Only a single, commercially available, pump laser is required for all amplification. The final output contains 60 mJ of energy in a 125 fsec pulsewidth. The output beam is nearly Gaussian with an e^{-2} diameter of 23 mm, and focuses to 1.2 times the diffraction limit. We describe the design and operation of the laser, and measurements of the final output pulse, including efficient second-harmonic generation at 403 nm.

The femtosecond oscillator for the system is a hybridly-modelocked dye laser[6] operated at 807 nm, and shown in Fig. 1. The gain and saturable absorber dyes are LDS-751 and HITC-I. The gain dye is pumped with 70 psec pulses of a frequency-doubled light from a cw mode-locked Nd:YAG laser. The average power of the

Proceedings on Short-Wavelength Coherent Radiation, Vol. 11, Philip H. Bucksbaum and Natale M. Ceglio (eds.)
© 1991 Optical Society of America

dye laser is 5 mW, with a pulse width of 85 fsec and a bandwidth of 8 nm. In order to provide reproducibly short, satellite-free pulses for amplification, we employ stabilization of the pump laser amplitude, use a birefringent filter in the dye laser cavity to restrict wavelength and control bandwidth, and actively stabilize the dye laser cavity length. The presence of satellite pulses is observed by an increase in the output power of the oscillator. We use this information to inhibit the regenerative amplifier, which would be damaged by such pulses.

The dye laser beam is collimated by a 200 cm focal length lens and double-passed through an anti-parallel grating pair containing a telescope[7] as shown in Fig. 1. This expander introduces a large, positive chirp to the pulse, stretching the initial pulsewidth from 85 fsec to 180 psec. The expander gratings are gold-coated, 1800 lines/mm holographic diffraction gratings (Milton Roy Co.), separated by 128 cm. The incident and diffracted angles for the first grating are 54.9 degrees and 38.9 degrees. Two 50 cm focal length cemented doublet lenses, placed a distance 2f (at 800 nm) apart between the gratings, form a unit-magnification telescope to invert the sign of the grating dispersion. The effective length of the expander is 68 cm.

To obtain a gain of $\sim 10^{10}$, Ti:sapphire (anti-reflection coated with single layer of MgF_2) is used both in a regenerative amplifier and a triple-passed power amplifier. Both amplifiers are pumped with 532 nm from a single Q-switched and frequency-doubled 10 Hz Nd:YAG laser. The pump laser produces 750 mJ at 532 nm in 7 nsec pulses. The regenerative amplifier cavity, shown in Fig. 1, forms a TEM_{00} mode waist diameter of 1.9 mm, and has a round-trip time of 9 nsec. The 18 mm long Ti:sapphire crystal ($\alpha_{532} = 1.4\ cm^{-1}$) is end-pumped with 60 mJ of 532 nm energy. To provide a uniform pump energy distribution, a 35 cm focal

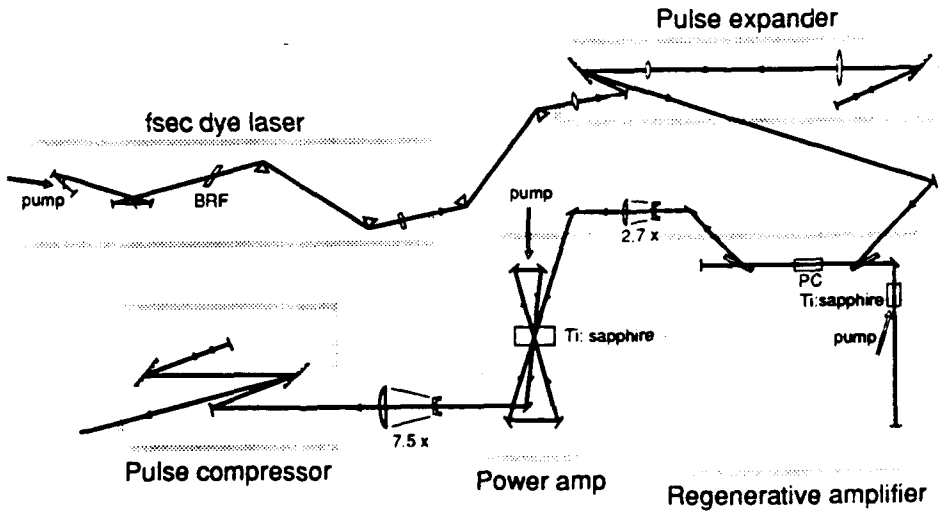

Figure 1. Layout of the terawatt, femtosecond laser system. For both the pulse expander and compressor, the entrance and the exit angles are the same, but the beam is displaced in the vertical dimension.

length lens images the green pump output from the Nd:YAG doubling crystal onto the face of the Ti:sapphire with a 4× demagnification. The focus of the imaging lens is not strong enough to spark in dust-free air.

Pulse selection is obtained with a single intra-cavity Pockel's cell and thin-film polarizers, which satisfy the requirements for high power and broad bandwidth. We have developed a three layer coating which exhibits 80% S-polarization reflectivity and nearly 100% P-polarization transmission at 72 degrees angle of incidence. These values remain constant within one percent over a bandwidth of 130 nm centered at 800 nm. An optical pulse is selected from the pulse train after the expander for injection into the cavity by the Pockels cell using a 5 nsec, 6 kV pulse from a thyratron pulse generator. Both optical injection and cavity dumping are accomplished with the same electrical pulse by returning it via a delay line. A typical seed pulse energy of 5 pJ increases to a maximum of 8 mJ after fourteen round trips. We employ a protection circuit to prevent amplifying seed pulses which contain satellite pulses. This reduces the repetition rate of the amplifiers from 10 Hz to $\sim$ 6 Hz.

Final amplification is obtained in a triple-passed power amplifier. The power amp is a 13 mm thick, 13 mm diameter Ti:sapphire crystal (α_{532} = 1.5 cm^{-1}), pumped over the central 5 mm diameter with 550 mJ of 532 nm energy. Relay optics image the pump beam onto the Ti:sapphire crystal with a 1.4 times demagnification. The high energy foci are contained in vacuum tubes. For an input pulse energy of 8 mJ, the power amplifier provides a total saturated gain of 15. The output energy is 110 mJ, and a 7.5 times Galilean telescope enlarges the beam to an e^{-2} diameter of 23 mm.

The pulse is then double passed through a grating pulse compressor to remove the positive frequency chirp due to the expander. The compressor gratings are identical to the expander gratings, except that the ruled area is 10 cm by 10 cm. The gratings are set with the same incident and diffracted angles as those in the expander. To compensate the material dispersion of the amplifier (equivalent to 2.5 m of silica after fourteen round trips), the grating spacing is increased by 8.9 mm over the nominal 68 cm required to compensate the expander. This results in negligible broadening of the pulse due to the higher order dispersion, and single-shot autocorrelation measurements of the amplified, compressed pulse yield a pulsewidth of 125 fsec, assuming a sech^2 temporal pulse shape. The output beam peak fluence and intensity is 15 mJ/cm^2 and 10^{11} W/cm^2. We separate the incoming and outgoing beams by propagating along a 0.5 degree incline.

The spatial beam quality of the amplified, compressed output was determined by focusing the attenuated output and measuring the spot size at the focus with either a pinhole or a scanning knife-edge. Beam attenuation is necessary to prevent destroying the pinhole and knife-edge at the focus. The output was attenuated by 10^7 by placing two high reflectors in the beam path following the power amplifier and an additional high reflector after the pulse compressor. This beam was measured to be very nearly gaussian with a e^{-2} beam radius of 11.5 mm. The attenuated output was then focused using a 200 mm focal length air-spaced

triplet lens. Transmission measurements using either a scanning knife-edge or a 10.8 micron pinhole determined the spot size. The pinhole measurements yielded 87% transmission, indicating a beam waist radius w_0 of 5.4 microns. The scanning knife-edge measurements gave 5 microns $\pm$ 10%. For this lens and the measured input beam radius of 11.5 mm, the calculated diffraction limited focal spot is $w_0 = 4.4$ microns. Thus, we infer that the output beam is 1.2 times diffraction limited. Using the measured values of spot size and power, we expect that with an $f/6$ optic, an intensity of 10^{18} W/cm^2 would be obtained. When the saturable absorber is used, we observe a 10% increase in the focused beam spot size over that without the saturable absorber cell, indicating a small degradation in the beam quality.

For the available seed energy, the regenerative amplifier delivers approximately 3 percent of the output energy as background amplified spontaneous emission. A saturable absorber placed after the compressor gratings reduces any such amplifier noise which precedes the main pulse by a factor of 1000. The main pulse fully saturates the IR-140 absorber and a large signal transmission of 75 percent is observed (whole beam). Since the output beam has a peak intensity of 10^{11} W/cm^2, the absorber cell must be kept to a minimum thickness to reduce nonlinear phase distortion of the pulse. The cell has a clear aperature of 5 cm and employs AR-coated, 3 mm thick fused quartz windows spaced by 4 mm.

An alternative approach to reduce the pre-pulse energy is to frequency double the output of the laser. Since low intensity background noise doubles with very poor efficiency, the peak intensity to background noise contrast ratio increases dramatically when the fundamental is removed with dichroic mirrors or a color filter. We have frequency-doubled the laser output to 403 nm using a 1.4 mm thick, 5 cm by 5 cm KDP crystal cut for Type 1 phase matching (Fig. 2). This thickness is chosen such that the group velocity mismatch between the fundamental and the

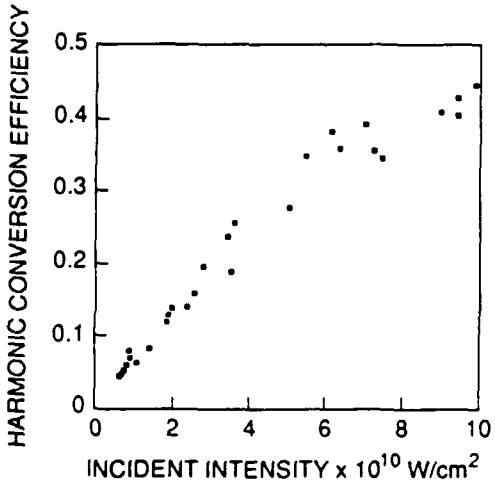

Figure 2. Plot of the second harmonic conversion efficiency versus the incident 807 nm laser intensity.

harmonic results in a 60 fsec pulse separation. We measure a maximum conversion efficiency of 45% at 10^{11} W/cm^2 and a whole beam conversion of 25%. We obtain these results by propagating the unfocused, collimated output beam through the free standing KDP crystal.

The authors would like to acknowledge discussions with R. Falcone. This work was supported by the U.S. Air Force Office of Scientific Research and the Strategic Defense Initiative Organization.

*current address: Department of Electrical and Computer Engineering, Rice University, Houston, TX, 77251.

References

1. J. S. Squier, F. Salin, G. Mourou, and D. Harter, "100-fs pulse generation and amplification in Ti : Al_2O_3," Opt. Lett. **16**, 324 (1991).
2. M. Pessot, J. Squier, G. Mourou, and D. Harter,"Chirped-pulse amplification of 100-fsec pulses,"Opt. Lett. **14**, 797 (1989).
3. J. D. Kmetec, J. J. Macklin, and J. F. Young, "A 0.5 terawatt, 125 femtosecond Ti:sapphire laser," Opt. Lett. (to be published).
4. A. Sullivan, H. Hamster, H. C. Kapteyn, S. Gordon, W. White, H. Nathel, R. J. Blair, and R. W. Falcone, "Multi-terawatt, 100 femtosecond laser," (in this conference).
5. J. D. Kmetec and S. E. Harris, "Targets for efficient femtosecond-timescale x-ray generation," in Proc. on Short Wavelength Coherent Radiation : Generation and Applications, R. W. Falcone and J. Kirz, eds. (Optical Society of America, Washington D.C., 1988).
6. W. H. Knox, "Generation and kilohertz-rate amplification of femtosecond optical pulses around 800 nm," J. Opt. Soc. Am B, **4**, 1771 (1987).
7. O. E. Martinez, "3000 times grating compressor with positive group velocity dispersion: application to fiber compensation in 1.3-1.6 micron region," IEEE J. Quant. Electron., **QE-23**, 59 (1987).

Multiterawatt Laser System Based on Ti:Al_2O_3

A. Sullivan, H. Hamster, H. C. Kapteyn,[1] S. Gordon, W. White,[2]
H. Nathel,[2] R. J. Blair,[3] and R. W. Falcone

Department of Physics, University of California at Berkeley,
Berkeley, California 94720

Abstract

Ultrashort duration, high-energy laser pulses have been generated using a titanium-doped-sapphire oscillator and amplifier system. The pulses have an energy of 0.45 Joules with a duration of 95 femtoseconds, and 0.23 Joules with a duration of 60 femtoseconds.

We have constructed a Ti:Al_2O_3 based laser system which uses chirped pulse amplification (CPA) and multipass amplifiers. Pulses are produced with a peak power of 3 TW, an energy of 0.45 J and a duration of 95 fs. Figure 1 shows a schematic layout of the system. The oscillator is a mode-locked Ti:Al_2O_3 laser (Spectra-Physics *Tsunami*) pumped by an cw-Ar^+ laser (Spectra-Physics 2040E). The *Tsunami* laser produces time-bandwidth-limited, 1 ps pulses at a repetition rate of 82 MHz. The output power is 1.6 watts at a wavelength of 807 nm when pumped by 9 watts (all lines) from the Ar^+ laser. Pulses from the oscillator pass through a Faraday isolator and a 65 cm length of 630 nm, polarization-preserving, optical fiber. Self-phase-modulation (SPM) in the fiber increases the bandwidth to 24 nm. The power out of the fiber is 750 mW. We obtained a pulsewidth of 70 fs by compression of these chirped pulses using a prism compressor.[1]

In order to maintain low peak power in the amplifier chain, pulses are stretched to 0.5 ns in a four-pass grating arrangement using two 1800 line/mm gold-coated, holographic gratings (Milton Roy) and two 60 cm focal length lenses. The lenses are corrected for chromatic and spherical aberrations at 805 nm. This is essential for achieving minimum compressed pulsewidths with CPA. Pulses are spectrally filtered in the stretcher by the use of spatial apertures, in order to eliminate nonlinear portions of the chirp. In the absence of amplification, stretched pulses could be recompressed to 70 fs.

The stretched pulses are amplified in four Ti:Al_2O_3 crystals; the first three are Brewster-cut crystals and the fourth is used at normal incidence and is antireflection coated. Spatial filters following each amplifier limit amplified spontaneous emission (ASE) and maintain beam quality. The first three amplifier stages are longitudinally pumped by the frequency doubled output of a Q-switched Nd:YAG laser (Quanta-Ray GCR-4) which produces 6 ns pulses with a total energy of 0.7 J at 532 nm and a repetition rate of 10 Hz. The fourth amplifier stage is longitudinally pumped by a flashlamp-pumped dye laser (Candela LFDL-20). This laser produces up to 12 J pulses with a duration of 3 μs at 576 nm and at a 5 Hz repetition rate.

Proceedings on Short-Wavelength Coherent Radiation, 181
Vol. 11, Philip H. Bucksbaum and Natale M. Ceglio (eds.)
© 1991 Optical Society of America

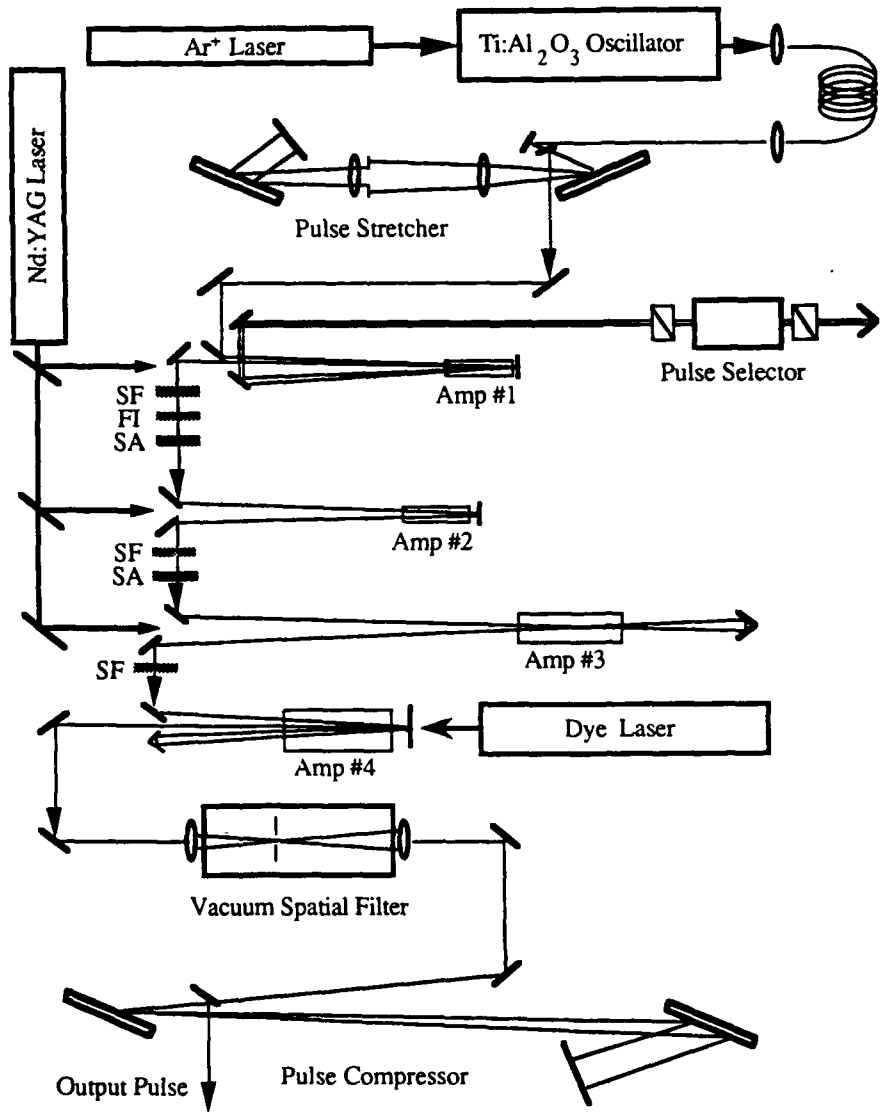

Figure 1 Schematic layout of the Ti:Al_2O_3 system. SF, FI, and SA represent a spatial filter, Faraday isolator, and saturable absorber, respectively.

The first amplifier is arranged in a four pass configuration and is pumped with an energy of 85 mJ. A Pockels cell pulse selector is placed between the second and third passes to limit ASE to a 4 ns window, as well as to select a pulse from the oscillator pulse train. A Faraday isolator following the amplifier prevents amplification backwards through the system. A color filter (Schott RG 850) is then used as a saturable absorber to improve the short pulse-to-ASE energy contrast by a factor of 90 while transmitting 70% of the short pulse.

The second amplifier is pumped with an energy of 65 mJ. The 807 nm pulses make two passes through this amplifier, which is followed by another color filter saturable absorber. At this point the energy contrast between signal and ASE is nearly 10^7 and the pulse energy is 7 mJ.

The third amplifier stage is pumped with an energy of 0.5 J in a 3.4 mm diameter beam. Following two passes through this amplifier the 807 nm pulses have an energy of 50 mJ.

The fourth amplifier stage is pumped with an energy of 9.9 J in a 1.2 cm diameter beam; this is also the final diameter of the amplified beam. After four passes the 807 nm pulses have an energy of 1.1 J. After a vacuum spatial filter the pulses are compressed in a two-pass grating configuration to 95 fs with an energy of 0.45 J. The corresponding peak power is 3 TW. At an output energy of 0.23 J we obtain a pulsewidth of 60 fs , indicating that either gain saturation in the amplifiers or SPM in air after recompression may be limiting the minimum pulsewidth at the highest energy. Pulsewidths are obtained using a single shot autocorrelator; the lorentzian profile probably results from spectral modification following either gain saturation or SPM. ASE from the system is less than 15 μJ, as determined by blocking the input to the amplifiers.

At the highest energy, the amplified pulse has a bandwidth of approximately 8 nm: the spectrum is asymmetric and peaked at long wavelengths because of gain saturation. The compressed pulse is spectrally broadened to a bandwidth of approximately 13 nm because of SPM in air. The beam also undergoes small-scale self-focusing[2] in air within a distance of one meter following the compressor at power densities between 10^{11} and 10^{12} W/cm^2. The nonlinear index (n_2) of air is 2×10^{-16} esu [3] leading to a phase shift (B-integral) of 0.1 rad/cm. Inhomogeneities in our large aperture Ti:Al_2O_3 crystal, used as the fourth amplifier, enhance the self-focusing. In order to obtain highly focused pulses we need to address the resulting non-uniform phase distortion across the beam spatial profile. Possible solutions include larger diameter optics and an evacuated chamber for the compressor.

This work was supported by the U.S. Air Force Office of Scientific Research and through a collaboration with Lawrence Livermore National Laboratory under Contract No. W-7405-ENG-48. H. Hamster acknowledges support by the Studienstiftung des deutschen Volkes. We also acknowledge the generous assistance of Spectra Physics Lasers and helpful conversations with Jeff Kmetic and John Macklin.

[1] Current address: Physics Department, Washington State University, Pullman, WA 99164
[2] Permanent address: Lawrence Livermore National Laboratory, Livermore, CA 94550
[3] Permanent address: Sparta Laser Systems, 5452 Oberlin Drive, San Diego, CA 92121

References

1. J. D. Kafka, *et al.*, in *Ultrafast Phenomena VII* , C. B. Harris, E. P. Ippen, G. A. Mourou, A. H. Zewail, Eds. (Springer-Verlag, Berlin, 1990) pp. 66.
2. W. Koechner, *Solid-State Laser Engineering* (Springer-Verlag, Berlin, 1976)
3. R. W. Hellwarth *et al.* Phys. Rev. A **41**, 2766 (1990).

Section IV: High-Intensity Laser–Matter Interactions

Atoms

Calculations of High-Intensity Multiphoton Ionization and Photoemission from Atoms

K. C. Kulander, K. J. Schafer, and J. L. Krause

Physics Department, Lawrence Livermore National Laboratory, Livermore, California 94550

Abstract

A method which involves the direct solution of the time dependent Schrodinger equation has been used in studies of the dynamics of excitation of and emission from atoms in intense, pulsed laser fields.

Introduction

A surprising array of effects have been observed during high-intensity, short-pulse laser excitation of atoms and molecules. To model the results of these measurements, we have developed methods to solve the time-dependent Schrödinger equation for an atom in a time varying, classical electromagnetic field.[1,2] Studies on many atomic and molecular systems have been performed over a range of intensities from the regime within which perturbative techniques are valid up to field strengths well above an atomic unit ($I > 3.51 \times 10^{16}$ W/cm^2). These calculations have provided predictions for ionization rates,[1] photoelectron energy and angular distributions[3] and photoemission rates.[4] The effects of ac Stark shifted and intensity broadened intermediate states on the emission processes have been investigated.

Method

We consider the case of a ground state atom in a strong, linearly polarized laser field which is turned on gradually starting at time t=0. The response of the atomic electrons to the laser pulse is calculated by integrating the time dependent Schrödinger equation using a finite-difference grid representation for the wave function. In order to completely determine the final state of the system after the pulse, the spatial grid must be large enough to contain the entire time-dependent wave function, which will have a finite but possibly substantial extent due to ionization which occurs during the pulse. Such large grids are necessary if the energy and angular distributions of the photoelectrons are desired. If only ionization or photoemission rates are required, much more modest size grids can be employed by absorbing the flux which reaches the boundaries of the grid either by using a imaginary potential confined to the edges of the grid or by using a mask

Proceedings on Short-Wavelength Coherent Radiation, 186
Vol. 11, Philip H. Bucksbaum and Natale M. Ceglio (eds.)
© 1991 Optical Society of America

function which reduces the wave function near the boundary smoothly to zero after each integration step. Provided the grid boundaries are far enough from the nucleus and reflections from the absorber are minimal, converged ionization and photoemission rates are obtainable.

Results

The hydrogen atom has been the system studied most extensively theoretically because of its simplicity. Although somewhat more difficult to study experimentally, there are excellent measurements of photoelectron energy and angular distributions for several wavelengths and intensities.[5] Because any experiment will involve a significant spatial distribution of intensities within the focal volume, some convolution of the theoretical results is necessary in order to compare the single atom calculations with a measured spectrum. Allowing for that we have obtained very good agreement with measured ATI energy distributions and for the angular distributions of the individual ATI peaks. These calculations used pulses which had rapid rise and fall times with an interval of constant intensity over many optical cycles. The rates obtained are appropriate to experimental pulses which have hundreds or thousands of optical cycles. Each ATI peak is found to have a weak oscillatory structure on either side of the peak which is consistent with the Fourier transform of the trapezoidal pulse employed. This pulse sweeps too rapidly through any possible resonance with a Stark-shifted intermediate state, so that no additional structure due to the excited states of the system is found. On the other hand, calculations using very short sine-squared pulses (20-60 optical cycles) which have relatively slower rates of rising and falling show quite complicated structure, some of which is attributable to resonance intermediates. However, additional structure, due to interferences between electrons emitted during the pulse rise and those emitted as the pulse falls, is evident. This mechanism has previously been shown to introduce Airy-like oscillations in ATI peaks in one dimensional, model calculations.[6] The structure resulting from these two interfering sources is very difficult to unravel unambiguously. Experimentally much of this structure will be averaged over in the observed distributions because of the intensity distribution in the medium.

During excitation, in addition to ionization, the atom can undergo the emission of photons at frequencies which are integer multiples of the pump frequency. This is called harmonic generation. Experimentally, surprisingly high-order harmonics have been observed in rare gas media.[7,8] Because of the inversion symmetry in the atom, only odd harmonics are produced. We can calculate the strength of this emission from our time dependent electronic wave function.[4] The power spectrum is proportional to the square of the Fourier transform of the time dependent dipole induced by the driving field. This dipole is simply the expectation value of z, the coordinate in the direction of polarization. We have calculated harmonic generation rates for a number of atoms, incident wavelengths and incident intensities. By considering the propagation of the harmonic fields through the focal volume, we can predict the conversion efficiency for harmonic generation from an excited gas.[9,10] Calculated emission rates, which include the spatial variation of the laser intensity along with the phase matching factors, agree quantitatively with the measured yields up through the 25th harmonic of Nd:YAG (1064nm) in xenon gas for incident intensities up to 3×10^{13}W/cm^2.[10]

Recently there has been considerable interest in the relationship between electron and photon emission, particularly with regard to the competition between processes of the same order. It has been proposed by several researchers that the emission of a photoelectron corresponding to the net adsorption of q laser photons should be closely

related to the strength of the single atom emission of the qth harmonic photon.[11,12] This has been demonstrated to some degree with careful calculations for both processes over a range of intensities for both hydrogen and xenon.[13]

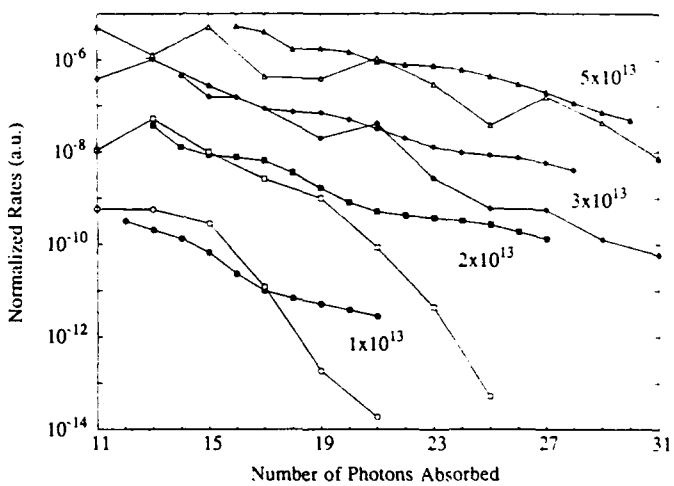

Figure 1. Harmonic photon (open symbols) and electron (closed symbols) emission rates for xenon at 1064 nm as functions of intensity.

In Fig. 1, we show the emission rates of photons and electrons from xenon for a 1064 nm laser at five different peak intensities. The photo-emission rates are proportional to $q^3|d(q\omega)|^2$. Because there is an arbitrary multiplicative factor between the different rates, we have scaled the photon rate to agree with the electron emission rate at $3x10^{13}$ W/cm^2 for the 17th harmonic. This figure clearly shows the intensity dependence of processes of equal order are generally in quite good agreement. Only for the higher orders at the lowest two intensities is there an appreciable discrepancy between the photoelectron and harmonic emission spectra. This difference occurs because the production of a photon of frequency $q\omega$ requires not only the net absorption of q laser photons, but also the emission of the harmonic photon due to dipole coupling between the excited state and the ground state. At low intensities, the dressed continuum states are poorly coupled to the ground state because the oscillator strength is concentrated within the bound state manifold. As the intensity increases, the dressed continuum states begin to include significant amplitudes of those bound state components which carry oscillator strength back to the ground state. Under these conditions the photoelectron and harmonic emission spectra become comparable. This agreement extends up to the point where the mixing between the bound and continuum states begins to decline. This point moves to higher and higher order with increasing intensity. These calculations provide dramatic evidence of the relationship between these processes. However, comparison between measured photon and electron rates must take into account the propagation of the harmonic fields through the excited volume, which may alter the apparent agreement which we have found between the single atom spectra.

The strengths of the time-dependent approach we have used to study these processes are first, that arbitrary pulse shapes can be employed in the calculations and second, that the time-evolving electronic wave function can provide detailed information about the character of the excitation dynamics.

Acknowledgment

This work was performed under the auspices of the U.S. Department of Energy at Lawrence Livermore National Laboratory under contract number W-7405-Eng-48.

References

1. K. C. Kulander, "Multiphoton ionization of hydrogen: a time-dependent theory," Phys. Rev. A 35, 445 – 448 (1987).
2. K. C. Kulander, K. J. Schafer and J. L. Krause, "Time-dependent theory of multiphoton processes," in Atoms in Intense Radiation Fields, M. H. Gavrila, ed. (Adv. Atom. Mol. Opt. Phys., Academic Press, New York, 1991), in press.
3. K. J. Schafer and K. C. Kulander, "Energy analysis of time-dependent wave functions: application to above threshold ionization," Phys. Rev. A 42, 5798 – 5801 (1990).
4. K. C. Kulander and B. W. Shore, "Generation of optical harmonics by intense pulses of laser radiation. II. Single-atom spectrum for xenon," J. Opt. Soc. Am. B 7, 502 – 508 (1990).
5. See, for example, B. Wolff, H. Rottke, D. Feldmann and K. H. Welge, "Multiphoton ionization of hydrogen atoms in intense laser fields," Z. Phys. D 10, 35 – 43 (1988).
6. J. N. Bardsley, A. Szöke and M. J. Comella, "Multiphoton ionization from a short-range potential by short-pulse lasers," J. Phys. B 21, 3899 – 3916 (1988).
7. A. McPherson, G. Gibson, H. Jara, U. Johann, T. S. Luk, I. A. McIntyre, K. Boyer and C. K. Rhodes, "Studies of multiphoton production of vacuum-ultraviolet radiation in the rare gases," J. Opt. Soc. Am. B 4, 595 – 601 (1989).
8. M. Ferray, A. L'Huillier, X. Li, L. Lompré, G. Mainfray and C. Manus, "Multiple-harmonic conversion of 1064 nm radiation in rare gases," J. Phys. B 21, L31 – L35 (1988).
9. B. W. Shore and K. C. Kulander, "Generation of optical harmonics by intense pulses of laser radiation. I. Propagation effects," J. Mod. Opt. 36, 857 – 876 (1989).
10. A. L'Huillier, K. J. Schafer and K. C. Kulander, "High-order harmonic generation in xenon at 1064 nm: the role of phase matching," Phys. Rev. Lett., submitted.
11. B. W. Shore and P. L. Knight, "Enhancement of high optical harmonics by excess-photon ionization," J. Phys. B 20, 413 – 423 (1987).
12. J. H. Eberly, Q. Su and J. Javanainen, "Nonlinear light scattering accompanying multiphoton ionization," Phys. Rev. Lett. 62, 881 – 884 (1989).
13. K. J. Schafer, J. L. Krause and K. C. Kulander, "Nonlinear effects in electron and photon emission from atoms in intense laser fields," J. Nonlin. Opt., in press.

Integration of the Schrödinger Equation on a Massively Parallel Processor

Jonathan Parker, Sayoko Blodgett-Ford, and Charles W. Clark

Physics Laboratory, National Insitute of Standards and Technology, Gaithersburg, Maryland 20899

Institute for Physical Science and Technology, University of Maryland, College Park, Maryland 20742

Abstract

We use a massively parallel computer to integrate the time-dependent Schrödinger equation for hydrogen in high-intensity radiation fields. Photoelectron and harmonic-radiation spectra are presented.

The behavior of atoms in strong radiation fields depends critically upon the time evolution of the field. For example, it has been found[1] that above-threshold ionization (ATI) spectra show radical changes as the duration of the exciting laser pulse decreases; there is also theoretical evidence[2] for novel phenomena, such as population trapping, which occur only for relatively short pulses. In order to treat problems of this sort theoretically, one must employ methods that accommodate general time variation of the radiation field. The most direct such method is numerical integration of the time-dependent Schrödinger equation. This would be an entirely non-controversial approach if vast computational resources were not required to implement it in practice. To date there have been only a few reports[3] of direct integration of the time-dependent Schrödinger equation for a three dimensional, one-electron atom in a radiation field.

Since one of the main limitations to numerical integration of the Schrödinger equation is the availability of computational resources, we are investigating the application of *massively parallel* computer architectures. Our basic approach involves dividing configuration space into discrete regions, and assigning a dedicated central processing unit (with its own local memory) to compute the wavefunction in each region. The wavefunction ϕ is represented on a discrete spatial grid, $\phi_j \equiv \phi(x_j)$, which leads to a set of equations of the form

$$i\frac{\partial \phi_j}{\partial t} = V_j(t)\,\phi_j + \sum_k U_{jk}(t)\,\phi_k \quad ,$$

where the index k refers to neighboring points on the grid. The sum over neighboring grid points derives from momentum-dependent terms in the Hamiltonian, such as the

Proceedings on Short-Wavelength Coherent Radiation, 190
Vol. 11, Philip H. Bucksbaum and Natale M. Ceglio (eds.)
© 1991 Optical Society of America

kinetic energy operator and the $\boldsymbol{A} \cdot \boldsymbol{p}$ form of the electron-field interaction. In the simplest cases, only nearest neighbors on the grid are coupled. One can then envisage a configuration in which each grid point has a dedicated processor, which solves the above equation using the contents of its own local memory and that of its nearest neighbors. With an appropriate interprocessor communication architecture, such as that provided by the Thinking Machines, Inc. Connection Machine, the time taken to solve this equation becomes independent of the number of grid points.

We have implemented several approaches of this type on a Connection Machine, to describe atomic hydrogen in a linearly-polarized radiation field. We have used both cylindrical-coordinate and a partial-wave discretization methods, and have performed calculations in both length and velocity gauges. Numerical results generated by these four methods are compared in selected cases to verify that the results are consistent.

The equations of motion are integrated typically over about ten optical periods. The field is ramped on linearly over 3.5 periods and ramped off in the same way. Harmonic-radiation spectra are determined from Fourier transforms of the time-dependent expectation value of the acceleration; photoelectron energy distributions are calculated by projecting the computed wavefunction onto continuum Coulomb wavefunctions after the field has been ramped off. We show in Fig. 1 some results for

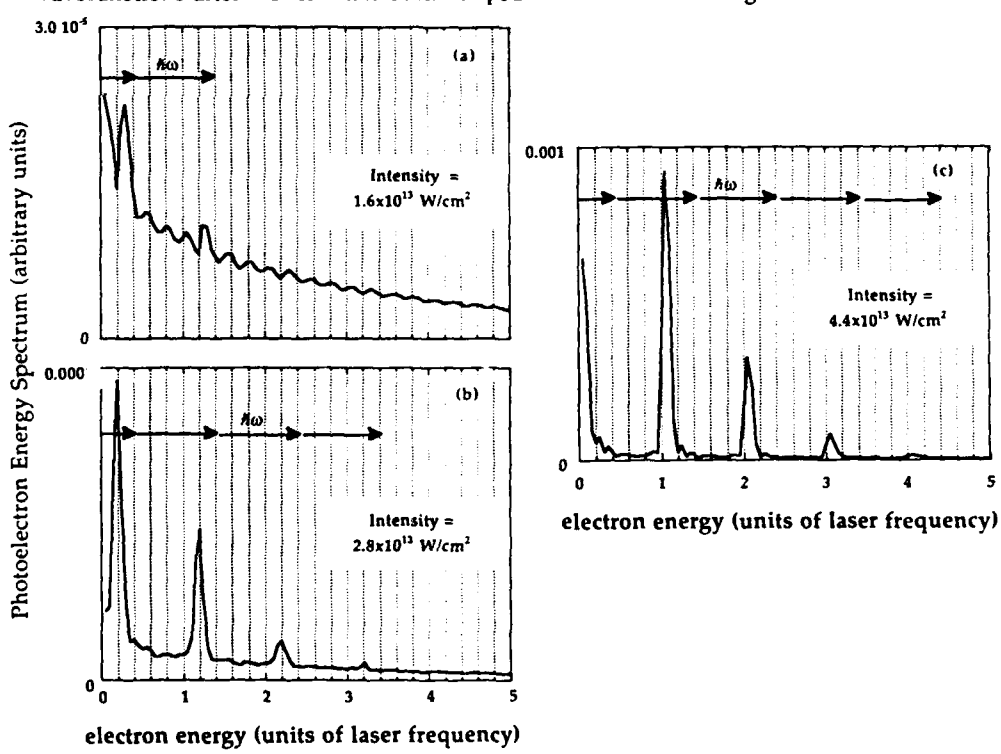

Fig. 1. Photoelectron spectra of atomic hydrogen. The atom was initially in the ground state, the laser wavelength was λ = 608 nm, intensities ranged from 1.6×10^{13} Wcm^{-2} to 4.4×10^{13} Wcm^{-2}, and the pulse was ten field periods in length.

radiation at λ = 608 nm and for intensities ranging from 1.6×10^{13} Wcm^{-2} to 4.4×10^{13} Wcm^{-2}. The arrows represent the expected positions of ionization peaks in the absence of shifts. In each case the peaks in our photoelectron spectra are shifted to lower energies by an amount that is equal to the ponderomotive energy, to within 10%. This is just the frequency shift of the ground state of hydrogen, as predicted by lowest order perturbation theory. This agreement holds to intensities as high as 2×10^{14} Wcm^{-2}. The figure also demonstrates the abrupt onset of ATI at 1.6×10^{13} Wcm^{-2}. The units of the y-axis, though arbitrary, give the correct relative cross sections for photoionization at the three intensities.

We have evaluated several algorithms for the integration of Schrödinger's equation in the length gauge and in the velocity gauge, with emphasis on determining their suitability to the Connection Machine architecture. Figure 2 shows predictions of population in partial waves $Y_{l,m}(\theta,\varphi)$ after four field periods, as predicted by length gauge and by velocity gauge calculations. The field frequency here is 1/3 the Rydberg frequency and the intensity is 7.0×10^{14} Wcm^{-2}. In this example, the wavefunction is expanded in spherical harmonics, and a finite difference scheme is used to integrate in the radial coordinates. It is apparent from the figure that fewer partial waves are populated in the velocity gauge calculation than in the length gauge calculation. The velocity gauge interaction Hamiltonian is less efficiently implemented in Connection Machine Fortran than the length gauge interaction Hamiltonian, but the velocity gauge calculations are faster overall, because fewer partial waves are needed.

Population in partial waves, $|\langle l | \Psi \rangle|^2$, is not a gauge invariant quantity and consequently the disagreement between length gauge and velocity gauge calculations

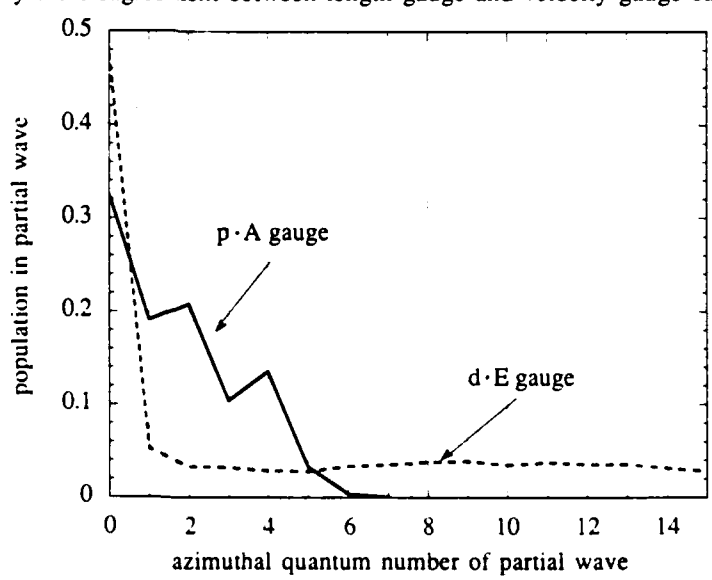

Fig. 2. Population in partial waves, $|\langle l | \Psi \rangle|^2$, where l is the azimuthal quantum number. The data is shown after four field periods of the laser, with field frequency at 1/3 the Rydberg frequency, and intensity at 7.0×10^{14} Wcm^{-2}.

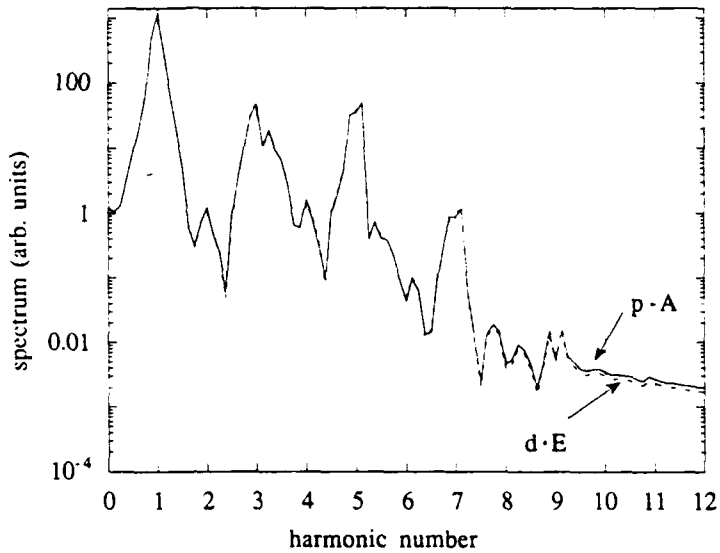

Fig. 3. Spectrum of radiation generated by atomic hydrogen undergoing ATI. The spectrum is calculated from the Fourier transform of the expectation value of the acceleration. Field intensity was 7×10^{14} Wcm^{-2}, the field frequency was 1/3 of the Rydberg frequency, and the atom was initially in the ground state. The dashed line is the length gauge prediction.

is expected. However, length gauge and velocity gauge calculations should give the same predictions of gauge-invariant quantities like acceleration. Figure 3 shows the results of such a calculation. In Fig. 3 the square of the Fourier transform of the expectation value of the acceleration is plotted, showing the expected harmonic generation. In this calculation the field intensity is 7×10^{14} Wcm^{-2}, and the field frequency is 1/3 the Rydberg frequency. Comparison of velocity gauge predictions in Fig. 3 with length gauge predictions reveals only slight differences. Comparisons of this sort between the predictions of different numerical methods proved to be helpful in detecting and tracking down subtle errors. In particular small failures in the numerical integration often showed up dramatically in the logarithmic plots of the Fourier transform of acceleration.

Acknowledgments

We gratefully acknowledge the support of the U. S. Air Force Office of Scientific Research.

References

1) R. R. Freeman, P. H. Bucksbaum, H. Milchberg, S. Darack, D. Schumacher, and M. E. Geusic, *Phys. Rev. Lett.* **59**, 1092 (1987).

2) J. Parker and C. R. Stroud Jr., Phys. Rev. A **41**, pp. 1602-1607 (1990).

3) See papers in the April 1990 Topical Issue of J. Opt. Soc. Am. B, *Theory of High-Order Processes in Atoms in Intense Laser Fields*.

Section IV: High-Intensity Laser–Matter Interactions

Molecules

Subpicosecond Studies of Molecules and Solids

T. S. Luk, A. McPherson, D. A. Tate, K. Boyer, and C. K. Rhodes

Laboratory for Atomic, Molecular, and Radiation Physics, Department of Physics, University of Illinois at Chicago, P.O. Box 4348, Chicago, Illinois 60680

ABSTRACT

Studies of the interaction of molecules and solids with subpicosecond (~ 600 fs) high intensity radiation ($\geqslant 10^{16}$ W/cm^2) are leading to the observation of new physical phenomena and the production of new classes of highly excited matter. The experiments indicate that a central factor is the ability to generate very high levels of electronic excitation in a manner which enables the heavy bodies of the system to remain kinetically cold for the time scale of the interaction.

I. INTRODUCTION

Advances in femtosecond lasers are extending the exploration of multiphoton interactions well into the strong-field regime, the physical situation in which the external field is considerably greater than an atomic unit (e/a_0^2). The performance projected for ultraviolet rare gas halogen laser technology is currently being realized[1–11] and new near-infrared solid state systems, such as Ti:Al_2O_3, are under vigorous development. Both technologies should reach a field strength of ~ 100 e/a_0^2 with instruments that produce an output energy of ~ 1 J in a pulse width of ~ 100 fs.

There is a growing body of evidence that fundamentally new forms of highly excited matter can be produced with strong-field interactions. Specifically, there is considerable interest in the response of (1) free molecular systems and (2) solid matter to intense subpicosecond irradiation. Important information on molecules has been derived from the study of coulomb explosions induced by the rapid multiphoton ionization characteristic of strong-field coupling.[12–20] Much data concerning the behavior of solids has come from the analysis of x-ray spectra.[21–25]

II. MOLECULAR COULOMB EXPLOSIONS

Assuming that the molecular potential is dominated by the Coulomb term, the time τ for two atoms, to undergo a Coulomb explosion and develop a separation of x,

Proceedings on Short-Wavelength Coherent Radiation, Vol. 11, Philip H. Bucksbaum and Natale M. Ceglio (eds.)
© 1991 Optical Society of America

with a reduced mass of M initially situated at a molecular bond distance of ~ $2\beta a_0$ and ionized suddenly by a pulse of radiation to charge states Z_1 and Z_2, is

$$\tau \simeq \frac{\lambda\!\!\!^{-}_C}{c\alpha^2}\left(\frac{\beta^3 M}{2m_e Z_1 Z_2}\right)^{1/2}$$

$$\times\left[\frac{x(1-2\beta a_0/x)^{1/2}}{2\beta a_0} + \frac{1}{2}\ln\left(\frac{1+(1-2\beta a_0/x)^{1/2}}{1-(1-2\beta a_0/x)^{1/2}}\right)\right] \qquad (1)$$

In Eq. (1), α is the fine-structure constant, m_e the electron mass, $\lambda\!\!\!^{-}_C$ the electron Compton wavelength, a_0 the Bohr radius, and c the speed of light. For x = 1.0 nm, with M = 7 amu, β = 1, Z_1 2, and Z_2 = 1, Eq. (1) gives $\tau \simeq$ 14.6 fs. For these parameters, the explosion of a homonuclear diatomic molecule would yield an ion kinetic energy of U_0 = 13.6 eV for each fragment, a magnitude that can be readily measured.

Studies of this nature have been performed on several systems, including N_2, N_2O, CO and CO_2. A basic question arises concerning the dynamical role, if any, of the frequency of the intense radiation causing the multiphoton ionization. There has been, in particular, a controversy between the results obtained with N_2 in experiments conducted with ~ 610 nm and 248 nm radiation.[16,20,27] Significantly, the recent experimental work of Lavancier et al.[20] on CO indicate that there is a strong frequency dependence in the coupling mechanism and that both of the earlier interpretations were basically sound. The ultraviolet wavelength favors a vertical pathway for excitation (small or negligible nuclear motion) while the coupling of the visible radiation appears to be substantially nonvertical and involves considerable nuclear displacement during the process of ionization. Interestingly, the comparison[26] of the Coulomb explosions observed with 248 nm radiation for CO and CO_2, with those arising from fast ion collisions,[28] also appears to confirm the vertical nature of the excitation occurring for the ultraviolet wavelengths. The basic finding is that, under appropriate conditions, the multiphoton process can remove a substantial number of electrons in a time interval sufficiently short that nuclear motion in the molecular frame is quite small. As a result of curve crossings that can be traversed during the process of dissociation, this finding presents a number of important implications for the production of electronically excited ions.[29]

III. SOLID MATTER INTERACTIONS

Studies of the interaction of condensed matter with short pulse (~ 600 fs) high intensity (~ 10^{17} W/cm^2) ultraviolet (248 nm) radiation show that intense spatially compact sources for x-ray emission in the kilovolt range can be generated from solid BaF_2 targets at close to the maximum volume specific rate allowed.[24] In this case the radiation is emitted in the 9 – 13 Å range by transitions involved M-shell electrons of Ba ions as shown in Fig. (1). The observed structure can be put in correspondence with previous measurements of the $3d^n \rightarrow 3d^{n-1}4f$ sequence in that material.[30] The measurements showed that the emitted intensity I_x fell in

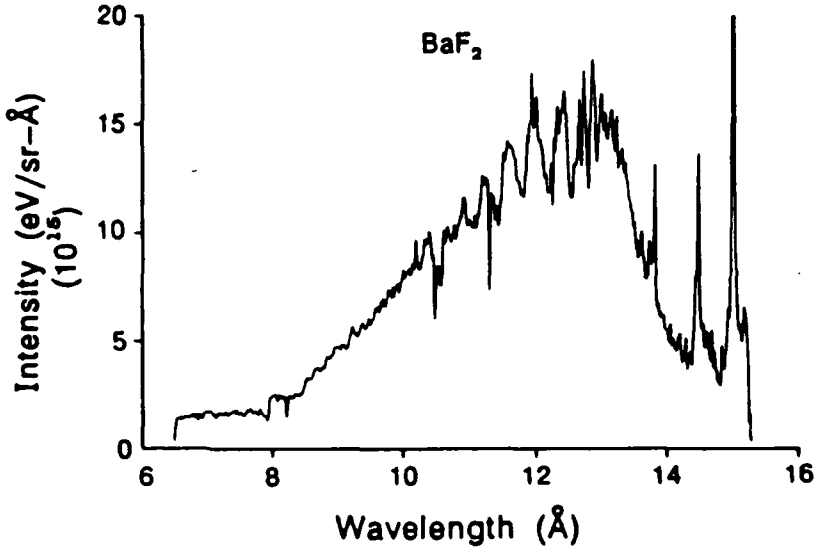

Fig. (1). Spectrum of x–ray emission observed from BaF_2 at a laser intensity of ~ 10^{17} W/cm^2.

the range $5 \times 10^{14} \leq I_X \leq 10^{15}$ W/cm^2, an extraordinarily high value. A simple, but experimentally based, analysis[24] shows that the upper bound of the emission rate is ~ 2×10^{15} W/cm^2, a magnitude only slightly above the measured intensity. Other high–Z materials are expected to exhibit similar characteristics.

Given the findings on Ba, if sufficient excitation is available, transitions involving M–shell electrons in uranium ions should produce very intense radiation in the 4–5 keV region. Estimates suggest that for this case intensities in the 10^{17} – 10^{18} W/cm^2 range would occur. Although this emission is incoherent, such sources provide extremely powerful and spatially compact x–ray emitters.

IV. SUMMARY

Studies of strong–field coupling to molecules and solids are producing experimental evidence that new classes of highly excited matter can be produced. The common factor in these two types of materials is the ability to produce extremely high levels of electronic excitation in a manner which enables the heavy bodies of the system to remain kinetically cold for the time scale of the interaction.

V. ACKNOWLEDGMENTS

The technical assistance of P. Noel and J. Wright and helpful discussions with J. C. Solem, B. E. Bouma and G. N. Gibson are acknowledged. The fruitful and congenial participation of A. Zigler, P. G. Burkhalter, D. J. Nagel and M. D. Rosen in the studies of solid materials is warmly acknowledged. Support for this research was provided by the U. S. Office of Scientific Research, the U. S. Office of Naval Research and the Strategic Defense Initiative Organization.

VI. REFERENCES

1. C. K. Rhodes, "Multiphoton Ionization of Atoms," Science 229, 1345–1351 (1985).
2. S. Szatmári, F. P. Schäfer, E. Müller–Horsche and W. Mückenhelm, "Hybrid Dye–Excimer Laser System for the Generation of 80 fs, 900 GW Pulses at 248 nm," Opt. Comm. 63, 305–309 (1987).
3. A. Endoh, M. Watanabe, N. Sarukura and S. Watanabe, "Multiterawatt Sub–picosecond KrF Laser," Opt. Lett. 7, 353–355 (1989).
4. J. R. M. Barr, N. J. Everall, C. J. Hooker, I. N. Ross, M. J. Shaw and W. T. Toner, "High Energy Amplification of Picosecond Pulses at 248 nm," Opt. Comm. 66, 127–132 (1988).
5. J. G. Glownia, J. Misevich and P. P. Sorokin, "160–fsec XeCl Excimer Amplifier System," J. Opt. Soc. Am. B 4, 1061–1065 (1987).
6. A. P. Schwarzenbach, T. S. Luk, I. A. McIntyre, U. Johann, A. McPherson, K. Boyer and C. K. Rhodes, "Subpicosecond KrF^* Excimer–Laser Source," Opt. Lett. 11, 499–451 (1986).
7. J. P. Roberts, A. I. Taylor, P. H. Y. Lee and R. B. Gibson, "High–Irradiance 248–nm Laser System," Opt. Lett. 13, 734–736 (1988).
8. T. S. Luk, A. McPherson, G. Gibson, K. Boyer and C. K. Rhodes, "Ultrahigh–Intensity KrF^* Laser System," Opt. Lett. 14, 1113–1115 (1989).
9. A. J. Taylor, C. R. Tallman, J. P. Roberts, C. S. Lester, T. R. Gosnell, P. H. Lee and G. A. Kyrala, "High–Intensity Subpicosecond XeCl Laser System," Opt. Lett. 15, 39–41 (1990).
10. A. J. Taylor, T. R. Gosnell and J. P. Roberts, "Ultrashort–Pulse Energy–Extraction Measurements in XeCl Amplifiers," Opt. Lett. 15, 118–120 (1990).
11. I. A. McIntyre and C. K. Rhodes, "High Power Ultrafast Excimer Lasers," J. Appl. Phys. 69, R1–R19 (1991).
12. J. Frasinski, K. Codling, P. Hatherly, J. Barr, I. N. Ross and W. T. Toner, "Femtosecond Dynamics of Multielectron Dissociative Ionization by Use of Picosecond Laser," Phys. Rev. Lett. 58, 2424–2427 (1987).
13. K. Codling, L. J. Frasinski, P. Hatherly and J. R. M. Barr, "On the Major Mode of Multiphoton Multiple Ionization," J. Phys. B 20, L525–L531 (1987).
14. T. S. Luk and C. K. Rhodes, "Multiphoton Dissociative Ionization of Molecular Deuterium," Phys. Rev. A 38, 6180–6184 (1988).
15. K. Codling, L. J. Frasinski and P. A. Hatherly, "On the Field Ionization of Diatomic Molecules in Intense Laser Fields," J. Phys. B 22, L321–L327 (1989).
16. K. Boyer, T. S. Luk, J. C. Solem and C. K. Rhodes, "Kinetic Energy Distributions of Ionic Fragments Produced by Subpicosecond Multiphoton Ionization of N_2," Phys. Rev. A 39, 1186–1192 (1989).
17. P. A. Hatherly, L. J. Frasinski, K. Codling, A. J. Langley and W. Shaikh, "The Angular Distribution of Atomic Ions Following the Multiphoton Ionization of Carbon Monoxide," J. Phys. B 23, L291–L295 (1990).
18. P. H. Bucksbaum, A. Zavriyev, H. G. Muller and D. W. Schumacher, "Softening of the H_2^+ Molecular Bond in Intense Laser Fields," Phys. Rev. Lett. 64, 1883–1886 (1990).
19. L. J. Frasinski, K. Codling and P. A. Hatherly, "Covariance Mapping: A Correlation Method Applied to Multiphoton Multiple Ionization," Science 246, 1029–1031 (1989).
20. J. Lavancier, D. Normand, C. Cornaggia, J. Morellec and H. X. Liu, "Laser–Intensity Dependence of the Multielectron Ionization of CO at 305 and 610 nm," Phys. Rev. A 43, 1461–1469 (1991).
21. M. M. Murnane, H. C. Kapteyn and R. W. Falcone, "High Density Plasmas Produced by Ultrafast Laser Pulses," Phys. Rev. Lett. 62, 155–158 (1989).

22. H. M. Milchberg, R. R. Freeman, S. C. Davey and R. M. More, "Resistivity of a Simple Metal from Room Temperature to 10^6 K," Phys. Rev. Lett. 61, 2364–2357 (1988).
23. M. M. Murnane, H. C. Kapteyn, M. D. Rosen and R. W. Falcone, "Ultrafast X–Ray Pulses from Laser–Produced Plasmas," Science 251, 531–536 (1991).
24. A. Zigler, P. E. Burkhalter, D. J. Nagel, K. Boyer, T. S. Luk, A. McPherson, J. C. Solem and C. K. Rhodes, "High Intensity Generation of 9 – 13 Å X–Rays from BaF_2 Targets," submitted to Appl. Phys. Lett.
25. A. Zigler, P. G. Burkhalter, D. J. Nagel, T. S. Luk, A. McPherson, C. K. Rhodes and M. D. Rosen, "Measurement of Energy Penetration Depth of Subpicosecond Laser Energy into Solid Density Matter," submitted to Appl. Phys. Lett.
26. T. S. Luk, A. McPherson, B. E. Bouma, K. Boyer and C. K. Rhodes, "Studies of the Interaction of Molecules and Solids with Intense Subpicosecond 248 nm Radiation," in Multiphoton Processes, edited by G. Mainfray and P. Agostini (CEA, Paris, 1991), p. 217–227.
27. L. J. Frasinski, K. Codling and P. A. Hatherly, "Multiphoton Multiple Ionization of N_2 Probed by Covariance Mapping." Phys. Lett. 142, 499–503 (1989).
28. T. Matsuo, T. Tonuma, M. Kase, T. Kambara, H. Kumagai and H. Tawara, "Production of Multiply Charged Ions from CO and CO_2 Molecules in Energetic Heavy–ion impact," Chem. Phys. 121, 93–98 (1988).
29. "Molecular X–Ray Laser Research," T. S. Luk, A. McPherson, G. N. Gibson, K. Boyer, and C. K. Rhodes, SWLA – 90 International Symposium, "Short Wavelength Lasers and Their Applications," Samarcand, USSR, May 14–18, 1990, in press.
30. G. Melman, P. G. Burkhalter, D. A. Newman, and B. H. Ripin, "Soft X–Ray Continuum from Laser–Irradiated High–Z Targets," J. Quant. Spectrosc. Rad. Transfer," in press.

Intense Field Nonresonant Multiphoton Absorption of Diatomic Molecules

B. Yang, M. Saeed, and L. F. DiMauro

Department of Chemistry, Brookhaven National Laboratory, Upton, New York 11973

Abstract

We report on the multiple photon ionization and dissociation of hydrogen, deuterium, and deuterium hydride molecules in intense ($8 \times 10^{11} - 4 \times 10^{13}$ W/cm^2) laser fields. The three isotopes give some insight into the intermediate states involved in the photoionization process. We are able to measure ratios of ATD peaks for H_2^+ and D_2^+ over a wide range of intensities. Our results support the dressed molecule picture at least qualitatively but differences do exist with the quantitative predictions.

Interest in the behavior of isolated atoms in intense radiation fields has resulted in a cumulative literature rich in new phenomena[1], unresolved issues, and exciting new predictions for future studies. Recently, the behavior of molecules in intense fields is attracting an increased amount of attention, especially in the studies of photodissociation dynamics. The additional challenge associated with studying molecules in strong fields result from the difficulty of sorting out the general behavior of field-induced effects from the details or specifics of the molecular structure. This becomes inherently more cumbersome due to the many internal degrees of freedom of molecules compared to atomic systems. However, these strong-field studies raise some interesting and unique questions concerning the role and interplay of ionization and dissociation. Furthermore, the attraction for studying molecules derives its fundamental interest from the ability to control molecular dynamics by external variation of a laser field. Although premature in realization, an understanding of the influence of both intensity and pulse duration in concert with frequency may ultimately lead to our ability or inability to control chemical dynamics.

Molecular hydrogen represents the "model" molecular system for these studies because of its simple and well known molecular structure and as a result should provide the foundation for future field-molecule studies. The effects of intense fields on H_2 have been studied lately by observing the above threshold ionization and dissociation (ATI and ATD) phenomena through resonant[2] and non-resonant[3-5] multiphoton ionization (MPI). Several models for the photodissociation of H_2, dressed molecular state model[5,6] for instance, have been proposed. Absence of rigorous treatments, difficulties in experi-

© 1991 Optical Society of America

ments and insufficient resolution of the results leave the picture of the interaction between the potential surfaces of the H_2 molecule and the field still less than very well understood. In this paper, we report on "non-resonant" ionization and dissociation of H_2, D_2 and HD molecules in intense ($8 \times 10^{11} - 4 \times 10^{13}$ W/cm^2) laser fields. The molecules were irradiated by the second harmonic of both Nd:YAG and Nd:YLF lasers. The first I.P. from the vibrationless H_2 ground state is 15.425 eV, requiring at least 7 photons for ionization in the current experiment. The well resolved intensity dependent electron and proton spectra along with the comparison of data taken at two wavelengths (527 and 532 nm) and for two different isotopes is very useful in elucidating the interaction dynamics predicted by existing models.

The intense laser field photodissociation of H_2^+ has been explained by the mechanism of bond-softening[5,6] using a dressed molecular state formalism. In this model, the laser field is considered as a strong perturber to the molecular potential. The potential curves couple and distort via the strong dipole interaction. Since the ground ionic state and the first repulsive state have symmetry $^2\Sigma_g^+$ ($1s\sigma_g$) and $^2\Sigma_u^+$ ($2p\sigma_u$) respectively, only 1, 3, 5, ...(odd number) photons can be used to dress the transition state because of parity conservation. However, a *net even number* of photon dissociation can also occur due to the absorption and stimulated emission of photons. Intense fields cause the laser induced avoided crossing gap to open up. Any ions with vibrational energy within the gap should become unstable. As the laser intensity is increased and the molecular potentials distort, one should observe a negative shift in the proton kinetic energy corresponding to dissociation from the lower vibrational states of H_2^+. Furthermore, the absorption of more photons ($N \geq 2$) from the same vibrational states results in a series of peaks separated by about a photon (total) kinetic energy (ATD). Likewise, the distorted potentials result in a change in the vibrational energy eigenvalues resulting in a positive shift in the photoelectron spectrum.

The photon sources used are well characterized Nd:YAG ($1.06\mu m$, 10 nsec, 10 Hz) and Nd:YLF ($1.05\mu m$, 50 psec, 1 kHz) lasers. Details of these laser systems have been described previously[7]. The intensity ranges for 532 and 527 nm radiations were 8×10^{11} to 9.7×10^{12} W/cm^2 and 5×10^{12} to 4×10^{13} W/cm^2, respectively. The apparatus consists of ultra high vacuum chambers equipped with time of flight electron and mass spectrometers. The photoelectron spectrometer has an energy resolution of about 50 meV for 1 eV electrons. It is calibrated by the well known ATI spectrum of xenon atoms. The mass spectrometer calibration was performed by weak-field photodissociation of chlorine[8] molecules. Its resolution was estimated to be about 100 meV for 1 eV protons. The background pressure in the ultrahigh vacuum system was 1×10^{-9} torr. During an experiment, the number of ions produced in the ionization region was kept less than 50 per shot to minimize space charge effects.

Figure 1 shows a typical time of flight mass spectrum resulting from the 532 nm nonresonant MPI of D_2 molecules at an intensity of 9.7×10^{12} W/cm^2. The three peaks are labelled according to the number of photons being absorbed by D_2^+ ions leading to dissociation. According to our experimental results at low intensity most H_2^+ ions are dissociated from the $v^+_{avg} = 5$ vibrational level following the absorption of a single photon (peak 1 in Fig. 1). The maximum of this peak is observed to shift from $v^+ = 5$ to $v^+ = 4$ at higher intensities. With increasing intensity another peak emerges corresponding to two photon dissociation via $v^+_{avg}=2$. Consequently, its separation is less than a photon total energy from the first peak due to differing initial vibrational states and is intensity dependent. At still higher intensities a third peak appears about one photon total

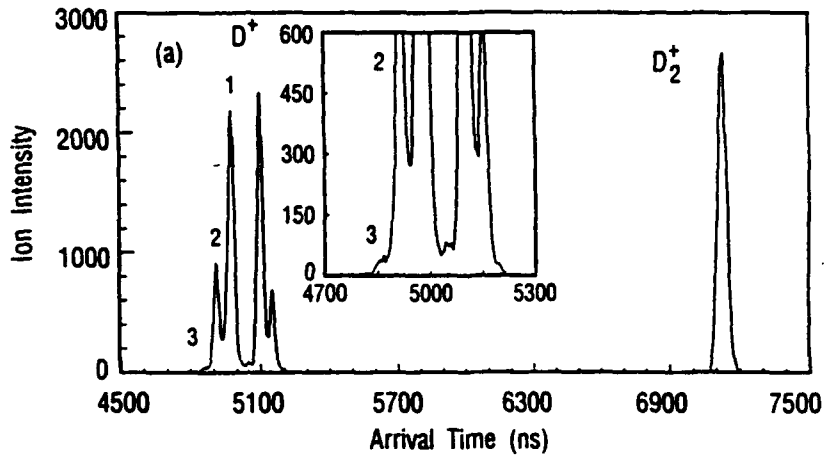

Figure 1: Time-of-flight mass spectrum resulting from 532 nm MPI and dissociation of deuterium at 9.7×10^{12} W/cm^2.

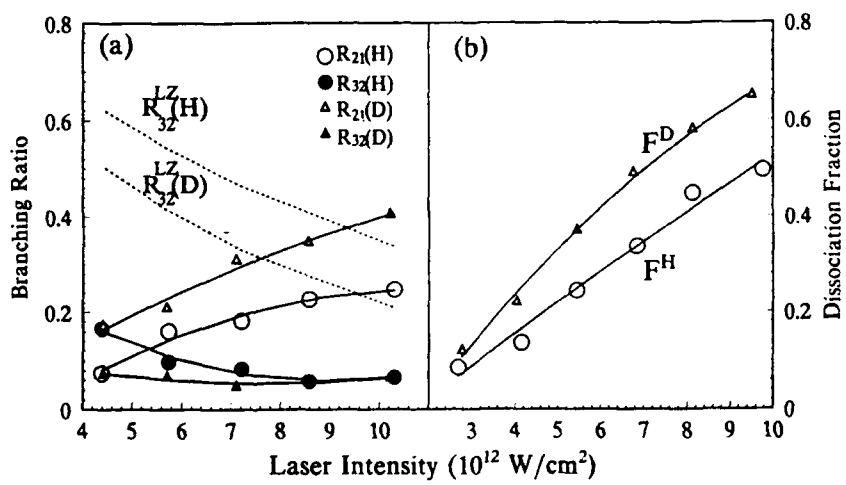

Figure 2: A plot of the (a) branching ratios, **R**, and (b) dissociation fraction, **F**, for H_2 and D_2 as a function of 532 nm intensity.

energy away from the second peak corresponding to a three photon dissociation. The same general behavior is observed for D_2 and HD molecules. Similar kinetic energy shifts were observed in the 527 nm (psec) spectra over an intensity range of 5×10^{12} to 4×10^{13} W/cm^2. Shown in Fig. 2(b) is the dissociation fraction $\mathbf{F}^H$ and $\mathbf{F}^D$ as a function of laser intensity for H_2^+ and D_2^+, respectively and where $\mathbf{F}^H = [H^+/(H^+ + H_2^+)]$ and $\mathbf{F}^D = [D^+/(D^+ + D_2^+)]$. Note, that the dissociation fraction for each molecule increases with intensity and that $\mathbf{F}^D$ is larger than $\mathbf{F}^H$ at all intensities shown.

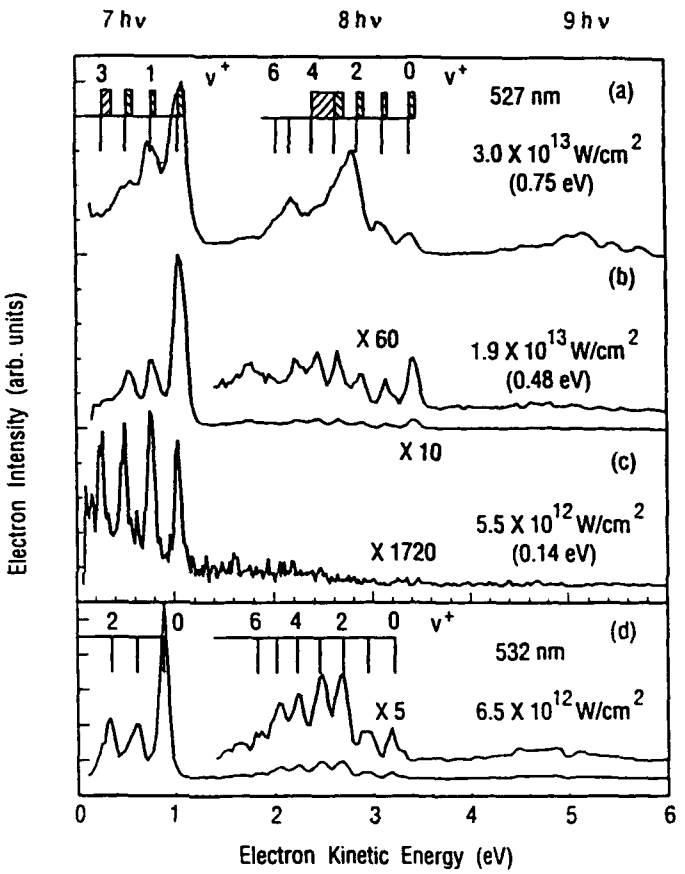

Figure 3: Photoelectron spectrum of H_2 molecule taken at different laser intensities with 527 and 532 nm radiations. The data is normalized for gas density and number of laser shots. The tick marks indicate the unperturbed vibrational levels of the H_2^+ ground state. The hashed boxes are the shifts calculated in ref. 5 using a Floquet method at the maximum 527 nm intensity of 3×10^{13} W/cm^2. The numbers in parenthesis are the corresponding Ponderomotive energies at each intensity.

We have carefully examined the photodissociation of H_2^+ molecules by recording the proton kinetic energy spectra and the H_2 photoelectron spectra simultaneously as a function of laser intensity. Our results verify that the mechanism responsible for H^+ and D^+ formation is the photodissociation of the parent molecular ion. It appears that the amount of H^+ produced is proportional to that of photoelectrons due to (7+1) molecular ionization. In addition, energy conservation implies that seven second harmonic photons of YAG(YLF) can populate only up to $v^+ = 3(4)$ vibrational levels in the ionic ground state, whereas the lowest intensity data have proton energies peaked at $v^+ = 5$. Thus, we conclude that the H^+ peak labeled 1 in Fig. 1 (0.7 eV total energy) is due to the eight photon ionization of H_2 followed by one photon dissociation of H_2^+.

Figure 3 shows the photoelectron spectra of H_2 at 532 and 527 nm at different laser

intensities. For the entire dynamic range of laser intensities, the vibrational structure of 7 and 8-photon processes is resolvable as well as assignable to the unperturbed vibrational frequency of H_2^+ within experimental error. Some important features of the spectra should be pointed out here. (1) The low intensity 527 nm photoelectron spectrum shown in Fig. 3(c) exhibits well resolved v^+=0–3 vibrational bands whose intensity distributions are similar to the Frank Condon factors expected from a direct 7-photon ionization between the H_2 $^1\Sigma_g^+$ and H_2^+ $^2\Sigma_g^+$ ground states. (2) As the 527 nm laser intensity is increased in Fig. 3 to 3 x 10^{13} W/cm^2, only the low energy electrons, specifically the $v^+ = 2$ and 3 bands, are suppressed proportional to the expected Ponderomotive shifts in the ionization potential. No such suppression is observed with the 532 nm excitation due to the lower saturation intensity of H_2 in nanosecond pulses. (3) Over the entire intensity region for 532 nm excitation and those above 10^{13} W/cm^2 with 527 nm the photoelectron spectrum (PES) profiles are similar, i.e. for the seven photon process most ions are formed in the $v^+ = 0$ level, suggesting a probable intermediate state resonance. (4) At the lowest intensity which results in an observable rate, the three molecules show different vibrational distributions (see Fig. 4) which is also indicative of intermediate state effects. (5) The maximum in the photoelectron distribution for the eight photon process (ATI) shifts gradually from $v^+ = 5$ to $v^+ = 2$ as the laser intensity is increased. (6) The amplitude shift in the 8-photon photoelectron distribution for all three molecules is independent of the molecule studied. That is, the most probable photoelectron kinetic energy at a given intensity is the same for H_2, D_2, and HD. (7) Finally, no dramatic shifts were observed in the positions of photoelectron kinetic energies as a function of laser intensities within our experimental resolution. However, the peaks are observed to become asymmetrically broadened towards lower electron energies at the highest intensities. This broadening is observed to be universal for all three isotopically substituted molecules.

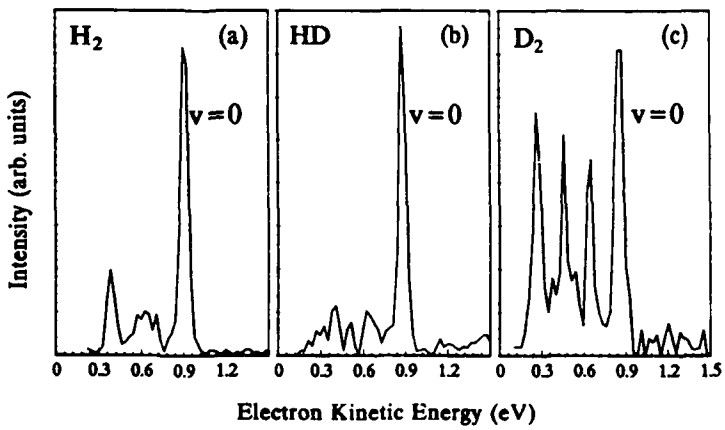

Figure 4: Low intensity 532 nm PES of (a) H_2, (b) HD, and (c) D_2 taken at 1 x 10^{12} W/cm^2.

Our results are generally in qualitative agreement with the bond-softening model but there remain some quantitative differences. In the current experiment, we observed apparent negative shifts in proton kinetic energies with increasing laser intensity with both 532 nm (ns) and 527 nm (ps) pulses. The maximum population of the 1-photon proton kinetic energy peak shifts by $\sim$ 200 meV over the entire intensity range. Likewise, the maximum of the ionic vibrational state distribution in the PES changes from high to low vibrational levels in a similar intensity range, although the shift in the amplitude of the vibrational distributions is independent of the molecule studied. Thus, the bond-softening to first order is predominantly an electronic coupling and not vibrational. However, we could not observe any commensurate positive energy shifts in the PES peak positions with increasing intensity although a broadening is clearly evident. An asymmetric broadening in our PES could result from spatial or temporal averaging in our experiment masking a "pure" energy shift. However, the sign of the observed broadening is opposite to that predicted by a bond-softening model[5] (see Fig. 3). This inconsistency could imply a shortcoming in the numerical method since only the vibrational motion in the distorted potential are included in the Floquet calculation. Another contributing factor to the peak width could result via strong-field rotational pumping with increasing laser intensity, causing the photoelectron peaks to broaden towards lower energies.

Referring to Fig. 2(a), the ratio ($\mathbf{R}_{21}$) of dissociation via 2-photon versus the 1-photon channels for H_2^+ changes from 7% to 25% as the intensity is increased to 9.7 x 10^{12} W/cm^2. Furthermore, the ratio $\mathbf{R}_{32}$ for 3 versus 2-photon dissociation decreases from 16.5 to 6.5% in the same range. Interestingly, the behavior in D_2^+ is somewhat different, here the fraction $\mathbf{R}_{21}$ changes from 17 to 40% which is larger than H_2^+. However, the D_2^+ ratio $\mathbf{R}_{32}$ is smaller than H_2^+ and relatively constant ($\sim$6%) over the entire intensity range. These branching ratio effects can be all understood with the same model[6]. Physically, the increasing laser intensity corresponds to a larger avoided-crossing gap resulting in a decrease in the 3-photon diabatic transition rate while favoring 2-photon adiabatic passage (3-photon absorption, 1-photon emission). Since H_2^+ and D_2^+ have a relatively large difference in vibrational frequencies due to their different masses, therefore at low intensities where the gap is not large enough to completely shut off the 3-photon channel, D_2^+ molecules branch more efficiently through the 2-photon adiabatic path as compared to H_2^+ due to the fact that a smaller vibrational frequency implies more adiabatic motion. Specifically, $\mathbf{R_{32}}(H) > \mathbf{R_{32}}(D)$ at low intensity. As the gap continues to widen, one should also observe the ratio $\mathbf{R}_{32}$ to decrease for both H_2^+ and D_2^+ molecules. Such behavior is clearly demonstrated in our experiments. Figure 2(a) also shows for comparison the results of the calculated fragment $\mathbf{R}_{32}^{LZ}$ ratios predicted by a simple Landau-Zener (LZ) theory[5]. The theory predicts well the general behavior of the ratios as the light intensity changes. However, the calculated ratios are approximately three times larger than the experimental values which could imply that the degree of deformation of the calculated potential curves is beyond the limits of applicability of simple LZ theory.

Speculations on the intermediate states involved in the 532 nm ionization of H_2 have been previously made by Verschuur et al.[4] and Zavriyev et al.[5]. In Verschuur's[4] experiment, the ionization through the B $^1\Sigma_u^+$ (v'=3) with five photon resonance and GK $^1\Sigma_g^+$ (v'=2) with six photons were considered to be the major processes. Unfortunately, the photoelectron spectra in either experiment could not be resolved. Figure 4 shows the 7-photon 532 nm photoelectron spectra of H_2, D_2, and HD taken at an intensity of 1 x 10^{12} W/cm^2. Each spectrum differs in the amount of contributions from higher

vibrations (v^+=1-3) but all share the v^+=0 peak as the dominant feature. In fact, the HD spectrum is predominantly v^+=0 and indicative of a diagonal δv=0 transition from a Rydberg state to the ionic ground state. However, for 527 nm excitation of H_2 (Fig. 3) at low intensity, the lowest four vibrations have comparable amplitude but the distribution becomes similar to 532 nm PES at high intensity. For 532 nm radiation, the energy difference ($E_{6h\nu}$-E_{level}) between 6 photons and unperturbed G $^1\Sigma_g^+$ (v'=0), I $^1\Pi_g$ (v'=0), and J $^1\Delta_g$ (v'=0) states of H_2 is only 121.9, 89.6, and 33.5 meV, respectively[9]. Ionization from these intermediate Rydberg states to the ionic ground states are diagonal transitions, i.e. δv = 0. Consequently, there will be a wide range of laser intensities for which one can expect a resonant enhancement via dynamical shifts to occur for the v'=0 level, explaining its dominant population in our 532 nm PES. Moreover, for 527 nm excitation this difference is 271.9, 239.6, and 183.4 meV, respectively. This larger detuning implies that for low intensities the 527 nm process will be virtually nonresonant [see Fig. 3(c)]. However, for moderately high intensities a Ponderomotive shift $\geq$0.18 eV (7 x 10^{12} W/cm^2) will bring the various v'=0 states into resonance resulting in a PES spectrum similar to the 532 nm excitation. Thus, we propose that the transition dynamics leading to the final state vibrational distribution via 532 nm excitation in the low intensity regime is dominated by the J $^1\Delta_g$ (v'=0) intermediate level but at higher intensities may be influenced by the G and I states.

In conclusion, the results presented in this paper support the qualitative predictions of a bond-softening model. Our well resolved electron and mass spectra also provide quantitative data which will facilitate some important tests of numerical methods. Evident in our studies is that the isotopic fragment branching ratios are predominantly a vibronic effect due to changing mass, whereas the bond-softening is electronic in nature. However, this could change in the *short pulse (< 1 ps) regime* due to rotational aligment effects.

Acknowledgments

The authors gratefully acknowledge the contributions of Phillip Bucksbaum and Anton Zavriyev to this work and thank them for the use of their Floquet results. The authors would like to thank Joseph Dolce for his technical assistance. This research was carried out at Brookhaven National Laboratory under Contract No. DE-AC02-76CH00016 with the U.S. Department of Energy and supported, in part, by its Division of Chemical Sciences, Office of Basic Energy Sciences.

References

1. See for example, Atomic and Molecular Processes with Short Intense Laser Pulses, A. D. Bandrauk, ed., (Plenum Press, NY and London, 1988).
2. C. Cornaggia, D. Normand, J. Morellec, G. Mainfray, and C. Manus, "Resonant multiphoton ionization of H_2 via the E, F $^1\Sigma_g^+$ state: Absorption of photons in the ionization continuum," Phys. Rev. A 34, 207-215 (1986) and S.W. Allendorf and A. Szöke, "High intensity multiphoton ionization of H_2," Phys. Rev. A (to be published).
3. T.S. Luk and C. Rhodes, "Multiphoton dissociative ionization of molecular deuterium," Phys. Rev. A 38, 6180-6184 (1988).

4. J. Verschuur, L. Noordam, and H. van Linden van den Heuvell, "Anomalies in above threshold ionization observed in H_2 and its excited fragments," Phys. Rev. A. 40, 4383-4391 (1989).
5. A. Zavriyev, P. Bucksbaum, H. Muller, and D. Schumacher, "Ionization and dissociation of H_2 in intense laser fields at 1.06μm, 532 nm, and 355 nm," Phys. Rev. A 42, 5500-5513 (1990) and B. Yang, M. Saeed, L.F. DiMauro, A. Zavriyev, and P. Bucksbaum, "High resolution multiphoton ionization and dissociation of H_2 and D_2 molecules in intense laser fields," Phys. Rev. A (to be published).
6. A. Bandrauk and M. Sink, "Photodissociation in intense laser fields: predissociation analogy," J. Chem. Phys. 74, 1110-1117 (1981) and A. Guisti-Suzor, X. He, O. Atabek, and F. Mies, "Above threshold dissociation of H_2^+ in intense laser fields," Phys. Rev. Lett. 64, 515-518 (1990).
7. M. Saeed, D. Kim, and L.F. DiMauro, "Optimization and characterization of a high repetition rate, high intensity Nd:YLF regenerative amplifier," Appl. Opt. 29, 1752 -1757 (1990) and L.F. DiMauro, D. Kim, M.W. Courtney, and M. Anselment, "Nonresonant multiphoton ionization of calcium atoms in an intense laser field," Phys. Rev. A 38, 2338-2346 (1988).
8. L. Li, R. Lippert, J. Lobue, W. Chupka, and S. Colson, "Adiabatic dissociation of photoexcited chlorine molecules," Chem. Phys. Lett. 151, 335-339 (1988).
9. K.P. Huber and G. Herzberg, Constants of Diatomic Molecules (Van Nostrand Reinhold Company, New York, 1979).

Molecular Multiphoton Ionization

G. N. Gibson* and R. R. Freeman

AT&T Bell Laboratories, Holmdel, New Jersey 07733

T. J. McIlrath

Institute for Physical Science and Technology, University of Maryland, College Park, Maryland 20742

Abstract

Resonant multiphoton ionization (MPI) of nitrogen has been studied using photoelectron spectroscopy in the short-pulse regime. Both Rydberg and valence states are identified as intermediate resonances in the photoionization process, although the valence states are seen only at low intensity. It is shown that the vibrational structure of the Rydberg states acting as intermediate resonances cancels out in the photoelectron spectrum, leading to sharp atomic-like spectra, even at high intensities. Finally, the ionization of the $3\sigma_g$, $1\pi_u$, and $2\sigma_u$ electrons are clearly distiguished.

Introduction

Over the past few years a good understanding of the basic aspects of the multiphoton ionization (MPI) of rare gas atoms has emerged.[1] The MPI of molecules has recently attracted interest because the extra molecular degrees of freedom have led to new expected and unexpected phenomena. The expected fragmentation of an ionized molecule can be analysed in terms of the fragment distribution and fragment kinetic energies to learn about the time scale of the MPI process.[2,3,4] Careful control of a spectral chirp can lead to efficient multiphoton dissociation.[5] The unexpected results include a strong wavelength dependence in molecular MPI,[3] ATI absorption in the fragments,[6] molecular bond softening,[6] and the observation of inner-orbital ionization.[7]

In this article we present high resolution photoelectron spectra produced by nitrogen in a strong laser field. The analysis relies on the spectroscopic techinque of using linearly polarized light in the short-pulse regime to reveal the resonant structure of the molecule in the presence of a strong field.[8]

The ATI electron energy spectra of atoms in the short pulse regime up to intensities of 10^{15} W/cm^2 are now well understood.[1] Applying this understanding of atoms to molecules would lead one to expect molecules to yield a very complex electron energy spectrum due to the multitude of potential curves and vibrational and rotational structure

Proceedings on Short-Wavelength Coherent Radiation, Vol. 11, *Philip H. Bucksbaum and Natale M. Ceglio (eds.)*
© 1991 Optical Society of America

in the molecule. On the contrary, recently obtained ATI electron spectra of nitrogen show relatively simple features, some of which are surprisingly similar to the spectra of atoms, and are straightforward to interpret. The simplification from what one might expect occurs because of the cancellation of the vibrational structure of the Rydberg resonances and the fact that the valence states play a rather small, though observable role. Besides identifying the intermediate resonances in the MPI process we can clearly distinguish the MPI of the $3\sigma_g$, $1\pi_u$, and $2\sigma_u$ electrons. This compliments a previous demonstration of the MPI of the more deeply bound $2\sigma_g$ electron in N_2 using fluorescence spectroscopy.[7]

Experimental Apparatus

The experiments discussed here were performed with both 616 nm and 308 nm radition produced as follows: a CPM dye laser running at 616 nm was amplified to 1 mJ, 150 fs pulses at 10 hz. These pulses were either sent to the experimental chamber or doubled to 308 nm and again amplified to 1 mJ in an XeCl excimer laser. The electron time-of-flight (TOF) spectrometer[9] consists of a 1 m drift tube and a parabolic electron mirror biased at -5 V or -10 V allowing greater than 2π collection solid angle and an energy resolution of 30 meV at an electron energy of 2 eV. Spectra were binned according to laser energy in a bin width of ± 10% in energy. Sample pressures ranged from 5×10^{-7} to 7×10^{-5} torr to aviod the effects of space charge.[10] The spectra are all normalized to electrons/ev/shot/mtorr.

Atomic Short-Pulse ATI

As with any photoelectron spectroscopy, the ionized electrons have a kinetic energy of $E_{elec} = mE_\gamma - E_{IP}$, where E_γ is the photon energy, m is greater than or equal to the minimum number of photons required to ionize, and E_{IP} is the ionization potential of the atom in the laser field. This is simply given by the ionization potential at zero field plus the ponderomotive potential, $U_p = e^2E^2/4m\omega^2$. The difference in a.c. Stark shift between the ground states of the atom and the ion is neglected. In the short-pulse regime the electron is not accelerated as it leaves the laser focus. As a result, the detected electrons will have an energy

$$E_{elec} = mE_\gamma - E_{IP}(\text{zerofield}) - U_P(I) \tag{1}$$

where I is the laser intensity. Since U_p is a linear function of I, the electron energy gives a direct measurement of the absolute intensity when the electron was ionized.

Although, in general, the atom has no resonances with the laser field, energy levels can be tuned into resonance with the a.c. Stark shift. A particular level will be in resonance at a well defined intensity and consequently will show up in the electron spectrum as a narrow feature at an energy given by Eq.(1).

In a molecule, there are two types of states, Rydberg and valence, and they will behave rather differently in a strong field. The Rydberg states have large orbits and, thus, tend to be relatively uncoupled from the ion core. As a consequence, the ac Stark shift is

very well approximated by the ponderomotive energy, U_p, and the different angular momentum sublevels of a Rydberg state are nearly degenerate. All the levels in a Rydberg state will stay together as they are shifted in energy by the laser field. In this special case, where the a.c. Stark shift is equal to the ponderomotive potential, the condition necessary for resonance is that $U_p = m'E_\gamma - E$, where E is the zero field energy of the state above the ground state. Eq.(1) then becomes, for Rydberg states in particular:

$$E_{elec}(\text{Rydberg}) = (m-m')E_\gamma - E_b \qquad (2)$$

where $E_b = E_{IP} - E$ is the binding energy of the state.

Unlike atoms, molecules have vibrational structure which would appear to complicate the ATI spectrum because of the many different ionization pathways. Fig. 1 shows a diagram of several potential curves of N_2,[11] although the following discussion is perfectly general. Consider two vibrational levels v' and v of the N_2^+ B final state and a Rydberg state built on the same B state, respectively. Let α' and α be the vibrational constants of these states and β' and β the energy difference between the v = 0 levels of these states and integral numbers of the photon energy. To bring the v level into resonance requires an a.c. Stark shift of β - αv; if the molecule is left in the v' level, the electron will have an energy of $mE_\gamma - (\beta - \beta') + (\alpha v - \alpha' v')$. There are two simplifications which result in a single value for this energy: first, for Rydberg states, α converges to the ionic limit α' and typically differs by only a few tens of wavenumbers,[11] and, second, the Frank-Condon overlap integral ensures that the will be a vibrational selection rule of Δv = 0 as the shape of the potential curves are nearly identical.[12] The only possible electron energy is $mE_\gamma - (\beta - \beta')$, exactly as is the atomic case.

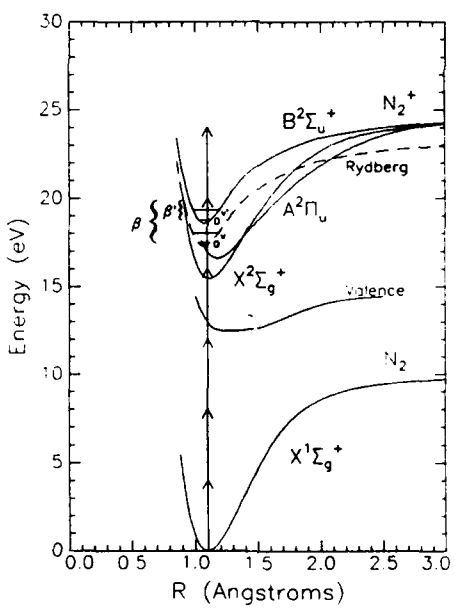

Figure 1. Various potential curves of N_2 from Ref.11. The arrows show the photon energy at 308 nm.

The behavior of the valence states in the strong field will be rather more complicated. The a.c. Stark shift will not have any simple relationship to the ponderomotive potential. Furthermore, the different angular momentum sublevels may not even shift together. Similarly, the Frank-Condon overlap between the valence state and the final ionic state will not lead to the simple selection rule Δv = 0, and, thus, a valence resonance may show vibrational structure. Finally, the a.c. Stark shift of a valence state may depend on the

molecules spatial orientation. This would lead to an additional broadening of the valence state resonances.

Analysis of the Data

Fig. 2 shows electron spectra of nitrogen using the 308 nm beam at four different laser energies. In the low intensity limit U_p in Eq.(1) will be small and so the electrons will come out with energies slightly less than $mE_\gamma - E_{IP}$. In nitrogen there are three low lying ionization potentials corresponding to the removal of the $3\sigma_g$, $1\pi_u$, and $2\sigma_u$ electrons (see Fig.1), resulting in the ionic states $X^2\Sigma_g^+$, $A^2\Pi_u$, and $B^2\Sigma_u^+$, respectively. The value of $mE_\gamma - E_{IP}$ is marked in Fig.2 by the vertical line at the base of the arrows for each of these electrons. It is evident, in Fig.2a, that the three peaks in the spectrum are the result of ionizing to the three final states X, A, and B of the ion. This, in itself, demonstrates the removal of any of the outer electrons of nitrogen with a strong field.

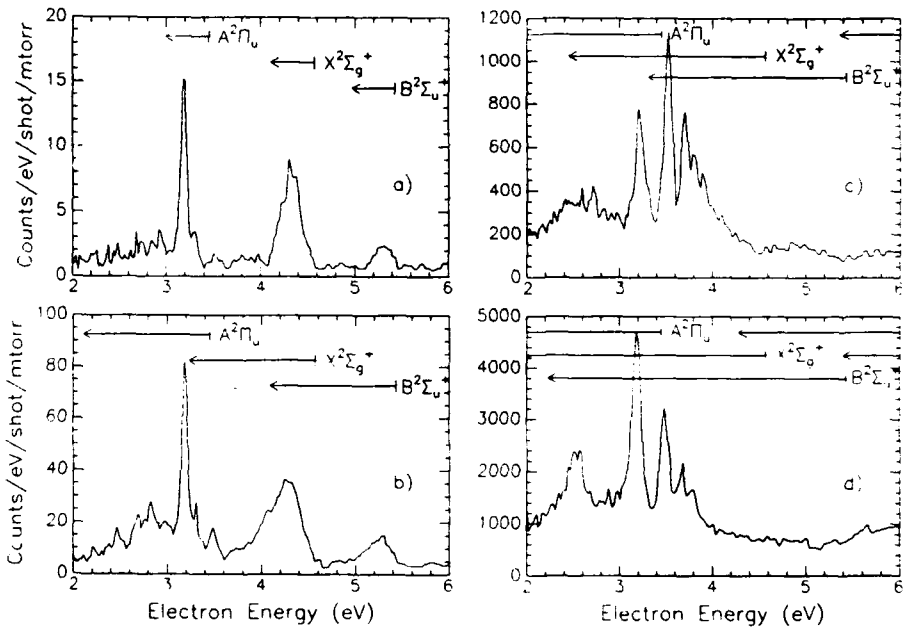

Figure 2. Photoelectron spectrum of N_2 using 308 nm radiation with a) 23 μJ, b) 67 μJ, c) 106 μJ, and d) 160 μJ corresponding to ponderomotive shifts of 0.46 eV, 1.34 eV, 2.12 eV, 3.20 eV, respectively.

This spectrum (Fig.2a) also shows two types of resonances: Rydberg and valence. The peak at 3.18 eV is due to the n=4 Rydberg state built on the N_2^+ $A^2\Sigma_g$ state. This resonance will be with four photons (E_γ = 4.03 eV) and, thus, the allowed states will have either np or nf character. The np states have a know quantum defect[12] of about 0.7 and would occur in the spectrum at 2.78 eV. The nf electrons will have essentially zero

quantum defect, placing the n=4 peak at 3.18 eV. The n=5 peak of the np series can be seen, however, at 3.79 eV. The strength of the nf series relative to the np series supports the propensity rule for high angular momentum states previously observed in atomic ATI. The a.c. Stark shift required to bring this state into resonance is, $4E_\gamma - (E_{IP}(1\pi_u) - E_b(4f)) = 0.27$ eV where $E_{IP}(1\pi_u)$ is the ionization potential of the $1\pi_u$ electron and $E_b(4f)$ is the binding energy of the 4f state. The laser energy required to just see this peak was determined to be 13 μJ. This gives an absolute measurement of the ponderomotive potential vs. laser energy for our focusing conditions: 20 meV/ μJ. (The arrows on the figures show the calculated value of the peak ponderomotive shift for the specified laser energy. Resonant features arising from a given threshold must occur within the the electron energy space delineated by the arrow.)

The other two peaks in Fig.2a are not in the correct position to be Rydberg resonances, and, thus must be due to valence states. Although the two peaks indicate ionization to different final states, they may be due to the same intermediate resonance state. There is also no indication of a similar broad peak associated with the A state, implying that the intermediate state preferentially ionizes to the X or B state. This could be due to its electronic configuration or a preferential Frank-Condon overlap with the X and B state, especially as the internuclear separation in the A state is somewhat larger than the X or B state.

While most of the conclusions of this paper can be drawn from Fig.2a alone, the spectra taken at higher laser energies support the analysis and show some additional interesting behavior. As the intensity is increased the Rydberg series based on the $N_2^+ X^2\Sigma_g^+$ state will be brought into resonance. The binding energy of the 5d state is 0.57 and will appear in the data at E_γ - 0.57 = 3.46 eV. The a.c. Stark shift required to bring this into resonance is 1.11 eV. Using the relationship between laser energy and a.c. Stark shift determined above the 5d peak should come in at 55 μJ. Indeed, it is seen in Fig.2b taken at 67 μJ.

As the laser energy is further increased the next resonance to come in will be the Rydberg series built on the $N_2^+ B^2\Sigma_u^+$ with five photons at roughly 100 μJ, and Fig.2c shows the fully developed Rydberg series, although the intensity in Fig.2c was not quite high enough to reach the 4d resonance.

An important observation from a more complete model of electron spectra in the short-pulse regime[10] is that when a Rydberg series is brought through resonance with a given number of photons the relative height of the different members of the series will decrease rapidly with principle quantum number, n. In argon it was predicted that the peak heights would decrease almost an order of magnitude between successive states. In Fig.2c it is seen that this is not the case for the B series. This implies that the laser intensity is sufficiently high to saturate those resonances.

At the highest intensity, Fig.2d, the 3d peak of the B Rydberg series has come in at around 2.45 eV. Finally, we note that at this intensity the A state has still not had a chance to go through the full Rydberg series of resonances, and, thus, the spectrum is dominated by resonant MPI to the $N_2^+ B^2\Sigma_u^+$ final state.

Electron spectra were also taken with 616 nm radiation, shown in Fig.3, and make an interesting comparison with the UV data. Two aspects are immediately apparent. First, the count rates in Fig.3 are much lower than in Fig.2. Second, they are rather more complex. However, these spectra can be analysed in the same way as the UV spectra.

All of the structure in Fig.3 can be attributed to Rydberg resonances. In Fig.3a the series' built on the N_2^+ A and B states have partially come in on top of the X Rydberg series. In Fig.3b all the Rydberg states associated with the X, A, and B states have gone through resonance, and, indeed, three overlapping series are evident.

Discussion

The differences in the spectra taken at 616 nm and 308 nm can be explained by the dependence of the ponderomotive potential and a.c. Stark shift on the wavelength ($U_p[eV] = 9.33x10^{-14}I[W/cm^2]\lambda^2[\mu m^2]$). In trying to identify different resonant pathways, it is clear from Fig.3 that once the ponderomotive potential exceeds the photon energy the identification becomes difficult. This condition occurs when $U_P \geq E_\gamma$ and the intensity at this point scales as λ^{-3}. For example, in Fig.2a the different pathways leading to different final states are clearly distiguished. Furthermore, the sequence in which different resonances come in can be easily traced through Figs.2a-d. In contrast, a similar spectrum to Fig.2a, where $U_p << E_\gamma$, using 616nm radiation would have a count rate far below the instrument sensitivity. Note that the signal in Fig.3a is already almost a factor of 20 smaller than Fig.2a.

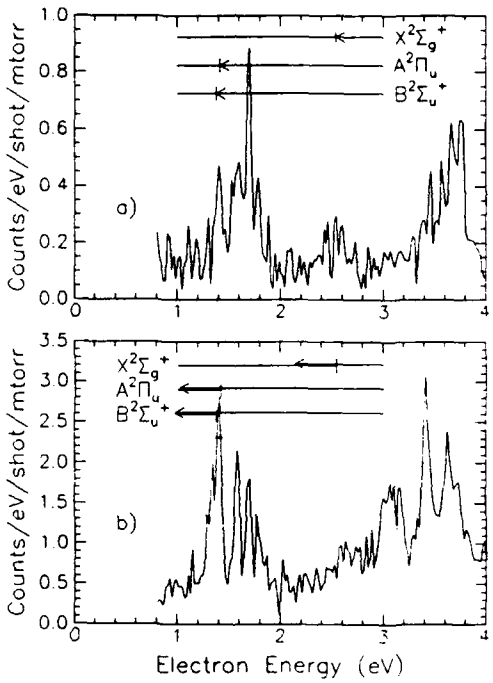

Figure 3. Photoelectron spectra of N_2 using 616 nm radiation with a) 50 μJ and b) 67 μJ corresponding to ponderomotive potentials of 1.8 eV and 2.4 eV, respectively.

Besides the practical consideration of identifying resonances, this scaling will also affect the selectivity in which different pathways contribute to the MPI process. At longer wavelengths many states are shifted into resonance at relatively low intensity. At shorter wavelengths the opposite is true. For example, in Fig.2c and 2d the spectra are dominated by the B Rydberg series, which, in fact, appears to be saturated. The X state went through resonance at much lower intensity and the full A Rydberg series has not yet come into resonance. This implies that the N_2^+B state will be preferentially populated while at 616 nm all the resonances will be competing before any one of them saturates. At either wavelength, however, at the higher intensities, the electron spectra end up dominated by Rydberg series' and look remarkably similar to atomic ATI spectra.

Conclusion

Using linearly polarized light in the short-pulse regime we have identified intermediate resonances in the MPI of nitrogen due to both valence and Rydberg states. The influence of valence states is only seen at low intensity and with 308 nm radiation. The vibrational structure of the Rydberg states is shown to cancel out in the photoelectron spectrum. The ionization of any of the outer three electrons was directly observed. Finally, a strong wavelength dependence was seen.

Acknowledgments

This work was partially supported by AFOSR grant 88-0018.

*Also at University on Maryland.

References

1. For a recent review, see R. R. Freeman and P. H. Bucksbaum, J. Phys. B: At. Mol. Opt. Phys. **24**, 325 (1991).
2. L. J. Frasinski, K. Codling, P. Hatherly, J. Barr, I. N. Ross, and W. T. Toner, Phys. Rev. Lett. **58**, 2424 (1987); K. Codling, L. J. Frasinski, and P.A. Hatherly, J. Phys. B **22**, L321 (1989).
3. C. Cornaggia, J. Lavancier, D. Normand, J. Morellec, and H. X. Liu, Phys. Rev. A **42**, 5464 (1990).
4. K. Boyer, T. S. Luk, J. C. Solem, and C. K. Rhodes, Phys. Rev. A **39**, 1186 (1989).
5. S. Chelkowski, A. D. Bandrauk, and P. B. Corkum, Phys. Rev. Lett. **65**, 2355 (1990).
6. A. Zavriyev, P. H. Bucksbaum, H. G. Muller, and D. W. Schumacher, Phys. Rev. A **42**, 5500 (1990).
7. G. Gibson, T. S. Luk, A. McPherson, K. Boyer, and C. K. Rhodes, Phys. Rev. A **40**, 2378 (1989).
8. R. R. Freeman, P. H. Bucksbaum, H. Milchberg, S. Darack, D. Schumacher, and M. E. Geusic, Phys. Rev. Lett. **59**, 1092 (1987); P. Agostini, P. Breger, A. L'Huillier, H. G. Muller, and G. Petite, Phys. Rev. Lett **63**, 2208 (1989).
9. D. J. Trevor, L. D. Van Woerkom, R. R. Freeman, Rev. Sci. Inst., **60**, 1051 (1989);
10. T. J. McIlrath, P. H. Bucksbaum, R. R. Freeman and M. Bashkansky, Phys. Rev. A, **35**, 4611 (1987); L. D. van Woerkom, R. R. Freeman, W. E. Cooke, T. J. McIlrath, J. Modern Optics, **36**, 817 (1989).
11. A. Loftus and P. H. Krupenie, J. Phys. Chem. Ref. Data **6**, 113 (1977).
12. E. Lindholm, Arkiv for Fysik **40**, 97 (1968).

Coulomb Explosion of Molecular Iodine with Ultrashort Pulses

Y. Beaudoin, D. Strickland, and P. B. Corkum

National Research Council of Canada, Ottawa, Ontario K1A 0R6, Canada

Abstract

We report the production of highly charged, unstable molecules which remain held together by their own inertia until after the termination of the excitation pulse. The subsequent molecular explosion occurs under field free conditions. Unambiguous explosions are observed from charged states as high as I_2^{5+} .

1. Introduction

Ultrashort pulse multiphoton ionization of atomic gas has been proposed as an important new approach to generating and controlling underdense plasmas[1,2]. In these plasmas the parameters are determined by laser and atomic considerations rather than, as is usual in plasma physics, the electron mean-free-path .

Studies of the plasma implications of multiphoton ionization need not be confined to atomic precursors. Inertially confined molecules will add a new variable since the most important parameter for multiphoton ionization, the ionization potential, can have a substantial (even dominant) contribution from the interaction energy. Thus, if a molecule can be ionized faster than it can disassemble, and if the field free ionization potential can be used to describe multiphoton ionization of the molecule, then the charge state of the ions that result from a molecular precursor will be very different from the charge state of ions formed from an atomic precursor which yields the same ions.

In this paper we demonstrate the first of these conditions. That is, the existence of inertially confined molecular ions. We also observe their decay channels. In addition to the plasma implications mentioned above, it will be possible to study the electronic structure of these highly unstable molecules.

Proceedings on Short-Wavelength Coherent Radiation, 216
Vol. 11, Philip H. Bucksbaum and Natale M. Ceglio (eds.)
© 1991 Optical Society of America

We have chosen I_2 to observe inertially confined highly charged molecular ions because of its large mass and therefore relatively slow explosion. When ionized by thirty femtosecond pulses, there should be almost no motion until after the termination of the excitation pulse. The resultant Coulomb explosion occurs under field free conditions. Ions are observed which derive from Coulomb explosions with energies characteristic of the charge states as high as I_2^{5+}.

In the dissociation products we observe both symmetric and asymmetric decay channels, as well as evidence of the creation of unstable molecular ions corresponding to dissociation in excited electronic states.

2. The Experiment

The experiment was performed on I_2, a weakly bound, heavy molecule with a rotational period of 10^{-9} J sec where J is the rotational quantum number. The ground state vibrational period is 155 fsec.

Since high power pulses as short as 20 fsec have been produced[3], and high power 10 fsec pulses appear technically feasible, the approach can be generalized to a wide variety of other diatomic or polyatomic molecules.

Iodine was leaked into the time-of-flight vacuum chamber which could be pumped to a background pressure of 5×10^{-9} Torr. The molecular explosions were diagnosed in a time-of-flight mass spectrometer.

The pump beam was produced by amplifying the output of a CPM dye laser in a Nd:Yag pumped dye amplifier chain which produced pulses of about 80 fsec duration. After spatial filtering, the pulse was compressed to 30 fsec using large aperture compression as described in Ref. 3.

The diffraction-limited pulses were focused into the target chamber with a F/5 on axis parabola. The focus was in the mid point between accelerating electrodes separated by 17 mm and maintained at a potential difference of 200 V. A field free drift region of 49 mm was terminated by an electrode containing a 2 mm diameter hole to select only those ions with no more than a small velocity component transverse to the drift axis of the tube. The ion current was registered on a microchannel plate.

3. Results

Figure 1 shows the full time-of-flight mass spectrum produced with the laser electric field pointing along the flight path.

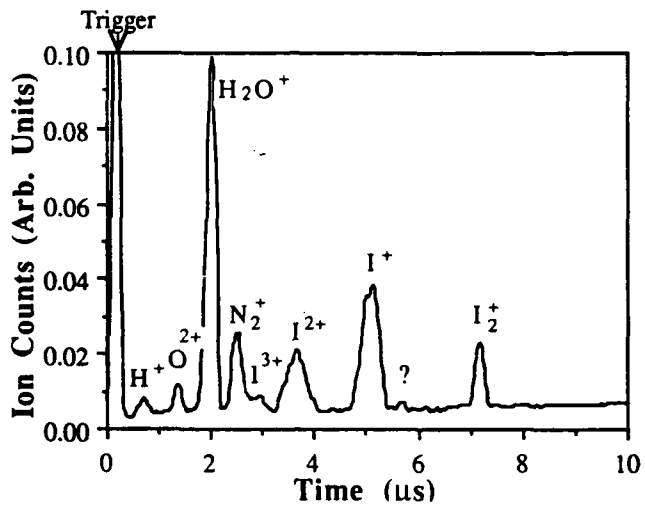

Figure 1 Time-of-flight mass spectrum. The charge states of I and I_2 are shown.

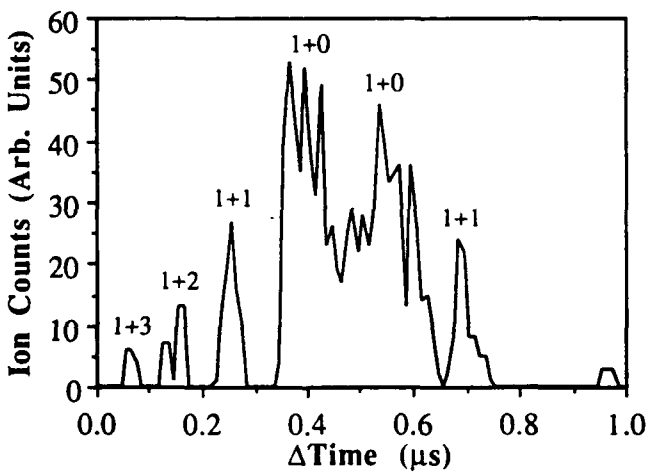

Figure 2 Time-of-flight mass spectrum of I^+. The characteristic feature in the figure are described in the text.

Water vapour in the chamber produced both hydrogen and water-vapour ions. These were used for calibration purposes.

The different charge states of Iodine are identified on the figure. Although I_2^+ has a stable ground state and should be very effectively collected in the mass spectrometer, it is not the dominant species measured. This is one indication that I_2^+ is created in an unstable (excited) electronic state.

Figure 2. shows the I^+ component of the time-of-flight spectrum obtained in the photon counting mode by analysis of approximately 50 shots. A number of features can be identified. At low energies we see a complex time-of-flight spectrum. These features appear to come from the dissociation of I_2^+ into a charged and a neutral ion although the dipolar excitation of I_2 is also possible. We have not as yet looked for the negatively charged ion of iodine. In either case, low energy ions of such a broad energy spread are only possible if the molecule is left in unstable states at the end of the pulse.

There are three other distinct features of the time-of-flight spectrum. These have energies characteristic of the explosion

of I_2^{++}, I_2^{+++} and I_2^{++++} . In all cases the spectra have a peak shift given by the explosive energy and are somewhat broadened on the low energy side. This broadening is not the result of nuclear motion on the timescale of the pulse. Even with the nuclear force expected for I_2^{++++} decaying into I^{+++} + I^{+} we expect ion motion of only 0.2 angstroms in 30 fsec, corresponding to a potential difference of about 1 ev. Since the highest charge state is produced near the peak of the pulse by a highly nonlinear process, the above conclusion probably over-estimates the effects of ion motion. We confirmed this conclusion experimentally by investigating multiphoton ionization with a 80 fsec pulse. As expected, we observed no significant broadening.

The asymmetric nature of the decay is a significant observation. The decay is occurring under field free conditions, as is indicated by the occurrence of such low ionization potential atoms as I^{+} (ionization potential of 19 ev) as a product of a much higher ionization potential precursor. Asymmetric decay has been suggested previously for relatively long pulses[4] (laser pulse longer than the explosion time). Our experiment unambiguously shows that these charge asymmetric molecular states are produced in significant quantities by the excitation process and are not associated with the dissociation dynamics in the strong laser field even though there is a field-free ionization potential penalty of approximately 6 ev for the asymmetric channel.

When consideration is given to the relative collection efficiency of the different components, it appears that asymmetric decay is at least as likely as symmetric decay. We can not as yet be more quantitative.

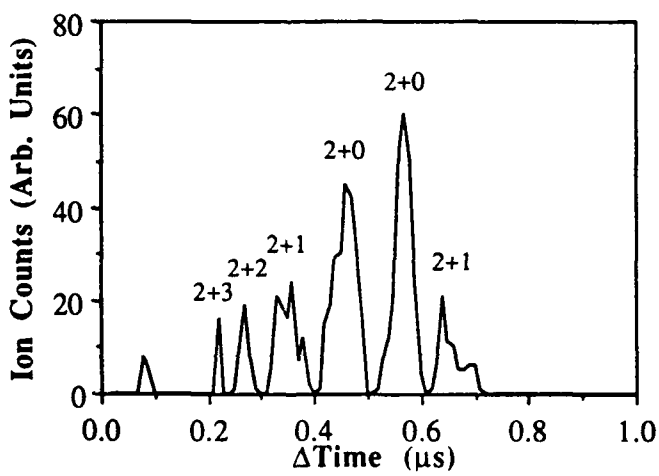

Figure 3 Time-of-flight mass spectrum of I^{2+}. The various features of the spectrum are identified in the text.

Figure 3 shows the I^{2+} decay channel. Again we see strong evidence of asymmetric decay. The central component shows ions with energy much less than the Coulomb decay energy of any molecular ion of charge greater than 2. We conclude it to be the decay of I_2^{++} into I^{++} + I. All other decay channels containing I^{++}, up to I_2^{5+} are observed at

their characteristic Coulomb explosion energy, slightly broadened to the low energy side.

In figures 1-3 we have presented data obtained from molecular explosions where the plane of polarization is parallel to the applied electric field. Thus, we observe explosions from those atoms aligned with both fields. When the laser field polarization is rotated by 90 degrees, a very different time-of-flight spectrum is obtained. Figure 4 illustrates the difference for I^{++}. The laser pulse duration was 80 fsec when the data in figure 4 was obtained. However, figure 4 would not be significantly different if a 30 fsec pulse had been used. The spectrum in figure 4 is much less rich than that in figure 3 and it is dominated by very low energy ions.

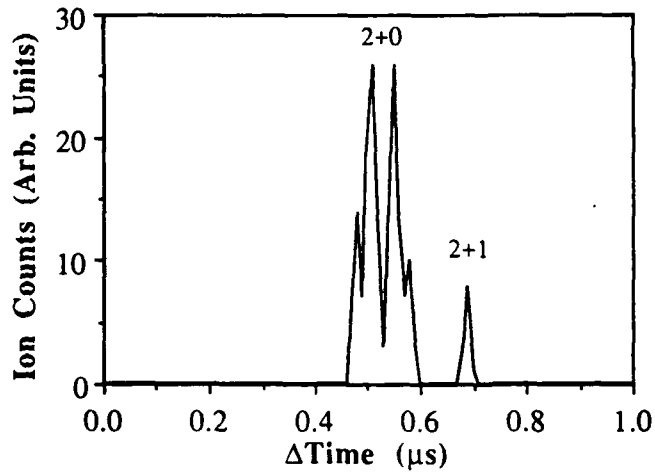

Figure 4 Time-of-flight mass spectrum obtained with light polarized perpendicular to the drift axis of the spectrometer but otherwise similar to figure 3.

It is clear from these experiments that it is possible to control the explosion energy in multiple pulse experiments and that the explosion occurs primarily along the laser electric field direction. We can now begin to explore the nature of the asymmetric decay channels. These appear to be highly charged analogues to the dipolar states of the neutral atom. Perhaps it is not surprising that they are preferentially excited in strong laser fields, for these states will have the strongest dipole moments.

In conclusion, the existence of clear molecular explosions indicates that the spectroscopy of highly unstable inertially confined molecules can now be studied. The presence of asymmetric decay channels suggests that the potential surface of the ion is modified by the strong laser field. Understanding the field dependent surface will be an important challenge for future work.

In the plasma context, inertially confined molecules of increasing complexity will allow us to investigate the role of molecular precursors in ultrashort pulse multiphoton ionization produced plasmas.

Acknowledgments:

The authors wish to thank D. Joines for his technical assistance and many helpful discussions with colleagues, particularly, N. H. Burnett. One of the authors acknowledges the financial assistance of a Government of Quebec FCAR fellowship.

References:

1. P.B. Corkum, N.H. Burnett and F. Brunel, Phys. Rev. Lett. 62, 1259, (1989).

2. N.H. Burnett and P.B. Corkum, J. Opt. Soc. Am. B6 1195, (1989).

3. C. Rolland and P.B. Corkum, J. Opt. Soc. Am. B5, 643 (1988).

4. K. Boyer, T.S. Luk, J.C. Solem and C.K. Rhodes, Phys. Rev. A39, 1186 (1989).

Ionization and Dissociation of Molecular Hydrogen by Ultrashort Light Pulses

A. Zavriyev,[a] D. W. Schumacher, F. Weihe, and P. H. Bucksbaum

Department of Physics, University of Michigan, Ann Arbor, Michigan 48109

J. Squier, F. Salin, and G. Mourou

Ultrafast Sciences Laboratory, University of Michigan, 2200 Bonisteel, Ann Arbor, Michigan 48109

ABSTRACT

We have observed above-threshold dissociation of H_2^+ and D_2^+ on time scales comparable to molecular rotation, by photoionizing the neutral molecules in 160 fs pulses of intense 769 nm light. We also see a new dissociation process at high intensities.

Much research has been done lately to investigate the interaction of intense coherent light with molecules. Even simple homonuclear diatomic molecules exhibit very complicated behavior in an intense light field, including multiphoton ionization and dissociation, multiple ionization, above-threshold ionization (ATI), and bond-softening, which has also been called above-threshold dissociation (ATD).[1,2]

In recent experiments at the Center for Ultrafast Optical Science at the University of Michigan, we subjected H_2 and D_2 molecules to radiation by ultrashort (160 fs) pulses of 769 nm (1.612 eV) light. Our aim was to observe ATD and ATI in a regime where the laser pulse length is comparable to the rotational period of the molecule. The pulse energy in these experiments ranged up to 0.8 mJ. The light was focused inside an ultrahigh vacuum chamber (base pressure 5×10^{-10} torr), backfilled with H_2, D_2 or Xe gas. The density of the gas was kept low to minimize space charge effects. The peak intensity of the light varied up to 2×10^{15} W/cm^2 (see comments on calibration below). We employed field-free time-of-flight spectroscopy to obtain the photoelectron kinetic energy spectra and angle-resolved ion energy spectra. We also had a charge-to-mass ratio spectrometer, providing us with information about relative abundance of different ionic species following the laser interaction.

Xenon was used to calibrate the electron spectrometer, and to measure the peak intensity in the laser focus. Since our experiments were performed in the "short pulse regime" (negligible ponderomotive acceleration of photoelectrons), the spectrometer

Proceedings on Short-Wavelength Coherent Radiation, Vol. 11, Philip H. Bucksbaum and Natale M. Ceglio (eds.)
© 1991 Optical Society of America

could be calibrated by observing xenon ATI fine structure, as well as spacing between different order ATI peaks. To measure the maximum light intensity in the focus, we detected multiple ionization of xenon in our charge/mass spectrometer. Then, using the simple "suppressed barrier ionization" model, we estimated the peak intensity.[3] We should emphasize that the validity of the suppressed barrier model for 160 fsec pulses has not been tested; however, even if the intensity for the onset of high stages of ionization is not accurately given by this model, at least multiple ionization is an easy standard of comparison between different experiments.

Previous experiments performed at AT&T Bell Laboratories, using 50-100 psec pulses at 532 nm and 355 nm, showed repetitive clusters of ATI peaks in the photoelectron spectrum of H_2, similar to the peaks seen in ATI spectra in atoms. In the same experiments performed at 1064 nm, however, a broad and relatively featureless continuum spectrum of photoelectrons extended nearly to 100 eV.[4] The new sub-picosecond experiments produce a continuous photoelectron spectrum more like the 1064 nm light. In this case, the broad intensity independent distribution is maximum around 5 eV, and continues to 25 eV. However, unlike the 1064 nm results, a distinct ATI-like structure appears superimposed on this distribution (Fig.1).

Dissociation energies are measured by time-of-flight ion spectroscopy. A typical fragment kinetic energy spectrum consists of a series of broad "above-threshold dissociation" peaks extending to 2 eV. These peaks were also observed with much longer laser pulses.[1] The new short pulse spectra reveal an additional feature as well: a broad distribution of fast fragments with energies ranging up to 6 eV. Unlike photoelectron spectra, the ion kinetic energy spectrum changes dramatically with the laser intensity. When the peak intensity is below 10^{15} W/cm^2, the low energy ATD

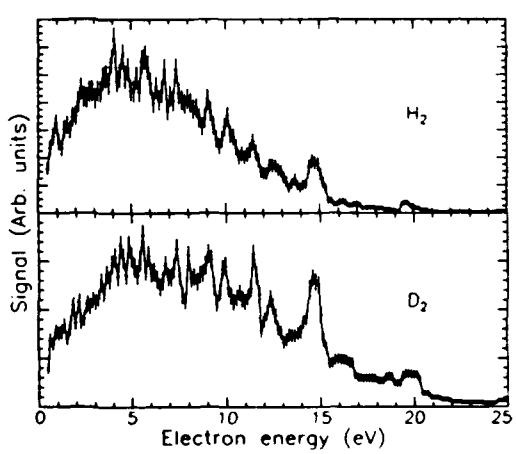

FIGURE 1: The kinetic energy spectra of photoelectrons detected during irradiation of H_2 and D_2 by 769 nm linearly polarized light. The spectra shown were obtained for electrons emitted along the laser polarization. Each run contains ≈10000 laser shots. Laser peak intensity was estimated at 2×10^{15} W/cm^2.

peaks contain the most signal (Fig.2a). As the light intensity increases, the high energy signal climbs much faster than these low ATD peaks. At 2×10^{15}W/cm^2 the high energy fragments dominate the spectrum (Fig.2b).

Up to 55% (depending on light intensity) of the dissociation fragments have kinetic energies below 2 eV. These ions emerge primarily along the light polarization, as predicted by the mechanism of bond softening (ATD). The laser-dressed internuclear potential curves undergo ac Stark shifts, particularly near positions where different electronic states of the molecule are separated by an integer number of photons. For the ground $1s\sigma_g$ states and excited $2p\sigma_u$ states of H_2^+ and D_2^+, one- and three-photon couplings are particularly strong for light parallel to the molecular axis. At the experimental light intensity they deform the shape of the potential. The deformation becomes greater as the light intensity goes up.

Fig.3 shows a "dressed state" energy level diagram illustrating bond-softening. The passage of an ion through an odd-photon crossing can result in an adiabatic transition to the other potential, corresponding to absorption or emission of additional photons; or diabatic passage to the original potential, with no net photon exchange. The probability for making these adiabatic and diabatic crossings can be estimated by Landau - Zener theory, which states that the ion must follow the adiabatic curve so long as its rate of passage through the gap is slow compared to the Rabi rate $V_{12}/\hbar$ for transitions between the interacting states[5]. V_{12} is equal to a half of the separation between the perturbed curves.

In our previous experiments with molecular hydrogen we employed 80-100 psec light pulses, which are far longer than molecules' vibrational periods ($\approx$20 fs for H_2^+ and 30 fs for D_2^+) or rotational periods ($\approx$500 fs for H_2^+ and 1 ps for D_2^+). As a result, the initial orientation of an H_2^+ molecular ion was not as important -- the laser

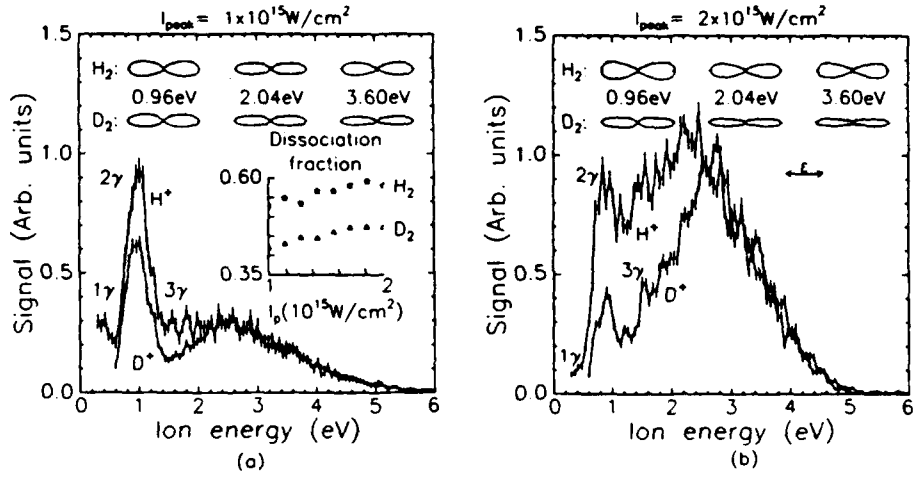

FIGURE 2: The kinetic energy spectrum and angular distribution of dissociation fragments detected during irradiation of H_2 and D_2 by 769 nm linearly polarized light. The spectra shown were obtained for ions emitted along the laser polarization 0°. Each run contains $\approx$6000 laser shots. Additional spectra were observed for the laser polarization rotated in 15° increments from 0° to 60°. There is practically no signal between 60° and 90°. The insert shows the dissociation fraction as function of the peak laser intensity.

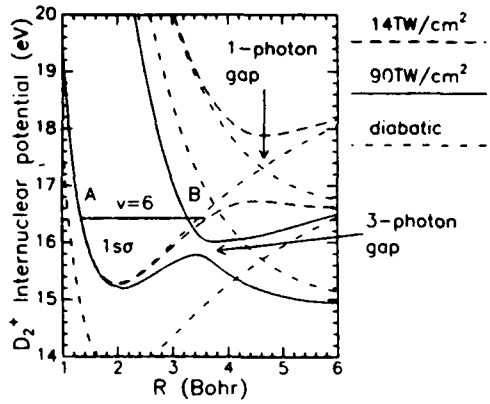

FIGURE 3: Dressed state (Floquet) energy level diagram for D_2^+ in the presence of a 769 nm laser field polarized along the molecular axis.

had enough time for the ion to rotate into alignment with the field and dissociate. Likewise, the laser field in these experiments was changing very slowly compared to the internuclear motion; H_2^+ molecular ions were effectively seeing a steady AC field. This slow intensity change enhances the probability of one-photon dissociation early in the pulse, when the intensity is low and the three-photon gap is still closed.

H_2^+ and D_2^+ ions vibrate rapidly, even compared to the 160 fsec laser pulse. However, our experimental results show that the laser intensity change is nonetheless fast enough to affect the dissociation process, as shown in Fig.2. Comparing the distribution of the signal in different ATD peaks to the results that we observed with 100 ps pulses, we see that the one-photon absorption is not the preferred dissociation path any more. In the case of short laser pulse more molecular ions dissociate via three-photon gap than via simple one-photon absorption (see Fig.2).

In order to explain this phenomenon, we have to refer to the potential curves in Fig.3 (note that both isotopes have similar curves). As an example we consider an D_2^+ ion, initially in 6th vibrational level of $1s\sigma_g$ ground state. We assume that the ion was produced as a result of ionization of a deuterium molecule near its inner turning point (point A on Fig.3). Let us also assume that the ionization occurs on the rising edge of the laser pulse. We can think of the ion as a vibrational wave packet moving in the slightly perturbed $1s\sigma_g$ potential well. By the time the vibrational packet reaches the outer turning point (about 15 fs after it was born) the one-photon gap is still closed, so the packet just turns around (point B on Fig.3) and heads toward the inner turning point where it starts a new vibrational cycle. The ion reaches the three-photon crossing (point C on Fig.3) about 40 fs after it was born; the curves are much more distorted and a three-photon gap in the dressed potential is now open. As a result, the wave packet adiabatically switches to the dissociating state at this three photon crossing, i.e. it absorbs three additional photons. As the nuclei fly apart, they pass through the one-photon crossing, which is now wide open. An adiabatic passage here corresponds to the emission of a photon, so that the resulting dissociation fragments emerge with energies characteristic of *net* two-photon absorption (the 2γ peak on Fig.2).

The dynamics of molecules in ultrashort light pulses can be explored further by comparing angular distributions of dissociating protons and deuterons, and by looking at the dissociation fraction for both isotopes (Fig.2). The $1s\sigma_g$ and $2p\sigma_u$ states couple to fields polarized along the nuclear axis. Therefore, ions aligned with the field see the most perturbed potential curves and have greater dissociation probability. The angular distributions of fragments are strongly peaked along the laser polarization for both isotopes. However, the laser pulses employed in these experiments are short enough to probe the difference in the rotational frequency of hydrogen and deuterium molecular ions. The rotational period of an H_2^+ ion in the lowest rotational state is approximately 500 fsec, about three times longer than the duration of the light pulses. The deuterium molecular ion rotates at half this rate Therefore, only the molecules that are initially close to alignment, or can move into alignment during the pulse, have a good chance to dissociate. Since hydrogen rotates faster, there is more dissociation of H_2 than D_2. In addition, if we compare the angular distribution for the two isotopes, we see that the deuterons on average come out closer to the laser polarization. Since the ions rotate as they dissociate, more rapidly rotating ions are detected at wider angles.

These rotational effects deplete the D^+ signal with respect to H^+ signal between 0 and 2 eV. However, as is seen from spectra on Fig.2, the 2γ peak is depleted less then 3γ. Since H_2^+ ions move faster than D_2^+ through one-photon gap, there is a better chance for diabatic passage.

In addition to ATD, the 160 fsec pulses also produce a broad distribution of faster protons, with kinetic energies up to 6 eV. The intensity dependence of these fast protons differs markedly from the ATD ions. We have considered several explanations for this new feature in the proton kinetic energy spectrum. Additional experiments are required to sort out these possibilities. It may be significant that the high energy part of the dissociation spectra for the two isotopes are identical. This suggests that the new dissociation mechanism is not sensitive to the different vibrational and rotational levels of the two isotopes, but rather is due to an electronic process, where vibration and rotation are unimportant.

[a] Also at: Applied Physics Department, Columbia University, N.Y., N.Y.

References

[1] P.H. Bucksbaum, H.G. Muller, D.W. Schumacher, and A. Zavriyev, Phys. Rev. Letters **64**, 1883 (1990).

[2] A. Giusti-Suzor, X.He, O. Atabek, and F.H. Mies, Phys. Rev. Lett. **64**, 515 (1990).

[3] S. Augst, D. Strickland, D.D. Meyerhofer, S.L. Chin, and J.H.Eberly, Phys. Rev. Lett. **63**, 2212 (1989).

[4] A. Zavriyev, P.H. Bucksbaum, H.G. Muller, and D.W. Schumacher, Phys. Rev. A **42**, 5500 (1990).

[5] See, for example L.D. Landau and E.M. Lifshitz, *Quantum Mechanics*, Course of Theoretical Physics Vol.3 (Pergamon, New York, 1965), p.322ff.

High-Intensity Photoionization of H_2

Sarah W. Allendorf and Abraham Szöke

High Temperature Physics Division, L-395, Lawrence Livermore National Laboratory, Livermore, California 94550

Abstract

A tunable, high-intensity picosecond dye laser system has been employed with electron energy analysis to investigate the dynamics of (3+1) resonance-enhanced multiphoton ionization of H_2 via different vibrational levels of its $B\ ^1\Sigma_u^+$ and $C\ ^1\Pi_u$ electronic states. We observe production of molecular ions in various vibrational levels, with a shift to increased population of lower vibrational states of H_2^+ consistent with the a. c. Stark shift of the correspondingly lower vibrational levels of the C state into resonance with the three-photon energy of the laser . Clear evidence of direct dissociation of H_2 followed by single-photon ionization of the excited H atom is observed as well. Above threshold ionization of these two processes occurs readily. We also find that dissociative ionization is an increasingly important ionization pathway as the wavelength is increased. Finally, we see evidence of a new ionization pathway, which we assign to photoionization into a transient bound state created by the avoided crossing of the first repulsive electronic state of H_2^+, $|2p\sigma_u, n\rangle$, with the single-photon-dressed ground state of H_2^+, $|1s\sigma_g, n+1\rangle$.

Introduction

As theory and experiment converge on an understanding of intense-field photoionization of atoms,[1] the interest of the multiphoton community has turned to molecules. Specifically, the role of internal degrees of freedom in above-threshold ionization (ATI) has been examined, leading to discussions of above-threshold dissociation (ATD) of the H_2^+, molecular ion.[2,3] Most of the ATI experiments in H_2 have employed limited laser wavelengths, specifically Nd:YAG harmonics or excimer frequencies. For our study of the effects of resonances on the ATI of H_2, we employ a tunable dye laser system. This allows us to examine specific intermediate state resonances in the multiphoton ionization scheme, and trace their behavior in the presence of the intense laser field.

In this paper we discuss the results of our tunable ultraviolet H_2 photoionization dynamics study.[4] We excite rovibronic levels of the $B\ ^1\Sigma_u^+$ and $C\ ^1\Pi_u$ electronic states at the three-photon level, and ionize with a fourth photon. We use photoelectron energy

Proceedings on Short-Wavelength Coherent Radiation, Vol. 11, Philip H. Bucksbaum and Natale M. Ceglio (eds.)
© 1991 Optical Society of America

analysis to probe the details of the photoionization process. Our experimental apparatus was described elsewhere;[4] briefly, we focus the frequency-doubled output of a pulse-amplified picosecond dye laser between the pole pieces of a "magnetic bottle" photoelectron spectrometer. We record the photoelectron time-of-flight distributions for a number of different excitation wavelengths (288.5 nm$\leq\lambda\leq$304 nm) and peak laser intensities I_o, adjusting the H_2 pressure as I_o is increased in order to keep the number of electrons produced each laser shot constant. The spectra presented here have all been converted to photoelectron energy and normalized to 1 x 10^{-8} torr pressure of H_2.

Molecular Photoionization

Typical photoelectron energy spectra recorded at 288.5 nm are presented in Fig. 1 for electron energies from 0.6 to 2.0 eV. Each spectrum was recorded at a different I_o (left vertical axis), and has been divided by the indicated scale factor (right vertical axis) then offset from the horizontal axis for display. At 288.5 nm the energy of three photons is just above the field-free energy of the $C\ ^1\Pi_u$ (v'=2) vibrational state. The peaks in Fig. 1 are assigned to molecular photoionization of H_2, producing H_2^+ in several vibrational levels (v^+). At the lowest I_o, most of the ions are produced with two quanta of vibrational energy, with some population of v+=1 and v+=3. This predominantly Δv=0 ionization is consistent with the Franck-Condon (FC) overlap of the vibrational manifolds of the neutral $C\ ^1\Pi_u$ and the ionic $X\ ^2\Sigma_g^+$ electronic states. As I_o increases, the relative production of v^+=1 increases until the v^+=1 peak equals the v^+=2 peak. This happens because the C v'=2 state is a.c. Stark shifted up and out of three-photon resonance by the electric field of the laser. Likewise, the C v'=1 state is shifted <u>into</u> three-photon resonance, then Δv=0 ionization produces H_2^+ ions in the v^+=1 vibrational level. The energy of the v^+=1 peak initially decreases as I_o increases, due to the increased Ponderomotive energy U_p in the

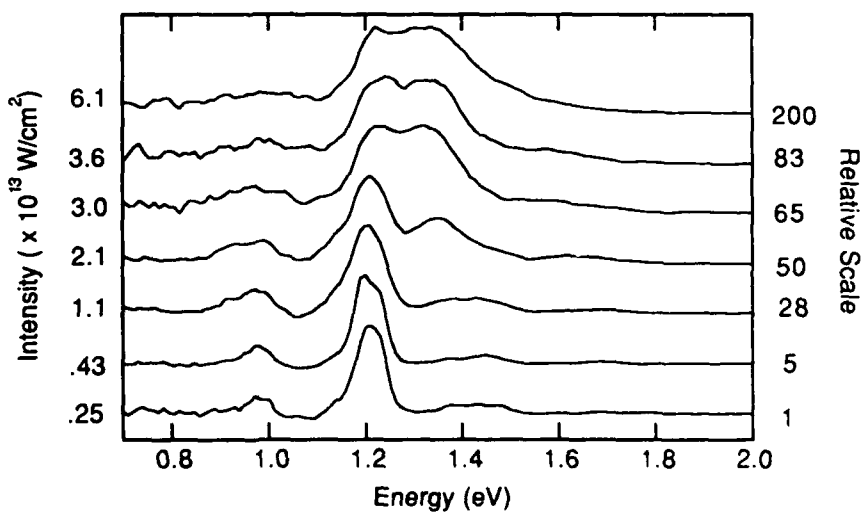

Figure 1. Photoelectron energy spectra recorded at 288.5 nm. Peak laser intensity for each spectrum is indicated on the left axis, and the amount by which each spectrum was divided for presentation purposes is indicated on the right axis.

portion of the laser focus where C v′=1 is in resonance. Further increases in I_0 do not shift this peak further: it arises predominantly from Δv=0 resonant photoionization of the C v′=1 state, and at higher I_0 this state is no longer in resonance. Similarly, the v^+=2 peak is initially shifted 20 meV (consistent with a small U_p at $I_0 \approx 5 \times 10^{12}$ W/cm^2) but does not move further as I_0 increases. This v+=2 peaks arises from the ever-expanding volume of the laser focus where the laser intensity is less than 10^{13} W/cm^2, and C v′=2 is in three-photon resonance. This behavior is the hallmark of resonances in ATI, as has been discussed in great detail by others.[1] Finally, we assign a broad photoelectron peak at 5.4 eV (not seen in Fig.1) to ATI of this molecular photoionization. We lack sufficient energy resolution to resolve the vibrational levels in this above-threshold electron peak.

Dissociation followed by atomic ionization

Electron energy spectra between 1.5 and 6.0 eV are presented in Fig.2 for λ= 297.5 nm. As the laser wavelength is tuned, the positions of the peaks shifts in a manner attributable to the change in total energy available. At 297.5 nm, the energy of three photons is just below the field-free energy of the $C\ ^1\Pi_u$ (v′=1) vibrational state. At the lower laser intensities this energy region of the photoelectron spectra is dominated by a peak at 2.63 eV which is very sharp at most laser intensities, occurs at the energy expected for single-photon ionization of H(3ℓ), and does not shift in position as I_0 increases (the large shoulder toward lower photoelectron energy observed in Fig. 2 is assigned to a different ionization mechanism because of its wavelength dependence). We assign this peak to photoionization of H(3ℓ), resulting from direct dissociation of neutral H_2 followed by ionization. Photoionization occurs readily of H(3ℓ) since only one photon is required;

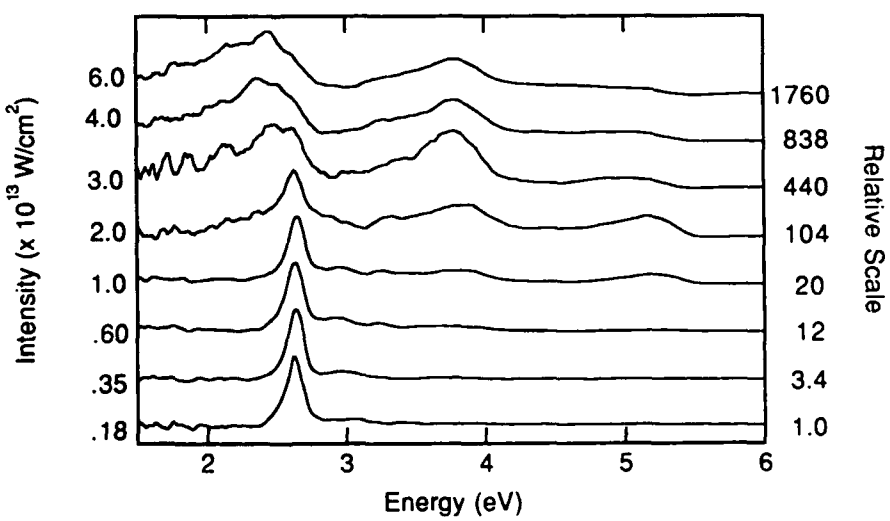

Figure 2. Photoelectron energy spectra recorded at 297.5 nm, all else the same as Fig.1.

however, we see no evidence for ionization of any other states of atomic H. At 297.5 nm, absorption of four photons is above the dissociation limit to produce H(3ℓ) but below the energy required to produce H(2ℓ). The absence of any H(2ℓ) suggest this dissociation occurs at internuclear distances R too large to curve-cross to potentials which correlate to H(2ℓ)+H(1s) dissociation products. This is consistent with the population at the three-photon level of high vibrational levels in the $B\ 1\Sigma_u^+$ state which have rather large (R > 5 bohr) outer turning points. Absorption of a fourth photon at this R will have a favorable FC overlap for transition into a neutral, doubly excited state similar to the $H_2^+\ |2p\sigma_u>$ repulsive state, converging to the dissociation limit of H(1s) + H(3ℓ). The narrowness of the peak is understood in the context of the relative a.c. Stark shift of the excited (n=3) state and the ionization potential. Recent calculations[5] have shown that our use of >4 eV photons permits us to use the "high frequency approximation", because this excited state has an a.c. Stark shift nearly equal to that of the ionization potential. Therefore, no matter what intensity the ionization occurs at, the excess energy available for the photoelectron is always the same for our 1.5 ps laser pulses.

Dissociative Ionization

For 297.5 nm, the energy of the final peaks observed in these experiments are 2.4 eV and 3.75 eV. These high-energy peaks do not correspond to any low field processes. We traced the energy of these peaks as a function of laser wavelength to determine the responsible mechanisms. For the 2.4 eV peak, we observe a marked decrease in photoelectron energy as the photon energy decreases, but the decrease is not a simple function of the photon energy. We assign the 2.4 eV peak to dissociative ionization occurring after a two-photon absorption from the outer turning point of a vibrational level in the B state. This process can be resonantly enhanced by any of a number of doubly-excited states at the four-photon level (the same states which dissociate to produce excited H atoms). If we estimate R=5.5 bohr, the energy of the $H_2^+\ |2p\sigma_u>$ state at that R is 18.45 eV. Five photons at λ=297.5 nm add to 20.84 eV. The excess energy available for partitioning between the electron and the dissociating H(1s) + H^+ is 20.84 - 18.08 = 2.76 eV; the excess energy above the $H_2^+\ |2p\sigma_u>$ state is 2.39 eV. The observed electron energy of 2.4 eV falls neatly between these two bounds. This behavior occurs at each wavelength studied, with the exception of the last wavelength (304 nm), where the observed electron energy is less than 5% larger than the upper bound calculated using our simple delta-function model for this absorption followed by dissociative ionization model. Dissociative ionization has been observed at other laser wavelengths by others, most notably by Rhodes and coworkers.[6]

Ionization into a transient laser-induced bound state

The evidence for a fourth photoionization mechanism in our study is as follows. With the possible exception λ= 288.5 nm, the electron spectra display a prominent electron peak near the photon energy. Although the peaks are broad, they are fairly symmetric and we find a decrease in peak energy that is nearly 1:1 with decreasing photon energy. This rules out a conventional, multiple-photon ATI explanation for these high-energy electrons. We assign these electrons to ionization into the adiabatic state formed by the avoided crossing of the n+1-photon dressed ionic bound state potential $\left|1s\sigma_g, n+1\right\rangle$ and the n-photon

dressed ionic repulsive $|2p\sigma_u, n\rangle$ potential. This crossing creates two adiabatic states (upper and lower adiabatic potentials, UAP and LAP) from the diabatic states; it is the LAP that is responsible for the "bond softening" observed by others.[2,3] We are concerned with the UAP. Three-photon excitation of the *B* state prepares an H_2 molecule with large R. Two further photons are absorbed, and photoionization occurs into the UAP formed by the avoided crossing. We estimated the depth of the UAP by a simple two-state avoided crossing calculation involving only the $|1s\sigma_g, n+1\rangle$ and $|2p\sigma_u, n\rangle$ diabatic potentials. We diagonalized our adiabatic potentials to obtain their eigenvalues and eigenfunctions. For example, at λ=304 nm and I_0=1 x 10^{13} W/cm^2, the UAP is bound by 1 eV, and supports 14 vibrational states. Finally, we calculated the FC overlap between vibrations in the *B* state and vibrations in the UAP. We found that the electron energies predicted by the best FC overlap with the *B* state agree qualitatively with the observed electron energies, but are approximately 0.4 eV lower than those observed. We are satisfied with this agreement, given the simple nature of our computation. Further computations await a better understanding of the effect of the strong laser field on the valence *B* state: our computation used the field-free potential which is almost certainly invalid at the laser intensities employed.

Acknowledgment

This work was performed under the auspices of the U. S. Department of Energy at Lawrence Livermore National Laboratory under contract number W-7405-Eng-48.

References

1. R. R. Freeman and P. H. Bucksbaum, "Investigation of above-threshold ionization using subpicosecond laser pulses", J. Phys. B: At. Mol. Phys. 24, 325-347 (1991).
2. A. Zavriyev, P. H. Bucksbaum, H. G. Muller, and D.W. Schumacher, "Ionization and dissociation of H_2 in intense laser fields at 1.064 μm, 532 nm, and 355 nm", Phys. Rev. A 42, 5500-5513 (1990).
3. A. Giusti-Suzor, X. He, O. Atabek, and F. H. Mies, "Above-threshold dissociation of H_2^+ in intense laser fields", Phys. Rev. Lett. 64, 515-518 (1990).
4. S. W. Allendorf and A. Szöke, "High-intensity multiphoton ionization of H_2", Phys. Rev. A, 1991 (in press).
5. S. N. Dixit, S. W. Allendorf, and N. M. Khambatta, "Exact, frequency dependent a. c. Stark shifts in hydrogenic systems", Bull. Am. Phys. Soc. 36, 1298 (1991).
6. T. S. Luk and C. K. Rhodes, "Multiphoton dissociative ionization of molecular deuterium", Phys. Rev. A 38, 6180-6184 (1988).

Multiphoton Ionization of I_2, HI, and CF_3I, and Above-Threshold Ionization in I_2

C. J. Zietkiewicz, Y. Y. Gu, A. M. Farkas, and J. G. Eden

Everitt Laboratory, University of Illinois, 1406 W. Green Street, Urbana, Illinois 61801

Abstract

Multiphoton ionization (MPI) spectroscopy of several iodine-bearing molecules has shown that molecular dissociation and subsequent ionization of the atomic fragment is the channel preferred to direct ionization of the molecule. ATI has also been observed.

I. Introduction

While a number of elegant experiments over the past several years have explored the photoionization of atoms (and Xe, in particular) at high field intensities, considerably less has been reported for molecules. Our interest lies in the fragmentation of diatomic and polyatomic molecules at optical field intensities $>10^{11}$ W/cm^2 and this paper describes the results of experiments in which the photoionization of small iodine-bearing molecules has been studied by time-of-flight photoelectron spectroscopy.

II. Experimental

These experiments utilized a magnetic bottle, electron energy spectrometer operated in tandem with a time-of-flight mass spectrometer. Initial calibration of the electron spectrometer was accomplished by photoionizing Xe at 532 nm and recording its electron kinetic energy spectrum. This and subsequent tests showed the spectrometer resolution to be <15 meV. The heavy-particle spectrometer was also calibrated with Xe. One set of experiments were conducted at a fixed wavelength (532 nm) and used a frequency-doubled, injection-seeded Nd:YAG laser having a pulse width of 10 ns, while a second set of dye laser experiments involved a Littman type oscillator which was amplified in a two stage, longitudinally-pumped dye amplifier chain. The upper limit on the linewidth of the dye laser after amplification is estimated to be ~ 3 GHz.

Proceedings on Short-Wavelength Coherent Radiation, Vol. 11, Philip H. Bucksbaum and Natale M. Ceglio (eds.)

© 1991 Optical Society of America

Photoelectron energy spectra were acquired in 100 ns segments with a Tektronix 7912AD transient digitizer which provided an effective sampling resolution of 200 ps per channel, several times greater than the detector response time. Electron density at the laser focus was maintained below 10^{10} cm^{-3} to avoid space charge distortion effects in the photoelectron spectra.

III. Results

Photoionization of I_2, HI and CF_3I at 532 nm reproducibly demonstrated that, at the optical intensities examined, the scission of the R-I bond (R=I, H or CF_3) is favored over direct photoionization of the molecule. Only weak features attributable to photoelectrons of molecular origin were observed and, as illustrated in Fig. 1, the dominant features arise from the five photon ionization of the $^2P_{3/2}$ and $^2P_{1/2}$ spin-orbit terms of the atomic iodine ground state. This result differs from those of previous studies carried out at shorter wavelengths[1,2] in which the I_2 ionization process was demonstrated to be dominated by three photon ionization of the parent molecule, followed by the absorption of a fourth photon, and the subsequent dissociation of the molecular ion. The similarity of the three photoelectron spectra in Fig.1 and the absence of any peaks attributable to I_2 suggest that the direct production of I_2^+ by MPI under the present experimental conditions is negligible.

Branching ratios associated with the production of I^+ ions in the $^3P_1$, $^3P_2$ and $^3P_0$ states were also examined for I_2 photoionized at 532 nm and the results are given in Table 1. Similar results were obtained for CF_3I and HI despite the fact that the photodissociation of CF_3I at 532nm is characterized by a larger fractional yield of I ($^2P_{1/2}$) than that for I_2 at the same wavelength. Another interesting feature of these spectra is the strength of the I^+ ($^3P_1$) ← I ($^2P_{1/2}$) + 5hν process as compared to the

Table 1
Electron Yields for Atomic Iodine Produced by Photodissociation/Ionization of Molecular Iodine at 532 nm.

Ionization Channel	ΔE_∞ (cm^{-1})	$nh\nu$-ΔE_∞ (eV)	Order n	Avg. Abs. Yield
I^+ [$^3P_2$]←I [$^2P_{3/2}$]	84295.1	1.20	5	80%
I^+ [$^3P_0$]←I [$^2P_{3/2}$]	90743.0	0.40	5	1.0%
I^+ [$^3P_1$]←I [$^2P_{3/2}$]	91382.1	0.32	5	11%
I^+ [$^1D_2$]←I [$^2P_{3/2}$]	98022.3	1.83	6	Not Obs.
I^+ [$^1S_0$]←I [$^2P_{3/2}$]	113796.4	2.21	7	Not Obs.
I^+ [$^3P_2$]←I [$^2P_{1/2}$]	76,692.0	2.14	5	Weak
I^+ [$^3P_0$]←I [$^2P_{1/2}$]	83,139.9	1.35	5	0.6%
I^+ [$^3P_1$]←I [$^2P_{1/2}$]	83,779.0	1.27	5	5.8%
I^+ [$^1D_2$]←I [$^2P_{1/2}$]	90,419.2	0.44	5	1.9%
I^+ [$^1S_0$]←I [$^2P_{1/2}$]	106,193.3	0.82	6	Not Obs.

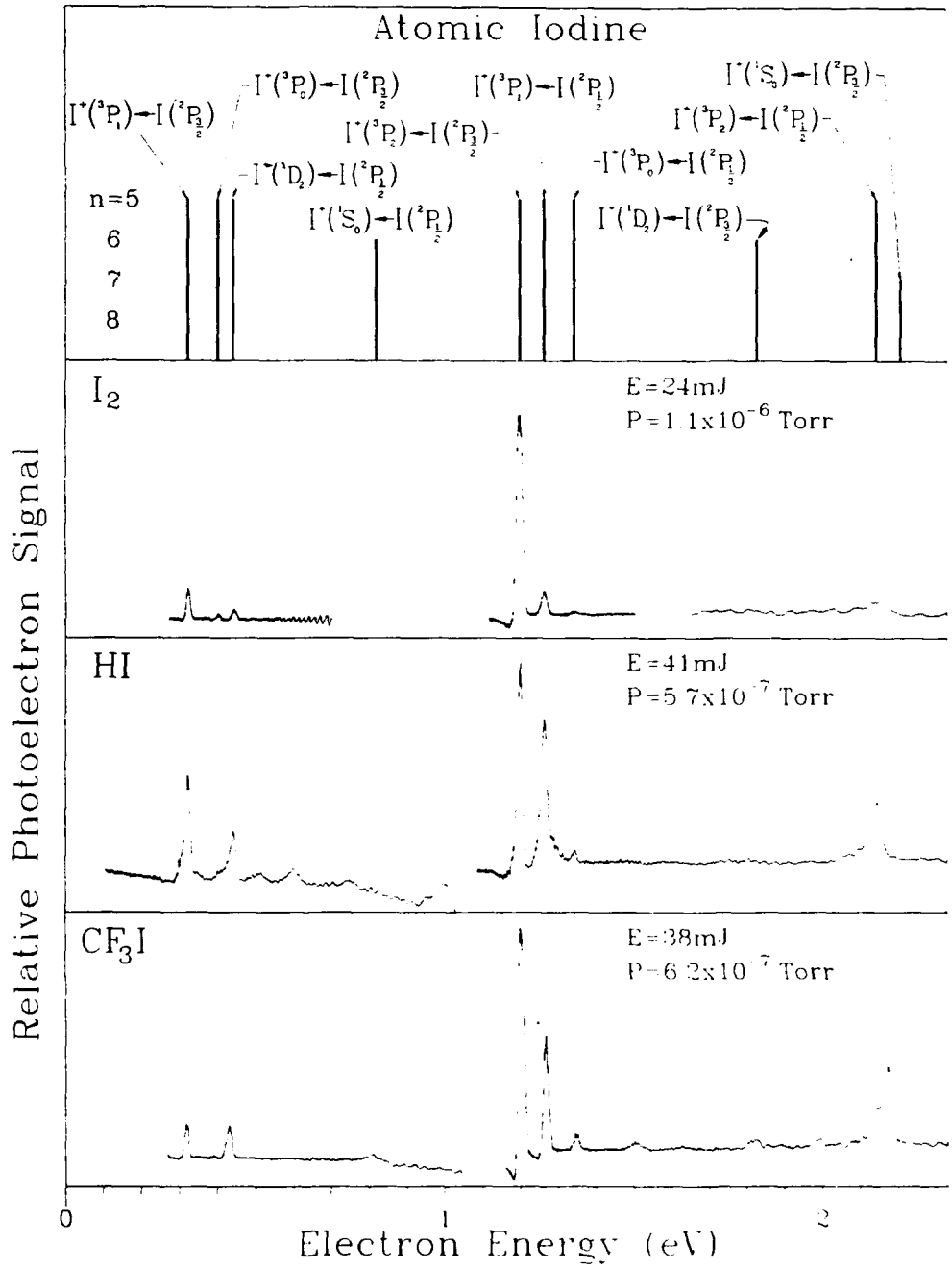

Figure 1. Photoelectron spectra for several iodine-bearing molecules photoionized at λ = 532nm. The top panel indicates the expected positions of photoelectron peaks resulting from various MPI processes. The number of absorbed photons is denoted by n.

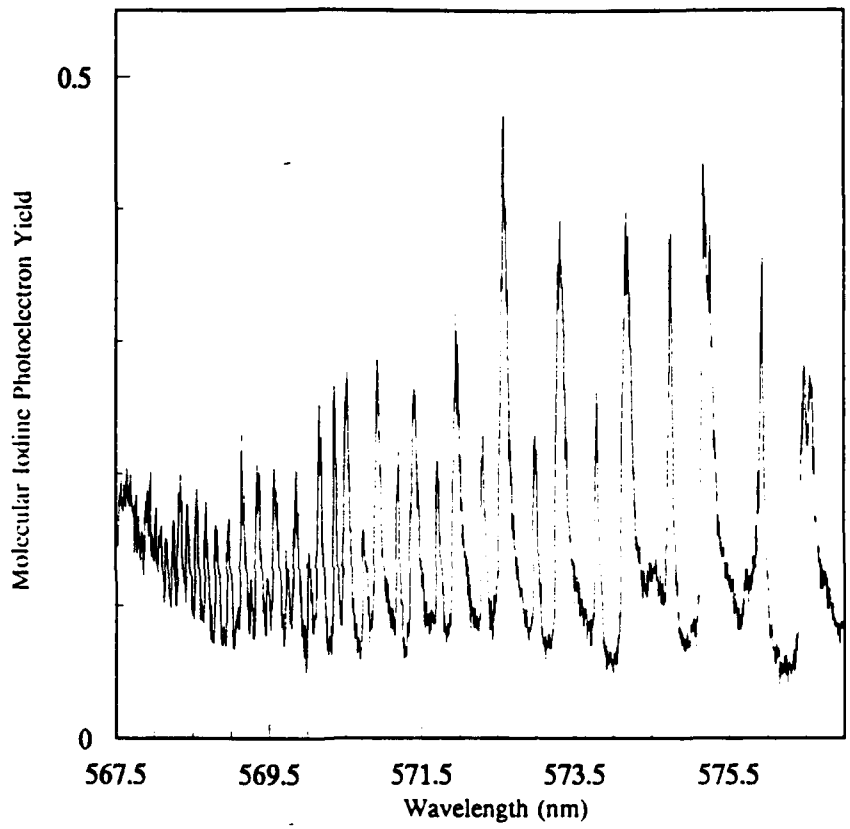

Figure 2. Photoelectron spectrum of I_2 acquired with a scanning Littman-type dye laser ($\Delta\nu < 0.1$ cm^{-1}).

$I^+ (^3P_2) \leftarrow I (^2P_{1/2}) + 5h\nu$ transition, especially when one considers the near resonances that occur in the latter case with the 12p and 7p terms of Rydberg series that converge to the $^3P_2$ ion limit[3]. ATI of iodine also was reproducibly observed for intensities on the order of 10^{12} W/cm^2.

Preliminary results have been obtained using the Littman dye laser-amplifier system which indicate that the overall 5 photon ionization cross section in the wavelength range 575-585 nm is considerably larger than that at 532 nm. Multiphoton ionization of molecular iodine has also been observed in the yellow. As the dye laser wavelength was scanned, resonant enhancements due to the intermediate B $^3\Pi_{0_u}^+$ state were clearly noticeable when monitoring the atomic and molecular iodine photoelectron peaks. Measurements of the electron yield as a function of laser wavelength in the 566 - 599 nm region revealed considerable structure and a portion of the spectrum observed by monitoring the I_2 photoelectron peak is illustrated in Fig. 2. At least two clear Rydberg series are observed and details regarding the characteristics of these series will be discussed elsewhere[4].

IV. Summary

Multiphoton ionization of I_2, HI and CF_3I at 532nm has vividly illustrated that the dissociation of the parent molecule and subsequent ionization of the atomic fragment is the preferred ionization channel. Atomic and molecular ATI has also been observed in the halogen-bearing molecules and at least two strong Rydberg series have been observed in I_2 by photoelectron spectroscopy.

Acknowledgment

The support of this work by NSF under grant CTS 89-15795 is gratefully acknowledged.

References

[1]J. C. Miller, J. Phys. Chem. 91, 2589(1987).
[2]J. C. Miller and R. N. Compton, J. Phys. Chem. 75, 2020(1981).
[3]S. T. Pratt, Phys. Rev. A. 32, 928(1985).
[4]Y. Y. Gu, A. M. Farkas and J. G. Eden (unpublished).

Section IV: High-Intensity Laser–Matter Interactions

Low-Density Targets

Resistance of Short Pulses to Self-Focusing

D. Strickland and P.B. Corkum
National Research Council of Canada
Ottawa, Ont. Canada K1A 0R6

Self-focusing arises in all materials, gases, liquids, solids or plasmas. Yet, it has been investigated only in the limit where the beam diameter is significantly less than the pulse length ($c\tau$, where τ is the pulse duration). In this case, the beam is predicted to self-focus to moving singularities in the absence of other nonlinear effects. However, there is another extreme which is rarely, if ever, noted where the beam diameter is much larger than the pulse length and the pulse will disperse before any self-focusing can occur. Short pulse self-focusing is more related to the second extreme than the first.

We introduce a model for intermediate pulse durations that shows how a short pulse evolves through self-focusing, growing transient temporal microstructures. These very short structures then disperse and stop the self-focusing process, stabilizing the beam. We will also show that it is these very short temporal structures that lead to the phenomena of continuum generation. The model explains three experimental features of continuum generation that were previously poorly understood, namely (1) the spectral modulation of the continuum, (2) the spatial structure of the continuum, and (3) the insensitivity of continuum generation to the duration of the input pulse. Predictions of the model are confirmed experimentally with detailed studies of femtosecond continua.

The model differs from previous models of continuum generation in that self-focusing plays a central role. As a consequence, continuum radiation is produced by the transient substructure throughout the portion of the pulse that is above the self-focusing threshold. Therefore the frequency does not continuously vary throughout the pulse as

would be the case for SPM alone, but rather the entire continuum spectrum is produced at each point in the pulse with a definite phase relationship between each point determined by the original phase of the pulse. The continuum radiation produced by the transient substructures can therefore be modeled as emanating from a line array of phased sources. Both spectral modulation and conical emission occur as a result of interference of the radiatiation emanating from a line array of sources.

An experiment was performed to investigate the above predictions. Pulses of 50 fs duration and energies of ~500 μJ were generated by amplifying the output of the CPM dye laser in a Nd:YAG pumped prism dye amplifier. The beam was focused by f/150 optics into a 75 cm long gas cell which could be filled to a pressure of up to 40 atmospheres. We show that the modulation period decreases with increasing pressure as expected, since the critical power decreases and so more of the pulse has the required power to self-focus. We also show qualitative agreement between the modeled and experimental spatial profile of the transmitted radiation.

We conclude by emphasising that concepts, well established in long pulse self-focusing, do not always scale to the short pulse regime. In particular, short pulses resist nonlinear changes to their geometrically determined focal spot size.

Reversible Multiphoton Ionization of Gases Observed by a Femtosecond Pump/Probe Schlieren Imaging Technique

J. P. Geindre, P. Audebert, and J. C. Gauthier

Laboratoire de Physique des Milieux Ionisés, Ecole Polytechnique, 91128 Palaiseau, France

R. Benattar

Laboratoire LULI, Ecole Polytechnique, 91128 Palaiseau, France

A. Mysyrowicz, J. P. Chambaret, and A. Antonetti

Laboratoire d'Optique Appliquée, ENSTA-X, Batterie de l'Yvette, 91120 Palaiseau, France

ABSTRACT

Using femtosecond time-resolved Schlieren imaging, we observe a light-induced reversible plasma-like change of the refractive index of a gas during optical irradiation by 80 fs laser pulses.

The development of lasers delivering ultra-short pulses at the multigigawatt power level opens new perspectives for the study of laser-matter interaction at very high intensities. Extensive studies of multiphoton ionization, continuum and harmonic generation in gases have been reported during the last few years[1]. These experiments detected mainly the photodetached electron spectrum or the self-emission from the interacting area. We report here an experiment using a probe beam which allows to analyze the time- and space-resolved change of the refractive index of a gas perturbed by a short intense optical pulse.

We have used a CPM dye laser delivering optical pulse of 80 fs duration at 620 nm with a maximum energy per pulse of 1.5 mJ. The repetition rate of the laser was 20 Hz. The laser was focussed with a f/8 lens inside a chamber filled with gases at 1 atmosphere pressure. The focal spot size was determined by an image plane technique to be 10 μm in diameter. The energy per pulse was measured with a calibrated calorimeter.

A weak part of the laser beam was used as a probe beam crossing the interaction area at an angle of 90° from the main pulse. When a light beam propagates through a region of varying refractive index, it becomes deflected. When projected with a lens on an image plane, the refracted beam directly yield informations on the time and spatial profile of the variation of the refractive index in the interaction area. A schematic view of

Proceedings on Short-Wavelength Coherent Radiation, Vol. 11, Philip H. Bucksbaum and Natale M. Ceglio (eds.)
© 1991 Optical Society of America

the principle of the experiment is shown in Fig. 1. The rays of the probe beam which are not (or only weakly) deflected are stopped by a knife edge placed at the focal plane of the imaging lens. The more strongly deflected rays are imaged with a lens (magnification ratio x170) on the detection plane of a CCD camera. The image was stored and processed by a minicomputer.

We observed the image of the refracted probe light beam as a function of pump intensity and time delay between the probe and the pump beams. The signal due to the refracted light appeared abruptly at a threshold pump intensity $I_0 = 2.10^{14}$ W/cm^2. The sign of the variation of the refraction index was determined to be negative. Near threshold, a gas length of only 30 μm in the beam waist induced a deviation of the probe beam. This corresponds to the spatial extent of an optical pulse of 100 fs duration When we changed the time delay between the probe pulse and the pump pulse, we observed the refraction signal moving without any change in its length as shown in Fig.2a. This indicates that the gas undergoes a strong modification of its polarizability during the irradiation and recovers very rapidly when the pump pulse has left. When the intensity of the pump pulse was increased, the recovery was no more complete and a long-lived signal became observable. This trailing signal of refracted light lasted for a long time (τ>100 ps) as expected for a plasma created by multiphotoionization followed by recombination. For a pump intensity $I > 2\ 10^{15}$ W/cm^2, beam filamentation became

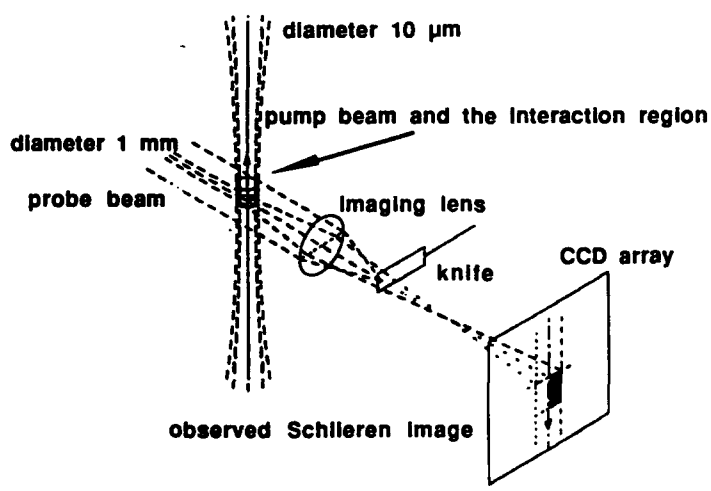

Figure 1: Schematic diagram showing the interaction region and the principle of the Schlieren imaging technique

apparent in the image, as shown in Fig.2b. At these intensities, continuum generation along the pump axis was also clearly observable. All the above results were essentially the same when the pressure in the chamber was decreased by a factor of three or when argon was replaced by air.

Both the the magnitude and the sign of change of the refractive index at or above threshold are characteristic of a singly-ionized plasma. By contrast, the usual non-linear response of a neutral gas would lead to a much smaller change in the refractive index and, moreover, with opposite sign. Simulations show that a cylindrical plasma of $3\ 10^{19}$ cm^{-3} electron density with a 6 μm FWHM gaussian radial profile is required to reproduce the observed signal.

The effect of the relative polarization and wavelength of the probe and the pump beam has been investigated. With crossed polarizations, the prompt signal shown in Fig.2a at "low" intensities vanishes completely. By detuning the probe wavelength with respect to the pump wavelength (with parallel polarizations) the intensity of the refracted signal was greatly reduced.

The surprizing new result here is the reversibility of this light-induced, plasma-like, response suggesting that even after the interaction with many photons, the system

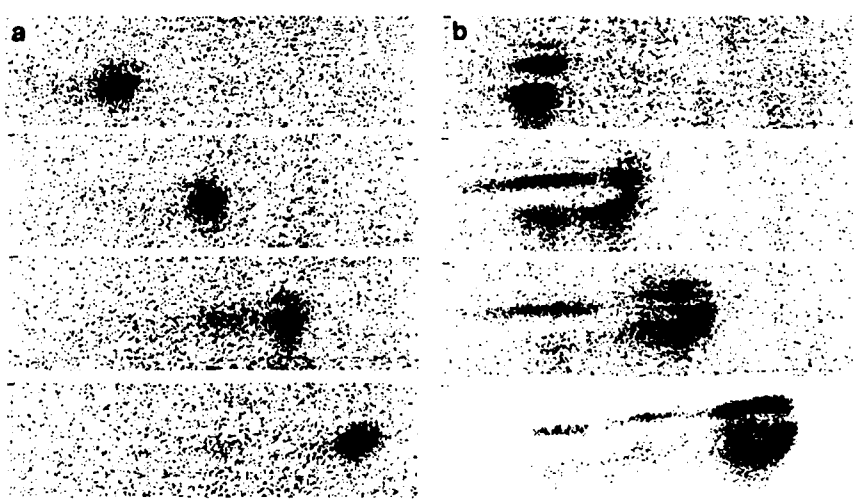

250 fs between frames

Intensity: 3.6 10^{14} W/cm^2 **Intensity: 2.2 10^{15} W/cm^2**

Figure 2: Schlieren images of the plasma-refracted probe as a function of the time delay between the pump and probe beams for two laser intensities. Each frame corresponds to a different location in the pump beam waist.

can be coherently driven back to the initial state. Similar observations of rapid variations of the refractive index in a plasma[2,3] have been observed through time-resolved spectral shifts. Blue shifts during the rising edge of the pulse were observed, followed by a rapid red shift attributed to the collisional dynamics of the plasma.

The behavior of the time-resolved refraction signal when the polarization or the wavelength of the probe beam are varied cannot be explained merely by plasma dynamics effects. Our 90° angle pump/probe technique can lead to wave mixing phenomena in the interaction region. Due to the nonlinear behavior of the plasma refractive index as a function of laser intensity, an index grating is created at the beam crossing which diffracts the pump beam towards the detector. Parallel orientation of the refracted pump wave vector and the probe wave vector is ensured by conservation laws of the four-wave mixing process. This may explain the polarization and wavelength dependence of our signal.

In conclusion, the existence of a transient plasma state with a nonlinear refractive index $n<1$ may have relevance to the understanding of continuum and harmonic generation in gases irradiated with laser light at intensities below the multiphoton ionization saturation limit.

References

1. H Rottke, B. Wolff, M. Brickwedde, D. Feldmann and K.H. Welge
Phys. Rev. Letters 64,404 (1990) and references therein.
2. W.M. Wood, W.C. Banyai, J.L. Trisnadi and M.C. Downer in "Ultrafast Phenomena VII", (Springer, Berlin, 1990),p.101.
3. W. Wodd and M.C. Downer, in Technical Digest Series Volume of Conference on Short Wavelength Coherent Radiation: Generation and Applications (Optical Society of America, Washington, D.C., 1991), paper MD3.

Spectral Blueshifts of Femtosecond Pulses in Atmospheric Density Kr and Xe Plasmas

Wm. M. Wood and M. C. Downer
Physics Department
University of Texas at Austin
Austin, TX 78712
Tel.: (512) 471-6054

Collisionless multiphoton ionization of atmospheric density gases with intense femtosecond pulses can produce a cold, dense plasma of highly stripped ions, thus providing a promising medium for XUV recombination lasers[1]. We have shown in several recent papers [2-4] that rapid ionization and the subsequent development of of plasma temperature in atmospheric density plasmas cause macroscopic refractive index changes which in turn induce characteristic spectral shifts on the ionizing pulse, or a time delayed probing pulse. Theoretical analysis of detailed features of these shifts in the lighter rare gases (He, Ne, Ar) has revealed several key aspects of femtosecond ionization: 1) an ab initio model of spectral shifts based on fundamental strong field ionization theory (e.g. Keldysh, Ammosov [5,6]); 2) the occurence of anomalously large blue shifts at higher pressures and intensities, when the ionization rate is significantly enhanced by impact-ionizing collisions of the quivering electrons [4]; and 3) evidence for low plasma temperatures, based on red shifts induced on a time-delayed probe [4]. In this paper we present new results with Kr and Xe gases, which reveal a distinct "double-humped" feature in the blue shifted single pulse spectra not seen in the lighter noble gases. A quantitative model is presented that attributes this effect to two characteristic rates at which multiple stepwise ionization occurs: a "fast" rate corresponding to each ionization stage during the early part of the pulse (e.g. $Kr^{n+} \rightarrow Kr^{(n+1)+}$) that produces the more shifted peak; and a "slow" rate which corresponds to the primarily impact ionization during the peak and latter parts of the pulse. The dwell time following the saturation of each ionization level in the early part of the pulse also contributes to a significant broadening of the bluer shifted part of the spectrum. This two-humped effect is more pronounced in Kr and Xe because of the lower ionization potentials, and therefore greater ionization rates; in addition, the larger number of levels ionized in these heavier noble gases cause a greater broadening of the further-shifted peak. Details of the double-humped blue shifted spectra depend on the role of impact ionizing collisions in the strong field, and also on the presence of chirp on the incident pulse.

Spectra of pulses after high intensity breakdown in Xe and Kr gases typically display a tall, narrow peak that is blue-shifted by about 5-6 nm. from the original pulse spectrum, and a short, broad "shoulder" towards the blue. This shoulder separates into a clearly discernible peak as either the intensity or the pressure is increased. This feature can be seen in the top figure, where we present the spectrum of a 100 fs. pulse with peak intensity 5×10^{15} W/cm^2 shifted by ionizing breakdown in 3 atm. pressure of Krypton gas. The spectrum can be fitted quite well with a sum of two gaussians, accentuating the

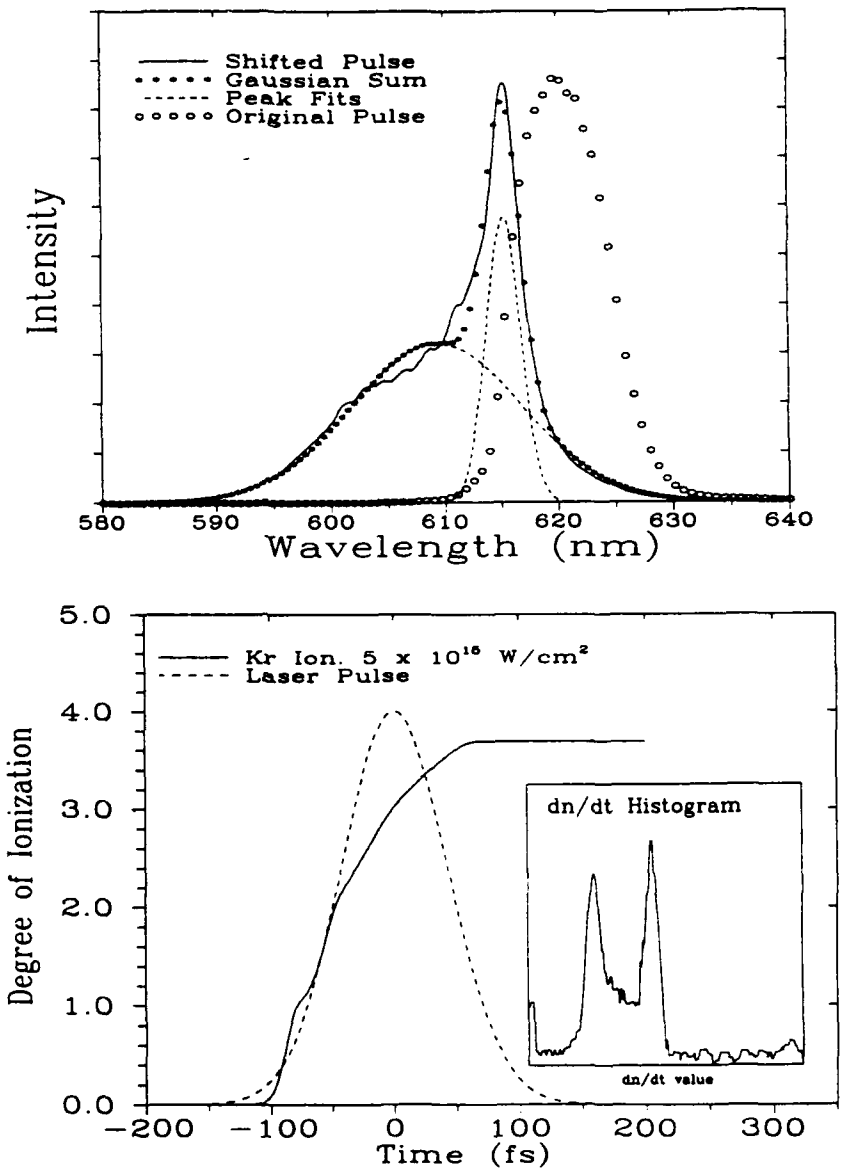

FIGURES: The top figure shows observed spectral shift of breakdown in 3 atm. pressure Krypton gas with peak intensity 5×10^{15} W/cm^2. Included is the unshifted spectrum, and a pair of gaussian functions that add to approximate the shifted spectrum. The bottom figure shows calculated free electron density as a function of time for a 5×10^{15} W/cm^2, 100 fs pulse incident on Krypton gas at 3 atm. pressure. The pulse profile is shown for reference. Inset is a time histogram of the corresponding dn/dt.

twin-peaked behaviour of the shifted spectrum, as indicated in the figure. It is seen that the narrow gaussian is shifted by about 5 nm. and the low, broad gaussian is shifted by about 11 nm. Since the magnitude of the blue shift is proportional to the derivative of the refractive index, we expect that a histogram describing the relative amount of time that the derivative spends at any given value should reveal two strong, distinct peaks. In the lower figure we have plotted the degree of ionization of Krypton atoms at 3 atm. pressure when illuminated by a 100 fs. with peak intensity of 5×10^{15} W/cm^2 , as predicted by our ab initio model. Note the stepwise structure of the ionization caused by one level saturating, and a short "wait" before the intensity increases enough for the next level to begin ionizing. We have inset in the lower figure a histogram of dn/dt from the resulting index caused by the pictured ionization. As expected, there are two very distinct peaks in the distribution of values for the derivative, which result in the type of "twin-peaked" behaviour that is observed in the shifted spectra. The values of the derivative where these peaks occur correspond to the shifts of the two peaks in the shifted spectra. The significant narrowing with respect to the original pulse spectrum of the tall peak can be seen in the top figure. This feature results from the ionization-induced phase modulation actually negating the chirp on the laser pulse being shifted. Such a chirp on the incident pulse is expected, since the observed pulse spectrum from the amplifier will support a pulse of less than 50 fs, while the measured pulsewidth is 100 fs. It is possible to include the effects of the chirp on the laser pulse in modelling the spectral shifts by simply measuring the interferometric autocorrelation of the incident pulse.

In conclusion, we see two important features in the shifted spectra from high intensity breakdown of the heavier noble gases at higher pressures: a double-humped appearance, and a significant narrowing of the taller peak. The double-humped feature comes directly from the primarily double-valued derivative of the refractive index, as we can see from our ab initio model. The narrowing of the taller peak results from the chirp that exists on the amplified laser pulses, and can also be included in our model.

1. N.H. Burnett and P.B. Corkum, J.Opt.Soc.Am. B 6,1195. (1989)
2. W.M. Wood, G. Focht, and M.C. Downer, Opt. Lett. 13, 984. (1988)
3. M.C. Downer, W.M. Wood, and J.I. Trisnadi, Phys. Rev. Lett. 65, 2832. (1990)
4. W.M. Wood, W.C. Banyai, J.L. Trisnadi, and M.C. Downer in Ultrafast Phenomena VII (Springer Verlag 1990), p. 101; M.C. Downer, J.I. Trisnadi, W.M. Wood, and W.C. Banyai, Proc. International Conference on Spectral Line Shapes (Am. Inst. Phys 1990), in press.
5. L.V. Keldysh, Sov. Phys. JETP 20, 1307. (1965)
6. M.V. Ammosov, N.B. Delone, V.P. Krainov, Sov. Phys. JETP 64, 1191. (1986)

Creation of Relativistic Plasmas Using Ultrahigh-Intensity Laser Radiation

J. N. Bardsley and B. M. Penetrante

High Temperature Physics Division,
Lawrence Livermore National Laboratory, Livermore, California 94550

Abstract

Recent theoretical work on the relativistic dynamics of electrons in plasmas produced by short laser pulses is reviewed. The effect of the electron motion upon the laser propagation is discussed, and brief comments are made about the feasibility of laser-induced nuclear reactions and laser wakefield accelerators.

I. Introduction

The importance of relativistic effects in laser-produced plasmas can be judged from the parameter

$$q = \frac{eA_p}{mc^2} = \frac{eE_p}{mc\omega}$$

where A_p and E_p are the peak magnitudes of the vector potential A and electric field strength E, respectively, and ω is the laser frequency. The effects are significant when $q \geq 1$. This is achieved when the intensity I reaches a critical value $I_0(\omega)$ which has the values 1.2×10^{16}, 1.2×10^{18} and 2.1×10^{19} W/cm^2 for CO_2, neodynium and KrF lasers, respectively. These values seem well within the capability of current technology.

In Sec. II, we will review the dynamics of electrons in intense fields, showing how the magnetic fields add a longitudinal component to the basic transverse oscillations. Gradients in laser intensity lead to "ponderomotive forces" which push electrons away from the regions of highest intensity. In dense plasmas all displacements of electrons away from their parent ions are resisted by the space charge forces. The competition between the ponderomotive and space charge forces leads to a wide range of interesting phenomena.

The effects of the electron dynamics on the laser propagation are discussed in Sec. III and IV. The non-linearities in the relativistic quiver motion lead to the presence of high harmonics in the reradiated light. Changes in the refractive index caused by changes in the electron mass, and by induced gradients in the electron density, can lead to convergence or divergence of the transmitted beam.

Some preliminary conclusions will be given in Sec. V.

1991 Optical Society of America

II. Relativistic Electron Dynamics

The relativistic dynamics of single electrons in plane-wave electromagnetic fields can be solved exactly, for arbitrary pulse shapes, in both classical and quantum mechanics. Sarachik and Schappert[1] have provided a particularly lucid account of the classical theory, assuming that the electron is at rest before the pulse arrives. A solution with more general boundary conditions was given by Kruger and Brown[2] and analysed by Bardsley, Penetrante and Mittleman.[3] We believe that quantum effects are not important in the context of this review.

Since the transverse component of the canonical momentum (p - eA/c) remains a constant of the motion, the transverse velocity is determined by the instantaneous local value of the vector potential. Magnetic fields drive the electrons forward with a longitudinal velocity component that is proportional to A^2, and so oscillates at twice the frequency of the laser radiation. For large values of q, most of the energy is in the longitudinal motion. The maximum energy is given by $mc^2(1+q^2/2)$. The relativistic electron mass thus increases as q^2, and since the transverse momentum is proportional to q, the maximum transverse velocity decreases as q rises. However, because of time dilation, the amplitude of the transverse quiver motion approaches a constant limit of $\lambda/4$.

In this ideal solution, ambient electrons which are at rest before the arrival of the pulse always return to rest after the passage of the pulse. Thus all the energy that was transferred from the laser to the electron as the intensity rises is fed back into the laser as the intensity wanes. This is also true for electrons which are released with zero velocity during the pulse at a time and place where the vector potential is zero. This is approximately the situation for photoelectrons produced by linearly polarized light, since the electrons are ejected from their parent atom with a low velocity when the electric field strength is close to its maximum value, and thus A is small. For circular polarization the amplitude of A does not vary rapidly and there no points in the optical cycle at which A is close to zero. Thus the residual energy of photoelectrons produced by intense circularly-polarized light is usually high, as has been observed by Corkum, Burnett and Brunel.[4] Electrons that are created by electron impact ionization in a high field region will also have a large residual energy at the end of the pulse. Furthermore, the change in the trajectory of the primary electron will usually increase its own residual energy. Electron impact ionization near the laser focus will thus result in the extraction of a large amount of energy from the laser.

We have pointed out that most of the energy gained by relativistic electrons in intense plane-wave fields is associated with forward motion. At high plasma densities, such displacements will be restrained by the space charge forces, and the maximum energy that is attained may be reduced. One dimensional simulations[3] have confirmed this effect for electrons that are created early in the pulse. However, electrons that are born in intense fields may follow chaotic orbits, leading to even higher maximum energies. The onset of chaos due to the non-linearities associated with the relativistic mass increase and with time dilation effects has been partially analyzed[3] but further study would be worthwhile.

Since very intense fields can only be achieved at present by strong focusing, the study of plane wave fields is only of theoretical interest. Given transverse variations in intensity, electrons tend to move away from the high field regions where greater energy is needed to maintain the quiver motion. In most situations they move as though they are being propelled by a "ponderomotive" force equal to the gradient of the quiver energy.

Electrons that are created in the early portion of a pulse are pushed away from the focal region[5], and thus may not reach the energies that they would in plane waves of the same intensity. Once again, electrons that are born in high-intensity regions can reach very high energies.

III. Harmonic Production

Sarachik and Schappert[1] have analyzed the radiation emitted by individual electrons in plane-wave pulses. They show that at high intensities the radiation peaks along the surface of a cone making an angle $\sqrt{8}/q$ with the direction of propagation. The radiation contains strong contributions from all orders, both even and odd, up to $3(q^2/2)^{3/2}$. Along the preferred directions, the intensity rises as q^7.

Mohideen *et al.*[6] have pointed out that for strongly focused lasers in low density gas targets, the number of electrons remaining near the focal point at the peak of the pulse may be very small. One might then be able to do realistic 3-D calculations by following the motion of each electron individually. As a first step in this direction, they have computed the radiation emitted by 100 electrons, initially placed at random in a sphere of radius 80 nm, when irradiated by a focused short pulse with a peak intensity in excess of 10^{19} W/cm^2. They find that in the lower order harmonics, the contributions from each electron add coherently and the power rises as the density squared. For the higher harmonics, incoherent superposition occurs and the power rises only linearly with the number of electrons.

At higher plasma densities, space charge forces may have significant effects on the harmonic production. A courageous attempt to study the harmonics for plane wave incident radiation has been made by Sprangle, Esarey and Ting[7], using a quasistatic approximation. They show that it is helpful to distinguish between two regimes, depending on whether the pulse length L is smaller or greater than the plasma period λ_p. We prefer to think of these two regimes as low and high density regimes, since the pulse length is usually constrained by the laser technology, whereas the plasma period can be varied over a wide range by changing the plasma density. At low densities, they find that the power radiated in the third harmonic is proportional to the square of both the laser intensity I and the electron density n_e. At high densities, this power is also proportional to n_e^2, but it decreases as I increases. This latter result is very surprising, and should be checked by numerical computation.

Umstadter *et al.*[8] have reported observations of harmonic generation at high intensities in light gases that show some of the scaling characteristics predicted by Sprangle *et al.*[7] Further experiments of this kind would be very useful.

IV. Focusing and Defocusing

A second important feature arises from variations in the refractive index

$$\left(1 - \frac{n_e}{\gamma n_c}\right)^{1/2}$$

where n_e is the electron density, γ is the usual relativistic mass factor, and n_c is the non-relativistic critical density. The first consequence is that penetration into super-critical plasmas becomes easier as γ increases and as the electron density is reduced by ponderomotive expulsion. Radial variations in the refractive index lead to focusing or

defocusing of the beam. Usually γ decreases as one moves away from the focal axis in a transverse direction, so that the refractive index decreases and the beam may converge. On the other hand, if the electron density also peaks on axis, the refractive index may have a positive radial derivative and the beam may diverge. But if the ponderomotive forces push out the electrons enough to produce a positive gradient in the electron density, both effects lead to convergence of the beam. Indeed, it may be possible to produce a wall of electrons with super-critical density. Rhodes and his collaborators[9,10] have developed a theory, assuming a quasistatic electron distribution in which the ponderomotive and space charge forces are balanced. They conclude that such channeling may well be feasible over many Rayleigh lengths. Unpublished experimental observations at the University of Illinois[11] and Lawrence Livermore National Laboratory[12] of extended propagation may be due to these effects. However, the time-dependent evolution of the electron density and relativistic mass factor must be studied before this conjecture can be confirmed theoretically.

V. Conclusions

Boyer *et al.*[13] have pointed out that some of the most dramatic signatures of the formation of relativistic plasmas should come through electron-induced nuclear reactions. Pair production should be seen at electron energies above 1 MeV and laser induced fission should be observable at about 10 MeV. Single electrons reach these energies with $q = 1.5$ and 4.5, respectively. In developing more detailed solutions, one should examine whether the maximum electron velocity is significantly changed. For example, electrons freed early in the pulse may be pushed out of the most intense fields and not attain the expected quiver velocity. Strong space charge forces may also restrain the electrons. Nevertheless, we believe that these two processes will be observable, using 1 μm radiation, at intensities of 10^{19} and 10^{20} W/cm^2, respectively.

There has been much speculation about the use of intense lasers to drive wakefield accelerators. In a recent analysis of this phenomenon, Bulanov *et al.*[14] conclude that a laser pulse of length 0.3 ps, at a wavelength of 1 μm and an intensity of 10^{19} W/cm^2, propagating through a plasma of density 10^{15} cm^{-3}, will produce a longitudinal electric field of order 2 GV/m. This would permit the acceleration of an electron from 0.5 GeV to 0.3 TeV in a length of 150 m. The maintenance of a high laser intensity over such a length scale provides a grand challenge for those who believe they understand relativistic channeling!

Acknowledgment

This work was performed under the auspices of the U. S. Department of Energy by the Lawrence Livermore National Laboratory under Contract Number W-7405-ENG-48.

References

1. E. S. Sarachik and G. T. Schappert, "Classical theory of scattering of intense radiation by free electrons," Phys. Rev. D 1, 2738-2753 (1970).
2. J. Kruger and M. Bovyn, "Relativistic motion of a charged particle in a plane electromagnetic wave with arbitrary amplitude," J. Phys. A 9, 1841-1846 (1976).

3. J. N. Bardsley, B. M. Penetrante, and M.H. Mittleman, "Relativistic dynamics of electrons in intense laser fields," Phys. Rev. A 40, 3823-3835 (1989).
4. P. B. Corkum, N. H. Burnett, and F. Brunel, "Above-threshold ionization in the long wavelength limit," Phys. Rev. Lett. 62, 1259-1262 (1989).
5. B. M. Penetrante and J. N. Bardsley, "Residual energy in plasmas produced by intense subpicosecond lasers," Phys. Rev. A 43, 3100-3113 (1991).
6. U. Mohideen, H. W. K. Tom, R. R. Freeman, J. Bokor, and P. H. Bucksbaum, "Nonlinear Compton scattering in a pulsed focused laser beam," in this volume (1991).
7. P. Sprangle, E. Esaray, and A. Ting, "Nonlinear interaction of intense laser pulses in plasmas," Phys. Rev. A 41, 4463-4469 (1990).
8. D. Umstadter, X. Liu, J. S. Coe, C. Y. Chien, E. Esarey, and P. Sprangle, "Harmonic generation by an intense picosecond laser in an underdense plasma," in this volume (1991).
9. J. S. Solem, T. S. Luk, K Boyer, and C. K. Rhodes, "Prospects for X-ray amplification with charge-displacement self-channeling," IEEE J. Quant. Elec. 25, 2423-2430 (1989).
10. A. B. Borisov, A. V. Borovskiy, V. V. Korobkin, A. M. Prokhorov, C. V. Rhodes, and O. B. Shiryaev, "Stabilization of relativistic self-focusing of intense subpicosecond ultraviolet pulses in plasmas," Phys. Rev. Lett. 65, 1753-1756 (1990).
11. C. K. Rhodes, University of Illinois at Chicago, (personal communication).
12 M. D. Perry, Lawrence Livermore National Laboratory, (personal communication).
13. K. Boyer, T. S. Luk, and C. K. Rhodes, "Possibility of optically induced nuclear fission," Phys. Rev. Lett. 60, 557-560 (1988).
14. S. V. Bulanov, V. I. Kirsanov, and A. S. Sakharov, "Ultrarelativistic theory of a laser plasma wake accelerator," Fiz. Plazmy 16, 935-944 (1990) [Sov. J. Plasma Phys. 16, 543-548 (1990)].

Nonlinear Compton Scattering in a Pulsed Focused Laser Beam

U. Mohideen,[a] H. W. K. Tom, R. R. Freeman, and J. Bokor

AT&T Bell Laboratories, Holmdel, New Jersey 07733

P. H. Bucksbaum

Department of Physics, University of Michigan, Ann Arbor, Michigan 48109-1120

ABSTRACT

The relativistic motion and radiation spectrum of free electrons in the focus of an ultrashort high intensity laser pulse is solved. Motion and radiation of electrons in a novel axicon focus is also analyzed.

We have calculated the radiation emitted from free electrons in an ultrashort pulsed laser focus. For low electron densities, where space charge is negligible, we find that ponderomotive forces limit the effective volume where the radiation is emitted to a region much smaller than the waist at the focus. For typical focal parameters, the emitting region is significantly smaller than the fundamental wavelength. Nonetheless, constructive inteference plays a significant role in the collective radiation spectrum. Phase mismatch becomes important only for the higher harmonics. These studies are intended as a prelude to experiments with high intensity ultrashort laser pulses.

To investigate the motion of individual free electrons, we solve the relativistic Lorentz force[1] equation

$$\frac{d^2x^\mu}{d\tau^2} = \left[\frac{e}{mc}\right] F^{\mu\nu}\frac{dx_\nu}{d\tau} \tag{1}$$

for an electron placed in the gaussian focus of a pulsed laser. The electric fields at the focus is given by:

$$E_x = \frac{E_o}{(1+i\xi)}\left\{\exp-\frac{(x^2+y^2)}{\omega_o{}^2(1+i\xi)}\right\}\left\{\exp i(kz-\omega t)\right\}\left\{\exp-\left[\frac{(kz-\omega t)}{T}\right]^2\right\}$$

$$E_z = \frac{-iE_o}{(1+i\xi)^2}\left[\frac{2x}{k\omega_o{}^2}\right]\left\{\exp-\frac{(x^2+y^2)}{\omega_o{}^2(1+i\xi)}\right\}\left\{\exp i(kz-\omega t)\right\}\left\{\exp-\left[\frac{(kz-\omega t)}{T}\right]^2\right\}$$

$$\xi = \frac{2z}{k\omega_o{}^2} \tag{2}$$

Proceedings on Short-Wavelength Coherent Radiation, Vol. 11, Philip H. Bucksbaum and Natale M. Ceglio (eds.)

© 1991 Optical Society of America

These calculations neglected the space charge effects of ions on the electrons. If the electrons are made by completely ionization of 1 Torr of H_2 the space charge fields are only 10^{-4} of the applied field. Also hard collisions (collisions with low impact parameters between the electrons, and electrons and protons) can be neglected as the collision frequency is only about 10^{-9} per laser pulse [4]. Also, radiation damping is not important as the ratio of the total radiated energy per cycle to the average kinetic energy is about 10^{-6}.

The electrons are strongly influenced by ponderomotive forces, proportional to the gradient of the laser intensity[2,3]. Figure 1 shows the maximum intensity seen by electrons at different radial positions before the arrival of the pulse. We see that electrons only a tenth of the waist away see only half the peak intensity of the pulse. If the focusing is too strong the electron is driven radially out of the focus long before the peak of the pulse arrives. For example an electron located one wavelength (800 nm) away from the center of an f/5, 100 mJ, 100 fs focus is forced out with a kinetic energy of 60 keV after a few optical cycles.

Next we investigated the radiation spectrum from electrons in the focus. The radiated electric field from a moving electron is given by the Lienard-Wiechert formula[1]:

$$\mathbf{E}(\mathbf{x},t) = \left[\frac{e}{c}\right]\left[\frac{\mathbf{n}\times\left[(\mathbf{n}-\boldsymbol{\beta})\times\dot{\boldsymbol{\beta}}\right]}{(1-\boldsymbol{\beta}\cdot\mathbf{n})^3 R}\right]_{ret} \tag{3}$$

The spectrum of the radiation is found by a Fourier transform of the radiated electric field. In the non-relativistic regime ($\beta << 1$) of Thomson scattering, the electron emits radiation at the incident frequency, in a dipole pattern peaked perpendicular to $\hat{\varepsilon}$. At higher intensities, relativistic motion leads to radiation at harmonic frequencies as well [5]. The often-cited rule that only odd harmonics can be radiated by a centrosymmetric medium, does not hold for free electrons in a laser field. The presence of the magnetic field breaks inversion symmetry in a travelling wave; in general, even harmonics are as strong as odd, but propagate in a different direction. The second harmonic is due to the "figure-8" motion (in the average rest frame - trajectory in the lab frame is nearly saw toothed) of the electron responding to the electromagnetic wave.

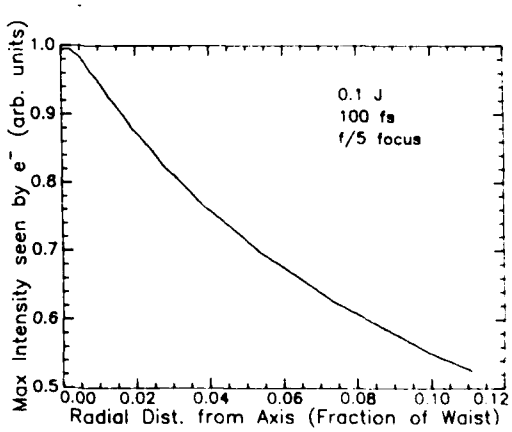

Figure 1: Maximum intensity seen by electrons with different intial radial positions (fractions of waist) for a 100 mJ, 100 fs pulse focussed using f/5 optics.

For very high intensities, there are two important additional effects. First, the electrons, if initially at rest before the laser pulse, are set into motion in the **k** direction as the laser turns on (**E**×**B** drift). We see from Eq.(3) that the maximum in the radiation occurs when the velocity is highly relativistic and the direction of observation makes a very small angle ($\theta=\frac{1}{2\gamma}$) away from the direction of the electron velocity . Under these conditions the denominator goes to zero leading to a huge radiated electric field. The points of maximum radiation on the trajectory occur close and are symmetric to the oscillation axis. At these points the electron is travelling at an angle to the incident **k** direction. The other arm of the trajectory leads to radiation on the other side of the oscillation axis. So, the angular distribution of radiation looks like that from two flashlights at acute angles to the **k** (intensity dependent angle) direction in the plane of polarization. Figure 2 shows the radiated spectrum from the plane wave of the same peak intensity as in a 4J, 100fs pulse of wavelength 800 nm focussed with f/10 optics (peak intensity is $3.6\times10^{19}\,W/cm^2$) observed at an angle of 30° to the **k** direction in the plane of polarization. The harmonics are not integral multiples of the incident frequency; but are integral multiples of $\frac{1}{(\Delta T'-\Delta z\cos\theta)}$ where, $\Delta T'$ is the time interval for two consecutive identical events to occur (eg. the time elapsed for the electron to go from one peak to the next in its trajectory in the lab frame) and Δz is the distance travelled in the beam direction during that time and θ is the angle made by the observer to the **k**. ($\Delta T'-\Delta z\cos\theta$) is the time interval seen by a far away observer making an angle 'θ' to the **k** for the same two identical events. This is seen in Figure 2 where there are three radiated frequencies for an interval of $2\omega_{incident}$. The harmonic frequencies are therefore angle- and intensity-dependent. The radiated harmonics peak at some high frequency because the electric field comes from a very small high velocity region of the trajectory. This high frequency electric field is made by a superposition of the this peak frequency component plus a component at three times this peak frequency and another component at five times the peak frequency and so on. This leads to radiated components which have peaks also at three times the peak frequency, five times the peak frequency as seen in the Figure 2.

Figure 3 shows the radiated spectrum of 10 electrons, observed at an angle of 30° away from the incident direction in the plane of polarization. The electrons are located in random positions

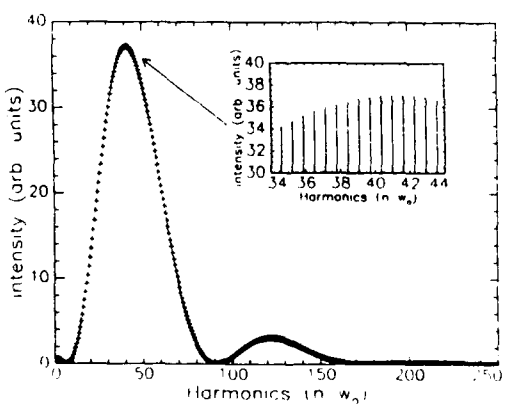

Figure 2: Radiation spectrum of single electron, observed at an angle of 30° away from the **k** direction, in the plane of polarization for a plane wave of the same intensity as the peak intensity of the f/10 focussed 4J, 100 fs pulse of 800 nm wavelength.

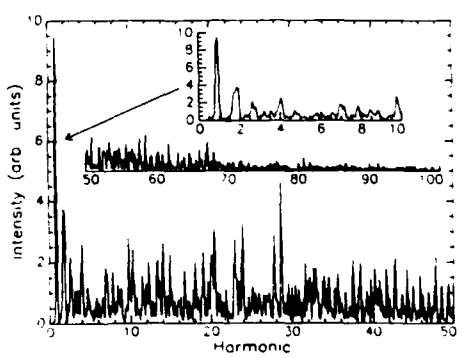

Figure 3: Radiation spectrum of 10 electrons, observed at an angle of 30° away from the **k** direction, in the plane of polarization for a f/10 focussed 4J, 100 fs pulse of 800 nm wavelength.

within a sphere of radius 80 nm of the f/10 focus of a 4 J, 100 fs pulse of wavelength 800 nm (peak intensity is 3.6×10^{19} W/cm^2). The wide peaks at the lower harmonics are due to various intensities that are present in the exponential pulse. Figure 4 is the radiated spectrum, at the same angle, from 100 randomly placed electrons in the same focus. There is considerable constructive inteference for the lower harmonics. The power increases roughly as the square of the density of electrons. However, at the higher harmonics the random spacing between the electrons becomes comparable to the wavelength, and the constructive inteference is lost. For these higher harmonics, viewed off the axis of the laser beam, the power radiated increases only linearly with the number of electrons. The spectrum from the electrons placed in the pulsed laser focus have naturally a large low harmonics component due the lower intensity at the rising edge of the pulse.

AXICON FOCUS

We have used the same equation of motion to study the behaviour of electrons in the focus of a conical axicon[6] which has been suggested as a means of accelerating electrons. Fontana, et al. have suggested that electrons can be continually accelerated if their initial energy is very high (few GeV). However, when lower energy electrons are injected into the same laser beam they tend to lose phase matching[7] due to their relatively large increase in velocity during acceleration. We have found that there exists a range of initial velocities for a given laser intensity, where the electron becomes trapped between opposing phases of the axial electric field, first accelerating, slipping out of phase by π, and then decelerating back to its original position in phase with respect to beam. Figure 5 is a plot of the trapped region for 100 fs pulses of different energies with a waist of 2.5 cm. The electrons were all launched at the phase for maximum acceleration 'π'. The refractive index corresponds to about 4 atmospheres of Nitrogen. The Cerenkov angle was 17.5 mrad. The region of allowed initial gamma for trapping is larger for larger pulse energies as any deficit in the initial velocity for phase matching can be made up by the acceleration from the field. Similarly, any excess in the velocity can be reduced in the regions of the field where retardation occurs, again leading to trapping.

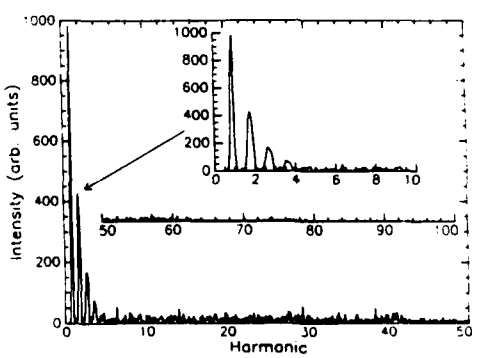

Figure 4: Radiation spectrum of 100 electrons, observed at an angle of 30° away from the k direction, in the plane of polarization for a f/10 focussed 4J, 100 fs pulse of 800 nm wavelength.

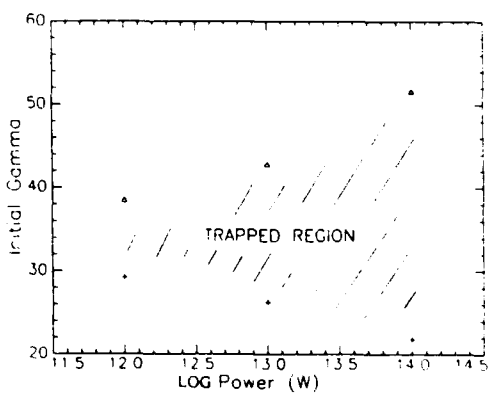

Figure 5: Initial values of Gamma for the electrons for trapping in a axicon focus as a function of the input laser power.

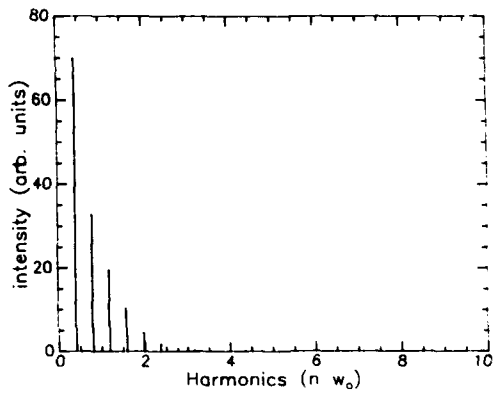

Figure 6: Radiation spectrum from a electron with a initial gamma of 25 trapped in a axicon focus made with a 10 J, 100 fs pulse of waist 2.5 cm.

Next we tried to study the radiation spectrum from one such trapped electron. The radiation could be used as diagnostic to monitor the phase slippage suffered by the electrons. Figure 6 is a plot of the radiation spectrum from an electron with an initial gamma of 25 in the axicon focus formed by a 10 J, 100 fs pulse with a waist of 2.5 cm. Following the earlier discussion the radiation peaks at angle ($\theta = \frac{1}{2\gamma}$) of 10 mrad to the beam axis and has an angular width of 20 mrad, consistent with a $\gamma_{average} = 50$. As expected the radiation has azimuthal symmetry.

(a) Physics Department, Columbia University, New York City,N.Y.10027.

References

1. J.D.Jackson, Classical Electrodynamics, (J.Wiley&Sons,N.Y,1975),pp.657.
2. P.H.Bucksbaum,et. al.,"Scattering of Electrons by Intense Coherent Light," Phys. Rev. Lett. 58,pp.349-352 (1987).
3. J.N.Bardsley,et. al.,"Relativistic Dynamics of Electrons in Intense laser Fields,"Phys.Rev. A40,pp.3823-3835 (1989).
4. E.S.Sarachik and G.T.Schappert,"Classical Theory of Scattering of Intense Laser Radiation by Free Electrons,"Phys.Rev. D1,pp.2738-2753 (1970).
5. J.F.Seeley and E.G.Harris,"Heating of a Plasma by Multiphoton Inverse Brehmsstrahlung,"Phys.Rev. A7,1064-1067 (1973).
6. J.R. Fontana, et. al.,"A high-energy, laser accelerator for electrons using the inverse Cherenkov effect,"J. Appl. Phys. 54,pp.4285-4288 (1983).
7. R.D.Romea and W.D.Kimura,"Modeling of Inverse Cerenkov laser acceleration with axicon laser-beam focusing,"Phys.Rev. D42pp.1807-1818 (1990).

Electromagnetically Induced Transparency

A. Imamoglu, K. -J. Boller, and S. E. Harris

E. L. Ginzton Laboratory, Stanford University, Stanford, California 94305

Abstract

We report the first observation of electromagnetically induced transparency in optically thick medium. The transparency results from a destructive interference of two dressed states which are created by applying a temporally smooth coupling laser between a bound state of an atom and the upper state of the transition which is to be made transparent. The transmittance of an autoionizing transition in Sr is changed from exp(-20) to exp(-1).

Introduction

This paper reports the results of an experiment showing how an opaque transition may be rendered transparent to radiation at its resonance frequency. This is accomplished by applying an electromagnetic coupling field between the upper state |3> of the transition and another state |2> of the atom (Fig. 1). In this work, the transmittance of an ultraviolet transition to an autoionizing state of neutral Sr is changed from exp(-20) to exp(-1) using a coupling laser field with a Rabi frequency of 1.5 cm^{-1} [1].

This transparency is best understood in the dressed state picture [Fig.1 (inset)]. The two upper dressed states created by the coupling laser experience a Fano-type interference that cancels the absorption completely [2]. This viewpoint emphasizes two important features of this process: The transparency does not require coherence of the probe laser and may be observed with white light and a monochrometer; even though bare state |3> decays to many different channels, to the extent that bare state |2> is metastable, the dressed states have the same weighted per channel decay and therefore the same interference profile for each channel.

Proceedings on Short-Wavelength Coherent Radiation, 257
Vol. 11, Philip H. Bucksbaum and Natale M. Ceglio (eds.)
© 1991 Optical Society of America

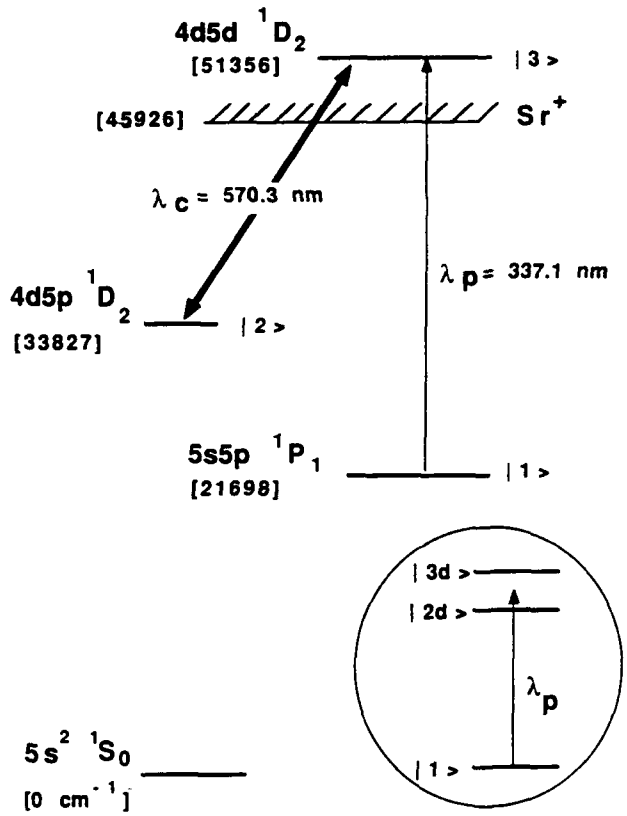

Figure 1. Energy level diagram of Sr. Inset: Dressed state picture

Strontium system

Fig. 1 shows a partial energy level diagram of neutral Strontium. The probe transition which is to be rendered transparent is 5s5p $^1P_1$ - 4d5d $^1D_2$ with a transition wavelength of 337.1 nm. The absorption oscillator strength of this transition is gf = 0.15. The upper level 4d5d $^1D_2$ decays by autoionization [3] and has a measured width of 1.2 cm^{-1}, corresponding to an autoionizing time of 4.4 psec. The lower level 5s5p $^1P_1$ is populated from ground by a resonant 460.7 nm pulsed dye (pumping) laser. We use a ground state ($5s^2$ $^1S_0$) Sr density of $5x10^{15}$ atoms/cm^3 and a pumping laser energy density of about 10 mJ/cm^2 in a pulse width of 4 nsec, and obtain a population density in 5s5p $^1P_1$ of $1x10^{14}$ atoms/cm^3. This population is radiatively trapped for about 50 nsec.

The laser which is used to create the transparency is termed as the coupling laser and is tuned to the line center (570.3 nm) of the 4d5p $^1D_2$ - 4d5d $^1D_2$ transition, which has an experimentally determined oscillator strength of gf = 0.25. Both the coupling and probe lasers are σ^+ polarized and are co-propagating.

A fundamental requirement on the observability of an electromagnetically induced transparency is to have a coupling laser that is free of amplitude fluctuations and mode beating effects. To eliminate these effects, we built a single mode Littman dye laser [4] which is pumped by a frequency doubled injection seeded (Quanta Ray) Nd:YAG laser. Although each pulse is near transform limited, changes in the refractive index of the dye cause a pulse-to-pulse frequency jitter corresponding to a time averaged linewidth of 0.03 cm^{-1}. The output of the oscillator is amplified by a three stage dye amplifier to an energy of 20 mJ in a pulse length of 3 nsec with a pulse-to-pulse peak intensity fluctuation of 10%. The probe laser is a commercial PDL Quanta Ray dye laser with an intracavity etalon. The linewidth at 337.1 nm is 0.15 cm^{-1}.

Experimental results

Fig. 2a shows the transmission profile of the probe laser when the delay between the pump and probe lasers is 110 nsec. The medium is almost optically thin with a minimum transmission on line center of exp(-1.7 ± 0.1). By curve fitting (theory dashed) with a Voigt profile convolved with the probe laser linewidth, we determine a linewidth of 1.2 cm^{-1} for the transition. Fig. 2b shows the transmission vs. probe laser frequency at a coupling laser Rabi frequency of 1.3 cm^{-1}. This Rabi frequency is estimated by measuring the frequency spacing between the two transmission minima (dressed state frequencies).

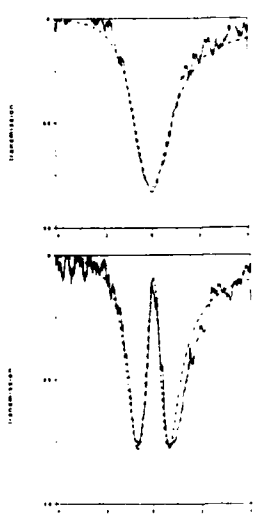

Figure 2. Transmission vs. probe laser detuning for (a) $\Omega_{23} = 0$, (b) $\Omega_{23} = 1.3$ cm^{-1}. Minimum transmission is exp(-1.7).

Fig. 3a shows the transmission when the delay is only 20 nsec. In this case, the medium is optically thick with a minimum transmission on line center of exp(-20 ± 1). As we can only measure down to exp(-7) transmission, this value is determined by curve fitting with a Voigt profile. Fig. 3b shows the transmission when the coupling laser Rabi frequency is 1.5 cm^{-1}. We observe a change in transmitted intensity from exp(-20±1) to exp(-1±0.1) on line center.

We see that especially in the optically thick case, there is a consistent asymmetry in the tails of the transmission profile. In searching for the possible causes for this, we measured a background absorption cross-section of $2x10^{-16}$ cm^2, constant over a frequency range of ±40 cm^{-1} (the peak absorption cross-section of the 4d5p $^1D_2$-4d5d $^1D_2$ transition is $2x10^{-14}$ cm^2). By assuming that there is a Fano-type interference between 4d5d $^1D_2$ level and this background in our theoretical calculations, we can account for the asymmetry, as shown in Figs. 2 and 3.

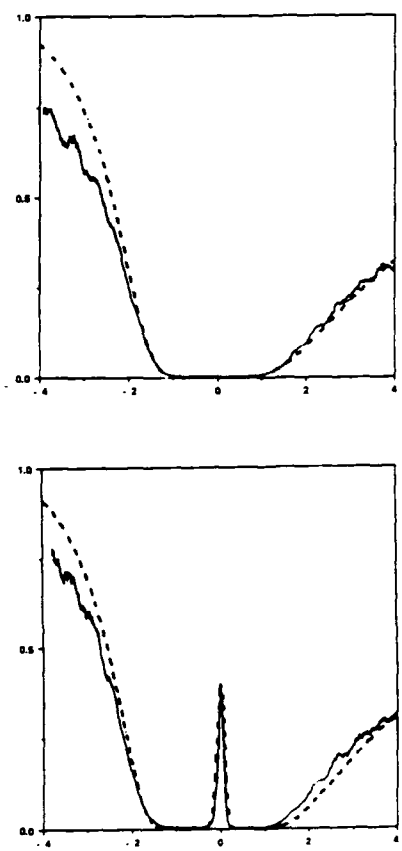

Figure 3. Transmission vs. probe laser detuning for (a) $\Omega_{23} = 0$, (b) $\Omega_{23} = 1.5$ cm^{-1}. Minimum transmission is exp(-20).

Conclusion

The transparency in this experiment results from a combination of ac-Stark splitting of two dressed states and the destructive interference in absorption, in between these states. The interference in emission or in $\chi^{(3)}$ profile (obtained when state |2> is coupled to state |1> by two coherent photons) is constructive and allows for lasing without inversion and resonant nonlinear devices that generate into a transparency window [2]. This work is an essential step in the implementation of these devices. Although the transparency here has been shown in a lifetime broadened system, theoretical results predict that electromagnetically induced transparency is observable in collisionally broadened systems as well, provided that the dephasing rate of the |3>-|1> coherence exceed that of |2>-|1> coherence.

Acknowledgments

This work was jointly supported by the U.S. Air Force Office of Scientific Research, the U.S. Army Research Office, the U.S. Office of Naval Research, and the Strategic Defense Initiative Organization.

References

1. K.-J. Boller, A. Imamoglu, and S. E. Harris, "Observation of electromagnetically induced transparency," submitted for publication.
2. A. Imamoglu and S. E. Harris, "Lasers without inversion: interference of dressed lifetime-broadened states," Opt. Lett. 14, 1344-1346 (1989) ; S. E. Harris, J. E. Field, and A. Imamoglu, "Nonlinear optical processes using electromagnetically induced transparency," Phys. Rev. Lett. 64, 1107-1110 (1990).
3. G. H. Newsom, S. O'Connor, and R. C. M. Learner, "Re-examination of the spectrum of strontium: autoionization in the spectrum of neutral strontium," J. Phys. B: Atom. Molec. Phys. 6, 2162-2176 (1973).
4. M. G. Littman, "Single-mode pulsed tunable dye laser," Appl. Opt. 23, 4465-4468 (1984).

Pump–Probe Investigation of Picosecond Laser-Gas Target Interactions

C. G. Durfee III and H. M. Milchberg

Institute for Physical Science and Technology and Department of Electrical Engineering, University of Maryland, College Park, Maryland 20742

ABSTRACT

We report on a time-resolved investigation of the hydrodynamics of a laser-produced plasma. A 100 ps pulse is focused into a chamber filled with xenon for various pulse energies and pressures. This pulse (the pump pulse) forms a plasma, which is probed by a second pulse (the probe pulse) with a variable delay of up to 2.5 ns. The gradients in the plasma density profile produce a lensing effect on the probe pulse. The beam transmitted through the plasma is viewed with a CCD camera. The diffraction pattern of the probe pulse can be seen by subtracting the image of the first pulse beam from the image produced by the two-pulse beam.

EXPERIMENT

The laser system consists of a Nd:YAG mode-locked oscillator providing the seed pulses for a flashlamp-pumped regenerative amplifier which is followed by a two-pass power amplifier. A Pockels-cell pulse selector lets through a 100 ps seed pulse into the amplifier at 10 Hz. At the input of the regenerative amplifier, the seed beam is split into two paths. The ratio of the pulse energies in the two paths is adjustable. Using a motor-driven translation stage the path length of one of the inputs can be changed to provide a delay from -0.5 to 2.5 ns. The calibration of the zero point of the delay line was done using a streak camera. The delay line uses a corner cube to ensure the coupling into the regenerative amplifier is not changed as the stage moves.

The regenerative amplifier is a self-filtering unstable resonator[1] with a single intra-cavity Pockels-cell to switch the pulses in and out. The spatial filtering in this cavity design eliminates the need to use mode-matching on the input and gives a good output beam profile. The pulses are amplified to a few mJ, then are double-passed through a power amplifier. Streak camera measurements of frequency-doubled pulses were used to check the pulse duration. The amplified beam focused at f/50 onto a CCD camera gave a waist diameter of 126 microns.

The beam from the amplifier is focused by an f/10 lens in a chamber filled with a background pressure of xenon. A collection lens recollimates the beam which is viewed by a CCD camera. The images from the camera are digitized, averaged and stored in a computer. First the image resulting from a single reference pulse is collected, then it is subtracted from the

Proceedings on Short-Wavelength Coherent Radiation, Vol. 11, Philip H. Bucksbaum and Natale M. Ceglio (eds.)
© 1991 Optical Society of America

image produced when two pulses are sent through the chamber.

Due to the non-linearity of the plasma formation and evolution, it is important to be sure the energy of the reference pulse matches the first of the two pulses. Since the amplifiers are run to saturation, simply blocking the delay line input will leave more energy in the rods for the single pulse. A fast diode is used to measure the relative intensity of the two pulses. An energy meter is then used to match the energy of the reference pulse with that of the first pulse of the two-pulse train.

Measurements have been taken for gas pressures of Xe, Ar, and He in the range 3 to 10 Torr, with a 5:1 ratio of the pump pulse to the probe pulse energy. For a pump pulse of 8.4 mJ in Xe, although there is a spark at 3.3 Torr, there is little effect on either the pump or probe pulse. At 10 Torr in Xe, the plasma density disturbances are great enough to produce diffraction rings on the probe pulse. When the intensity of the pump pulse is increased to 39 mJ, these diffraction rings can be seen even at the lower density.

The plasma is clearly undergoing rapid change within the first hundreds of picoseconds. The diffraction rings move rapidly as the plasma expands. Two such images are shown below (see figs. 1 and 2) for a pressure of 6.6 Torr with the 39 mJ pump pulse. The first image is taken at a delay of 134 ps, the second is at a delay of 274 ps. If the plasma formed at the focus is hot enough, it will undergo a shock expansion, leaving a channel in the focal region.

Figure 1: Probe pulse pattern for a delay of 134 ps. The pressure of Xe is 6.6 torr and the energy of the pump pulse is 39 mJ.

Figure 2: Probe pulse pattern for a delay of 274 ps and the same experimental conditions as Fig. 1.

An estimate of the expansion time scale can be made by measuring the time taken for the diffraction pattern to reverse. This indicates that the plasma channel has expanded on the order of a half a wavelength. The pattern shown below has undergone a reversal in 140 ps, giving a disturbance "speed" of approximately 1.9×10^5 cm/s. The measured speed is very close to this at the 10 Torr pressure for the same pump pulse. For the lower energy pump pulse (8.9 mJ), although there is clearly diffraction of the probe beam, there is not a complete reversal of the pattern by the maximum delay time of 2.5 ns. This plasma disturbance likely has a much lower rate of change.

We have described the preliminary results of a time-resolved measurement of the influence of a rapidly evolving short-pulse heated plasma on a probe pulse. Current work includes using much shorter pulses to improve the temporal resolution and a gas jet to control the interaction length.

ACKNOWLEDGMENTS

This work is supported by the National Science Foundation (contract No. ECS-8858062), and the AFOSR (contract No. 88-0018). The authors thank Prof. Julius Goldhar for the use of the streak camera.

REFERENCES

1. P. G. Gobbi and G. C. Reali, Opt. Commun. **52**, 195 (1984).

Section IV: High-Intensity Laser–Matter Interactions

High-Density Targets

Transport in Ultra-Dense Plasmas Produced by a 1-ps Laser Pulse

M. Chaker, Y. Beaudoin, J. C. Kieffer, and H. Pépin

INRS-Energie, C.P. 1020, Vareness, Québec J3X 1S2, Canada

C. Y. Chien, S. Coe, and G. Mourou

Ultrafast Sciences Laboratory, University of Michigan, 2200 Bonisteel, Ann Arbor, Michigan 48109-2099

ABSTRACT

Recent experimental results obtained with the picosecond laser system of the Ultrafast Science Laboratory (University of Michigan) are reported. In particular, laser absorption, keV X-ray spectroscopy and transport studies are presented. The measurements have been performed at both 1.06 μm and 0.53 μm laser wavelengths for intensities ranging from 10^{14} Wcm^{-2} to $2x10^{15}$ Wcm^{-2}.

1. INTRODUCTION

The recent development of picosecond and subpicosecond laser technology has made possible the production of extremely bright laser sources. This progress enables the study of a new regime of plasma physics with high density, high temperature and short-lived plasmas produced by the interaction with solid-matter of the very short and intense laser pulses [1-4]. Short X-ray pulses in both sub-keV and keV range [2,5-8] can then be generated, opening to way to use these unique X-ray sources for time-resolved X-ray scattering studies or for table-top X-ray laser developments. In order to optimize such X-ray sources, it is crucial to study the laser light absorption and the energy penetration processes together with the X-ray emission characteristics. In this paper, we examine these different aspects. The emphasis is put on the comparison of the experimental results obtained at 1.06 μm and 0.53 μm laser wavelengths. We expect that, when the frequency is doubled, at 0.53 μm, the laser intensity contrast ratio C between the prepulse and the main pulse is better than at 1.06 μm ($C=7x10^{-4}:1$) by at least one order of magnitude.

The experiments were carried out at the Ultrafast Science Laboratory (University of Michigan) using the Table Top Terawatt laser. The laser (λ=1.06 μm) delivers up to 300 mJ in a 1 ps laser. The laser beam is focused by an f/7 lens. At the best focus, the focal spot diameter is found to be 100 μm as obtained from X-ray pinhole camera and from the first-order transmission grating results. The peak laser intensity achievable on target is estimated to be $3x10^{15}$ Wcm^{-2}. Finally, for the experiments at 0.53 μm, the laser beam is frequency doubled using a KDP crystal of 5 mm thickness which provides a 30% laser energy conversion.

Proceedings on Short-Wavelength Coherent Radiation, 266
Vol. 11, Philip H. Bucksbaum and Natale M. Ceglio (eds.)
© 1991 Optical Society of America

2. ABSORPTION MEASUREMENTS

Recently, there have been several measurements of reflectivity and absorption obtained with very short laser pulses [1-4, 8-10]. We have previously shown that the variation of absorption with incidence angle and polarization could be used to infer submicron plasma density scale lengths L/λ [10] (where L is the density scale length and λ the laser wavelength). In this paper, the same analysis is used to study and to compare the absorption with Al at 1.06 μm and 0.53 μm.

The absorption measurements have been performed using an integrating Ulbricht sphere [3]. The variations of the measured absorption with laser intensity I at normal incidence show that the absorption rapidly increases as the laser intensity varies between 10^{11} Wcm^{-2} and $5x10^{12}$ Wcm^{-2} and then remains fairly constant (30% at λ=1.06 μm and 50% at λ=0.53 μm) for $5x10^{12}$ $Wcm^{-2} < I < 5x10^{14}$ Wcm^{-2}. At the highest intensities ($I > 5x10^{14}$ Wcm^{-2}), the absorption decreases but remains relatively high (20%). Figure 1 shows the variation of the measured absorption at λ=1.06 μm and λ=0.53 μm as a function of the incidence angle θ for s- and p-polarizations, the laser intensity being constant ($I \approx 10^{14}$ Wcm^{-2}). As expected, the absorption decreases as the incidence angle increases for s-polarized light at both laser wavelengths. On the opposite, for p-polarized light, a maximum absorption is observed at $\theta_m = 45°$ for λ=1.06 μm and at $\theta_m \geq 60°$ for λ=0.53 μm (note that the value of θ_m depends on the plasma density gradient). Applying the model described in Ref. [10] to our experimental data, we find that, at the same laser intensity ($I=10^{14}$ Wcm^{-2}), the density gradient is steeper for λ=0.53 μm (L/λ=0.05) than for λ=1.06 μm (L/λ=0.13). This could result from the better laser intensity contrast expected at λ=0.53 μm.

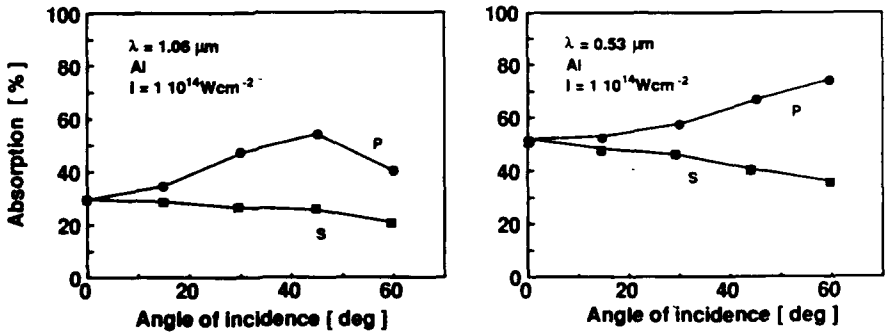

Fig. 1. Variation of the absorption with aluminium as a function of the incidence angle at $I=10^{14}$ Wcm^{-2} for s- and p-polarized light and for 1.06 μm and 0.53 μm laser wavelengths.

3. KEV X-RAY SPECTROSCOPY

High resolution keV X-ray spectroscopy is very useful to analyze the density of the most emitting region of the plasma during the interaction. For this purpose, we have performed at both λ=1.06 μm and λ=0.53 μm experimental measurements of the dielectronic satellites of the $1s^2$-1s2p resonance lines of the He-like aluminium. The X-ray emission from the plasma in the range (7.6-8 Å) was monitored by two crystal spectrometers. The

first one is a Johann-type RAP (2d=26.12A) crystal spectrometer which provides a high resolving power ($\lambda/\Delta\lambda \approx 5000$). In this case, each spectrum is recorded on SB392 Kodak film under 100 and 200 laser shots at λ=1.06 µm and λ=0.53 µm, respectively. We have also used a high efficiency Von Hamos crystal spectrograph. Its design allows a larger detection sensitivity since X-ray are focused by means of a 30x50 mm X-ray diffracting PET crystal (2d=8.735 Å) bent to a 100-mm radius of curvature. In these conditions, the X-ray spectrum can be recorded in only one laser shot at λ=1.06 µm using SB392 as a film.

Figure 2 presents the Lyman He-like line $1s^2$-1s2p accompanied by its Li-like satellites. We can identify the intercombination line and the various dielectronic satellites q, r, a-d and j,k,l, labelled according to Gabriel [11]. The analysis of the two spectra (λ=1.06 µm and λ=0.53 µm) shows a decrease of the intercombination lines together with an enhancement of the a-d satellite group at λ=0.53 µm as compared to 1.06 µm. This result indicates that the electron density is much higher at λ=0.53 µm than at 1.06 µm. The density can be inferred from both the ratio of the intercombination line to the resonance line [12] and from the intensity ratios of the a-d+q,r to j,k,l satellite lines [13]. Using these tabulations, we find that the electron density is close to 10^{21} cm^{-3} at λ=1.06 µm and $8x10^{22}$ cm^{-3} at λ=0.53 µm.

These values of the density associated with the maximum of emission are only approximate since a transient plasma such as the one we consider necessitates a time-dependent modelling. Nevertheless, it seems reasonable to assume that the maximum emission takes place very close to the critical density ($n=n_c$) at λ=1.06 µm and at much higher electron density ($n \approx 20\ n_c$) at λ=0.53 µm. These results indicate that a significant energy transport to densities close to that of solid occurs for the 0.53 µm laser pulse.

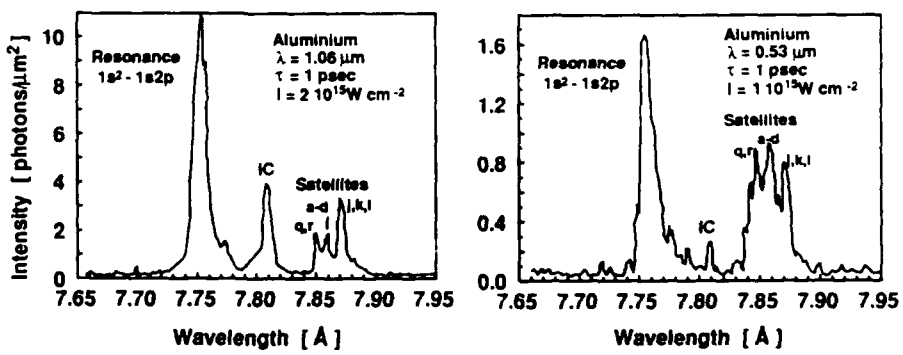

Fig. 2. Lyman α He-like line $1s^2$-1s2p of aluminium with Li-like satellites at $I=2x10^{15}$ Wcm^{-2} for λ=1.06 µm and at $I=1x10^{15}$ Wcm^{-2} for λ=0.53 µm.

4. ENERGY PENETRATION DEPTH MEASUREMENTS

A complete analysis of the laser plasma interaction in this short pulse regime requires at least to understand the electron heat transport under these new conditions where the hydrodynamic expansion is small or negligible. For this purpose, targets composed of very flat silicon wafers coated with aluminium layers of different thicknesses (100, 300, 500, 1000, 3000 and 5000 Å) have been irradiated by the 1 ps laser pulse at both 1.06

μm and 0.53 μm laser wavelengths. The emission of the Si XIII resonance line at 6.65 Å and of the aluminium He β line at 6.635 Å were monitored as a function of the aluminium thickness using the Von Hamos spectrograph. Typical spectra were obtained by the accumulation of 1 to 6 laser shots.

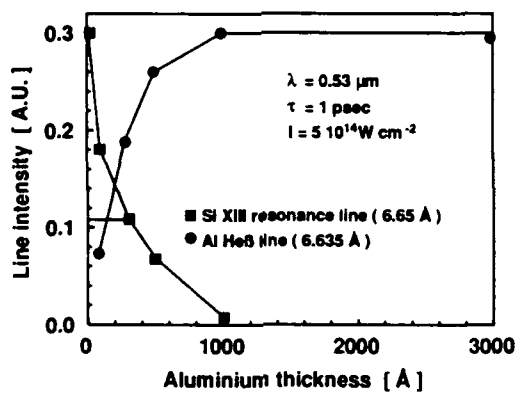

Fig. 3. Variation of the SiXIII resonance line at 6.65 Å and of the aluminium Heß line at 6.635 Å as a function of the aluminium thickness for $I=5\times10^{14}$ Wcm^{-2} and $\lambda=0.53$ μm.

As the aluminium thickness increases, we observe a decrease of the silicon line intensity accompanied by an enhancement of the Al line intensity as shown in Fig. 3. For Al thicknesses larger than a given value which depends on the laser parameters, the Al line intensity saturates and the Si line disappears. This value is close to 1200 Å for $\lambda=0.53$ μm and $I=5\times10^{14}$ Wcm^{-2}. We define the energy penetration depth Δ as the aluminium thickness for which the Si line intensity has decreased by a factor of e. We find that for $\lambda=1.06$ μm, Δ is close to 700 Å at $I=1.8\times10^{15}$ Wcm^{-2} and 300 Å at $I=4\times10^{14}$ Wcm^{-2}. Shorter energy penetration depths are obtained at $\lambda=0.53$ μm, namely $\Delta=300$ Å at $I=5\times10^{14}$ Wcm^{-2} and $\Delta\approx200$ Å at $I=1.5\times10^{14}$ Wcm^{-2}. Preliminary analysis of these data show that energy penetration depths are consistent with a simple model based on the assumption of a classical thermal conduction in a solid dense plasma. Further details will be reported elsewhere.

5. CONCLUSION

Laser absorption, keV X-ray spectroscopy and energy penetration depths results obtained with a 1 ps pulse incident on solid targets with an intensity between 10^{14} Wcm^{-2} to 2×10^{15} Wcm^{-2} have been presented. The measurements have been performed at both $\lambda=1.06$ μm and 0.53 μm laser wavelengths. Regarding both the absorption and the keV X-ray spectroscopy, we find that the interaction at $\lambda=0.53$ μm, as compared to the results obtained at $\lambda=1.06$ μm, is characterized by a steeper density gradient ($L/\lambda=0.05$) and by a maximum X-ray emission which takes place well above the critical density ($n\approx20\ n_c$). This can be due to the better laser intensity contrast of the 0.53 μm pulse. Finally, it is found that, at both laser wavelengths, the energy penetration depths are consistent with a simple model based on the assumption of a classical thermal conduction.

REFERENCES

1. H.M. Milchberg, R.R. Freeman, S.C. Davey and R.M. More,"Resistivity of a simple metal from room temperature to 10^6 K", Phys. Rev. Lett. 61, 2364-2367 (1988).
2. M. Murname, H.C. Kapteyn and R.W. Falcone,"High-density plasmas produced by ultrafast laser pulses", Phys. Rev. Lett. 62, 155-158 (1989).
3. J.C. Kieffer, P. Audebert, M. Chaker, J.P. Matte, H. Pépin, T.W. Johnston, P. Maine, D. Meyerhofer, J. Delettrez, D. Strickland, P. Bado and G. Mourou,"Short pulse laser absorption in very steep plasma density gradients", Phys. Rev. Lett. 62, 760-763 (1989).
4. O.L. Landen, D.G. Stearns and E.M. Campbell,"Measurement of the expansion of picosecond laser-produced plasmas using resonance absorption profile spectroscopy", Phys. Rev. Lett. 63, 1475-1478 (1989).
5. D. Kühke, U. Herpers and D. Von der Linde,"Soft X-ray emission from sub-picosecond laser-produced plasmas", Appl. Phys. Lett. 50, 1785-1787 (1985).
6. H.W.K. Tom and O.R. Wood II,"Study of soft X-ray generation by laser heating solid and gaseous tantalum plasmas with subpicosecond pulses", Appl. Phys. Lett. 54, 517-519 (1988).
7. J.A. Cobble, G.A. Kyrala, A.A. Hauer, A.J. Taylor, C.C. Gomez, N.D. Delamatar and G.T. Shappert,"Kilovolt X-ray spectroscopy of a subpicosecond-laser excited source", Phys. Rev. A 39, 454-457 (1989).
8. M. Chaker, J.C. Kieffer, J.P. Matte, H. Pépin, P. Audebert, P. Maine, D. Strickland, P. Bado and G. Mourou,"Interaction of 1 psec laser pulse with matter", Phys. Fluids B 3, 167-175 (1991).
9. R. Fedoseyevs, R. Ottman, R. Sigel, G. Kühnle, S. Szatmari and F.P. Shäfer,"Absorption of femtosecond laser pulses in high density plasma", Phys. Rev. Lett. 64, 1250-1253 (1990).
10. J.C. Kieffer, J.P. Matte, S. Bélair, M. Chaker, P. Audebert, H. Pépin, P. Maine, D. Strickland, P. Bado and G. Mourou,"Absorption of an ultrashort laser pulse in very steep plasma density gradients", IEEE J. Quantum Electron. 25, 2640-2647 (1989).
11. A.H. Gabriel, "Dielectronic satellite spectra for highly charged helium-like ion lines", Mon. Not. R. Astron. Soc. 160, 99-119 (1972).
12. J.P. Apruze, D. Huston and J. Davies,"K-shell aluminium resonance line ratios for plasmas diagnosis using spot spectroscopy", J. Quant. Spectrosc. Radiat. Transfer 26, 339-344 (1986).
13. V.L. Jacobs and M. Blaka,"Effects of angular-momentum-changing collisions on dielectronic satellite spectra", Phys. Rev. A 21, 525-546 (1980).

Propagation Effects for a Femtosecond Laser Pulse

S. C. Rae and K. Burnett

Clarendon Laboratory, Department of Physics, University of Oxford, Parks Road, Oxford OX1 3PU, UK

Abstract

A model has been developed for the propagation of a femtosecond laser pulse through an ionizing medium, which predicts the spectral shift and broadening in the transmitted pulse, and the electron energy distribution within the plasma. For gaseous targets at laser intensities of 10^{15}–10^{16} W/cm^2, the calculated blue-shifts do not agree with predictions from a homogeneous Drude model. The importance of the electron energy distribution for cold-plasma production in solid-target experiments is discussed.

Introduction

The propagation of an ultrashort laser pulse through a gaseous, liquid or solid medium has been the subject of extensive study. At relatively low intensities, nonlinearities in the neutral medium can lead to spectral broadening of the laser pulse; above the threshold for self-focusing, a near-universal 'super-broadening' is observed.[1] These mechanisms do not require ionization of the medium, but at higher intensities, direct field-induced ionization (MPI, tunneling or over-the-barrier) plays an important role. Rapid plasma production causes a spectral blue-shift and broadening of the incident laser pulse.[2] Field-induced ionization also results in a much colder plasma than would be expected if collisions were dominant, and such highly-stripped, cold plasmas are of potential interest for recombination x-ray lasers.[3]

We have developed a model to describe the propagation of a femtosecond laser pulse through a slab of ionizing material, concentrating particularly on the spectrum of the transmitted pulse, and the electron energy distribution within the plasma. By solving Maxwell's equations coupled with a tunneling ionization expression and a dynamical evolution of the electron population, we obtain the complete time and space dependence of the electron distribution function for the plasma. By

Proceedings on Short-Wavelength Coherent Radiation, 271
Vol. 11, Philip H. Bucksbaum and Natale M. Ceglio (eds.)
© 1991 Optical Society of America

performing a Fourier transform on the reflected and transmitted pulses we also obtain their spectral shifts and broadening.

In the following sections we first outline our model, and go on to present simulation results for the spectral shifts obtained with gaseous targets. We compare our results with those from a commonly-used Drude model. We conclude with a discussion of the solid-target case, with reference to possible x-ray laser schemes.

Outline of the Propagation Model

We assume a plane wave laser pulse propagating through an initially neutral slab, consisting of a single atomic element (typically a rare gas). For linearly-polarised light propagating in the x-direction, the wave equation in 1-D is

$$\frac{\partial^2 E_z}{\partial x^2} - \frac{1}{c^2}\frac{\partial^2 E_z}{\partial t^2} - \mu_0 \frac{\partial J_z}{\partial t} = 0 \ . \tag{1}$$

where J_z is the total plasma current. Rather than using the refractive index, the plasma current is calculated directly from the electron distribution function,

$$J_z(x,t) = -e \int f(x,v,t)\ v\ dv + J_i(x,t) \ . \tag{2}$$

In order to conserve energy, an ionization current, J_i, is introduced, which produces a dissipation equal to the rate of ionization energy loss. Ionization is calculated from a tunneling expression,[4]

$$W = \frac{\omega_0}{2} C^2_{n^*l} \frac{\mathcal{E}_i}{\mathcal{E}_h} \frac{(2l+1)(l+|m|)!}{2^{|m|}(|m|)!(l-|m|)!} \times \left[2\left(\frac{\mathcal{E}_i}{\mathcal{E}_h}\right)^{3/2}\frac{E_0}{E}\right]^{2n^*-|m|-1} \exp\left[-\frac{2}{3}\left(\frac{\mathcal{E}_i}{\mathcal{E}_h}\right)^{3/2}\frac{E_0}{E}\right] \ . \tag{3}$$

Here, ω_0 is the atomic unit of frequency, E is the electric field, E_0 is the atomic unit, $\mathcal{E}_h$ is the ionization potential of hydrogen, $\mathcal{E}_i$ is that of the given atom or ion, l and m are the initial state quantum numbers, n^* is the effective principle quantum number, and C_{n^*l} is a constant of order unity.[5]

This is not cycle-averaged: ionization is calculated using the instantaneous electric field. Most ionization will occur near the laser cycle peaks, where the quiver velocity of the bulk free electrons is instantaneously zero. For electrons freed at this point in the cycle, the phase shift and hence the energy absorption is also zero. A small fraction of the ionized electrons, however, will appear slightly displaced from the zero-phase-shift point, and these electrons acquire a dephasing energy, which remains as kinetic energy after the pulse has passed. In the limit where the quiver energy is much greater than the ionization potential, this is the classical equivalent of ATI energy.[3]

Spectral Shifts from Gaseous Targets

Experiments[2] with a 100 fs, 620 nm pulse at 10^{16} W/cm^2 have, by focusing the pulse into a cell containing near-atmospheric-density rare gas, demonstrated blue-shifts of order 10 nm. Here we present simulation results based on a wavelength of 250 nm, which corresponds to the output from KrF-amplified systems. Computer time limitations restrict the pulse lengths to less than 100 fs and plasma dimensions to less than 100 laser wavelengths. For these short plasma lengths we observe virtually no blue-shift at atmospheric density, so we have used a higher pressure to allow comparisons to be made. Figure 1 shows the transmitted pulse spectra for a 20 cycle pulse and 20 λ_0, 40 atm argon plasma, for a range of peak intensities. A number of points should be noted: the blue-shift is a maximum for an intensity of 5×10^{15} W/cm^2; there is almost no discernable blue-shift for intensities above 10^{17} W/cm^2; there is more than one shifted peak in several cases; and there are indications of small red-shifted features at the lowest intensities.

The blue-shift disappears at the highest intensities due to extremely rapid ionization on the leading edge of the pulse; a slower change in electron density creates a larger mean shift, hence the greater structure observed at more moderate intensity. The multiple smaller peaks seen roughly correspond to the appearance of successive ionization stages, but this is considerably distorted by the propagation (for instance, it cannot explain the small red-shifted peak at 10^{15} W/cm^2).

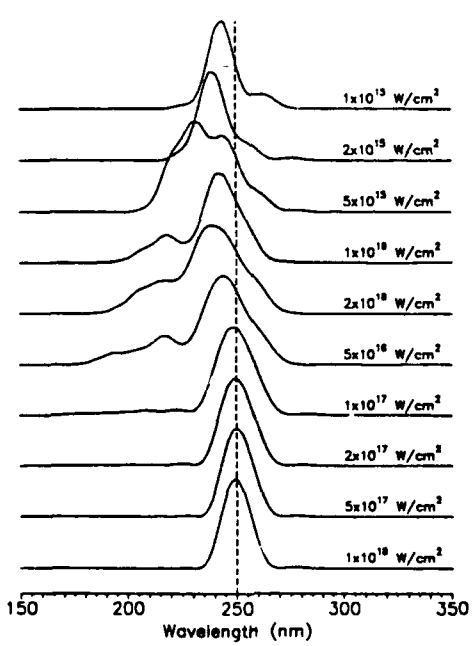

Figure 1: Transmitted pulse spectra for a 20 cycle sine-envelope pulse and a 20 λ_0, 40 atm. argon plasma.

Experiments have shown that the blue-shift in argon is greater than that in neon; this can be explained by the higher ionization potentials in neon, compared with the corresponding levels in argon. At present there is no collisional ionization in our model; we estimate its effect to be small compared to the field-induced process. We shall, however, be giving a more careful analysis of their contribution in future work.

Comparison with Drude Model

A Drude model has been commonly used to analyse blue-shifts in gases. This assumes that the entire plasma can be described by a single value of the refractive index, which (neglecting collisions) is given by

$$n^2 = 1 - \frac{\omega_p^2}{\omega_0^2} = 1 - \frac{e^2 N_e}{\epsilon_0 m_e \omega_0^2} \,. \tag{4}$$

For an incident wavelength λ_0, and an interaction length z, the shift is given by

$$\Delta\lambda = -\frac{\lambda_0 z}{c}\frac{dn}{dt} = -\frac{e^2 z \lambda_0^3}{8\pi^2 \epsilon_0 m_e c^3}\frac{dN_e}{dt} \,. \tag{5}$$

The time-dependent electron density can be obtained by solving a set of coupled rate equations, using the cycle-averaged form of the tunneling ionization expression Eq. (3). Knowing the incident pulse spectrum, and dN_e/dt as a function of time, the transmitted pulse spectrum is easily obtained.

As a comparison of the two methods, we have calculated the transmitted spectrum for a 10^{16} W/cm^2, 20 cycle pulse in a 20 λ_0, 40 atm argon plasma. Figure 2 shows dN_e/dt (normalized to the neutral density), as determined from the coupled rate equations; a final degree of ionization of 4.6 is reached. Figure 3 shows the transmitted pulse spectrum, compared to both the incident spectrum and the spectrum determined from the propagation model. Neither the shifts nor the relative peak heights agree for the two models. In the Drude model, the two peaks clearly correspond with the two stationary regions in Fig. 2, but in the propagation model, such a simple correspondence cannot be made. In neglecting propagation effects, the Drude model fails to address a key aspect of the problem: the spatial-variation within the plasma.

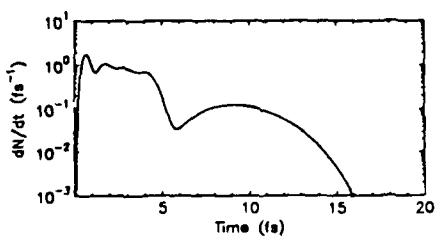

Figure 2: Rate of change of electron density for Drude model (see text for parameters).

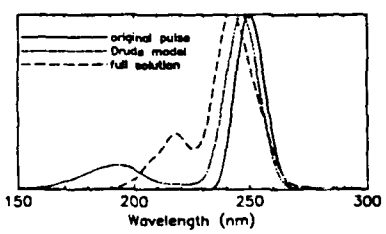

Figure 3: Comparison of incident pulse spectra with propagation model and Drude model results.

Relevance to High-Density Targets

It is possible to perform simulations with our propagation model at near-solid-density, where only a small fraction of the incident pulse is transmitted, and the total energy is split between reflection, ionization and ATI absorption. Typically, we observe the formation of a narrow layer (on the order of a few λ_0) with a very high degree of ionization, and following this, a large fraction of the remainder of the pulse is reflected. During the pulse risetime, there is a certain amount of out-of-phase ionization, and once the pulse has passed the remaining ATI energy in the plasma corresponds to a kinetic temperature of 1–10 eV.

In order to assess the viability of an MPI-initiated plasma as a x-ray recombination laser, several other effects would need to be considered. Primary amongst these is electron-ion collisions, which will lead to additional heating, transferring some of the coherent quiver energy of the electrons into out-of-phase kinetic energy. There are also questions relating to plasma motion and instabilities, and 2-D effects such as self-focusing. Much remains to be done before accurate predictions can be made.

References

1. P. B. Corkum and C. Rolland, "Femtosecond continua produced in gases," IEEE J. Quantum Electron. 25, 2634–2639 (1989).
2. W. M. Wood and M. C. Downer, "Spectral blueshifts of femtosecond pulses in atmospheric density Kr and Xe plasmas," in this volume (and ref's therein).
3. N. H. Burnett and P. B. Corkum, "Cold-plasma production for recombination extreme-ultraviolet lasers by optical-field-induced ionization," J. Opt. Soc. Am. B 6, 1195–1199 (1989).
4. A. M. Perelomov, V. S. Popov, and M. V. Terent'ev, "Ionization of atoms in an alternating electric field," Sov. Phys. JETP 23, 924–934 (1966).
5. M. V. Ammosov, N. B. Delone, and V. P. Kraĭnov, "Tunnel ionization of complex atoms and of atomic ions in an alternating electric field," Sov. Phys. JETP 64, 1191–1194 (1987).

Density Profile Steepening by the Ponderomotive Force of an Intense Picosecond Laser

D. Umstadter, X. Liu, J. S. Coe, and C. Y. Chien

Ultrafast Science Laboratory, University of Michigan, Ann Arbor, Michigan 48109-2099

1 Abstract

We report theoretical and experimental results indicating that the ponderomotive force of a high-intensity laser significantly modifies the thermal expansion of a laser-plasma in the regime where the density scale length is much less than the laser wavelength. Our theoretical calculations predict that the effect should become important when the average electron quiver energy ($mv_{os}^2/2$) becomes comparable to the electron thermal energy (kT_e). Doppler measurements of 0.53 μm light reflected from a solid target of aluminum agree with this prediction. After a time equal to a laser pulsewidth (1 ps), at an incident laser intensity of 2×10^{15} W/cm^2, and a peak electron temperature of 200 eV, the critical surface expands at only approximately 30% of the velocity it would if it were driven by free expansion due to thermal pressure alone. Agreement is found with a hydrodynamic numerical code using similar input parameters.

2 Introduction

The high-density plasmas produced by the interaction of short-pulse lasers with solid targets have been proposed as candidate coherent x-ray sources [1]. Large absorption of laser light and rapid cooling of the plasma—both of which are required for this scheme to work—depend strongly on the evolution of the electron-density profile during the laser pulse. We report experimental and theoretical results indicating that when the quiver energy of the electrons approaches their thermal energy, the ponderomotive pressure of the laser significantly modifies the density profile.

When a laser pulse interacts with a plasma, the pump laser light is absorbed and reflected near x_c, the critical surface—the point of the profile where the electron density, n_e, equals the critical density, n_c, *i.e.*, $n_c/n_e \equiv (\omega_0/\omega_p)^2 = 1$, where ω_0 is the incident laser frequency and ω_p is the plasma frequency. For densities greater than n_c, the light wave is evanescent and is attenuated exponentially in a skin depth. This has two consequences: one, local heating and ionization creates a sharp electron pressure gradient, driving expansion of the plasma into the vacuum; and two, the sharp laser intensity gradient creates a ponderomotive force oppositely directed to the expansion, steepening the profile.

Since x_c is moving relative to the laboratory frame, the reflected pump light is Doppler-shifted by an amount proportional to the velocity of expansion $v_{\rm exp}$, equal to $\Delta\lambda/\lambda = 2(v_{\rm exp}/c)\cos\theta$, where θ is the angle of incidence of the laser. This Doppler shift may thus

Proceedings on Short-Wavelength Coherent Radiation, Vol. 11, Philip H. Bucksbaum and Natale M. Ceglio (eds.)
© 1991 Optical Society of America

be used to determine the motion of the plasma. A simple model, assuming the motion is governed only by thermal pressure, has previously been used to determine the plasma temperature from measurements of the Doppler shift [2]. However, at high laser intensities the motion of the plasma is more accurately determined by a balance between both the thermal pressure of the plasma and the ponderomotive pressure of the laser [3] [4]. Our study of ponderomotive steepening is the first in the regime in which the density scale length (d) is much less than the laser wavelength (λ). The effect was first observed in a regime in which $\lambda \leq d$, in long pulse CO_2 laser experiments [5].

3 Theory

The laser-plasma interaction is described by the one-dimensional two-fluid conservation equations of mass density, momentum and energy. These equations are coupled to a collisional radiative model for the ionization stages, a modified Spitzer-Harm model for heat conductivity, and the Helmholtz wave equation for the electric field [6]. This model will be discussed in greater detail in a future publication. The momentum equation describing the motion of the ions to first order is given by [3]

$$\rho\frac{\partial \mathbf{v}}{\partial t} + \rho(\mathbf{v}\cdot\nabla)\mathbf{v} \quad = \quad -\nabla P_e - n_e\nabla p_l \tag{1}$$

The ion mass density is $\rho = n_i M$, and the ion flow velocity is v. Assuming an isothermal equation of state, then the thermal pressure is the kinetic energy density, $P_e = n_e kT_e$, where kT_e is the electron temperature. The laser pressure on a single electron is the time-averaged quiver energy density, $p_l = (1/2)m\langle v_{os}^2\rangle$, which, by using $v_{os} \simeq eE/mc\omega_0$, may be written as $p_l = (1/16\pi)(1/n_c)E^2$, where E is the electric field of the laser in the plasma.

Equation 1 may be solved analytically for the free isothermal expansion of the plasma into the vacuum—neglecting for the moment the last term, the ponderomotive force—yielding a density profile given by $n_e = n_0 e^{-x/d}$, where $d = v_s t$, and $v_s = (ZkT_e/M)^{1/2}$ is the acoustic velocity [3].

The electric field E at normal incidence can only be determined by solving the Helmholtz equation [3],

$$\frac{\partial^2 E}{\partial x^2} + (\frac{\omega}{c}n)^2 E = 0, \tag{2}$$

where n is the complex index of refraction of the plasma, since the WKB approximation is invalid whenever the density scale length is less than the laser wavelength. Fig. 1 shows the normalized amplitude of the electric field E and the ponderomotive force ∇E^2 on a single particle for an exponential density profile, with $d = 400$ Å, corresponding to the peak of the pulse, $ZkT_e \sim 2000$ eV, and n_0 equal to a few times solid density. It can be seen that, like the density, the ponderomotive force on a single particle ∇E^2 near x_c also has an exponential dependence on distance, $\nabla E^2(x) \propto e^{-x/l}$.

Figure 1 shows that $l/d \sim 1$, *i.e.*, the scale length of $p_l \propto E^2$ is approximately equal to the scale length of $P_e \propto n_e$. The peak value of E^2 near x_c is swelled in the plasma by a factor of about 3.6 over the incident electromagnetic field $E_{\rm inc}^2$. Thus, the ponderomotive force $n_e\nabla p_l$ equals the thermal force ∇P_e at x_c if the quiver energy of the electrons equals their thermal energy, or, since $I_{\rm inc} = (c/8\pi)E_{\rm inc}^2$,

$$\frac{m\langle v_{os}^2\rangle}{2kT_e} \equiv 3.2\times 10^{-13}\frac{I_{\rm inc}\lambda_0^2}{T_e} \sim 1, \tag{3}$$

($I_{\rm inc}$ is in W/cm^2, λ_0 is in μm, and T is in eV).

In order to model the dynamics of the density profile self-consistently, the full set of equations described in the first paragraph of Sec. 3 must be solved with the ponderomotive

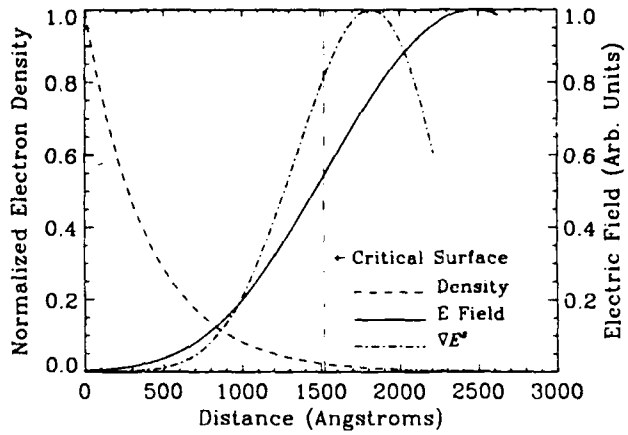

Figure 1: Solution of the Helmholtz wave equation, Eq. 3 for an exponential density profile.

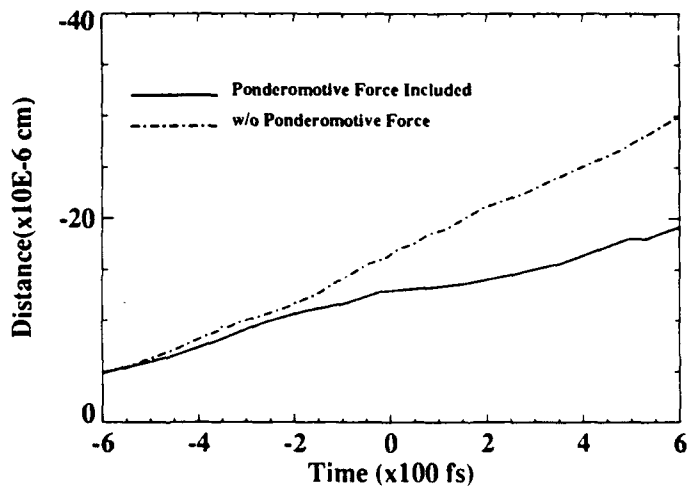

Figure 2: Numerical solution of the dynamics of the critical surface with and without including the ponderomotive force of the laser, the last term in Eq. 1. Notice that the expansion velocity (30 % of the free-expansion velocity) is minimum at $t = 0$, corresponding to the peak of the laser pulse, when the ponderomotive force is maximum.

force included in the momentum equation, Eq. 1. As shown in Fig. 2, the results of such a simulation predict that, with the ponderomotive force included in Eq. 1 the critical surface expands at a velocity that at the peak of the pulse ($t = 0$) is only 30% or what it is without the ponderomotive force included in Eq. 1 (for a Gaussian laser pulse with 1-ps FWHM centered at $t = 0$, $I = 1 \times 10^{15}$ W/cm^2, and $\lambda = 0.53$ μm). The original vacuum plasma interface is at $x = 0$ with the vacuum in the negative x direction. Note that as expected Eqn. 3 is satisfied for these parameters using the maximum value of T_e predicted by the simulation, $T_e \sim 200$ eV.

4 Experiment

We recently performed an experiment that may be explained by the effects discussed in Sec 3. Frequency-doubled 1-ps pulses with $I \simeq 5 \times 10^{14} - 2 \times 10^{15}$ W/cm^2 ($\lambda = 0.53$ μm) were focused at normal incidence ($\theta = 0°$) onto a solid target of aluminum. By frequency doubling the light, the intensity contrast ratio was increased to $\simeq 10^5$ from a value of 10^3 for the fundamental, which was measured using a third-order autocorrelator. The absence of intercombination lines in the X-ray spectrum confirmed that no long-scale-length plasma was created by a prepulse [7].

The back-reflected light was sampled with a beam splitter that was placed before the target in the path of the laser. The light was frequency analyzed with a multichannel analyzer, which had a dispersion of ~0.5 Å/pixel. A Doppler shift to the blue and a broadening—characteristics of an expanding plasma—were observed and are shown in Fig. 3 for $I_{\rm inc} \sim 2 \times 10^{15}$ W/cm^2.

If we assume either isothermal, or adiabatic free expansion, as is done in [2], an estimate of $ZkT_e < 150$ eV is obtained from $\Delta\lambda/\lambda$. In the isothermal case, the expansion velocity of n_c is given by $v_{\rm exp} = v_s \ln(n_0/n_c)$. In the adiabatic case, $v_{\rm exp} = [2/(\gamma - 1)]v_s$, where γ, the ratio of the specific heats, is chosen to be 1.7 [2]. In either case, however, this result for ZkT_e is inconsistent with the full simulation results, which indicate that ZkT_e was in excess of 2000 eV. The expansion was apparently slowed by the ponderomotive force of the laser as we would expect from Eqn. 3, assuming $T_e \sim 200$ eV. The measured expansion was 30% of what it would have been assuming free expansion and $ZkT_e \sim 2000$ eV, and was thus consistent with the simulation results discussed in Sec. 3.

As the laser intensity was decreased to $I \simeq 5 \times 10^{14}$ W/cm^2, the Doppler shift did not change significantly. As is seen in the simulation, the decreased ponderomotive pressure was balanced by the decreased thermal pressure that is expected from decreased absorbed laser energy.

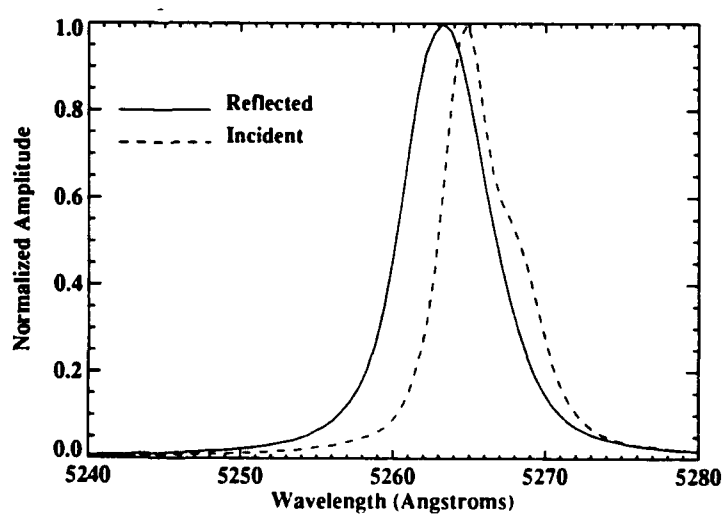

Figure 3: Blue shift of the pump light reflected from a moving critical surface. The motion driven by thermal pressure is reduced by the laser light pressure.

Clearly, if Eq. 3 is satisfied, the effects of ponderomotive steepening on the density evolution must be considered, whether when determining the electron temperature from Doppler shift data, or, perhaps more importantly, whenever studying processes that depend strongly on the density scale length, such as resonance absorption of high intenstiy laser light.

5 Acknowledgments

This work was partially funded by the National Science Foundation Center for Ultrafast Optical Science, contract #PHY8920108. We would like to thank Norm Schryer for help with the computer algorithm used in the numerical sumulations.

References

[1] R.W. Falcone and M.M. Murnane, in *Short Wavelength Coherent Radiation: Generation and Application*, D.T. Attwood and J. Bokor, Eds. (AIP , New York, 1986), 81.

[2] H.M. Milchberg, R.R. Freeman, and S.C. Davey, *Phys. Rev. Lett.* **61**, 2364 (1988).

[3] W.L. Kruer, *The Physics of Laser Plasma Interactions* (Addison-Wesley, New York, 1988), 116.

[4] The resonant excitation of electrostatic plasma waves at x_r will also result in a ponderomotive force (*ibid.*).

[5] R.L. Fedosejevs, *et al.*, *Phys. Rev. Lett.* **39**, 932 (1977).

[6] D. Umstadter, *et al.*, *Digest of Topical Meeting on High Energy Density Physics with Subpicosecond Laser Pulses, 1989* (OSA, Washington, D.C., 1989).

[7] M. Chaker, *et al.*, "Transport in Ultra-Dense Plasmas Produced by 1 ps Laser Pulses", to be published in *Proceedings of Short-Wavelength Coherent Radiation: Generation and Application*, P. Bucksbaum and N. Ceglio, Eds., Optical Society of America (1991).

Efficient Coupling of High-Intensity Subpicosecond Laser Pulses into Dilute Solid Targets

M. Murnane,* H. Kapteyn,* S. Gordon,† S. Verghese,† J. Bokor,‡ W. Mansfield,‡ R. Gnall,‡ E. Glytsis,¶ T. Gaylord,¶ and R. Falcone†

*Department of Physics, Washington State University, Pullman, Washington 99164-2814

†Department of Physics, University of California at Berkeley, Berkeley, California 94720

‡AT&T Bell Laboratories, Holmdel, New Jersey 07733

¶School of Electrical Engineering, Georgia Institute of Technology, Atlanta, Georgia 30332

Abstract

We have demonstrated that high-intensity sub-picosecond laser pulses can be efficiently absorbed by a dilute solid material. We have measured laser reflectivities as low as 10% from certain targets, in contrast to the 90% reflectivity observed from flat solid surfaces. The hot plasmas generated on dilute solids exhibit greatly increased x-ray emission due to the enhanced laser absorption. Laser-to-x-ray conversion efficiency greater than 1% have been observed for x-ray energies above 1keV.

Introduction

Sub-picosecond laser-produced plasmas have been demonstrated[1, 2] to be good sources of ultrashort x-ray pulses in the soft x-ray region. However, the measured laser-to-x-ray energy conversion efficiency has remained low (≈ 0.3%), due to relatively low plasma temperatures (≈ 400 eV) and inefficient laser solid coupling (< 10%). When a flat solid is illuminated with a high-intensity sub-picosecond laser pulse, the solid rapidly evolves into a highly reflective hot metal. There is negligible expansion of the hot material during a 100 fs excitation pulse - the expansion scale length is only ≈ 0.01 λ. Therefore, typically only 10% of the laser energy is absorbed in an optical skin depth of the hot solid.

Figure 1 shows the measured reflectivity of a flat silicon wafer, when the wafer is irradiated with 150 fs laser pulses,[3] extending from low fluences (below damage threshold) up to incident intensities exceeding 10^{16} W cm^{-2}. At the highest fluences, corresponding to the production of a 400 eV plasma on the silicon surface, the average reflectivity measured was 86%. The peak reflectivity at the center of the focal spot and peak of the laser pulse was therefore ≥ 90%.

The high reflectivity observed can be explained by using a Drude model to calculate the refractive index of the hot solid-density plasma.[2] For silicon at 400 eV, $N = n + ik \approx$

© 1991 Optical Society of America

4 + i 10, where n is the real part and k the imaginary part of the complex refractive index N. The reflectivity R is given by -

$$R = \frac{(n-1)^2 + k^2}{(n+1)^2 + k^2}$$

Therefore, for the high values of n and k characteristic of a hot, dense plasma, the reflectivity is predicted to be large. These predictions are not changed by the presence of a layer of low density material (<< λ) in front of the target, due to plasma expansion.

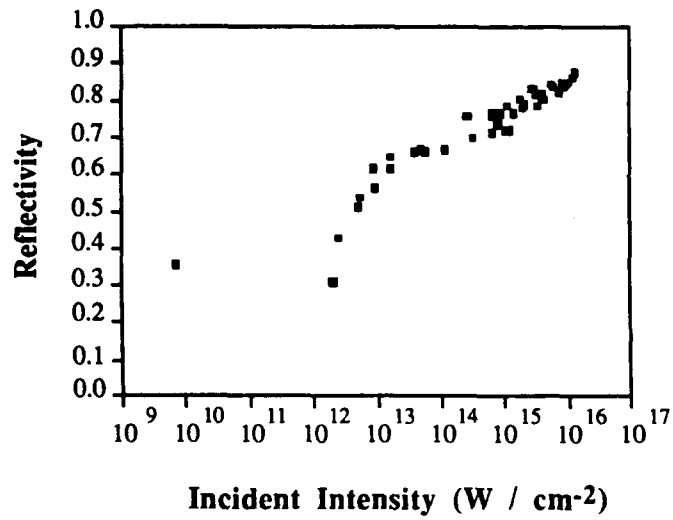

Figure 1: Reflectivity of a flat Si target, as the laser intensity is increased.

Results

In contrast, for low values of n and k, the reflectivity of a target surface will be low. Therefore, if the solid is "dilute" i.e. of low density, and the scale length of interaction is sufficiently long, the laser light will be absorbed. However, merely reducing the material density alone and increasing the interaction length will result in a hot, low-density plasma. Such plasmas have been shown to exhibit slow cooling[4], resulting in relatively long (> 100 ps) x-ray pulse durations. On the other hand, materials such as gold smoke or black[5], consisting of chains of clusters of ≈ 100 Å particles, have a low average density but high cluster density. This material is typically between 0.1% and 1% of solid density, and has large voids which are not filled in as a result of plasma expansion during the laser light absorption. The refractive index in the visible region can be approximated using a Drude model and an average material electron density. For a laser of frequency ω, collision time τ, and plasma frequency ω_p, the refractive index N is given by -

$$N^2 = (n + i\,k)^2 = 1 - \frac{\omega_p^2}{\omega^2 + i\,\omega\,\tau^{-1}}$$

where
$$\omega_p^2 = \frac{n_e e^2}{m_e \varepsilon_o}$$

The reduced average density implies that $\omega_p << \omega$, and because of the increased surface area and small particle size, τ is also lower than in a solid. Therefore, for gold black in the visible region, $n \approx 1$, $k \approx 0$ and therefore $R \approx 0$. The imaginary part of the refractive index scales as $k \approx k_s n_b / n_s$, where k_s is the solid value, n_s is the density of solid gold and n_b is the density of the black. The optical absorption depth δ is therefore given by -

$$\delta = \frac{c}{\omega k} = \frac{c\, n_s}{\omega\, k_s\, n_b} \approx 10^3 \times 100\ \text{Å} = 10\ \mu\text{m}$$

Experimentally, gold black exhibited low diffuse reflectivity, which was not measured.

A second type of dilute target, consisting of gratings of periodicity less than the laser wavelength of 6160 Å, was also studied[6]. The gratings were chosen such that 1) their periodicities were less than the laser wavelength, to avoid energy loss as a result of diffraction, and 2) the groove width was sufficiently wide (≥ 1000 Å) so that the groove structure did not fill with low density blow-off vapor during the laser pulse.

For the grating targets, the reflected beam was specular, and the reflectivity could be measured accurately. Figure 2 shows the incident laser reflectivity as a function of grating depth, at an incident power density of 10^{16} W cm^{-2}, and for incident laser polarization perpendicular to the grooves.

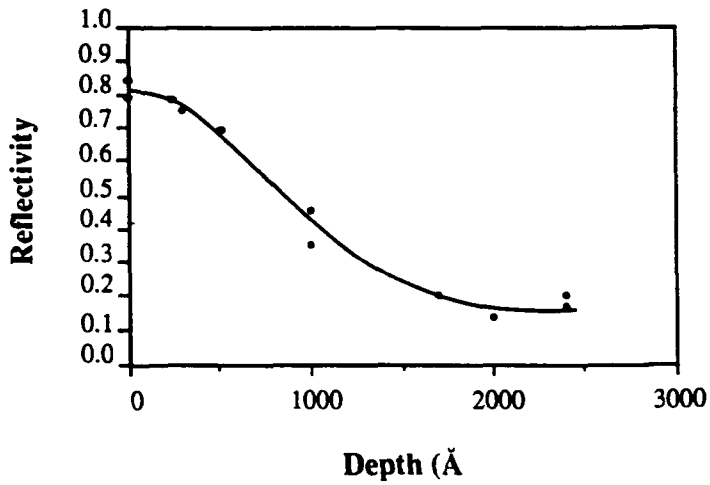

Figure 2: Measured reflectivity of grating targets as a function of groove depth, at an incident laser intensity of 10^{16} W cm^{-2}.

The increased absorption is not merely due to the increased surface area presented to the incident laser by the grating surface - the absorption per unit area actually increases by > 3. Since the periodicities of the grating structures were between $\lambda/2$ and $\lambda/3$, a long wavelength approximation, which simply averages the material density, cannot be used to calculate the refractive index. A different average index model is more appropriate in this case.[7, 8] Preliminary calculations show that the grating targets behave like a lossy waveguide structure, and that the laser penetrates to depths of ≈ 1500Å. The walls of the groove structure absorb the laser energy, and the laser does not penetrate to the substrate

below the grating. The laser penetration into the grooves leads to an enhanced electric field within the grating grooves, which leads to an effective increased incident laser intensity on target, and therefore increased absorption. Rigorous calculations are in progress to exactly model the experimental results.

The absolute x-ray yields from both types of targets were measured using a United Detector XUV005HS x-ray diode. For gold black, we measured a total laser-to-x-ray conversion efficiency of $\gtrsim 20\%$, and a conversion efficiency of $\geq 1\%$ into x-rays with energies above 1 keV. For sufficiently deep gratings, we observed total laser-to-x-ray conversion efficiencies of $\geq 12\%$, with $\geq 0.6\%$ of the x-rays at energies above 1 keV. These high conversion efficiencies were obtained using gold-coated gratings. (The measured reflectivities on the other hand, were insensitive to the material of the grating.)

The x-ray pulsewidths from both the gold black and grating targets, were measured using a fast x-ray streak camera.[9] Data for different energy regions were taken by inserting different x-ray filters between the plasma and the streak camera. We measured instrument-limited x-ray pulsewidths of 2 ps for the high-energy photons above 1 keV from both targets. The true pulsewidth is sub-picosecond[9] when the instrument response is deconvolved. For x-rays below 1 keV, the measured pulsewidth was somewhat longer. Gold black emissions in the soft x-ray region were approximately a factor of 2 longer than those of grating targets, possibly due to slower cooling at lower material density. We have not determined to date if this increase in x-ray pulsewidth has contributions from space-charge effects in the streak camera, which can be severe for short pulses.

In conclusion, we have succeeded in coupling most of the energy of high-power short laser pulses into solids. The solids used were structured, with dense solid-like portions and large voids. This simultaneously lowered the incident laser reflectivity, while maintaining fast cooling in the plasma when the solid portions expanded. We have measured conversion efficiencies of laser light to sub-picosecond x-rays above 1keV of $\approx 1\%$. This corresponds to a peak x-ray flux of 20 MW, at a repetition rate of 10 Hz.

Acknowledgments

The authors wish to thank Andrew Hawryluk and Russell Wallace of Lawrence Livermore National Laboratory (LLNL) for fabricating some of the targets, and Ernie Glover for help with the laser. The authors acknowledge helpful conversations with Harald Hamster, Thomas McIlrath and Gary Collins. This work was supported by the U.S. Air Force Office of Scientific Research, and the Department of Energy through a collaboration with (LLNL). MM and HK acknowledge support from WSU.

References

1. M. M. Murnane, H. C. Kapteyn, M. D. Rosen, R. W. Falcone, Science **251**, 531 (1991).
2. M. Murnane, Ph. D. Thesis (University of California at Berkeley, 1989).
3. M. M. Murnane, R. W. Falcone, J. Opt. Soc. Am. B **5**, 1573 (1988).
4. M. M. Murnane, H. C. Kapteyn, R. W. Falcone, Phys. Rev. Lett. **62**, 155 (1989).
5. S. Verghese, P. L. Richards, K. Char, S. A. Sachtjen, IEEE Trans. Mag. **27**, 3077 (1991).
6. H. C. Kapteyn, M. M. Murnane, A. Szoke, A. Hawryluk, R. W. Falcone, in *Ultrafast Phenomena VII* , C. B. Harris, E. P. Ippen, G. A. Mourou, A. H. Zewail, Eds. (Springer-Verlag, Berlin, 1990),Vol. 53, pp. 554.
7. N. F. Hartman, T. K. Gaylord, Appl. Opt. **27**, 3738 (1988).
8. T. K. Gaylord, E. N. Glytsis, M. G. Moharam, Appl. Opt. **26**, 3123 (1987).
9. M. M. Murnane, H. C. Kapteyn, R. W. Falcone, Appl. Phys. Lett. **56**, 1948 (1990).

Direct Measurement of Nonequilibrium Electron Energy Distribution in Sub-Picosecond Laser-Heated Gold Films

W. S. Fann, R. H. Storz and J. Bokor
A. T. & T. Bell Laboratories
Crawford Corner Road 4C328
Holmdel, NJ 07733
(201) 949-2657

Electron heating in metals by ultrashort laser pulses has been under intensive investigations in recent years[1,2]. It is generally believed that in a very short time (< 1-2 fsec) after the optical excitation, the electrons equilibrate among themselves via the electron-electron interaction, and establish a thermal Fermi-Dirac distribution at an elevated temperature. The electron-phonon interaction operates on a longer timescale of several psec to equilibrate the electrons with the lattice phonons.[1,2] During those several psec, the electrons are decoupled from lattice and it is possible to heat the electrons alone up to several thousand K. However no direct measurements of the electron energy distribution function in laser-heated metals have been reported so far. We have used ultraviolet photoemission spectroscopy to directly obtain the energy distribution function with 500 fsec time resolution. We confirm that on this time scale, the distribution is well described by a Fermi-Dirac function and we thus directly measure the time-dependence of the electron temperature.

In this experiment a 674 nm wavelength (1.84 eV photon energy) pump laser pulse of 500-fs duration is used to heat a 300 Å gold film. The

incident fluence is around 1 mJ/cm^2 and 15 % of light is absorbed. The photoelectron spectrum is measured in the normal direction by the time-of-flight technique using a 500-fs probe pulse of 225 nm wavelength (5.52 eV photon energy) light. The work function of gold is 4.3 eV and thus single-photon photoemission by the probe beam extends to 1.22 eV below the Fermi-level. Extreme care is exercised to eliminate space-charge effects on the photoemission spectrum. However, at the pump fluences required to produce substantial electron heating, multiphoton photoemission from the pump alone could not be completely avoided. The single-photon probe spectrum is recovered by subtracting the spectrum taken with the pump alone from the raw spectrum taken with both the pump and probe. A companion "pump only" spectrum was taken immediately after each pump/probe spectrum in order to insure the integrity of this procedure. Fig.1(a) is the photoelectron spectrum processed in this way at +13 picoseconds time delay between the pump and probe. The smooth curve is the best fit of a Fermi-Dirac function to the edge region. The electron temperature is determinated as 360 K. Fig.1(b) is the spectrum taken with the pump and probe overlapped in time. Here, as well, the distribution is well fit by the Fermi-Dirac function and the electron temperature is determinated as 1200 K. By using the electronic heat capacity[2] of Au it is estimated the temperature rise should be 1000 K which is consistent with our measurement. Fig.2 is a plot of the fitted electron temperature versus time delay when 0.12 mJ/cm^2 of pump is absorbed. With our present signal/noise ratio, the measured temperatures are accurate to $\pm$ 50 K. The electron-phonon coupling constant, $G = 4 \cdot 10^{16} W/m^3K$, is determinated by fitting the data with coupled

Fig. 1

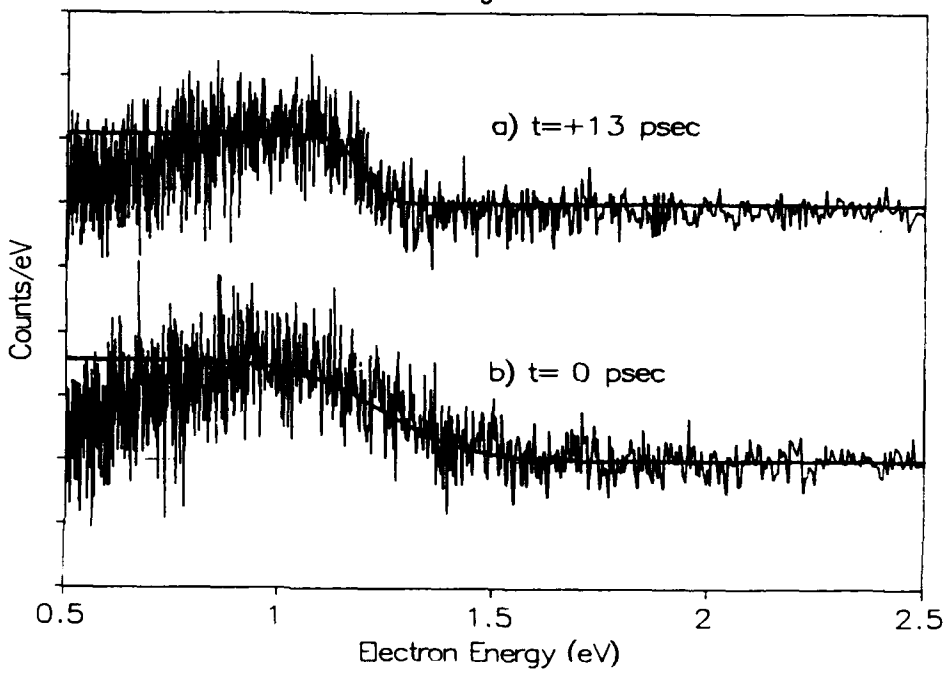

Fig.1 (a) The photoemission spectrum at +13 ps delay with 0.18 mJ/cm^2 absorbed. The smooth curve is a best fit Fermi-Dirac function with an electron temperature of 360K. (b) The photoemission spectrum at 0 ps delay. The best fit electron temperature is 1200K .

differential equations between the electron and lattice described in Ref.1. The result is consistent with the measurement in Ref. 2.

In summary, we have demonstrated that ultraviolet photoemission spectroscopy can be used as a tool to measure the energy distribution of nonequilibrium electrons in sub-picosecond laser-heated materials. With further improvement in time resolution[4], it may be possible to directly observe the initial thermalization within the electron system itself.

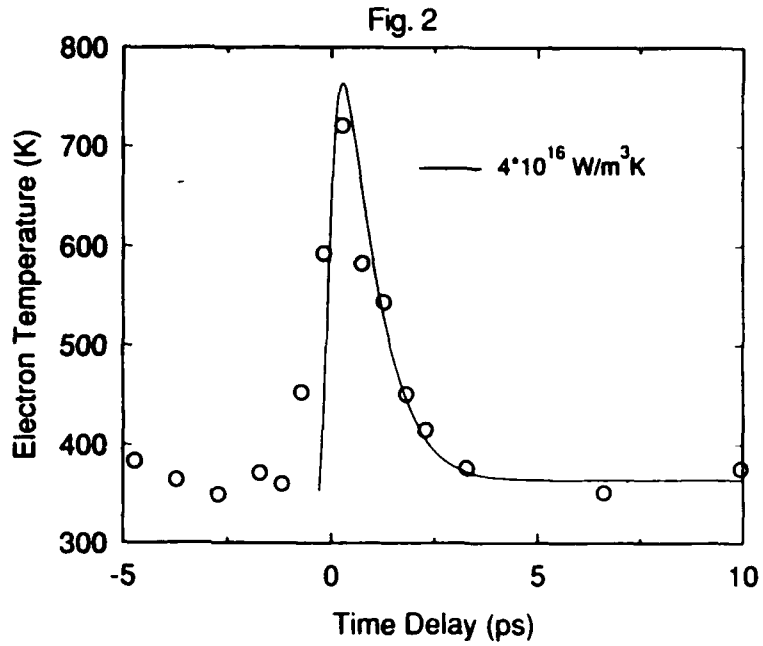

Fig. 2 Electron temperature measurements vs time delay with 0.12 mJ/cm^2 absorbed . The solid line is the fit with $G= 4*10^{16} W/m^3K$.

References

1. H. E. Elsayed-Ali, T. B. Norris, M.A. Pessot, and G. A. Mourou, Phys. Rev. Lett. **58**, 1212 (1987); R. W. Schoenlein, W. Z. Lin, J. G. Fujimoto, and G. L. Eesley, Phys. Rev. Lett. **58**, 1680 (1987).

2. H. E. Elsayed-Ali, T. Juhasz, G. O. Smith, and W. E. Bron, in **Ultrafast Phenomena VII,** C. B. Harris, E. P. Ippen, G. A. Mourou, and A. H. Zewail, eds. (Springer-Verlag, Berlin, 1990).

3 C. Kittel, **Introduction to Solid State Physics** (John Wiley & Sons, 1976).

4. R. W. Schoenlein, J. G. Fujimoto, G. L. Eesley, T. W. Capehart, Phys. Rev. Lett. **61**, 2596 (1988).

Soft-X-Ray Spectra from Laser Plasma Effectively Heated by a Pulse Train Laser

Hideo Hirose,* Tamio Hara, Kozo Ando, Fumiko Negishi-Tsuboi, Hidehiko Yashiro,** and Yoshinobu Aoyagi

The Institute of Physical and Chemical Research (RIKEN), Wako-shi, Saitama 351-01, Japan

Abstract

A pulse train laser with low peak power can heat a dense plasma effectively and promote ionization of atoms up to higher stages such as Li-like Al. This fact was proved by soft x-ray spectra.

Introduction

X-ray emission from laser produced plasma has been extensively studied for many years and now has found new promising application in variety of field, including, for example, various forms of x-ray spectroscopy, x-ray laser, as well as microscopy and lithography. Among them, considerable progress has been made in the development of soft x-ray laser since 1985[1-2]. Until now a powerful laser of a single pulse has often been used to produce high density plasma. Recently we observed ASE (Amplified Spontaneous Emission) in some lines of Al X and Al XI in a recombining plasma produced by a very low power laser of only 2 J which was composed of a train of many pulses separated by about 350 ps.

To study in detail the effect of multi-pulse irradiation on the production of laser plasma and on x-ray emissions including ASE, we constructed a pulse train forming system and investigated the emitted soft x-ray spectra for various pulse trains. As is shown later, a pulse train laser can effectively produce the higher stages of ions such as Li-like ions from which some of ASE lines have been reported. Our final goal is to develop a table top x-ray laser in the water window wavelength by using the pulse train laser.

© 1991 Optical Society of America

Experiment

Laser plasma was produced by focusing a pulse train Nd;glass laser on an Al slab target. Various kind of pulse trains was generated by an optical pulse stacker[4] which is consisted of three optical delay loops connected in series by four half mirrors (50 % reflector). Each pulse has almost the same peak power(I_p) and the same interpulse time (T). The pulse width of each pulse was about 100 ps. By blocking more than one loop, the number of pulses within a train can be changed. In order to vary time interval(T) between pulses, the optical delay was changed by moving prisms parallel to the optical paths.

The pulse train was amplified by glass amplifiers and line-focused on an Al target with a 7.5mm length by a cylindrical lens (focal length is 450mm). Focal line width was about 50 μm. Soft x-ray spectra were observed along the axial direction of a line plasma at a distance of 300 μm from the Al target surface by using a XUV

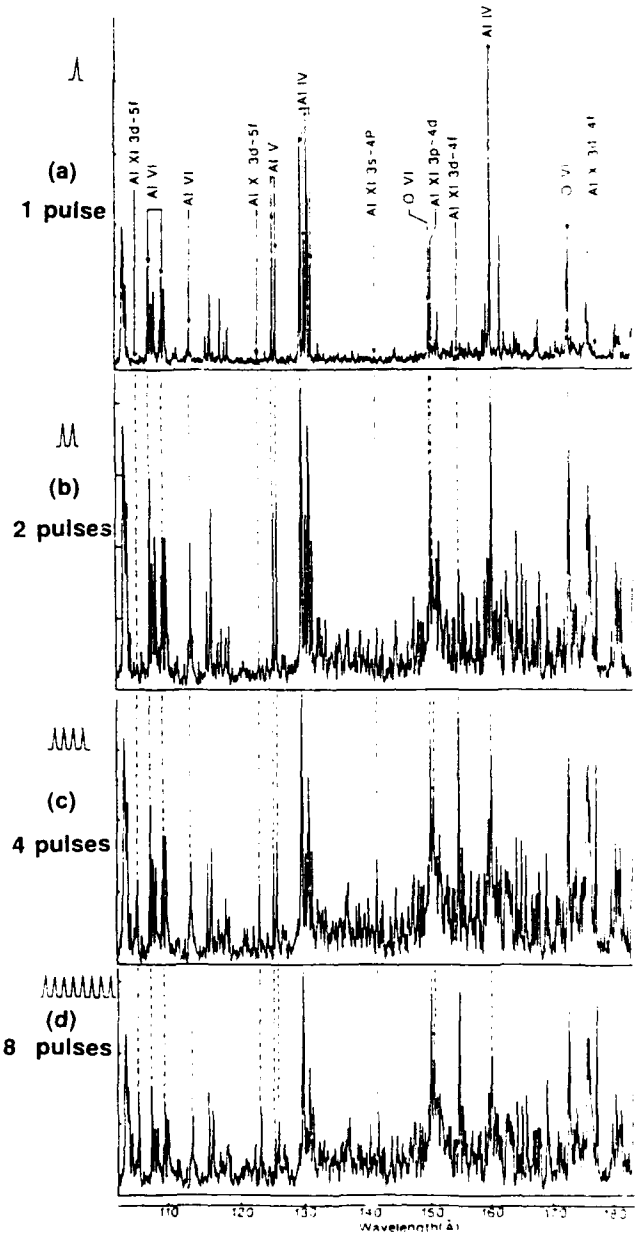

Fig. 1 Microdensitometer traces of time integrated XUV spectra obtained from (a) a single, (b) two, (c) four and (d) eight pulses train laser. Exposures are 8, 4, 2 and 1, respectively. Peak power is 4×10^{11}W/cm^2.

spectrograph. Pulse energy irradiated onto the target was estimated to be 0.15 J/pulse which corresponded to the power density of 4×10^{11} W/cm^2.

Result

Typical examples of Al spectra in the range of 100-185 Å are shown in Fig. 1(a), (b), (c) and (d) for trains of one, two, four and eight pulses, respectively. Note that each spectrum has different exposures, that is, different number of laser shots in order to get almost equal line intensities on a SWR plate. There was a large difference among these spectra. Most of lines obtained by a single pulse irradiation [Fig. 1(a)] were emitted from relatively low ionization stages (Al IV, V, VI etc.). With increasing the number of pulses, many spectral lines appear in spectrum. Lines of highly ionized aluminum atoms such as Al XI grew dramatically with increasing the number of pulses (4 or 8), while lines of lower ionized atoms were also present. Lines of higer ionized atoms also appeared in a spectrum with eight pulses train, even if the peak power was reduced below 10^{11}W/cm^2.

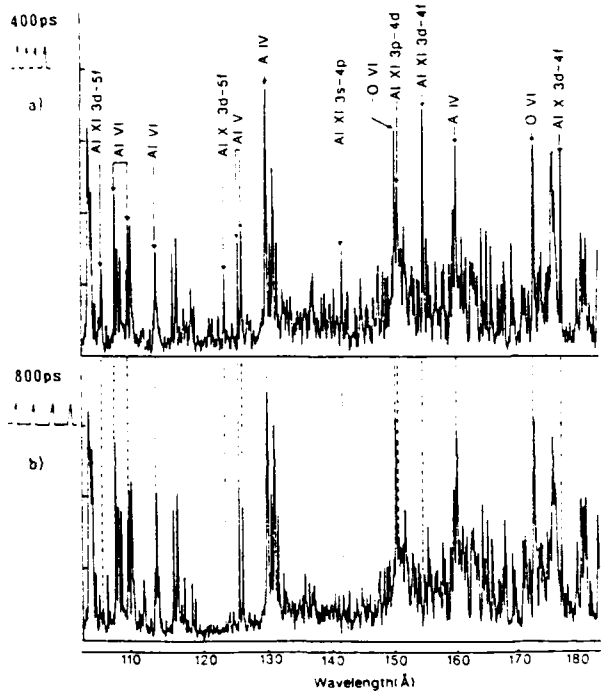

Fig. 2 Dependence of X-ray spectrum on interpulse time. The number of pulses is four. Exposures are twice.

It is important to study variation of plasma for time interval between pulses while keeping the peak power and number of pulses constant. Figure 2(a) and (b) shows spectra of 400 ps and 800 ps intervals, respectively. Surprisingly, in a spectrum of 800 ps time interval, Li-like four lines disappeared and only Al X 3d-4f (Be-like) line are hardly alive. Spectral behavior of other lines were almost independent to time intervals. The spectrum of 600 ps interval, which is not shown here, was very similar to that of 800 ps.

When interpulse time is decreased to zero, pulses are irradiated at the same time on the target and hence pulse train become a single pulse. A spectrum obtained from a single pulse irradiation whose peak power (13×10^{11}W/cm^2)is four times higher than that of a pulse train used in Fig. 1. Emissions from Li- and Be-like ions also appeared. It is

interesting that spectral characteristics was very similar to that which was obtained from four pulses train [see fig. 1(c)], although production mechanism of Li- and Be-like ions may be quite different in both temporally and spatially. When peak power of a single pulse laser was increased by twice, an X-ray spectrum was also similar to that of eight pulses train shown in Fig. 1(d).

Line intensities of three different kind of ionization stages (Al VI, Al X and Al XI) are plotted as a function of interpulse time for a train of four pulses in Fig. 3. Line intensities are normalized at 100 ps. From this figure, optimum time interval for efficient heating of plasma is estimated to be about 200 ps.

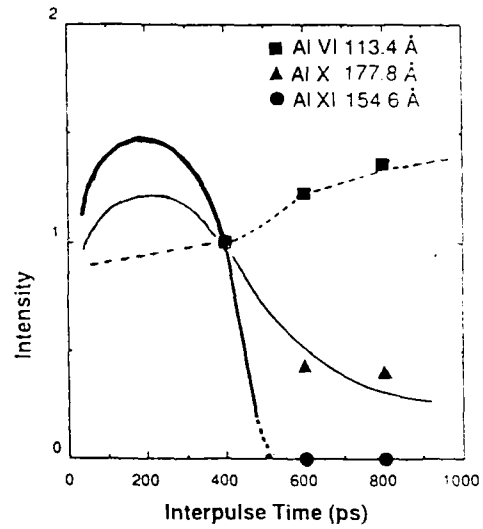

Fig. 3 Line intensity as a function of interpulse time T for three different kind of ion spices (Al VI, X, XI). Intensities are normalized at 100 psec.

Discussion

The above results has shown very clearly the effect of pulse train laser on the soft X-ray spectra and give understanding of the production mechanism of highly ionized atoms in a high density laser plasma. Electron temperature plays an important role to produce high ionization stages in plasma. Our experimental results show that multi-pulse irradiation creates hotter plasma than single-pulse irradiation and therefore higher ionization stages such as a Li-like ion can be attained. Each pulse may act as a pre-pulse for next incoming pulses, part of which is absorbed by the pre-formed plasma, and therefore raises the electron temperature of plasma more effectively. As a result, efficient and successive heating near the target surface may occur with increasing the number of pulses. In this consideration, interpulse time (T) is an important factor in order to attain the higher electron temperature of plasma, because such a plasma heating must be done successively before electron temperature decreases due to adiabatic expansion. Our experimental result shows that efficient heating must be achieved within the 400 ps.

In this way, irradiation of a multiple pulses significantly promotes ionization of atoms as a result of successive heating of a plasma. Production of Li- or Be-like ion is very important to get ASE in the recombination mode of Al plasma, because recombination processes of such ions in plasma can produce population inversion.

Conclusion

In conclusion, ionization to highly charged stages in laser produced plasma is enhanced by using a pulse train laser. The advantage of this novel method is that peak power needed for producing a Li-like ions can be reduced greatly to less than 10^{11}W/cm^2. Enhancement of the X-ray conversion efficiency might also be expected[5-6]. The invention of pulse train laser will further accelerate the development of a table top X-ray source including X-ray laser.

* Shimadzu Corporation, Nakagyo-ku, Kyoto 604, Japan.
** Faculty of Engineering, Saitama Univ., Urawa, Saitama 338, Japan.

References

1. D.L.Matthew, P.L.Hagelstein, M.D.Rosen, M.J.Eckart, N.M.Ceglio, H.M.Medecki, B.J.MacGowan, J.E.Trebes, B.L.Whitten, E.M.Camphell, C.W.Hatcher, A.M.Hawryluck, B.L.Kauffman, L.D.Pleasance, G.Rambach, J.H.Scofield, G.Stone, and T.A.Weaver, "Demonstration of a Soft X-ray Amplifier," Phys. Rev. Lett. 54, 110-113(1985).
2. S.Suckewer, C.H.Skinner, H.Milchberg, C.H.Keane, and D.Voorthees, "Amplification of Stimulated Soft-X-ray Emission in a Confined Plasma Column," Phys. Rev. Lett., 55, 1753-1756(1985).
3. T.Hara, K.Ando, Y.Aoyagi, and H.Yashiro, "Compact Soft X-ray Laser," in *Fifteenth International Conference on X-Ray and Inner-Shell Processes*(Knoxville, Tennessee, 1990).
4. C.N.Danson, C.B.Edwards and I.N.Ross, "A Pulse Stacker for Time-resolved Laser Plasma Diagnostics," Optics and Laser Technology, 11, 99-101(1985).
5. F.O'Neill, I.C.E.Turcu D.Xenakis, and M.H.R.Hutchinson, "X-ray Emission from Plasmas Generated by an XeCl laser picosecond pulse train," Appl. Phy. Lett., 55, 2603-2604(1989).
6. R.Kodama, T.Mochizuki, K.A.Tanaka, and C.Yamanaka, "Enhancement of keV x-ray emission in laser-produced plasma by a weak prepulse laser," Appl. Phys. Lett., 50, 720-722(1980).

Hydrodynamic Evolution and Radiation Emission from an Impulse-Heated Solid Density Plasma

I. Lyubomirsky, C. G. Durfee III, and H. M. Milchberg

Institute for Physical Science and Technology and Department of Electrical Engineering, University of Maryland, College Park, Maryland 20742

ABSTRACT

We present results from a 1-D plasma dynamics calculation, describing the evolution of strongly heated material in the vicinity of a solid-vacuum interface. We find that the radiation emitted by the hot material in the range $h\nu > kT_e$, where T_e is the initial peak plasma temperature, comes primarily from the region of the original step function interface. This emission is dominated by recombination radiation. The emitted radiation pulse is extremely short; the cooling at the interface is dominated by expansion.

1. INTRODUCTION

The interaction of energetic subpicosecond laser pulses with solid matter is of great current interest because of the possibility of producing ultrashort x-ray pulses from the resulting plasmas,[1] or for the study of the properties of the novel, highly excited material.[2]

Here we describe a simple model of the evolution of a solid target given a specified temperature profile behind a step function interface at t=0. The laser beam energy deposition process is not modelled; we are interested in the impulse response of the system, which would indicate a minimum for the x-ray pulsewidth produced by the plasma. A somewhat low Z material, carbon, is the material modelled, mainly for the purpose of reducing the calculation time.

2. MODEL

We use the "one-fluid" model[3] (equations for density, momentum, and energy balance) for the macroscopic plasma variables ε, ρ, v, where these variables refer, consecutively, to internal energy, mass density, and velocity. Internal energy includes electron thermal energy and energy stored in ionization states of carbon. It is assumed that the ion kinetic temperature is zero; on the timescales considered here, electron-ion energy transfer is mainly through ionization, excitation, and recombination of the ions. Pressure and temperature are related by the ideal gas equation of state, while electron and ion densities are determined by a collisional radiative[4]

Proceedings on Short-Wavelength Coherent Radiation, Vol. 11, Philip H. Bucksbaum and Natale M. Ceglio (eds.)
© 1991 Optical Society of America

model, which was run either in steady-state or in transient mode.[5] A gradient heat conduction term with Spitzer thermal conductivity[9] was used in the energy balance equation. The thermal conduction may actually be considerably less than this, either through large plasma resistivity[2] or flux-limited heat flow,[8] but the effect of thermal conduction will, in any case, be seen as less important than expansion to the generation of ultrashort x-ray pulses in the range of frequencies $h\nu > kT_e$. The bulk material temperature (to the left of the initial temperature profile) is taken to be 5 eV, in order to provide non-zero thermal conduction there. The electrons are assumed to be thermally equilibrated among themselves (Maxwellian at high T_e), with collisional mean free paths smaller than any density scale lengths; a space dependent temperature can be defined.

Expressions for recombination and bremsstrahlung radiation have been obtained from ref. 6, which assumes Maxwellian electrons and well defined bound states. Line radiation was calculated by assuming that the populations of the two lowest excited states of each ion are in local thermal equilibrium with their corresponding ground state populations, a reasonable approximation at near-solid density. Opacity effects are ignored: the mean free path for continuum absorption is thicker than the heated layer, and collisional deexcitation at solid density strongly competes against repopulation through reabsorption of line radiation. We take high density plasma effects such as continuum lowering into account by considering recombination into and line radiation from only the two most strongly bound states of each ion.

3. RESULTS

As an initial condition at t=0, the peak temperature at the interface is taken as 200 eV, and decays in a half-Gaussian profile with a FWHM of 500 Å. This corresponds roughly to the depth that the heat front would penetrate in 100 fs. The results of three runs are shown: (a) Time-dependent collisional-radiative model, conduction "on" (heat conduction included in energy balance equation); (b) steady state collisional-radiative model (time derivatives in atomic rate equations set to zero), conduction "on"; and (c) time dependent collisional-radiative model, conduction "off".

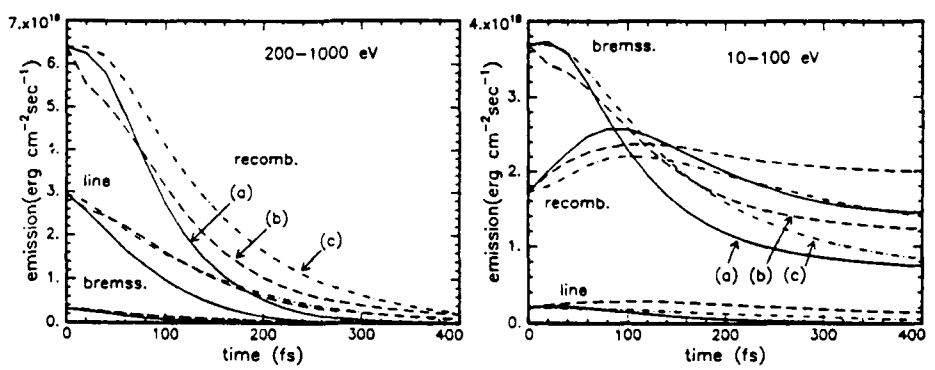

Figure 1: Time evolution of space-integrated recombination, bremsstrahlung, and line radiation in the energy intervals (i) 200-1000 eV (left panel) and (ii) 10-100 eV (right panel) for a carbon plasma under conditions (a), (b), and (c) (see text).

Figure 1 shows the space integrated recombination, line, and bremsstrahlung radiation emitted from the plasma under conditions (a), (b) and (c). Recombination radiation clearly dominates line and bremsstrahlung radiation in interval (i), while recombination and bremsstrahlung emission are comparable in region (ii), dominating line radiation. It is seen that for the higher energy radiation (i), the pulsewidths are all less than 200 fs, for (a), (b), *and* (c).

These results can be explained by examination of Fig. 2, which shows the spatial dependence of the recombination emission at various times, for conditions (a), (b) and (c) in spectral regions (i) and (ii). The emission clearly comes from the interfacial region, which is rapidly cooled by expansion and is rapidly decreasing in density. In the bulk, high ion stages are suppressed (see Fig. 3), even at the high temperatures conducted into the target, because of the high degree of three-body recombination.[7] Since the high ionization stages have relatively low densities in the bulk, recombination radiation from the bulk is relatively weak. Long before the eroding interface moves appreciably to the left, the electron temperature has decreased substantially.

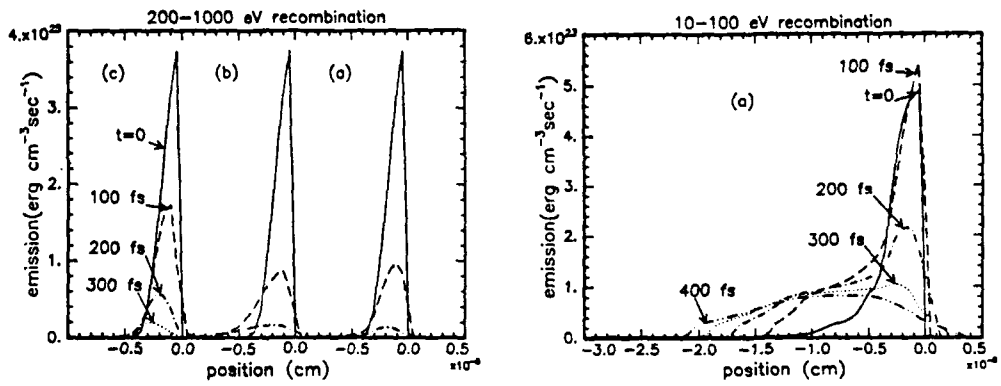

Figure 2: Spatial distribution of recombination radiation emission at various times for energy intervals 200-1000 eV (top panel, for conditions (a), (b), and (c) (see text)) and 10-100 eV (bottom panel, for condition (a)).

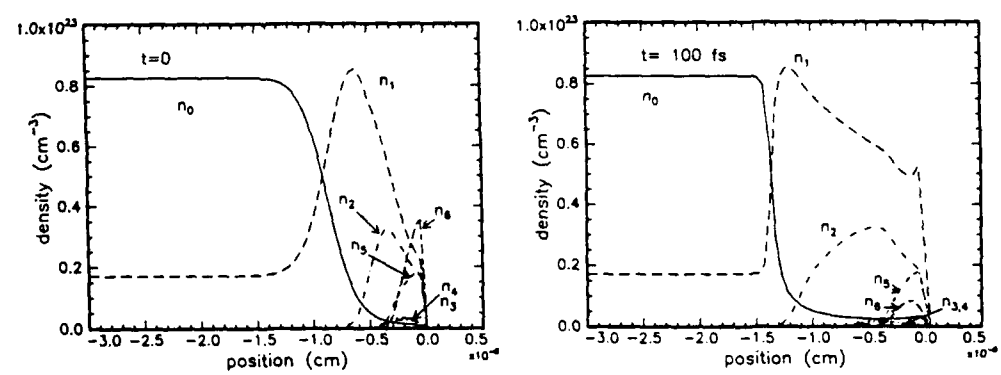

Figure 3: N_i is the density of i times ionized carbon. Both plots under condition (a) (see text)

5. ACKNOWLEDGMENTS

The authors gratefully acknowledge the helpful assistance of Chris Keane of Lawrence Livermore Lab (LLNL) for providing the ionization and recombination rates and A. C. Hindmarsh (LLNL) for providing us with his package of ODE solvers. This work is supported by the National Science Foundation (contract No. ECS-8858062), and the AFOSR (contract no. 88-0018). I. Lyubomirsky acknowledges the support of an NSF Research Experiences for Undergraduates Award.

6. REFERENCES

1. M. M. Murnane, H. Kapteyn, and R. Falcone, Phys. Rev. Lett. **62**, 155 (1989).
2. H. M. Milchberg, R. R. Freeman, S. C. Davey, Phys. Rev. Lett. **61**, 2364 (1988).
3. N. A. Krall and A. W. Trivelpiece, *Principles of Plasma Physics*, (McGraw-Hill, New York, 1973).
4. H. P. Summers, Mon. Not. R. Astr. Soc. **169**, 663 (1974).
5. A. C. Hindmarsh, *ODEPACK, a Systemized Collection of ODE Solvers*, (LLNL UCRL-88007 report, August 1982).
6. S. Von Goeler, W. Stodiek, H. Eubank, H. Fishman, S. Grebenshchikov, and E. Hinnov, Nuc. Fusion **15**, 301 (1975).
7. H. M. Milchberg and H. R. Griem, Phys. Rev. Lett. **63**, 338 (1989).
8. C. E. Max, in *Interaction Laser-Plasma, Les Houches, 1980*, R. Balian and J. C. Adam, eds. (North Holland, Amsterdam, 1982).
9. L. Spitzer, Jr., *Physics of Fully Ionized Gases*, (Interscience, New York, 1962).

A

Allendorf, Sarah W., 28, 227
Amendt, Peter, 91, 96, 116
Ando, Kozo, 289
Antonetti, A., 240
Aoyagi, Yoshinobu, 289
Audebert, P., 240
Augst, S., 23
Azuma, H., 77

B

Baldis, H. A., 69, 87, 119
Baldwin, K. G. H., 12
Balmer, J. E., 53
Bardsley, J. N., 247
Beaudoin, Y., 216, 266
Belenov, E. M., 127
Benattar, R., 240
Blair, R. J., 181
Blodgett-Ford, Sayoko, 190
Bogacz, S. A., 82
Bokor, J., 170, 252, 281, 285
Boller, K. -J., 257
Boyer, K., 42, 196
Brunel, F., 62
Bucksbaum, P. H., 222, 252
Budil, K. S., 28
Burkhalter, P. G., 42
Burnett, K., 271
Burnett, N. H., 62

C

Capjack, C. E., 62
Carillon, A., 123
Carter, M. R., 116
Carver, J. H., 12
Casperson, D. E., 47
Ceglio, N. M., 135
Chaker, M., 87, 119, 266
Chambaret, J. P., 240
Chen, Shisheng, 52
Chien, C. Y., 7, 266, 276
Clark, Charles W., 190
Cobble, J. A., 47
Coe, J. S., 7, 266, 276
Corkum, P. B., 62, 216, 238
Crane, J. K., 28

D

Daido, H., 77
Davey, S. C., 160
Dhez, P., 123
DiMauro, L. F., 201
Downer, M. C., 244
Dunn, J., 69, 87, 119
Durfee III, C. G., 262, 294
Dyer, Mark J., 58

E

Eden, J. G., 232
Eder, D. C., 96
Ellenberger, U., 53
Enright, G. D., 62, 69, 87, 119
Esarey, E., 7

F

Falcone, R. W., 181, 281
Fann, W. S., 285
Faris, Gregory W., 58
Farkas, A. M., 232
Feit, M. D., 116
Fleck, J. A., 116
Freeman, R. R., 160, 170, 209, 252
Fulton, R. D., 47

G

Gaines, D. P., 135
Gang, Y., 77
Gauthé, B., 123
Gauthier, J. C., 240
Gaylord, T., 281
Geindre, J. P., 240
Gibson, G. N., 209
Gibson, S. T., 12
Glytsis, E., 281
Gnall, R., 281
Goedtkindt, P., 123
Gordon, S., 181, 281
Grigoriev, S. V., 127
Gu, Y. Y., 232
Gullikson, Eric, 167

H

Hamster, H., 181
Hara, Tamio, 289
Harris, S. E., 257
Hawryluk, A. M., 135
Hirose, Hideo, 289
Howells, M., 130

I

Imamoglu, A., 257

J

Jacobs, V. L., 42
Jacobsen, C., 130
Jaegle, P., 123
Jamelot, G., 123
Jones, L. A., 47

K

Kanabe, T., 77
Kaplan, A. E., 163
Kapteyn, Henry C., 36, 181, 281
Kato, Y., 77
Key, M., 77
Kieffer, J. C., 87, 119, 123, 266
Kincaid, Brian M., 146
Klisnick, A., 123
Kmetec, J. D., 176
Kortright, Jeffrey B., 167
Krause, J. L., 186
Kulander, K. C., 186
Kyrala, G. A., 47

L

La Fontaine, B., 69, 87
Lewis, B. R., 12
Lewis, C., 77
L'Huillier, A., 2
Lindaas, S., 130
Liu, X., 7, 276
Lompré, L. A., 2
London, Richard A., 91, 116, 135
Lucatorto, T., 160
Luk, T. S., 42, 196
Lyubomirsky, I., 294

M

MacGowan, Brian J., 67
Macklin, J. J., 176
Mainfray, G., 2
Mansfield, W. M., 170, 281
Marconi, M. C., 106
Matthews, D. L., 69, 116
Maxon, S., 116
McIlrath, Thomas J., 12, 18, 160, 209
McPherson, A., 42, 196
Meyer, J., 106
Meyerhofer, D. D., 23
Midorikawa, Katsumi, 111
Milchberg, H. M., 262, 294
Miura E., 77
Mohideen, U., 170, 252
Moore, C. I., 23
Morrison, G. R., 141
Mourou, G., 222, 266
Murai, K., 77
Murnane, Margaret M., 36, 281
Mysyrowicz, A., 240

N

Nagel, D. J., 42
Nakai, S., 77
Nantel, M., 119
Nash, J. K., 96
Nathel, H., 181
Nazarkin, A. V., 127
Neely, D., 77
Negishi-Tsuboi, Fumiko, 289
Newman, D. A., 42
Nguyen, Tai D., 167

O

Obara, Minoru, 111
O'Neill, D., 77

P

Pakula, Ricardo A., 101
Palmer, J. R., 141
Parker, Jonathan, 190
Peatross, J., 23
Penetrante, B. M., 247
Pépin, H., 87, 119, 266
Perry, M. D., 28
Pert, G., 77

Q

Qian, Aidi, 52

R

Rae, S. C., 271
Ramsden, S., 77
Rankin, R., 62
Raucourt, J. P., 123
Rhodes, C. K., 42, 196
Rocca, J. J., 106
Rosen, Mordecai D., 69, 73, 96
Rosen, R. S., 152

S

Saeed, M., 201
Salin, F., 222
Schafer, K. J., 186
Schappert, G. T., 47
Schumacher, D. W., 222
Seppala, L. G., 135
Sher, M. H., 170
Shiraga, H., 77
Shkolnikov, P. L., 163
Smetanin, I. V., 127
Soom, B., 53
Sprangle, P., 7
Squier, J., 222
Stearns, D. G., 152
Stewart, R. E., 116
Storz, R. H., 285
Strauss, Moshe, 91, 116
Strickland, D., 216, 238
Sullivan, A., 181
Szöke, Abraham, 227
Szapiro, B. T., 106

T

Takabe, H., 77
Takagi, M., 77
Tanaka, K., 77
Tashiro, Hideo, 111
Tate, D. A., 42, 196
Taylor, A. J., 47
Togawa, T., 77
Tom, H. W. K., 170, 252
Trebes, J. E., 116

U

Umstadter, D., 7, 276

V

vanWoerkom, L. D., 160
Verghese, S., 281
Vernon, S. P., 152
Villenueve, D. M., 69, 87, 119

W

Wahlin, E. K., 47
Wang, Xiaofang, 52
Waskiewicz, W. K., 160
Watabe, Toshihisa, 111
Weber, R., 53
Weihe, F., 222
Westbrook, Chris I., 18
White, W., 181
Wilks, Scott C., 33, 96
Wood II, O. R., 170
Wood, Wm. M., 244

X

Xiong, Xiaoxiong, 18
Xu, Zhizhan, 52

Y

Yamakawa, K., 77
Yamanaka, M., 77
Yang, B., 201
Yashiro, Hidehiko, 289
Young, J. F., 176
Young, P. E., 69

Z

Zavriyev, A., 222
Zietkiewicz, C. J., 232
Zigler, A., 42